DSE - Velo-E-Raptor Group 18

Final Report

M.J.M Aarts	4298446	J.T. van der Maten	4279247
K.M. Boon	1518844	R.A.A. Mink	4207491
S.J.L.B. Bourier	4292502	N.C. Nyessen	4377079
C.S.E. Geuens	4352343	T.O. Rootliep	4195728
R.J.A. van der Hulst	4307410	W. Schaberg	4290380

Final Report
Design Synthesis Exercise

TU Delft Delft University of Technology

Aerospace Engineering

July 3, 2017

This page has unintentionally been filled.

Acknowledgements

This report presents the final design of the Velo-E-Raptor DSE assignment from study group 18.

We would like to thank our principal tutor Ronald van Gent for his dedication, support, and his never ending enthusiasm for the project. Furthermore, thanks to our coaches Jesse van Kuijk and Weibo Hu for their help in the design process and enthusiasm in the project. Their frequent visits were much appreciated. Lastly, we would like to thank the staff of the faculty of Aerospace Engineering for providing us with an inspirational and safe environment.

Kind regards,

Group 18

Executive Summary

The goal of this project is to develop a foot launched, electrically assisted human powered air sport by 10 students within 10 weeks, called the Velo-E-Raptor. It aims to make flying accessible, safe and thrilling for the wider public. To promote accessibility, it aims to decrease regulation by developing an aircraft with a stellar safety record and zero nuisance to its surroundings during normal operations.

In the previous phase of the design process, several configurations were considered, from which the canard configuration was selected, in part due to its inherent stall safety. Other trade-offs determined that energy would be stored using batteries, the use of a single push propeller and the use of a windshield instead of a complete fairing.

In this report, a detailed configuration is presented, which was developed after several iterations. The aircraft has a wingspan of 16 m and a canard span of 5.2 m. To decrease the effect of the canard on the main wing and provide roll and yaw control, a V-tail is placed under the wing, with a height of 1.6 m and dihedral of 45°. It has a maximum takeoff weight of 190 kg combined with a maximum pilot weight of 90 kg and a target operational empty weight of 70 kg.

In the design phase leading up to this report, several verification and validation strategies were used. The general strategies can be found in their own chapter, with the implementation found embedded in each chapter. These strategies are split between the requirements, subsystems, and models. In addition, the approach for the sensitivity is also stated. The technical risks inherent in the design were rated according to the United States Airforce Analogue Rating system and mitigated. These mitigations were included in the design process and presented in a chapter in the report.

In the design phase leading to this report the first step taken was the selection of an airfoil. XFoil was used for generating the data for the trade-off, with 33 airfoils used for the wing and 20 for the canard. The trade-off was based on the maximum lift coefficient, minimum drag, maximum glide ratio, stall characteristics and other qualitative criteria. Different Reynolds numbers were chosen to use for the analysis to account for the root and chord lengths and cruise and stall speeds. For the main wing the MH201 was chosen, while the E214 was selected for the canard, due to the different requirements of both lifting surfaces.

After the airfoil selection, the three-dimensional shape of the wings was designed. All the relevant design parameters and their budgets were first defined. Using XFLR5 the wings were analyzed on their performance. The design was a highly iterative process between the different departments. It was important that the requirement for the stall speed was met in combination with an acceptable structure size.

During the design of the planform, an increasingly better drag estimation was made. The drag estimation was divided into two parts: the wing drag and the body drag. Doing this the estimation was made easier. Later the two parts were merged by looking at their interference. The wing drag was analyzed using XFLR5 were for the planform the viscous and induced drag were calculated. The body drag is the drag caused by all non-lifting parts of the aircraft. This has been estimated using the book on fluid dynamic drag of Hoerner (1965). After a sufficient estimate of the two parts was made the interference between the bodies was analyzed.

At last a design was made for the aircraft regarding the aerodynamics which can comply with the requirements imposed on it. The stall speed of the aircraft is 8.75 m/s with the use of plain flaps. The canard will stall gently before the main wing which results in the aircraft immediately reducing its angle of attack without losing to much lift, giving the design a gentle stall. The main wing stalls at a higher angle of attack and when it does limited amounts of control will be lost. The maximum glide ratio will be 19.4 at a speed of 16.5 m/s.

Combining the maximum glide ratio and its speed with the aerodynamic drag, the required propeller power is determined to be 1.6 kW. This is much higher than what an average human can generate, making that the electrical assist becomes a prerequisite to sustain leveled cruise flight. Maximal endurance can be achieved at a velocity of 15.4 m/s, with a required power of 1.5 kW. A minimum climb performance and takeoff requirement is used to obtain a minimal needed thrust value. In the end, the takeoff distance until lift-off is found to be 27 m, with a possible climb angle larger than 8 degrees. Furthermore, a climb rate of 2.3 m/s can be achieved.

This means that it will take the Velo-E-Raptor little more than 7 minutes to ascend 1000 m.

Then, a noise analysis is performed. Literature research points out that the main noise source for the Velo-E-Raptor will be loading noise of the propeller. All other noise sources are gathered in a safety noise factor. The noise pressure level is converted into A-weighted decibels (dBA). This corresponds to the level as experienced by the human ear. The propeller noise is found to be 40 dBA at a distance of 10 m. However, due to the propeller being in disturbed flow behind the pilot, an extra noise level of 20 dBA is added. The final noise found at 250 m is 30 dBA, equal to the sound level of a silent library. This is less than the noise generated by the Lockheed YO-3A “Quiet Star" which is generally regarded as undetectable.

A suitable propeller is designed using JavaProp. After an airfoil trade-off and a design parameter trade-off, an optimal design was found for the Velo-E-Raptor. This resulted in a propeller with an optimal efficiency of 79%. A suitable market option is found, which is the H25K 140m R-E-13-2 propeller from Geiger Engineering.

The propeller is driven by a motor. Its power output should be around the 10 kW and the weight should be as low as possible. A direct current motor will be used, because of the high efficiency and power source. The Turnigy RotoMax 150cc Size Brushless Outrunner Motor with a power output of 9.8 kW and weight of 2.53 kg has been selected.

The power source of this motor is a 16 kg lithium polymer battery. The battery provides for a climbing or cruise flight of 13 or 29 minutes, respectively. It is fully recharged in 26 minutes. In case of safety concerns regarding the lithium polymer battery, a 13 kg lithium ion battery can be used. This battery has a climbing or cruise flight of 8 or 16 minutes, respectively. It is recharged in 60 minutes. Both batteries are manufactured by Geiger Engineering.

The motor and propeller are connected through a gearbox. The gearbox transforms the high input rotation speed of the motor to the required propeller rotation speed. The PLHE060 Economy Planetary Gearbox is selected. It has a weight of 1.4 kg and an efficiency of 96 %. An additional power management system of 0.15 kg is required for this configuration.

All the selected parts have to be positioned in the structure. For the propeller positioning, a maximum angle of attack of 10 degrees and obstacle clearance of 0.1 m is taken into account. The gearbox and motor are positioned behind each other to avoid the use of a shaft. Furthermore, the batteries are positioned in front of the square beam of the structure for safety and performance reasons. Two out of fourteen cells are fixed to provide for takeoff, while the rest is taken as luggage. This leaves weight budget for other subsystems.

The stability and control is analyzed using a self-made Python tool and Athena Vortex Lattice Method[1]. Using the Python tool a quick estimation is made where to place the canard for a given size, using the airfoils determined by the aerodynamics department. Then AVL was used to create a more detailed design.

First, a configuration was defined that assures longitudinal stability for a center of gravity range that can be achieved with the position and weights of the pilot and aircraft elements. The canard's size and position are altered, next to its incidence angle. Several options are discussed with the other departments, as other factors, such as stall performance, have to be kept in mind. In the end, the canard's position and size ensure stability for the used configuration and makes that small elevator deflections are needed for leveled flight.

A V-tail is present at the rear of the aircraft, under the wing. Its size is altered to find a stable configuration regarding yaw. This tail also holds the ruddervators, which then were sized regarding controllability.

The aircraft has to be controllable during all operations. The aircraft is the least controllable during takeoff, at low speeds with the flaps extended. The control surfaces are sized to achieve proper rotational rates during takeoff and to make aerobatics possible at higher speeds. As the aerodynamics department found that flaps over the whole wing surface are needed, flaperons are used for roll control. Next to this elevators are placed at the canard and ruddervators at the V-tail. Aileron differential is implemented to reduce the adverse yaw. Linear actuators are used to control the deflections.

The result is an operative center of gravity range of 20 cm, positioned just before the main wing. Below takeoff speed, angular rates larger than 5 deg/s are achieved, and at maximum velocities a pitch rate larger than 100 deg/s can be reached.

A structural analysis tool was developed to analyze the airframe, wing, V-tail, and canard of the Velo-E-Raptor. First, the limiting load case was determined using the V-n diagram. The maximum load factor experienced by the structure is 9, including a safety factor of 1.5, at the optimum aerobatic velocity of 35 m/s. The never exceed speed is set at 100 m/s.

The aircraft consists of four main structural parts: the main wing, canard, fuselage and the V-tail. For the structure of the main wing and canard, two options were considered: a completely rigid and a semi-rigid wing.

[1]URL http://web.mit.edu/drela/Public/web/avl/ [cited 27 June 2017]

The rigid wing consists of an I-beam at quarter chord, for bending, and a rigid skin that counteracts torsion. The semi-rigid skin is made up of a D-cell, for all the loads, and foam ribs with a Dacron/Mylar sailcloth that shape the remainder of the airfoil. The V-tail is a swept forward, tapered NACA 0005 airfoil with a rectangular spar. A V-tail is necessary to keep the main wing out of the wake of the canard, control the yaw of the aircraft with ruddervators, and prevent the main wing from being a fully cantilevered structure. The fuselage consists of two main parts; a rectangular main frame, and a circular nose tube. The nose tube connects the canard to the main frame. The main frame houses the pilot, batteries, pedal system and engine.

The materials used for the Velo-E-Raptor include carbon fiber, Divinycell H100 sandwich core material, Dacron/ Mylar sailcloth and polyurethane foam. Due to the stringent weight requirements, all materials have been selected for their high specific strength and low density. The carbon fiber laminate used in the wing and canard is a 4-layer, 0/90/45/45° orientation, making the material quasi-isotropic. A sandwich core is added to reduce buckling.

In order to calculate the forces and stresses on the structure, a Python tool was constructed. It uses the dimensions, airfoils, lift and drag distributions and maximum takeoff weight as inputs. Consequently, the structure of the wing and canard were idealized using boom theory. Then, a stress analysis was conducted employing loading diagrams, normal, bending and shear stresses, buckling, and torsion. The Tsai-Hill failure criterion, which accounts for the interaction between different failure modes, and tip deflection are used as guidelines for finding the optimal design. After several iterations, exact dimensions and their weights of all structural elements were established. The ribs are idealized as either a truss structure, in the wings and canard or an I-beam, in the V-tail.

The final mass of the structure is 80.87 kg for the rigid skin and 54.01 kg for the D-cell. Thus, due to the significantly lower mass, a D-cell with foam ribs and Dacron/Mylar sailcloth is applied to the final design. The structural analysis Python tool was verified with a simplified wingbox geometry and hand calculations. As future recommendations, a more detailed analysis of materials and composite sandwich panels is advisable, as well as manufacturing techniques. Also, more optimized D-cell and ribs could positively affect in the total mass.

The sustainability of the Velo-E-Raptor is ensured through a combination of the long lifespan of the product, the materials used and the operational model. The use of the circular economy ensures that the product is maintained well, ensuring longevity. This is beneficial for the sustainability of the material and battery choice.

The operational aspects of the design process consist of two parts. These are integrating the required parts into the design and investigating how the product will be used. This starts with the transport of the product. The structures department investigated how the product can be disassembled into smaller parts for transport. The first step was to determine how these parts could be transported. A trailer was designed to transport these parts as good as possible.

After that, the human/machine interface was researched and designed. The Velo-E-Raptor will be flown using a triplex fly-by-wire system. One of the three computers was placed at the back of the aircraft and the other two in the front to make the aircraft more redundant for impact or internal damages. In case of two flight computers failing the aircraft is controlled asymmetrically, but can be landed.

The controls of the Velo-E-Raptor are a new concept, which has not yet been implemented in other aircraft. The pilot will be wearing a harness with a chestplate which incorporates multiple parts; a comfortable chestplate to lay on, connection pins to connect the chestplate to the aircraft for the prone position, an optional chin support, and a frontal airbag. Using this chestplate the pilot can control the aircraft both in an upright position and in a prone position.

The pilot will control the entire aircraft with his right hand on the control stick. This control stick is a 3-axis control stick without feedback. The pilot controls pitch, roll, and yaw on this control stick. Furthermore, the power, flaps and emergency precautions can be executed from this control stick. The pilot can then use his left hand to control the navigation and perform other operational actions.

Flight in the Velo-E-Raptor is in prone position. The pilot is resting with his chest on the chest plate and his hips are supported by both the harness and extendable hip seat. His feet are clicked in the pedals behind him. This prone position was based on prone bicycles and other prone aircraft. While in prone position the pilot has to pedal to increase the power going to the propellers. This makes the Velo-E-Raptor not only an aircraft for transport but also for sporting purposes. Because the power delivered by the pilot is negligible compared to the power required for takeoff, it was decided to amplify this power using a power management system. The distance between the hip seat and the pedal system can be modified to accommodate for taller or shorter pilots.

Taking off with the Velo-E-Raptor can be done in multiple ways. The aircraft comes with two attachable support wheels which together with the front skid can be used for takeoff and landing. Furthermore, the Velo-E-Raptor also accommodates for a takeoff without the use of these support wheels or making use of a cart in combination with either a propeller or a winch. As for the landing using the support wheels is advised as they can carry the impact load and thus not injuring the pilot's legs during landing.

The instrumentation of the Velo-E-Raptor is advanced, it makes use of a HUD integrated in the windshield. Using this HUD it is much easier for new pilots to fly than making use of conventional instruments. Furthermore, safety precautions can be implemented into this HUD such as flight envelope alarms and angle of attack indicators for stall warnings. This way the Velo-E-Raptor can be a safe and enjoyable aircraft for everybody.

The focus concerning safety was on how to prevent the pilot from crashing, and not on what happens when the pilot crashes. The stall behavior of the aircraft was investigated as well as the transition layers before stall. Because the Velo-E-Raptor is a canard aircraft, when close to stall the canard stalls first, causing the nose to drop and having the aircraft going out of stall. Despite the high wing loading on the canard, this drop will not be too intense as the canard has gentle stall characteristics. Still stall is a risk and therefore certain stall prevention measures were implemented. An angle of attack indicator with the stall angles indicated is implemented so that the pilot can see if he or she is close to stalling. Furthermore, stall shields can be implemented to lower the stall speed and controllability speed. Not only alarms are integrated into the aircraft, but also both vocal and visual help for the pilot. When the pilot nears a stall or spin a voice tells this and also what to do to get out of the danger. This in combination with visual instructions on the HUD will ensure that the pilot is out of the danger as soon as possible.

When the pilot goes into a deep stall a pyrotechnic parachute is implemented in the nose of the aircraft. When the aircraft stalls the pilot can activate this parachute and this parachute will let the aircraft with the pilot in it down. This is because at a height of 50 m, where the parachute is still deployable, the pilot does not have enough time to get clear of the aircraft and eject a personal parachute. Furthermore, when going into spin the voice and HUD will tell the pilot what to do to get out of the spin. Investigations were also conducted on what happens in turbulence, gusts and when subjected to g values in maneuvers. This has influence on the neck muscles of the pilot, therefore the chin support was implemented to support this neck during positive g values. As for the integrity, the dive speed is below the never exceed speed. A system is implemented into the HUD indicating the load factor at which the pilot is flying at the moment and the critical load factor at that speed. This way, the risk of the pilot breaking the aircraft is minimized.

Might the pilot crash, multiple precautions are implemented. The pilot can wear a suit which can sustain the impacts and speeds of landing, this way the pilot can slide over the ground in this suit and remain relatively unharmed. Furthermore, the airbag is important safety aspect. When in a crash the front skid registers an impact exceeding a threshold the airbag is inflated. This airbag prevents the pilot injuring his neck in a hard landing. As for the push propeller, it is advised to turn off and fold the propeller in landing. Since a gliding landing is possible in the Velo-E-Raptor it is preferred since the risk of the push propeller hitting the ground and shooting off in the pilot's direction is minimized. Finally, the reliability, availability, and maintainability were discussed. The highlighted aspects of the RAMS are the Dacron foil degradation, carbon fiber degradation, the propeller, batteries, wings, actuators, and propeller.

The market in which the Velo-E-Raptor competes is primarily sailplanes and hang gliders, with the addition of the Archaeopteryx and Aèriane Swift. To compete with these, the cost of producing the Velo-E-Raptor is estimated, from investment to production costs. With an estimated production cost of €56 600 and a recommended price of €100 000, it is expected for the break-even point to be reached after the sale of 50 units. The Velo-E-Raptor tries to compete with the existing market by providing a free-as-a-bird flying experience in combination with very good flight performance and a sportive aspect.

Based on the results of the above, the system is represented through a hardware diagram, software diagram and a data handling and communications flow diagram. The hardware diagram clearly displays the complexity of the entire system. The software diagram is simple in comparison, as the software design needs to be completed during the Post-DSE Activities. The different factors that also affect the software design are displayed in the data handling and communication flow diagram.

The collated results are then shown to comply with the requirements derived from the functional analysis, the market analysis, and the customer. Clearly indicated are the requirements that run a risk of not being fulfilled, due to influences outside the control of the team. Even including these factors, the design presented in this report is considered feasible.

Even so, several recommendations are made for the activities that occur after the end of the DSE. Among these is a preliminary planning which would give enough time for the Velo-E-Raptor to be put on the market in 5 years time. Also included are several design options which the team did not have the time or expertise to investigate. These are present in the relevant chapters, but a short list is also presented at the end of the report.

List of Figures

List of Tables

Nomenclature

AHRS Attitude and Heading Reference System

AoI Angle of Incidence

AVL Athena Vortex Lattice

CATIA Computer Aided Three-dimensional Interactive Application

CFD Computational Fluid Dynamics

CFRP Carbon Fiber Reinforced Polymer

COG Center of Gravity

CS-23 Certification Specification-23

EASA European Aviation Safety Agency

FEM Finite Element Method

GmbH Gesellschaft mit beschränkter Haftung

GPS Global Positioning System

GUI Graphical User Interface

HUD Heads Up Display

LiIon Lithium Ion

LiPo Lithium Polymer

MNS Mission Need Statement

MOI Moment of Inertia

MOS Marketing, Operations & Safety

MTOW Maximum Take Off Weight

NACA National Advisory Committee for Aeronautics

NASA National Aeronautics and Space Administration

PMS Power Management System

POS Project Objective Statement

RAMS Reliability, Accessibility, Maintainability, and Safety

RPM Revolutions Per Minute

UV Ultra Violet

VFR Visual Flight Rules

VLM Vortex Lattice Method

VMC Visual Meteorological Conditions

XFLR5 XFOIL Low Reynolds 5

List of Symbols

Symbol	Description	Unit
α	Angle of attack	deg
$\alpha_{C_{l_{max}}}$	Angle of attack at maximum 2D lift coefficient	deg
γ	Climb angle	deg
$\delta_{aileron}$	Aileron deflection	deg
δ_e	Elevator deflection	deg
δ_{max}	Maximum tip deflection	m
δ_{rudder}	Rudder deflection	deg
η	Efficiency	%
η_{gear}	Gear efficiency	%
η_{prop}	Propeller efficiency	%
$\frac{d\theta}{dz}$	Rate of twist	1/m
λ	Eigenvalue	-
μ	Friction coefficient	-
ρ	Density	kg/m^3
σ	Normal stress	Pa
τ	Shear stress	Pa
ω	Rotational velocity (context dependent)	rad/s
ω_{kV}	Rotational velocity per kiloVolt	rev/minV
ω_{maxin}	Maximum rotation velocity input	rad/s
ω_{maxout}	Maximum rotation velocity output	rad/s
ω_{minout}	Minimum rotation velocity output	rad/s
ω_{rpm}	Rotation velocity	rev/min
a	Acceleration	m/s^2
A	Area (context dependent)	m^2
A	Aspect ratio (context dependent)	-
A_b	Total blade area	m^2
b	Width	m
B	Number of blades	-
B_r	Boom area	m^2
cg	Center of gravity	m
$\bar{c}$	Mean geometric chord	m
C_d	2D drag coefficient	-
$C_{d_{min}}$	Minimum 2D drag coefficient	-
C_{D0}	Zero drag coefficient	-
$C_{D_{0_c}}$	Drag coefficient of canard at zero angle of attack	-
$C_{D_{0_w}}$	Drag coefficient of wing at zero angle of attack	-
$C_{D_{\alpha_c}}$	Change in C_{D_c} due to angle of attack	1/rad
$C_{D_{\alpha_w}}$	Change in C_{D_w} due to angle of attack	1/rad
C_{D_c}	Drag coefficient of canard	-
C_{D_w}	Drag coefficient of wing	-
$C_{D_{wet}}$	Drag coefficient with respect to the wetted area	-
C_f	Frictional coefficient	-
C_l	2D lift coefficient	-
$(C_l/C_d)_{max}$	2D maximum lift over drag ratio (glide ratio)	-
$(C_l/C_d)_{cruise}$	2D lift over drag ratio (glide ratio) at cruise	-
C_{l_α}	Airfoil lift coefficient over angle of attack curve	-
$C_{l_{\alpha=0}}$	2D lift coefficient at zero angle of attack	-

Symbol	Description	Unit
$C_{l_{max}}$	Maximum 2D lift coefficient	-
C_L	3D lift coefficient	-
$C_{L_{0_c}}$	Lift coefficient of canard at zero angle of attack	-
$C_{L_{0_w}}$	Lift coefficient of wing at zero angle of attack	-
$C_{L_{\alpha_c}}$	Change in C_{L_c} due to angle of attack	1/rad
$C_{L_{\alpha_w}}$	Change in C_{L_w} due to angle of attack	1/rad
$C_{L,a}$	Available 3D lift coefficient	-
C_{L_c}	Lift coefficient of canard	-
$C_{L_{max}}$	Maximum 3D lift coefficient	-
C_{L_w}	Lift coefficient of wing	-
$(C_L/C_D)_{max}$	Maximum lift over drag ratio (glide ratio)	-
$(C_L/C_D)_{cruise}$	Lift over drag ratio (glide ratio) at cruise	-
C_m	2D pitching moment coefficient	-
C_{m_α}	Change in C_m due to angle of attack	1/rad
$C_{m_{\delta_e}}$	Change in C_m due to elevator deflection	1/rad
C_{m_0}	C_m at zero angle of attack	-
$C_{m_{0_{AC}}}$	Longitudinal stability contribution due to components other than the wings	-
$C_{m_{0_c}}$	C_m of the canard at zero angle of attack	-
$C_{m_{0_w}}$	C_m of the wing at zero angle of attack	-
C_{T_b}	Blade thrust coefficient	-
d	Width	m
D	Drag	N
D_{gr}	Ground drag	N
e	Oswald factor	-
E	Young's modulus	Pa
E_{batt}	Battery energy	Wh
E_{spec}	Specific energy	Wh/kg
F	Force	N
g	Gravitational constant	m/s^2
G	Shear modulus	Pa
h	Horizontal distance from leading edge of wing to center of gravity (context dependent)	m
h	Height (context dependent)	m
h_n	Horizontal location of neutral point	m
h_{AC}	Horizontal distance from leading edge to aerodynamic center of wing	m
I	Current	A
I_{ch}	Charging current	A
I_{xx}	Second moment of area about x-axis	m^4
I_{xy}	Product moment of area	m^4
I_{yy}	Second moment of area about y-axis	m^4
IF	Interference factor	-
$k_{N_{crit}}$	Turbulence factor	-
l	Length	m
l_c	Horizontal distance between aerodynamic centers of canard and wing	m
L	Lift (context dependent)	N
L	Length (context dependent)	m
L/D	Lift over drag ratio (glide ratio)	-
m	Mass	kg
M_{AC}	Moment around the aerodynamic centre of the wing	Nm
M_x	Moment around the x-axis	Nm
M_y	Moment around the y-axis	Nm
MAC	Mean aerodynamic cord	%
n	Load factor (context dependent)	-
n	Buckling mode (context dependent)	-
N_{crit}	Level of turbulence	-
Re	Reynolds number	-
p	Roll rate	rad/s
P	Power	W
P_a	Available power	W
$P_{a,prop}$	Available propeller power	W

Symbol	Description	Unit
$P_{a,shaft}$	Available shaft power	W
P_{crit}	Critical buckling force	N
P_{cruise}	Power at cruise speed	W
P_{max}	Maximum power	W
P_r	Required power	W
$P_{r,prop}$	Required propeller power	W
P_{spec}	Specific power	W/kg
q	Pitch rate	rad/s
q_s	Shear flow	N/m
r	Radius (context dependent)	m
r	Yaw rate (context dependent)	rad/s
R	Radius	m
R_{gear}	Gear ratio	-
RC	Rate of climb	m/s
s	Distance	m
S	Surface area	m^2
S_c	Surface area of canard	m^2
S_{ref}	Reference area	m^2
S_x	Shear force along x-axis	N
S_y	Shear force along y-axis	N
t	Thickness (context dependent)	m
t	Time (context dependent)	s
t_{ch}	Charging time	s
t_{climb}	Climbing time	s
t_{cruise}	Cruise time	s
T	Period (context dependent)	s
T	Torsion (context dependent)	Nm
T_2	Doubling time	s
T_a	Available thrust	N
T_c	Thrust coefficient	-
T_{max}	Maximum torque	Nm
T_r	Required thrust	N
u	Energy density	Wh/L
U	Voltage	V
U_{ch}	Charging voltage	V
U_{md}	Minimum discharge voltage	V
v_∞	Free stream velocity	m/s
V	Velocity	m/s
V_b	Design velocity for maximum gust intensity at maximum lift coefficient	m/s
V_c	Tail volume	m^3
V_C	Cruise velocity	m/s
V_D	Dive velocity	m/s
V_{LOF}	Lift-off velocity	m/s
$V_{max_{level}}$	Maximum sustained velocity at level flight	m/s
V_R	Rotation velocity	m/s
V_{stall}	Stall velocity (of discussed configuration)	m/s
$V_{stall_{clean}}$	Stall velocity in clean configuration	m/s
$V_{stall_{flap}}$	Stall velocity when flaps are deployed	m/s
V_t	Blade tip velocity	m/s
V_w	Wing volume	m^3
W	Weight	N
W_c	Vertical tail volume	m^3
W_{cable}	Cable weight	kg
W_p	Vertical propeller volume	m^3
W_w	Vertical wing volume	m^3
x	Position along x-axis	m
y	Position along y-axis	m
z	Position along z-axis	m
z_{cg}	Vertical distance from leading edge of wing to center of gravity	m

Symbol	Description	Unit
z_{cw}	Vertical distance between aerodynamic centers of canard and wing	m
z_n	Vertical distance from leading edge of wing to neutral point	m

Contents

1 Introduction

From Greek mythology with Daedalus and Icarus to Leonardo da Vinci with his glider, humans have had the desire to fly ‘free as a bird’. It was, however, not until Otto Lilienthal designed his first glider in 1876 that people thought it would be possible. Nowadays, after more than 100 years of heavier than air flight, the free as a bird feeling is unfortunately not as present anymore. Due to concerns about safety, many regulations have been set up which limit the freedom of pilots. Getting closer to free flight are are activities such as paragliding, hang-gliding or flying with a wingsuit. These, however, come with a drawback of being quite dangerous and may require the pilot to have a license. The challenge here is, therefore, to design a safe aircraft which still is able to deliver the ‘free as a bird’ feeling and that can be flown without too much effort needed for training, certification, and skill.
In addition, modern air sports as the Red Bull Air Races are mostly about flying skill and not about human power and produce a lot of noise to the annoyance of people on the ground. The rapid increase in the use of electrically amplified bikes led to the idea of combining this with an aircraft to obtain a new air sport. The faster someone cycles, the more power the propeller delivers. Delivering a lot of power makes it, however, very difficult to still fly the aircraft perfectly, so the pilot will need a combination of both skills.

The purpose of this report is to present the design of the aircraft that meets the challenges of being safe, available and ‘free as a bird’. It informs the reader on what the final design can perform, how it will look like, how the operations are performed, and how safe the aircraft is. Furthermore, a market analysis is presented.

The structure of this report is as follows. First, the mission objective and functional analysis are stated in Chapter 2. In addition, the basic configuration is set. This is followed by Chapter 3, wherein the verification and validation strategy that will be used throughout the design process is explained. Chapter 4 describes the risks and the mitigation plan for these risks. Then, the technical design is elaborated upon in Chapters 5 to 8, each covering a separate department. Summarized in Chapter 9 is the sustainability of the Velo-E-Raptor, after which in Chapters 10 and 11 the operations and safety measures of the aircraft are described, respectively. Next, Chapter 12 discusses the marketing plan. Lastly, the hardware, software, and communication diagrams are shown in Chapter 13. The report is then concluded by Chapter 14, covering the final results, and a conclusion and recommendations for further research in Chapters 15 and 16, respectively.

2 Mission analysis, Aircraft Configuration and Layout

2.1 Mission Analysis

Based on the requirements of the customer, in the Baseline Report the Mission Need Statement and Project Objective Statement where developed [Aarts *et al.* (2017a)]. These are reproduced below:

MNS Design an electrically assisted human powered next generation glider.
POS To develop a foot launched, electrically assisted human powered air sport by 10 students within 10 weeks.

2.2 Aircraft Configuration & Layout

In addition to this, in the Midterm Report, the configuration was determined for the Velo-E-Raptor. The canard configuration was determined as best for what we were designing, after a detailed trade level. In addition to the horizontal distance between canard and wing, it was also chosen to include a vertical distance between the two surfaces.

Further, a vertical tail was included in the form of a V-tail (Figures 2.2 and 2.3), to both decrease the structural loads on the wing as well as provide roll and yaw control. Finally, the MTOW is set at 190 kg, while an initial planform was selected, shown below in Figure 2.1. As can be seen, the V-tail is positioned underneath the main wing. Note that in Figure 2.2, the front of the aircraft is towards the left.

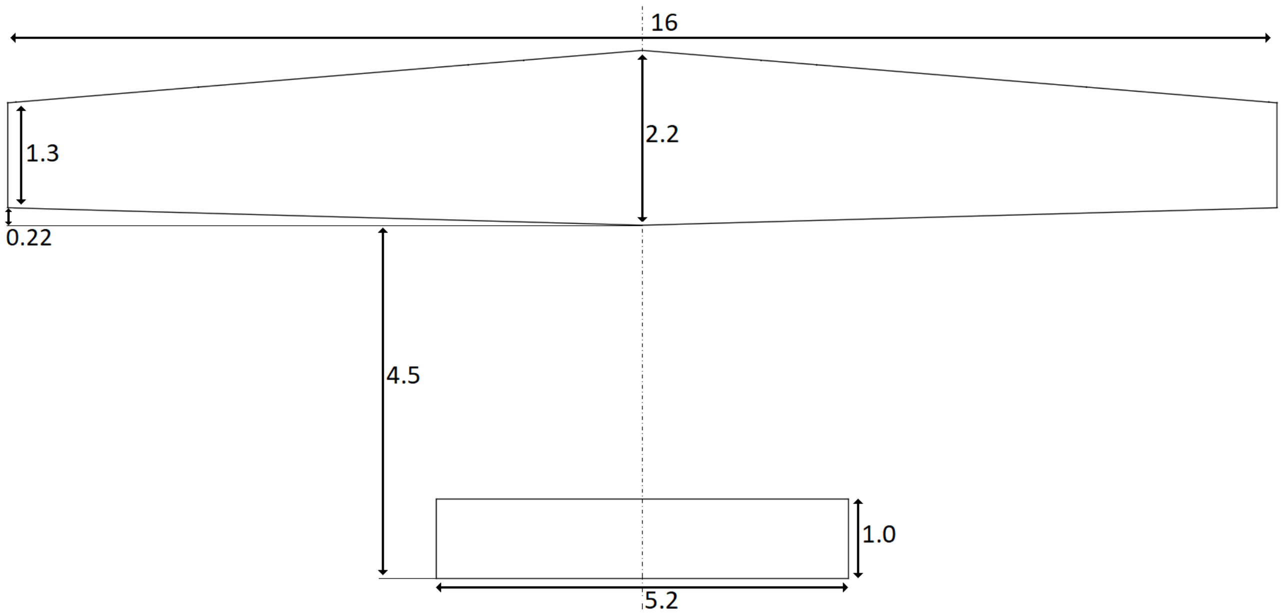

Figure 2.1: General layout top view (distances in meters)

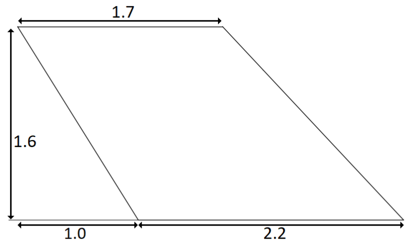

Figure 2.2: General layout V-tail side view (distances in meters)

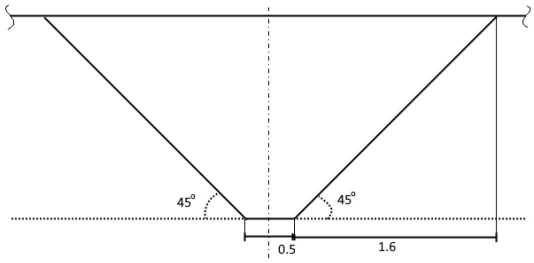

Figure 2.3: General layout V-tail front view (distances in meters)

2.3 Functional Analysis

The functions performed by the Velo-E-Raptor are shown in the functional breakdown structure in Figure 2.4. The functions are ordered by flight phase and by subsystem in the case the functions are not tied to a specific flight phase. The order of the functions relevant to each flight phase are displayed in the functional flow diagrams in Figures 2.5 to 2.8.

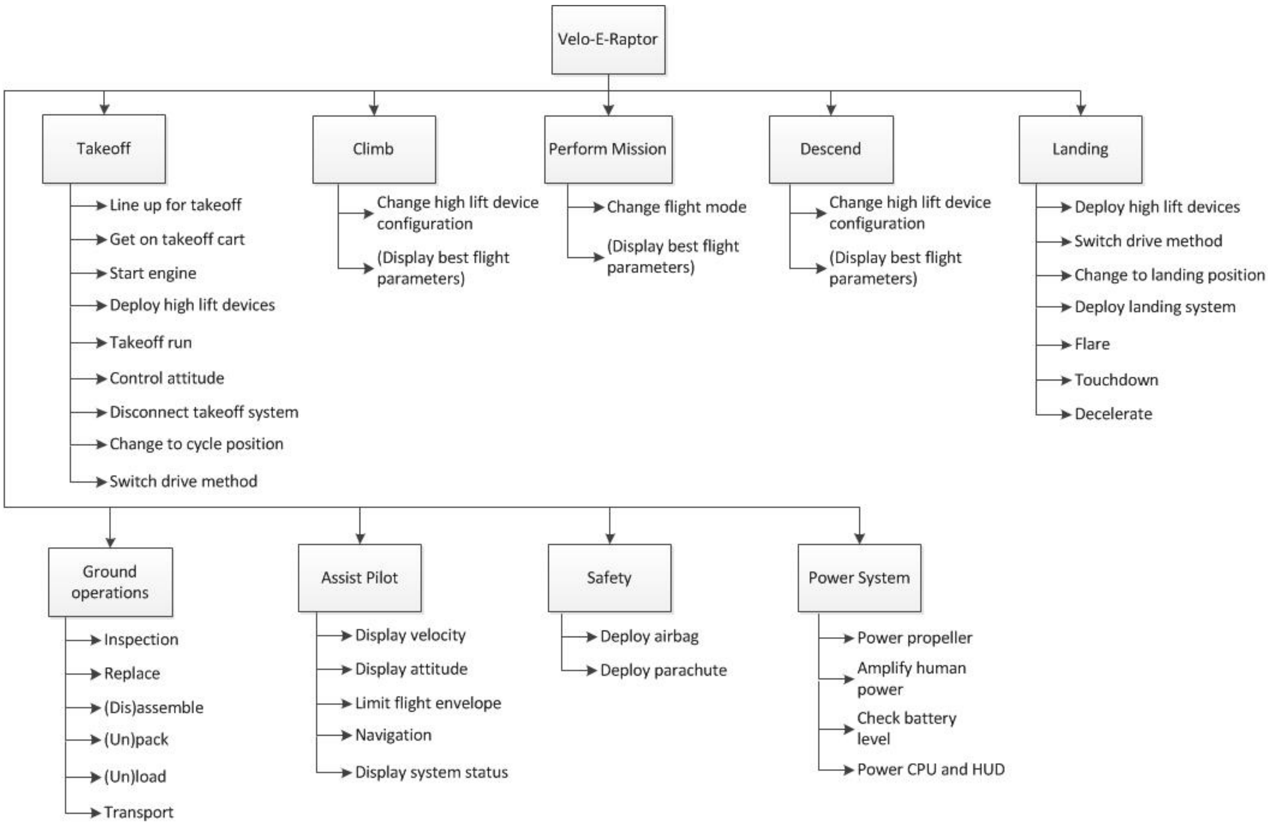

Figure 2.4: Functional breakdown structure.

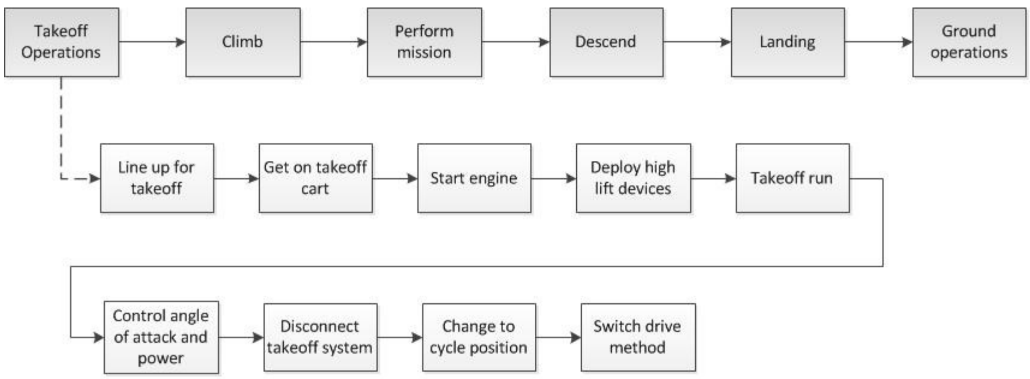

Figure 2.5: Expanded takeoff operations section of the functional flow diagram.

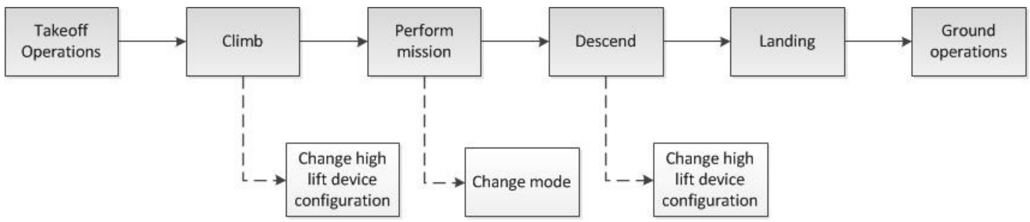

Figure 2.6: Expanded climb, mission and descend sections of the functional flow diagram.

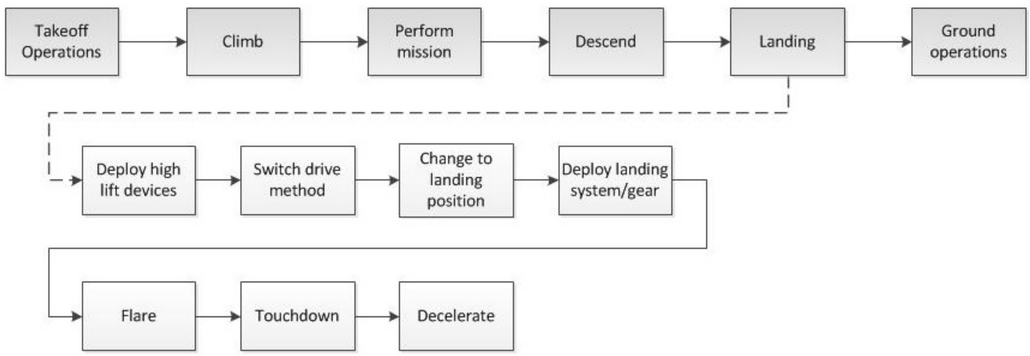

Figure 2.7: Expanded landing section of the functional flow diagram.

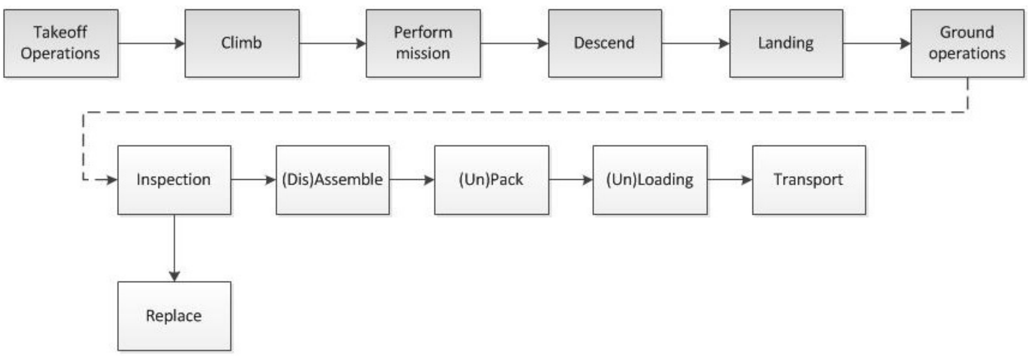

Figure 2.8: Expanded ground operations section of the functional flow diagram.

3 | Verification, Validation & Sensitivity

For every design it is important whether or not the results are correct and if they reflect reality. Therefore it is important that a good approach has been taken regarding verification and validation of the design. In this chapter the verification and validation approach will be explained together with the sensitivity. This approach will be used throughout the entire report and each chapter will be given with its own detailed verification and validation.

3.1 Verification of Requirements

Before anything can be said about the design, the requirements of the design have to be determined. However, each requirement needs to be verified in order to determine whether the requirement is coherent with respect to the design. In order to do this the following rules shall be applied to the requirements by Gill (2013):

1. **Each requirement shall have a unique identifier.**
2. **This identifier shall not be re-used in the event the requirement is deleted.**
3. **A requirement shall be unambiguous, use straightforward and simple words and phrases.**
4. **The inclusion of essential, design-to, requirements shall be complete.**
5. **Each sentence shall include only one requirement.**
6. **Terms vague or not verifiable as "or, etc., goal, relevant, necessary, appropriate, shall include, but not be limited to" shall not be used.**
7. **A requirement shall be unique (e.g. shall be included only once in a specification).**
8. **A requirement shall be verifiable.**
9. **A requirement shall be consistent, i.e. it shall be ensured that there is no conflict between any two requirements in a specification.**
10. **The content of a requirement shall not include the reason for the requirement or a description of the design. Rationales and design descriptions shall be documented separately.**
11. **The requirement shall be complete, i.e. it shall be ensured that all functions and performance items are defined, which are required during the foreseen life cycle of the system.**

Every requirement given in the baseline report Aarts *et al.* (2017a) should comply to the rules above. If they do not comply, then the requirement can be stated to be invalid or unattainable.

3.2 Verification of Subsystems

Besides the verification of requirements, it is also important to verify the codes used for calculations and visualizations. There are three general steps for this verification process. In this section the process for code error checking is described followed by a unit test description. Furthermore, the system test is described.

Coding Errors

An important aspect of the verification process is the code verification. Each tool has to be checked for syntax errors and input errors. In order to do this, a different person than the coder will verify the code, such that this person has no experience with the code itself and has to get grip on the code. Syntax errors can be solved using the debugger of, in this case, Python.

Unit Tests

Subsequently, a unit test should be performed and the code has to be corrected if an error occurs. For this unit test each code is checked in parts, by checking the formulas with a given input and its output. For- and while-loops are checked by printing several statements, such that each path of the loop will be checked and almost the entire part of the program is covered. Every function given in the code, will be checked by giving arbitrarily inputs and checking the output. Examples could be simplified geometry, simple load cases and such.

System Tests

After the models are tested separately, it is important to test the entire system in which the models are coupled to each other. This is done by checking consistency within the code and the transition from one model to the other. If the system gives outputs which are expected, one can validate the model. After the system is verified, the system also has to be checked with all the requirements given. This can be done with four different methods: inspecting, analyzing, demonstrating and testing. For each requirement, its corresponding method should be used in order to check compliance with the design.

3.3 Validation of Models

Model validation determines whether or not a certain value makes sense with respect to the reality. However, since no test data is available, reference aircraft data is necessary in order to validate the model. For the model, all output data is compared with reference data such that the model can be evaluated. In the next design phase, more advanced programs can be used as validation such as CFD and FEM analysis. In the sections below the verification and validation of each separate model will be described.

3.4 Sensitivity Analysis

In order to know how the system responds to a significant change in the design, it is important that a sensitivity analysis is done over each subsystem. For this particular design, a sensitivity analysis will be done by changing several design parameters, such as geometric properties or loads. By changing these parameters, the effects of these changes can be shown and the design can be adapted such that changing a specific parameter has minimum impact on the design. By reducing the sensitivity, the results become more reliable with respect to reality, such that significant changes do not affect the entire design and only subsystems should be adapted.

4 Technical Risk Management

In this chapter, the technical risks are identified and mitigated. This is an important part of design and manufacturing processes. When the mitigation strategies are not implemented the process is still sensitive to the identified risks. First of all, the approach will be discussed and then the results are presented. Finally, a risk map both before and after the mitigation is presented.

4.1 Approach

In order to determine the risk events, an investigation was conducted to the operations and processes in the design team. Furthermore, research was conducted concerning the manufacturing and assembly phase of the Velo-E-Raptor. The most relevant risk events are presented in this chapter. After the risks were identified, their probability, severity, and criticality were determined. This was done according to the United States Air Force analogue rating as can be seen in Figure 4.1. For each risk event, a probability and severity have been determined based on research. The criticality is the product of these two numbers, it is a good indication on how much effort should be put into mitigating this risk. Risks with a high criticality then received more man-hour consuming and/or costly mitigation strategies. After the mitigation strategies were determined, which reduces the probability and/or the severity of a risk event occurring, new probabilities and severities were determined.

Rating	1	2	3	4
Probability	Impossible P = 0	Improbable (Low) 0 < P < 0.4	Probable (Medium) 0.4 < P < 0.7	Frequent (High) 0.7 < P < 1.0
Severity	Negligable	Marginal	Critical	Catastrophic

Figure 4.1: Risk categorization ratings

4.2 Risk Events and Mitigation

The technical risk events and their mitigation are presented in Figure 4.2 and Figure 4.3. The risks are ordered by probability, lowest first. First, the risk ID and the event is presented after which the cause of that risk event is discussed. Then the probability, severity and critically is determined. Finally, the mitigation strategy is presented along with the new probability, severity and criticality after this mitigation.

4.3 Risk Map Before Mitigation

The criticalities of the risk events before mitigation in Figure 4.2 and Figure 4.3 are presented in the form of a risk map in Figure 4.4.

4.4 Risk Map After Mitigation

The criticalities of the risk events after mitigation in Figure 4.2 and Figure 4.3 are presented in the form of a risk map in Figure 4.5.

ID	Risk	Cause	Probability (p)	Severity (S)	Criticallity (P x S)	Preventive Measures	Preventive Probability	Preventive Severity	Preventive Criticallity
2	Product has security vulnerabilities	Use of unsupported or unprotected software in the Product	2	1	2	Using checked and protected software, avoiding too new or too old softweare	1	1	1
3	Product components lack stability	Use of new technology or software which hasn't been sufficiently tested.	2	1	2	Thourougly checking new technology or software when implementing it into the Product.	1	1	1
11	Regulation change	Changes in law or regulation	1	3	3	Staying up to date on changes in that field	1	1	1
8	Lack in technical development	The Product is designed for tecnology not ready for use	1	4	4	Prevent using unproven technologies in the design selected.	1	3	3
21	Off the shelf components not tested before implementation	Workplace regulations not followed and products deemed to be fully working due to good name.	2	2	4	Strict procedures to test each component. Always having two parties testing the products.	1	2	2
16	Product wrongly tested	Using a test setup that does not give reliable or usable results without the testing crew knowning.	2	2	4	Good record keeping and careful manual reading. Involving experts on the testing procedures.	2	2	4
10	Risk not predicted or forseen	Lack of experience	2	3	6	Frequent risk analysis and reevalution of listed risks. Request input from entire group and inform them of the listed risks.	1	2	2
19	Wrong connections used, such as wrong glue.	Connections too hastely performed or wrongly prepared. Old, weak or not fitting joints cause a wrong conenction as well	2	3	6	Supervising where the connections come from, glue factory or joint factory. Testing new batches of joints and glue.	1	3	3
12	Costs forgotten	Costs incorrectly mapped and predicted during design	3	2	6	Choose design for which costs can be decently estimated. Analyze and periodically update costs over entire product lifecycle	2	1	2
18	Too high tolerances used in manufacturing	Crew not up to date on allowed tolerances or crew too easily statisfied	2	4	8	Informing crew on dangers of wrongly used tolerances. Furthermore, not having too many assembly parts with very low tolerances.	1	3	3
20	Epoxy not good or sufficient mixed	Epoxy mixed by crewmember who does not have experience in that field or performed too ahstely.	2	4	8	Involving composite expert to do the mixing of the epoxy. Not trying to win time in this time of the manufacturing.	1	3	3
13	Wrong selection of materials	Wrong expectations on material performance or loads on material	3	3	9	Perform structural analysis on components to predict load cases. Perform property-based material selection	1	3	3
1	Product will not work as a system	Insuffient system engineering methods, unforseen influences between subsystems	3	3	9	generate project structure where frequent subsystem integration is checked	2	3	6

Figure 4.2: Risk events and their mitigation part 1

ID	Risk	Cause	Probability (p)	Severity (S)	Criticallity (P x S)	Preventive Measures	Preventive Probability	Preventive Severity	Preventive Criticallity
4	Product components aren't maintainable	Components lack documentation, are experimental, or require rare skills to maintain	3	3	9	Generate documentation for component and avoiding experimental components	2	2	4
6	Design tools not sufficient	Design tools use assumptions, which may not be valid in the Product design space, leading to inaccurate results.	3	3	9	Apply rigorous validation methods to test models and verify each assumption made	2	2	4
7	Insufficient project member skills	Tasks assigned to members inexperienced on the topic or lack of skill in the entire group	3	3	9	Assign team members to tasks related to previous assigned tasks. Stimulate seeking contact with experts, study material and other members	2	1	2
22	Components heavier or lighter than anticipated	Wrong weights given in manuals or manufacturing error from component manufacturer.	3	3	9	Weighting all the components and having methods to shift the center of gravity using other components when one component is too heavy or light but cannot be moved	2	2	4
17	Wrong tools used in assembly and manufacturing	Crew now knowing which tools are required for the tasks or not enough money to buy adequate tools	3	3	9	Using a factory with adequate tools, having clear instructions on which tool is required for which part of the assembly.	2	3	6
5	Product will not meet requirements	Wrongly set requirements in baseline phase, requirements forgot by subsystem engineers	3	4	12	Frequent requirements checks with all team members, having team members when requirements is questioned by team members	1	4	4
14	Design lacks flexibility	Design process to focussed on a single method of usage	3	4	12	Evaluate design for all relevant limit cases at all stages of the design process.	2	3	6
15	Decisions are low quality	Decisions based on poor understanding of data or made without enough supporting data	3	4	12	Discuss all available data with the entire group before decision. Evaluate assumptions before decision making process.	3	2	6
9	Requirement values wrongly estimated	The values in the requirements are not properly assumed	4	3	12	Regularly insepct and update requirements. Team members remain critical of requirements	2	3	6
23	Center of gravity shift during assembly	Connections such as joints and adhesive in unanticipated places and more than anticipated. Heavier or ligher adhesives or joints might cause this as well.	4	3	12	Weighing all the joints and adhesives and keeping track of where they are implemented and what this does to the center of gravity. This has to be an integral part of the assembly	4	1	4
24	New custom components deemed unfeasable or too expensive	Project team not experienced in engineering new components and/or	4	3	12	Having alternatives to the custom Velo-E-Raptor parts which are custom made.	4	2	8

Figure 4.3: Risk events and their mitigation part 2

Severity \ Probability	1	2	3	4
4	8	18, 20	5, 14, 15	
3	11	10, 19	1, 4, 6, 7, 13, 17	9, 23, 24
2		16, 21	12	
1		2,3,		

Figure 4.4: Risk map before the mitigation

Severity \ Probability	1	2	3	4
4	5			
3	8, 18, 19, 20, 13,	1, 14, 9, 17		
2	10, 21	16, 4, 6, 22	15	24
1	11, 2, 3	7, 12		23

Figure 4.5: Risk map after the mitigation

5 | Aerodynamics

5.1 Fundamental Design

During previous phases of the design effort [Aarts *et al.* (2017b)], a trade-off was performed in order to select the most optimal aircraft configuration which would fit the design space. In this trade-off, it was decided to use a canard configuration with a large, lifting canard, where the main wing is positioned 1 m higher than the canard in order to limit the disturbance of the airflow by the canard. The main advantage of this configuration was that the canard surface would produce a significant amount of positive lift, which would not have been the case for a more typical aircraft-configuration, where the tailplane often produces negative lift. Furthermore, a canard leads to smoother stall behavior, making the aircraft safer and more pleasant to fly. For this initial design, the canard was sized at 30% the surface area of the main wing. Both wings were designed to have a taper ratio of 0.4, in order to approximate an elliptical lift distribution on both wings separately. The aspect ratio of the main wing was 14.6, whereas the aspect ratio of the canard is 1.25 times this amount, in order to ensure that the canard would stall first. During the following process it is ensured that there is no detrimental local stall on the main wing before the canard stall.

5.2 Airfoil Selection

In order to be able to reach an aerodynamic design which is capable of reaching the product requirements, a careful selection of the airfoils to be used had to be performed. Various airfoils used in aircraft with a similar application as the Velo-E-Raptor were collected for both the main wing and the canard. These similar aircraft were mostly low-speed, single or two-person canard aircraft. In total 33 different airfoils were evaluated for the main wing, and 20 airfoils for the canard. The coordinates of the airfoils were collected from the UIUC Airfoil Database[1].

The most optimal airfoil was selected by trading off the different foils on several aspects. Several separate trade-offs were performed and their results combined to select the most optimal airfoil. These trade-offs were different in that the airfoils were evaluated at different Reynolds numbers, corresponding to the preliminary root and tip chord of the main wing, the chord of the canard, and both at a preliminary stall speed of 8 m/s and a cruise speed of 20 m/s. Since the Reynolds numbers of various segments were often close, they were rounded off to the nearest 100k. The Reynolds numbers used for the analyses are 2000k, 800k, 700k and 300k. This corresponds to the root of the main wing at cruise speed, both the root of the main wing at stall speed and the tip of the main wing at cruise speed, the canard at cruise speed and both the tip of the main wing at the stall speed and the canard at stall speed. This means that six different trade-offs were performed.

Each of the trade-offs used the same set of criteria. These are, in order, the lift coefficient at zero angle of attack, the maximum lift coefficient, stall angle, minimal drag coefficient and the lift coefficient at this drag, maximal lift-to-drag ratio, and the respective lift coefficient, lift to drag ratio at cruise and the moment coefficient at cruise. This set of criteria was selected, in order to be able to fully assess each of the airfoils on the desired criteria. It was also considered to judge each airfoil on its stall characteristics, laminar bucket, and upside-down flight capabilities. As these aspects were hard to numerically quantify, they were not directly included in the trade-off. However, especially for the stall characteristics, any airfoils which were not rated at least acceptable in these aspects would not be selected, no matter the score received.

For each of these trade-offs, the weights of each of the criteria were varied in order to match the specific desires for each location and each flight condition more specifically. As a baseline, the weights in the case of the main wing at cruise speed were decided upon. The results of this can be seen in the last column of Table 5.1. Logically, the performance in cruise conditions of airfoils was most important. However, the other criteria are not neglected entirely, as they still have a significant influence on the desired performance of the wing. In the

[1]URL `http://m-selig.ae.illinois.edu/ads/coord_database.html` [cited 6 June 2017]

case of airfoils for the wingtips, a higher weight was assigned to the maximum stall angle in order to help prevent tip stall. In the case of trade-offs at the preliminary stall speed, a higher weight was given to the maximum lift coefficient as this is the most important aspect in order to achieve low stall speeds. Lastly, for the trade-offs of the canard airfoil, the lift slope was given a greater weight, as a steeper slope was preferable for the stability and control of the aircraft, together with a decreased importance of the moment and lift coefficients of the airfoil, due to the significantly smaller area of the canard wing. The weights related to lift-to-drag ratios were also increased, in order to ensure that the canard will not be a major contributor to the drag of the aircraft and will not disturb the flow for the main wing too much.

The properties of each of the airfoils relevant to the trade-offs were found using Javafoil[2] and listed. These properties, such as the various lift, drag and moment coefficients at various angles of attack and Reynolds numbers allowed for the airfoils to be ranked. For the lift coefficient at an angle of attack of zero, airfoils would receive a higher score the closer this value was to the preliminary design lift coefficient, 0.35. This coefficient was obtained from the preliminary wing sizing and stall speed. The same is true for the lift coefficients corresponding to the minimum drag and maximum lift-to-drag ratio. For the maximum lift coefficient, stall angle of attack and maximum lift-to-drag ratio, higher scores were assigned for higher values. The opposite is true for the moment coefficient and minimum drag coefficient, thus receiving lower scores for higher values. For each criterion, the most desired airfoil was given a score of 1, whilst the least desirable received a score of zero. The other airfoils were scored based on a linear scaling between the two aforementioned airfoils.

During this process, it became obvious that the results given by Javafoil were often not reliable. Therefore it was decided to use XFLR5 instead. However, as this program does not allow the extraction of specific value as easily as Javafoil, the process was automated using a Python-program. Using these methods, the airfoils for use in the main wing and canard selected. The seven best scoring airfoils along with the weights used in each trade-off can be seen in Tables 5.1 to 5.6. The NACA 65(2)-415 airfoil is referenced as N65-415 in the tables for the sake of brevity.

From Tables 5.1 to 5.4 it can be seen that the MH201 airfoil scores the highest for three out of the four trade-offs related to the main wing. Only for the trade-off related to the Reynolds number at the stall speed at the tip of the wing, it received a lower score of 32. Because of this, it was considered to use a variable airfoil, varying from MH201 at the root of the wing, to S4061 at the tip. Upon investigation in the model provided by XFLR5, however, it seemed that no large gain would be achieved by using this variable airfoil. Instead, it seemed like the results for the MH201 airfoil were a bit off, as is sometimes the case with numerical methods such as Javafoil and XFLR5. Therefore, in order to prevent needless complexity, it was decided to use a single airfoil throughout the entire wing. Thus, the MH201 airfoil was selected, further reinforced by its excellent behavior in cruise condition, where most of the mission will be flown.

Table 5.1: The top 7 in the airfoil trade-off for the root of the main wing at cruise conditions

Airfoil	MH 201	MH 200	N65-415	Fx 60-126	N65-415$_{a=0.5}$	SG6040	S3021	Weight
$C_{l_{\alpha=0}}$	0.63	1.00	0.99	0.50	0.89	0.83	0.86	2
$C_{l_{max}}$	0.82	0.62	0.35	0.96	0.26	0.74	0.44	7
$\alpha_{C_{l_{max}}}$	0.71	0.61	1.00	0.64	1.00	0.75	0.29	5
$C_{d_{min}}$	0.92	0.94	0.79	0.69	0.79	0.69	0.90	8
C_l at $C_{d_{min}}$	0.92	0.77	1.00	0.78	0.61	0.78	0.90	6
$(C_l/C_d)_{max}$	0.40	0.42	0.28	0.42	0.53	0.43	0.45	8
C_l at $(C_l/C_d)_{max}$	0.83	0.88	0.88	0.54	0.81	0.64	0.82	9
$(C_l/C_d)_{cruise}$	0.87	0.82	0.69	0.57	0.72	0.55	0.69	7
$C_{m_{cruise}}$	0.76	0.56	0.57	0.83	0.43	0.66	0.39	5
Score	43.98	41.30	39.57	37.39	37.29	37.17	36.57	

For the canard wing, no such considerations were made. Since the wing would be significantly smaller than the main wing and with reduced or no taper, it would be needless to have a variable airfoil along the wingspan. Instead, for the canard the S4061, E214 and FX 60-126 airfoils were close contenders, as seen in Tables 5.5 and 5.6. In the end, it was decided to select the E214 airfoil, upon investigation of its stall characteristics and inspecting what the reasons were for its high score in cruise conditions, but lower score at stall speeds.

In Figure 5.1 the polar curve and lift coefficient over angle of attack curve for the chosen airfoil of the main wing is shown. As can be seen the stall is really gentle which will result in a safer aircraft. Also the the maximum lift coefficient and the glide ratio are good for this airfoil, as is expected from the trade-off.
In Figure 5.2 the polar curve and lift coefficient over angle of attack curve for the chosen airfoil of the canard

[2] URL `http://www.mh-aerotools.de/airfoils/javafoil.htm` [cited 27 June 2017]

Table 5.2: The top 7 in the airfoil trade-off for the tip of the main wing at cruise conditions

Airfoil	MH 201	S4061	S3021	Fx 60-126	RUTAN	RG 8	CLARK Y	Weights
$C_{l_{\alpha=0}}$	0.68	0.84	0.85	0.52	0.70	0.78	0.90	2
$C_{l_{max}}$	0.73	0.53	0.35	0.89	0.12	0.52	0.61	7
$\alpha_{C_{l_{max}}}$	0.44	0.29	0.24	0.44	1.00	0.24	0.35	7
$C_{d_{min}}$	0.51	0.57	0.57	0.45	0.50	0.50	0.52	8
C_l at $C_{d_{min}}$	0.59	0.74	0.86	0.72	0.88	0.79	0.67	6
$(C_l/C_d)_{max}$	0.58	0.92	0.63	0.65	0.20	0.47	0.60	8
C_l at $(C_l/C_d)_{max}$	0.78	0.67	0.81	0.54	1.00	0.71	0.81	9
$(C_l/C_d)_{cruise}$	0.73	0.67	1.00	0.61	0.72	0.80	0.46	7
$C_{m_{cruise}}$	0.75	0.61	0.44	0.83	0.38	0.75	0.60	5
Score	37.72	37.64	37.08	36.81	36.15	35.09	34.98	

Table 5.3: The top 7 in the airfoil trade-off for the root of the main wing at stall conditions

Airfoil	MH 201	S4061	Fx 60-126	S3021	RG 8	CLARK Y	E214	Weights
$C_{l_{\alpha=0}}$	0.68	0.84	0.52	0.85	0.78	0.90	0.28	2
$C_{l_{max}}$	0.73	0.53	0.89	0.35	0.52	0.61	0.52	8
$\alpha_{C_{l_{max}}}$	0.44	0.29	0.44	0.24	0.24	0.35	0.21	5
$C_{d_{min}}$	0.51	0.57	0.45	0.57	0.50	0.52	0.48	8
C_l at $C_{d_{min}}$	0.59	0.74	0.72	0.86	0.79	0.67	0.64	6
$(C_l/C_d)_{max}$	0.58	0.92	0.65	0.63	0.47	0.60	1.00	7
C_l at $(C_l/C_d)_{max}$	0.78	0.67	0.54	0.81	0.71	0.81	0.60	8
$(C_l/C_d)_{cruise}$	0.73	0.67	0.61	1.00	0.80	0.46	0.41	6
$C_{m_{cruise}}$	0.75	0.61	0.83	0.44	0.75	0.60	1.00	5
Score	35.48	35.32	35.01	34.51	33.16	33.01	32.69	

Table 5.4: The top 7 in the airfoil trade-off for the tip of the main wing at stall conditions

Airfoil	S4061	CLARK Y	Fx 60-126	MH 43	GOE 602	RG 8	S3021	Weights
$C_{l_{\alpha=0}}$	0.85	0.88	0.57	0.63	0.73	0.86	0.98	2
$C_{l_{max}}$	0.51	0.59	0.80	0.13	0.43	0.47	0.32	8
$\alpha_{C_{l_{max}}}$	0.41	0.35	0.38	1.00	0.22	0.24	0.30	7
$C_{d_{min}}$	0.95	0.94	0.84	1.00	0.96	0.90	0.98	8
C_l at $C_{d_{min}}$	1.00	0.97	0.92	0.47	0.82	0.69	0.76	6
$(C_l/C_d)_{max}$	0.96	0.79	0.89	0.68	0.83	0.78	0.80	7
C_l at $(C_l/C_d)_{max}$	0.48	0.73	0.37	0.97	0.65	0.72	0.65	8
$(C_l/C_d)_{cruise}$	0.97	0.82	0.72	1.00	0.88	0.74	0.92	6
$C_{m_{cruise}}$	0.64	0.61	0.87	0.26	0.76	0.74	0.47	5
Score	41.82	41.59	40.32	39.91	39.04	37.97	37.69	

wing is shown. The airfoil has a higher lift coefficient for angles of attack around zero which is important for the stability. The canard also stalls at a lower angle of attack than the main wing, further ensuring the safe stall characteristics of the aircraft. Three dimensional effects will also play a big role in whether or not the canard is going to stall first. This is explained in further detail in Section 5.3.

5.3 Planform Design

After the proper airfoils were selected, the three-dimensional shape of the wings was designed. This design would be formed by an iterative process, where the platform design presented in earlier design phases [Aarts *et al.* (2017b)] was taken as a basis. Based on the lectures by Steenhuizen (2015) all the relevant design parameters were identified. Their influence on the design was assessed and the desired values and budgets were made, using the previously established baseline and design requirements such as the stall speed of 8.0 m/s. The aircraft was to be designed to be able to comply with the requirements at an altitude of 1500 m. Based on the selected airfoils, a maximum lift coefficient of 1.4 was assumed. The additional lift generated by flaps was approximated

Table 5.5: The top 7 in the airfoil trade-off for the canard wing at cruise conditions

Airfoil	E214	Fx 60-126	S4061	MH201	S3021	RG 8	RUTAN	Weights
$C_{l_{\alpha=0}}$	0.98	0.84	0.67	0.75	0.48	0.70	0.38	6
$C_{l_{max}}$	0.51	0.86	0.51	0.70	0.32	0.48	0.08	7
$\alpha C_{l_{max}}$	0.10	0.24	0.21	0.38	0.10	0.07	1	5
$C_{d_{min}}$	0.83	0.76	0.94	0.85	0.94	0.84	0.84	8
C_l at $C_{d_{min}}$	0.64	0.87	0.72	0.59	0.88	0.93	1	7
$(C_l/C_d)_{max}$	1	0.68	0.93	0.61	0.65	0.51	0.23	8
C_l at $(C_l/C_d)_{max}$	0.58	0.61	0.66	0.76	0.84	0.70	1	7
$(C_l/C_d)_{cruise}$	0.70	0.63	0.69	0.69	1	0.81	0.73	9
$C_{m_{cruise}}$	1	0.83	0.61	0.75	0.44	0.75	0.38	4
Score	43.5	43.1	41.79	41.6	41.1	40.4	38.4	

Table 5.6: The top 7 in the airfoil trade-off for the canard wing at stall conditions

Airfoil	S4061	Clark Y	Fx 60-126	GOE 602	E214	RG 8	MH 43	Weights
$C_{l_{\alpha=0}}$	0.69	0.67	0.84	0.75	0.95	0.68	0.34	6
$C_{l_{max}}$	0.51	0.59	0.80	0.43	0.55	0.47	0.13	7
$\alpha C_{l_{max}}$	0.41	0.35	0.38	0.22	0.22	0.24	1	5
$C_{d_{min}}$	0.95	0.94	0.84	0.96	0.91	0.91	1	8
C_l at $C_{d_{min}}$	1	0.97	0.92	0.82	0.60	0.69	0.47	7
$(C_l/C_d)_{max}$	0.96	0.79	0.89	0.83	1	0.78	0.68	8
C_l at $(C_l/C_d)_{max}$	0.48	0.73	0.37	0.65	0.31	0.72	0.97	7
$(C_l/C_d)_{cruise}$	0.97	0.82	0.72	0.88	0.75	0.74	1	9
$C_{m_{cruise}}$	0.65	0.61	0.87	0.76	1	0.74	0.26	4
Score	46.6	45.4	45.4	44.1	43.1	41.6	41.5	

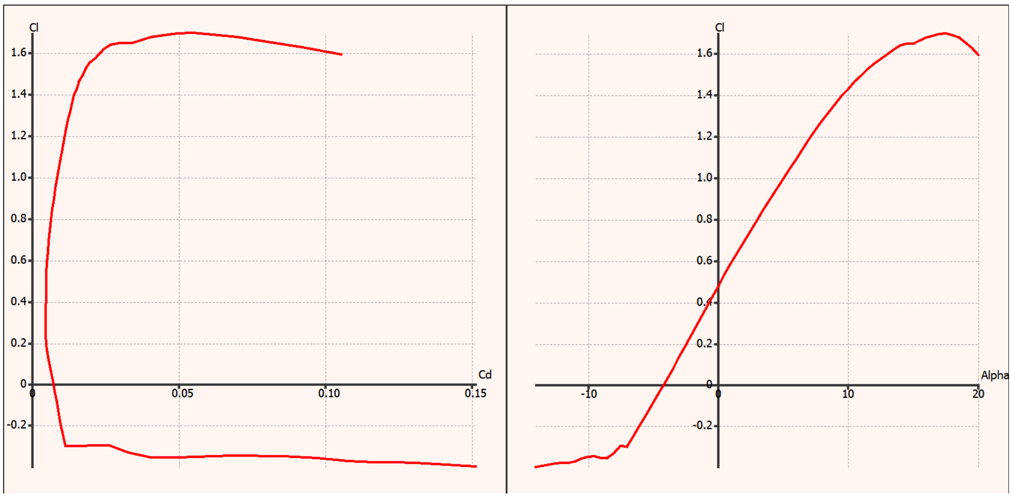

Figure 5.1: Polar curve and C_{l_α} curve of the MH201 airfoil, chosen for the main wing

as 0.5. In combination with the maximum takeoff weight of the aircraft of 155 kg, this leads to a total wing area of 28.59 m^2. This surface area does not take into account any further effects, such as interference caused by the body or canard on the main wing. Thus it could be expected that the final total wing area would be higher than this preliminary value.

With this initial sizing of the planform, the wings were modeled in further detail using XFLR5. From the lecture slides by Steenhuizen (2015), some initial decisions could be made. In the case of this low-speed aircraft with a canard, there was no reason for a sweep to be used in the design. Hence it was decided that the quarter-chord sweep is zero. Similarly, it was decided that no dihedral angle would be used. A taper ratio of 0.4 was also initially decided upon, as this would lead to the most optimal span efficiency factor. Using these design rules, coupled with a wing area required by the theoretical maximum lift coefficient and the desired stall speed, the planform was designed. In order to limit the wing span of the main wing the canard was designed to be quite

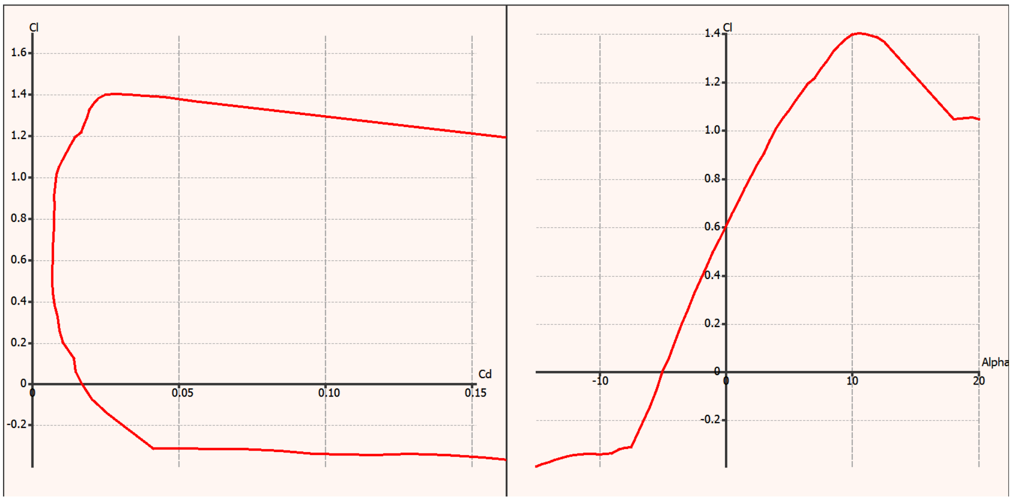

Figure 5.2: Polar curve and C_{l_α} curve of the E214 airfoil, chosen for the canard wing

large, producing half the amount of the lift produced by the main wing. Due to this large canard, however, the airflow to the main wing was spoiled, resulting in a lower effective lift coefficient. This resulted in a significantly larger wing.

This planform design was, however, not deemed acceptable from the point of view of stability and control. Instead, a significantly smaller canard size was desired. To limit structural mass, it was also desired to limit the wing span and thus the aspect ratio. In order to be able to more accurately predict the performance of the aircraft at take-off and landing speeds, it was decided to evaluate the use of high-lift devices. Based on the slides by Steenhuizen (2015), it was decided to use plain flaps as high lift devices, since they are simple devices which don't add too much structural mass. It was predicted that a deflection angle of 12° leads to the optimal increase in lift for plain flaps[3]. Higher angles would lead to early flow separation, whilst lower angles would not increase lift with a sufficient amount. The flaps take up the rearward 30% of the chord of the wing. The planform was redesigned, assuming the use of flaps on the entire trailing edge of the main wing and using a taper ratio of 0.6, as the lift by the canard required for more lift to be generated towards the wing tips in order to maintain the approximately elliptical lift distribution over the wing. In order to keep the canard free for the purposes of stability and control, no separate lift-enhancing surfaces were considered here. In this design, the size of the canard was kept minimal, leading to must of the lift being generated by the main wing. This was done to prevent the canard from spoiling the airflow to the main wing, allowing for a design with a smaller total surface area. Despite this, a wing surface area of over 30 m^2 was required to be able to reach the stall speed of 8 m/s.

This, in turn, resulted in a too small canard area and too high wing area, as now the desired angular rates, especially pitch, could not be reached. From the stability and control requirements, a limit on the canard was set to 20% the area of the main wing area. For structural reasons, the wingspan was limited to 16 m, with the height difference between the wing and the canard being 10% of this wing span. The focus of the following planform design efforts remained twofold. Firstly, the aircraft was designed to comply with the stall speed requirements whilst still following the various limits imposed for non-aerodynamic reasons. Secondly, the lift-to-drag ratio was to be maximized at a speed slightly above, but no less than 15 m/s. This first design goal, however, drove the design to an unacceptable extent. Therefore it was decided that the stall speed would be increased to 9 m/s, provided that this would not inhibit the take-off and landing performance of the aircraft. This is discussed in Chapter 10. For pilot safety reasons, it was also decided that the stall speed of the aircraft in clean configuration shall be no higher than 10 m/s. These changes in the requirements resulted in a less constrained design space from an aerodynamic point of view and allowed for better compliance with desires from structural, stability and power aspects. On the other hand, at this stage, the maximum takeoff weight of the aircraft was increased to 190 kg as discussed in Chapter 2, requiring more lift to be generated by the wing and canard.

At this stage, the decision was also made to put the propeller in between the two halves of the V-tail. In order to connect the main wing to the rest of the aircraft, the V-tail would essentially consist of two shrouded beams at a 45°, which runs along the quarter-chord length of the vertical tail, approximately where the aerodynamic center would be. Of course, the rudder would also be placed on the vertical tail. Since the main wing is quite close to the center of gravity, the tail was designed swept forward, such that the base of the tail is 1 m further

[3] URL `http://exp-aircraft.com/library/heintz/airfoils.html` [cited 12 June 2017]

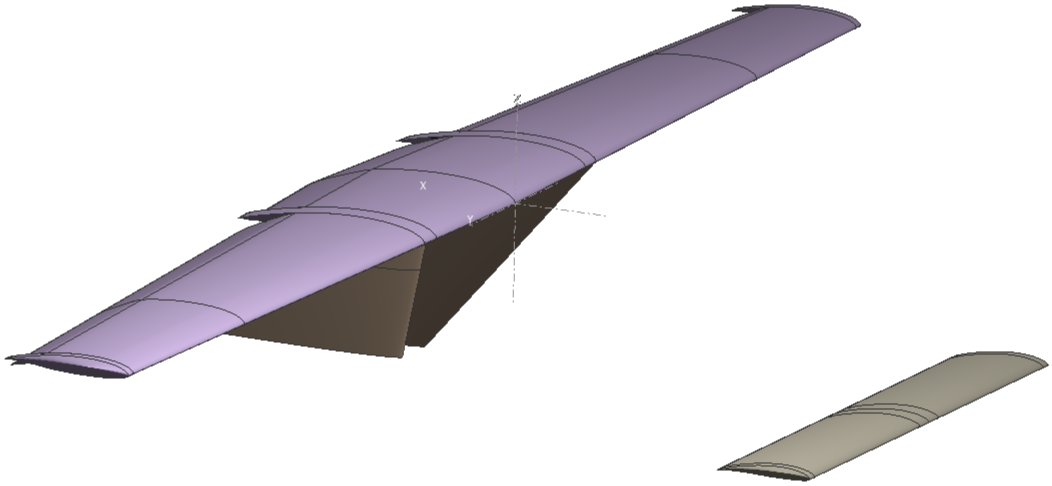

Figure 5.3: The aircraft model as seen in XFLR5.

back than the tip. This was necessary to reach sufficient yaw authority. The root chord of the tail is also 0.5 m longer than the tip chord for the same reason, where the tip chord is 1.7 m. The entire tail section was not translated backward, as that would have made the connection between the main wing and the tail impractical. Lastly, it was decided that the spacing between the roots of the two vertical tail segments would be 0.5 m, as this space would be necessary for the pedaling mechanism and the mounting of the propeller. Using these dimensions it was possible to determine that a NACA0005 airfoil could be used, as thinner airfoils would reduce the drag produced by the tail whilst still fitting the necessary structure inside.

With this more detailed sizing of the vertical tail, the flap locations could be specified. To maximize the lift generated at low speeds, it was decided to maintain the usage of flaps on as much of the wingspan as possible. As a result, flaps would be used on the entire section between the wingtip and the connection of one of the V-tail elements with the main wing. 10 cm of spacing is kept free at the wingtip for mounting reasons. Thus the flap extends from 1.875 m along the span of the one-half wing outwards, keeping some spacing for the mounting of the tail and rudder deflection until 7.9 m of the 8 m half wing. The most outboard section of this flap, from 5.6 m along the span and onward, the flap would also double as an aileron, thus being a flaperon. The most inboard section of the wing, in-between the mounting of the two halves of the V-tail, would also have a flap mounted. However, in order to allow for maximal rudder deflection and tail mounting, more spacing left. The flap runs from the root until 1.625 m of the wing on both sides of the symmetry plane. Furthermore, the maximum deflection of this middle flap is only 8°, in order to allow the rudder to fully deflect. The flaps have to be designed that they can be used at least a speed of 12.5 m/s, to allow the pilot time to properly adjust after takeoff and set the flaps at approach speed, as mentioned in Chapter 10 and Chapter 8.

Now each of the lifting surfaces of the aircraft had been designed in greater detail, the entire system could be put together. Using XFLR5, the combined design of the main wing, flaps, V-tail, and canard was modeled. Regarding the canard, the decision was made to not use any taper such that it would stall evenly and to prevent exceedingly low Reynolds numbers, which could lead to laminar separation. Now the entire aerodynamic design of the Velo-E-Raptor had been decided upon. Some small iterations were made, in order to achieve the best possible results regarding controllability, structural weight and power required. The resulting aircraft dimensions are detailed in the technical drawings in Chapter 14. A qualitative view of the aircraft in XFLR5 is shown in Figure 5.3.

One element which is not included in the current design is the possibility of adding winglets to the design. The usage of winglets could allow for a smaller wingspan, aspect ratio and/or increase the span efficiency of the wing. Despite this, an effort has been made to design winglets which could increase the performance of the Velo-E-Raptor. Based on preceding aircraft designs[4], a simple winglet design was created. It was found that the height of the winglet should be between 10% to 20% of the wingspan, thus a preliminary height of 15% was selected. Furthermore, the dihedral angle of the winglet would be 90°. The winglet would have a taper ratio of 0.6, whilst the root chord of the winglet, defined as the first cross-section at an angle of 90°, is 80% of wing tip chord. Furthermore, the winglet was designed with a 30° sweep angle, a 3° toe-in angle, and 2° twist angle to avoid the upper section from stalling and causing laminar separation. Lastly, the curvature radius towards the root of the winglet was 20 cm.

[4]URL `http://www.apollocanard.com/index_htm_files/Optimizinge%20Blended%20Winglet%20Radii%20on%20Homebuilt%20Canard%20Aircraft.pdf` [cited 13 June 2017]

When modeled in XFLR5, the addition of winglets with this design did not provide any significant benefits. The stall speed was decreased by a few percents, however, there was a significant increase in drag and a reduction in span efficiency. Since the purpose of these winglets is to reduce the induced drag of the aircraft, it was decided to not include these features at this stage. As the efficiency of winglets is very sensitive to small design variations, it is recommended to reinvestigate the potential benefits of utilizing winglets at a later stage. When enough resources are present to properly design and test these winglets, they could provide a significant increase in the performance of the Velo-E-Raptor. Furthermore, the potential benefits of using small winglets or similar wingtip devices on the canard should be investigated as well, as they could not only reduce the induced drag but also decrease the disturbance of the airflow towards the main wing by the canard.

Additionally, the design of the main wing could be reiterated upon as well. An alternative of the current, single-taper design of the main wing is to have the taper varying along various sections. This geometry is called a Scheumann planform. It was decided not to consider this option at this stage, as this would add a multitude of new variables to the wing design, namely the locations of the various sections and their respective taper ratios. With the limited analysis capabilities provided by XFLR5, it would be hard to the selection of these variables. Next to this, such as planform would also increase the amount of lift being produced near the center of the main wing with respect to the lift produced near the tips. In combination with the lift generated by the canard, this would remove the lift distribution of the aircraft further from approximating an elliptical lift distribution. Nevertheless, with more resources available and design tools which allow for better analysis of these variables, this design option could be analyzed in more detail.

5.4 Drag Estimation

In this section, an as good as possible estimate is made for the drag the Velo-E-Raptor will experience during flight. This is one of the design points the Aerodynamics Department.

It is really important to know how much drag the Velo-E-Raptor will experience as it influences the design to a great extent. It determines the amount of power the engine need for takeoff and for cruise. Also, the maximum velocity the aircraft will finally be able to achieve is entirely dependent on the drag. Finally, the glide ratio, one of the most important factors of the design, is determined by the amount of drag the aircraft experiences. Therefore it is crucial to have an as good as possible drag estimate early in the design phase and improving it during the project in order to design the Velo-E-Raptor as good as possible.

An estimate of the drag will never be a perfect representation of the reality. Due to viscous effects causing turbulence the drag can not be totally predicted. Furthermore, an aircraft is a very complex system with many components causing drag and influencing each other. However, many experiments have been performed and estimation methods have been developed which come very accurate in predicting drag. First of all, an example of this is the book on drag by Hoerner (1965). This book uses statistical data from wind tunnel tests and equations based on the data to come up with an as good as possible estimate. Another example is software designed to analyze the flow around bodies and come up with a drag estimate. An example for the software is XFLR5 which is specialized in low Reynolds numbers. Finally, a computational fluid dynamics (CFD) analysis can be made to further investigate the airflow around the aircraft. However, this lays outside the scope of this design project.

As the aircraft is a complex system it is divided into different components. In this way, the estimation will be easier. With the use of XFLR5, the wings will be analyzed. Using this software the three-dimensional effects are all taken into account. This is further explained in Section 5.4.1. All the other parts of the Velo-E-Raptor will be analyzed using the book by Hoerner (1965) and the slides of Steenhuizen (2015). The analysis of bodyies in XFLR5 is very inaccurate [Deperrois (2013)] and the modeling is a tedious process. Furthermore consist the body of the Velo-E-Raptor of many parts such as the structure, the windshield and the pilot itself who is cycling. The estimation process will be explained in Section 5.4.2. Of course there will be interference between the components. The total drag of the aircraft will be more than the drag of all the components added. This effect will be discussed in Section 5.4.3.

During the iteration phase, the drag is analyzed multiple times with increasing precision. At the end of every iteration, all requirements must be met. Therefore some design parameters regarding drag are checked. The amount of drag estimated will, for example, affect the glide ratio, the maximum achievable velocity, the maximum velocity in level flight and if the landing velocity can be sustained. The drag has thus a great impact on the performance of the aircraft and the results regarding this can be found in Chapter 6.

5.4.1 Wing Drag

In this section, the drag produced by the wings will be covered. This is the first estimation of drag as it a result of the planform design. The drag is estimated using XFLR5. This software is designed to calculate both the viscous drag and induced drag.
The drag estimated in this section is a combination of all lifting devices of the aircraft. This includes the canard wing, the main wing, and the V-tail. The V-tail is not meant as a lifting device but will generate lift as the angle of attack changes. This combination is chosen because XFLR5 is designed to analyze lifting surfaces. All other bodies will give a too big of an error when included.

The drag the wing experiences can be split into two parts: lift-induced drag and parasitic drag. Lift-induced drag is caused by the tip vertices of the wings which, as the name states, only are present when lift is produced. The induced drag has, in fact, quadratic dependence of the lift coefficient as can be seen in Equation (5.1). The induced drag is the second term in the equation. This means the induced drag is most present at low speeds when the aircraft is flying at a high lift coefficient. The parasitic drag depends on the shape and the roughness of the body in the airflow. Also, the transition from laminar flow to turbulent will increase the profile drag to a great extent. The parasite drag will grow rapidly with increasing velocity. There is an optimum where the summation of the induced drag and parasite drag is lowest and where the glide ratio is at its maximum.

$$C_D = C_{D_0} + \frac{C_L^2}{\pi * A * e} \tag{5.1}$$

To estimate the drag of the wings the ring vortex method is used. This method is further explained in Section 5.5.1. As stated in this section the program is good at calculating the parameters per panel but when wings come close together or overlap errors will occur. Also, XFLR5 does not take into account the interference between closely spaced wings [Deperrois (2013)]. In Section 5.4.3 this effect will be explained and an as good as possible estimation is made to include this effect in the drag analysis.
XFLR5 is also known to underestimate the drag [Deperrois (2013)]. This underestimation is most probably due to the viscosity in the parasite drag. For this, a correction has to be made in order to have a good estimate of the drag experienced by the wings. Note that when calculating the coefficients, XFLR5 uses the main wing area as reference area.

At cruise with a velocity of 16.5 m/s and an altitude of 1500 m XFLR5 predicts that the drag coefficient (CD) will be 0.016. With a lift coefficient of 0.461, this leads to a lift to drag ratio (CL/CD) of 28.28. This drag estimation is probably underestimated and does not take interference between components into account as stated before. Drag estimates for different speeds with their corresponding lift coefficient and glide ratio can be seen in Table 5.7.

Table 5.7: Estimates for the drag and lift coefficient together with the glide ratio of the wings for different velocities.

Velocity	V (m/s)	C_L	C_D	L/D
$V_{stall_{flap}}$	8.76	1.63	0.168	9.7
$V_{stall_{clean}}$	9.91	1.27	0.080	15.9
V_{cruise}	16.47	0.46	0.016	28.8
$V_{max_{level}}$	30.5	0.13	0.0098	13.3

5.4.2 Body Drag

The next step in the drag estimation process is to calculate the body drag. This will be explained in this section. During the first iterations a preliminary estimate has been made. This estimate is later updated to have a value which represents the reality as close as possible.
In Section 5.4.1 the drag of the wings is estimated. In this section the drag will be estimated all the other parts of the aircraft system will create. The body includes the windshield, the pilot, the structure and other non lifting components. All the different components of the body makes it a very complex system for which a perfect estimate of the drag is impossible.

Modeling the body in XFLR5 would be a tedious process and estimations for bodies in XFLR5 is not very accurate [Deperrois (2013)]. Therefore the estimation for the body drag has been done using the drag predictions provided by Hoerner (1965). In this book useful methods are shown to calculate different drag components for all sorts of shapes. Also estimates for drag due to the interference between bodies are present. The body will first be modelled as a simple shape. This oversimplification will lead to a easy first estimation for the body drag. Later detail will be added to further improve the drag estimate.

The estimation is started with the body modelled as a simple streamlined body. The body is first considered as an airship hull shape as can be seen in Figure 5.4 as shape C. This shape is thought to be the best shape to start with for the body drag analysis as the combination of a pilot with a windshield in front gives a shape close to the airship hull.
The drag of this shape can easily be calculated with Equation (5.2) which is based on statistics. This equation gives a good prediction for the drag of the streamlined shape [Hoerner (1965)]. The equation calculates the profile drag which should than be multiplied with the frictional coefficient (C_f) to get to the dimensionless drag coefficient ($C_{D_{wet}}$) with respect to the wetted area.

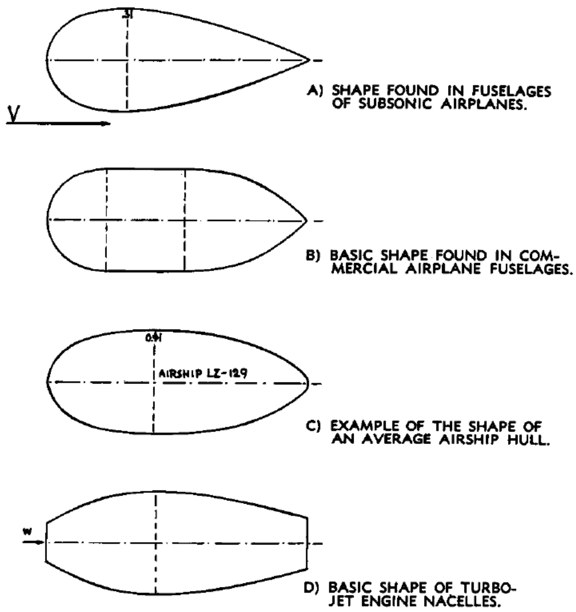

Figure 5.4: Streamlined bodies from [Hoerner (1965)]

$$\frac{C_{D_{wet}}}{C_f} = 1 + 1.5(\frac{d}{l})^{\frac{3}{2}} + 7(\frac{d}{l})^3 \tag{5.2}$$

The length of the chosen shape is the length (l) of the pilot windshield combination and will be 2.5 m. The width (d) is chosen to be 0.8 m as the average human shoulder width is 0.5 m. This will give a sufficient first estimate.

The frictional coefficient is an important factor and will be the first factor which is used to further improve the estimation. As the flow around the body will not at all be laminar due to all the different components the flow around the airship shape will be modelled turbulent. Equation (5.3) is used to calculate the frictional coefficient for a turbulent airflow [Steenhuizen (2015); Hoerner (1965)]. As can be seen the frictional coefficient depends on the Reynolds number. The equation used is based on statistics. The level of turbulence (N_{crit}) is deemed very high so a factor ($k_{N_{crit}}$) is used to account for this effect. The value N_{crit} is often used in software like JavaFoil and Xfoil. This value determines the level of turbulence used in the analysis. Clean windtunnels will have a value of around 9 [Deperrois (2013)]. Due to the high level of turbulence the value will be much lower and therefore a factor $k_{N_{crit}}$ of 1.7 is applied to account for the extra frictional drag coefficient.

$$C_f = \frac{0.455}{\log_{10}(Re)^{2.58}} \cdot k_{N_{crit}} \tag{5.3}$$

The results of this first estimation are shown in Table 5.8.
As the first estimation is very simplistic, further improvement is needed in order to get a more valuable drag estimation. However to make an very precise estimate of such a complex system is nearly impossible. Windtunnel test will be needed to get an idea of how all the components interact with each other. One improvement which can be performed is to model a gap in the streamlined body in order to simulate the gap between the windshield and the body. The added drag coefficient with respect to the drag area a gap will give is approximately 0.1 as can be seen in Figure 5.5 [Hoerner (1965)]. In order for it to be added to the drag coefficient of the body

Table 5.8: Estimates for the frictional coefficient and drag coefficient with respect to the wetted area and the main wing area at different velocities.

Velocity	V	$C_f \cdot 10^3$	$C_{D_{wet}} \cdot 10^3$	$C_D \cdot 10^3$
$V_{stall_{flap}}$	8.76	7.13	10.7	2.39
$V_{stall_{clean}}$	9.91	6.98	10.5	2.17
V_{cruise}	16.47	6.38	9.6	2.13
$V_{max_{level}}$	30.5	5.74	8.6	1.92

equation Equation (5.4) is used. In this equation 12.5 cm for the height (h) and the circumference of the streamlined body is used for the width (b).

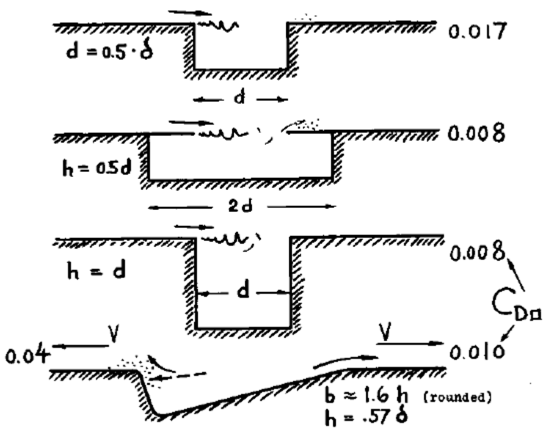

Figure 5.5: Drag coefficient of several types of holes [Hoerner (1965)]

$$C_{D_{gap}} = C_{D_o} \cdot \frac{h \cdot b}{S_{ref}} \tag{5.4}$$

The extra drag due to the gap between the windshield and the pilot will have a drag coefficient of $1.12 \cdot 10^{-4}$. As this value is very low and other effects like interference have a much bigger impact the estimation for the body is not further improved. The uncertainties with estimating the drag in this way are too big thus further improvement will not give a better or more reliable result.

5.4.3 Interference

Up until now the drag from the wings and the drag from the body has been estimated. These value can however not be simply added together. The sum of the two will be lower than the total drag. This is because of the interference between the all the bodies in the airflow.

When two bodies in an airflow are near each other they will alter the airflow the other experiences. This will change the drag the bodies experience. As the air accelerates when flowing around the body, an other body if placed near it, it experiences an airflow with a higher speed than the freestream velocity. This will cause a drag increase as the dynamic pressure is higher. Everywhere around the aircraft this interference is present. It is very hard to model this and XFLR5 does not take this effect into account [Deperrois (2013)]. However there are some correction factors present based on statistics. When adding the drag components the result should be multiplied with the corresponding interference factor. In figure Table 5.9 some factors are shown [Steenhuizen (2015)].
The body experiences interference from the canard in front and the V-tail behind. The corresponding factors will be that of a low wing and a V-tail with a value of 1.10 and 1.03, respectively. These will be used for the drag estimation of the body. As XFLR5 does not take the interference into account also this drag should be multiplied by an interference factor. The wings will experience interference from the body in between it. The factor is set at 1.30 which corresponds to a nacelle or external storage, under a fuselage, less than about one diameter away. This value is rather high but it is thought to be the best comparison as the body will have a big influence on the wings. Also, the viscous drag of the wings is most likely to be underestimated so this will also be factored out to some extent.

Table 5.9: Interference factors based on statistics.

Components	IF
Nacelle or external store, directly under a fuselage	1.50
Nacelle or external store, under a fuselage, less than about 1 diameter away	1.30
Nacelle or external store, under a fuselage, more than about 1 diameter away	1.00
Object, such as a fuel tank, mounted to a wingtip	1.25
High wing or mid wing with carefully designed fairing	1.00
Un-filleted low wing	1.10-1.40
Whitcomb winglet	1.04
"Airbus" style winglet	1.04
Modern blended winglet	1.00-1.01
Conventional tail	1.04-1.05
V-tail	1.03
T-tail	1.04

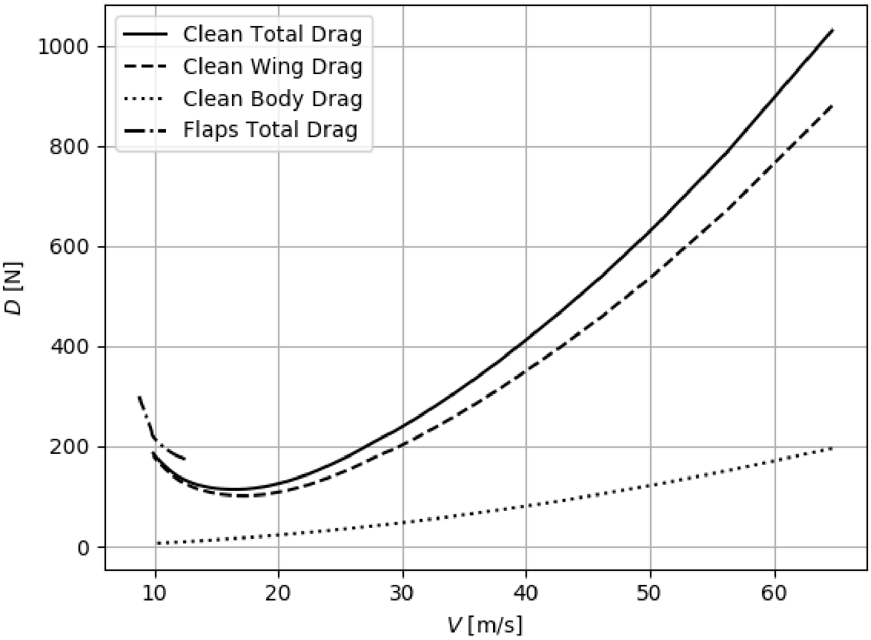

Figure 5.6: The estimation of the drag for every velocity

5.4.4 Final Drag Estimate

Now the drag of all components are estimated and the interference is known the final drag estimate can be made. The wings have been analyzed in XFLR5 and the drag of the body has been estimated with the methods by Hoerner (1965). Some factors for interference have been found so the total drag can be calculated. Equation Equation (5.5) is used to calculate the drag of the total aircraft.

$$C_D = C_{D_{Body}} \cdot IF_{Body} + C_{D_{Wing}} \cdot IF_{Wing} \tag{5.5}$$

The interference factor (IF) for the body and the wing will be 1.133 and 1.3 respectively. The final drag estimation of the total aircraft depends on the velocity and can be seen in Figure 5.6. Here the drag of the body is shown as the dotted line, the dashed line is the drag of the lifting wings and the continuous line represents the total drag. The dashed dotted line represents the total drag when the flaps are deployed.

The estimation done for the drag will be sufficient for the designing of the Velo-E-Raptor. The goal is to introduce a new sport where one of the biggest factors will be the free as a bird feeling. This means a better analysis of the drag will not be needed for now. When the sport has become well established a better drag estimate will be needed. For this CFD analysis and wind tunnel tests will be needed as the method used for this design will be insufficient.

5.4.5 Other Drag Sources

During the process of estimating the drag there, unfortunately, some drag sources could not be accurately accounted for and have been neglected. This has been done in order to get an as good as possible drag analysis in the limited time. However, these neglected drag sources have to be kept in mind.

The body has been modeled as a streamlined body. However, this shape will far from reality as no fairing or pilot harness-bag is used. The pilot is even constantly moving around while cycling which will give some disturbances.
Another, more dominantly present drag factor will be the propeller drag. When the propeller is spinning due to the incoming airflow instead of the power supplied by the engine it will generate a lot of drag. For the design, a propeller is used which is foldable backward. This will significantly reduce the drag it creates during soaring flight.
During the flight, the aircraft will fly at certain angles of attack. This means the body and the structure will be at some angle of attack to the airflow. At some point, the body and structure will generate a small amount of lift which will induce drag. In modern airliners this effect is not to be neglected however for the design of Velo-E-Raptor this is deemed very small and negligible.

5.5 XFLR5 Methodology and Limits

In this section, XFLR5 and the prediction method will be further explained. It is important to understand the math and assumptions behind the program as throughout the design of the Velo-E-Raptor much has been based on it. Some errors and underestimations present in the program will be addressed. Throughout this section Deperrois (2013), Steenhuizen (2015) and Anderson (2010) will be used as sources for the evaluation of XFLR5.

XFLR5 is a software tool with a general public license which means it is free and for everybody to use. The software was first intended as an user-friendly interface for XFoil. Later on, 3D analysis of wings were added which is optimized for low Reynolds numbers.

5.5.1 Airfoil Analysis

The airfoil analysis has been done in XFLR5 using XFoil. Both JavaFoil and XFLR5 were used in the early stage of the project but XFLR5 was thought to give better values with less numerical errors. It was also possible to modify certain airfoils in order to get better results. XFoil is robust and consistent even for viscous analysis. It uses the panel method to calculate the aerodynamics around an airfoil. The airfoil is divided into different panels with a fixed location where the strength of the elementary flow from the Laplace equation is calculated using superimposition. The accuracy of the solution depends greatly on the discretization of the airfoil. Therefore the number of panels used for the analysis are set to 80 or higher for every airfoil. This will give a smooth airfoil and makes it a quick computation. At the trailing edge where the panels from the upper line come close to those of the lower line sometimes numerical errors can occur which will make the analysis useless. For this airfoils, we applied a trailing edge gap in order to lose the numerical errors without changing the profile too much.

5.5.2 3D Wing Analysis

The panel method in the form of vortex lattice method (VLM) has been used for the 3D analysis. The lifting surfaces are divided using a grid where on discrete vortices are defined on. The boundary conditions for the resolution of the potential flow are applied on this grid in order to estimate the airflow. This analysis will give the global lift coefficient, pressure and lift distribution, the induced drag and aerodynamic derivatives. XFLR5 does not calculate the interference two bodies experiences when near each other. This will limit the analysis of the V-tail with the main wing. VLM makes the assumption of a small angle of attack. This means the trailing vortices are not aligned with the freestream velocity. The VLM algorithms first compute the lift coefficient (C_L). The viscous variables are interpolated from the value of lift coefficient on the XFoil generated polars. This means that when at a high angle of attack near stall the values will be incorrect. In general, VLM is adapted to configurations for thin lifting surfaces operating at small angles of attack. The assumption that should be kept in mind is that the 2D XFoil results are transitioned to finite wings. The 2D simulation corresponds with infinite wings where the separation bubble extends along the infinite span. This is not the case with finite wings.
The results from XFLR5 have been compared with wind tunnel tests. The conclusion was made that it predicts the behavior and parameters very good. The only value which was consistently predicted wrong was the drag. This drag is being underestimated probably due to a problem with the viscous drag.

5.6 Design performance

The methods described above resulted in a design of the wing, canard, and V-tail which can comply with the requirements imposed on it. To reiterate, the most important requirements were to achieve a stall speed of no more than 9 m/s and to maximize the lift-to-drag ratio at the design cruise speed, with the minimum allowable Lift-to-drag ratio being 15. The aircraft, as designed, is able to meet those requirements and is optimized as much as possible. The stall speed of the aircraft using flaps is 8.75 m/s. Without the usage of flaps, the stall speed increases to 9.9 m/s. Thus, the requirements regarding stall speed are met.

It was also desired that the aircraft would have safe stall characteristics. Currently, the aircraft in clean configuration stalls at an angle of attack of 9.3°. At this angle it is the canard that gently stalls, starting halfway along the span on both halves. The fact that the canard stalls first and gently results in the aircraft automatically decreasing its pitch angle when this occurs without losing too much lift, allowing the pilot to correct for the stall. The main wing will stall at an angle of 14.2°, thus giving ample amount of time to prevent this. Should the main wing stall, however, control is not directly lost, as the wing starts to stall 4 m from the root, only covering large sections of the ailerons at an angle of 15°. Similarly, with the flaps fully deflected, the stall angle of the canard is 8.9° whilst the main wing stalls at an angle of 10.1°, again allowing the pilot time to decrease the angle of attack of the aircraft.

As for the cruise condition, where the aircraft will be spending most of its mission, the maximum lift-to-drag ratio is 19.4. It should be noted that this glide ratio is not as high as for a planform which is specifically designed to maximize the glide ratio. This is because of the very low stall speed for which had to be achieved whilst minimizing the size of the wing and simultaneously avoiding tip stall. At cruise, the Oswald factor reached is 0.76. This corresponds to a flight speed of 16.45 m/s and an angle of attack of 0.60°. The performance of the aircraft under these and other conditions are further discussed in Chapter 6.
The final dimensions of the planform design to reach these properties are summarized in Table 5.10 below.

Table 5.10: Dimensions of the designed planform. The main wing is referenced to as simply wing.

Parameter	Value	Unit
Wing airfoil	MH201	-
Wing span	16.00	m
Wing area	28.16	m^2
Wing MAC	1.80	m
Wing aspect ratio	9.09	-
Wing taper	0.6	-
Wing sweep	0.0	deg
Canard airfoil	E214	-
Canard span	5.20	m
Canard area	5.20	m^2
Canard MAC	1.00	m
Canard aspect ratio	5.20	-
Canard taper	0.0	-
Canard sweep	0.0	deg
Canard incidence	2.0	deg
V-Tail airfoil	NACA0005	-
V-Tail span	4.53	m
V-Tail area	8.83	m^2
V-Tail MAC	1.95	m
V-Tail aspect ratio	2.32	-
V-Tail taper	0.78	-
V-Tail sweep	-26.4	deg
Height difference canard and wing	1.6	m
Horizontal distance leading edges canard and main wing	4.45	m

6 | Performance, Power, and Propulsion

6.1 Performance

This section will analyze the performance of the Velo-E-Raptor. First, the lift over drag data is obtained from Chapter 5, with which a curve is constructed to determine the ideal cruise velocity. In addition, the glide ratio directly follows from the lift over drag ratio. Then the drag curve is used to obtain a power versus velocity curve. After selecting an engine and propeller that fits this curve, the climb, maneuver and takeoff performance are discussed. When mentioned that the curves are constructed for steady, level flight, this means that lift equals weight and that the velocity does not change throughout the maneuver. The lift is, therefore, 190 kg times 9.81 m/s^2, or 1.86 kN. Furthermore, the height at which they are determined corresponds to the cruise height of 1500 m, which means, by assuming the International Standard Atmosphere [ISO 2533:1975 (1975)], an air density (ρ) of 1.058 kg/m^3 is used.

6.1.1 Cruise and Glide Performance

The aerodynamic properties of the Velo-E-Raptor are determined in Chapter 5. From these, a lift over drag curve can be constructed, as shown in Figure 6.1.

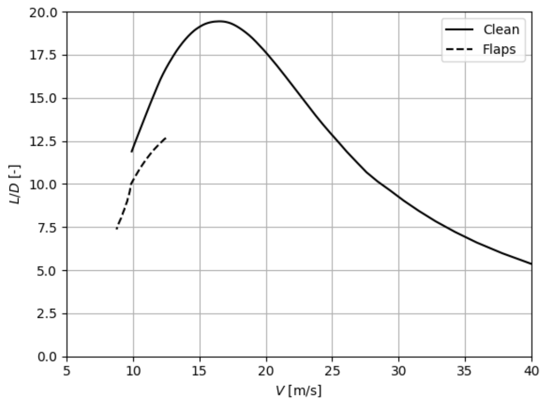

Figure 6.1: Lift over drag ratio versus velocity in steady, level flight for clean and flaps configuration

As can be seen in Figure 6.1, the highest L/D occurs at a velocity of 16.5 m/s, where its value is 19.4. In other words, a glide ratio of 19.4:1 can be reached without power at this velocity. This means that from a height of 1500 m down to sea level, the Velo-E-Raptor can glide more than 29 km. For propeller aircraft, the speed at maximum L/D is equal to the speed where a maximum range can be achieved. This speed is therefore chosen to be the cruise speed.

In Figure 6.2 the drag curve is shown. This is used to determine how much thrust is necessary to be delivered by the propeller. In addition, using Equation (6.1), a power required curve can be constructed, which is shown in Figure 6.3. It is used in combination with the drag curve, cruise speed and noise analysis (discussed in section 6.2) to come up with a suitable propeller. The selection of the propeller, engine, and gearbox will be discussed in more detail in section 6.3. That selection resulted in a thrust available curve and a power available curve, which are shown as well in respectively Figure 6.2 and Figure 6.3. The latter is split into an available shaft power and an available propeller power, which are related to each other as given in Equation (6.2).

$$P_{r,prop} = D \cdot V \tag{6.1}$$

$$P_{a,shaft} \cdot \eta_{prop} = T_a \cdot V = P_{a,prop} \tag{6.2}$$

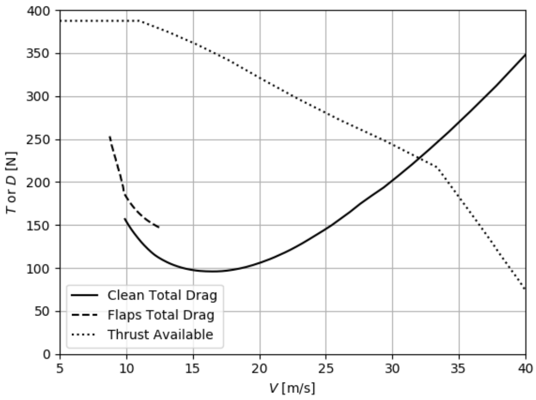

Figure 6.2: Thrust available and drag versus velocity in steady, level flight

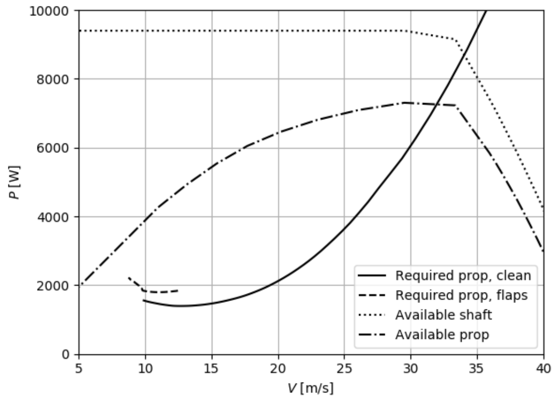

Figure 6.3: Power versus velocity curve for steady, level flight

Using the power required curve, a cruise power of 1.6 kW is required to be produced by the propeller. Combining this with the efficiency of the propeller, a required shaft power of 2.57 kW is needed. The propeller efficiency is treated in section 6.3.1. This value is much higher than what an average human can deliver, as will be discussed in section 10.2.3, which is why electrical assist is a prerequisite to sustain level cruise flight.
Furthermore, when combining the propeller efficiency with the power required, the minimal shaft power required to have a sustained flight can be determined. As this value would mean the least power consumption by the engine, it corresponds to the velocity at which the maximum endurance can be achieved. This velocity is determined to be 15.4 m/s, where the shaft power is 2.53 kW. Note that this value is quite close to the one from cruise flight.

6.1.2 Climb Performance

The climb performance can be deducted as well from Figures 6.2 and 6.3. The climb angle (γ) can be determined as given in Equation (6.3). Combining this with Equation (6.1), the rate of climb, or vertical velocity, can be determined as shown in Equation (6.4).

$$\sin(\gamma) = \frac{T_a - T_r}{W} \tag{6.3}$$

$$RC = V\sin(\gamma) = \frac{P_a - P_r}{W} \tag{6.4}$$

The maximum climb angle, therefore, occurs at the location where the difference between thrust available and thrust required is the greatest. In the current design of the Velo-E-Raptor, this occurs at 13.3 m/s, where an angle of 8.3° can be achieved. Hence, for every 10 meters forward, the Velo-E-Raptor can climb 1.5 meter without losing velocity.
The maximum rate of climb, on the other hand, can be achieved when flying 18.7 m/s. Here the rate of climb is 2.33 m/s. All in all, this means that in order to ascent 1000 m, it will take little more than 7 minutes.

6.1.3 Maneuver Performance

The maneuvering performance of the Velo-E-Raptor is limited by three different causes. Firstly, the structure is only capable of handling a specific load factor. This load factor is +6 up to the maneuver speed of 35 m/s. From there on it slowly degrades towards zero at the never exceed speed. This will be explained further in the V-n diagram of Figure 8.1.
Secondly, the achievable turn rate is limited by the aerodynamic capabilities of the Velo-E-Raptor. It can not deliver more lift than $C_{L,max}$, and as the necessary lift in a turn is $n \cdot W$, the achievable turn rate is limited by this factor.
Lastly, the available thrust plays a role when the pilot wants to make a sustained turn. As the drag is increased linearly with n, the available thrust also limits the achievable load factor.

The achievable turn rate (ω) is given by Equation (6.5). The load factor in this formula depends on one of the three cases as treated above. For the structural load factor, it is simply the load factor from the V-n diagram, whereas for the aerodynamic load factor this depends on Equation (6.6) as well. For the sustained turn load factor, Equation (6.7) is used. The obtained value of C_L is then inserted into Equations (6.5) and (6.6).

$$\omega = \frac{g\sqrt{n^2 - 1}}{V} \quad (6.5) \qquad n_{max} = \frac{0.5\rho V^2 S C_{L,max}}{W} \quad (6.6) \qquad C_{L,a} = \sqrt{\left(\frac{T_a}{0.5\rho V^2 S} - C_{D0}\right) \cdot \pi A e} \quad (6.7)$$

The resulting analysis can be seen in Figure 6.4. The highest turn rate that can be achieved is a bit more than 135 deg/s at a velocity of 24 m/s. This, however, does not mean that this is also achievable in reality, as the control surfaces also need to be capable of delivering enough pitch input. In addition, the curve for minimum turn radius is given in Figure 6.5. The achievable turn radius follows from $r = V/\omega$, and, therefore, has its minimum at a different velocity. Again, this diagram does not mean the control surfaces are able to perform such a turn. The gray area shown in both figures is impossible to achieve due to either aerodynamic or structural constraints. Bear in mind here that this result only looks at the force equilibrium and does not take into account the added effects of a curved flow field and self-induced turbulent air the radius is probably higher, whereas the rate is lower than calculated here.

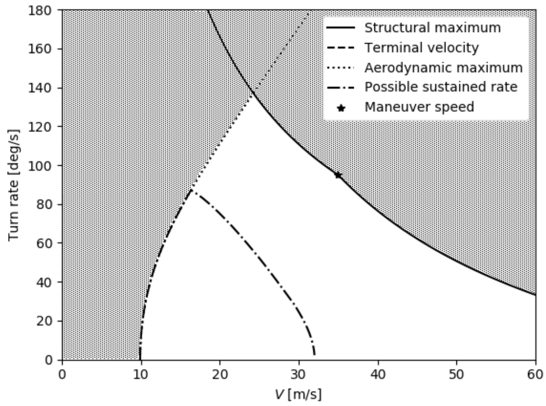

Figure 6.4: Achievable turn rate versus flight velocity for a steady, level turn

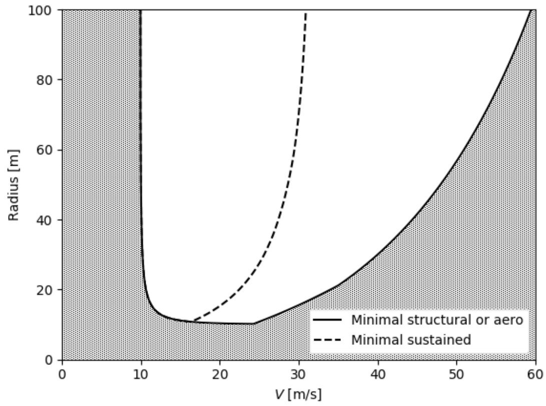

Figure 6.5: Achievable turn radius versus flight velocity for a steady, level turn

6.1.4 Takeoff Performance

During takeoff on a level surface, the Velo-E-Raptor needs to be accelerated up to the lift-off speed V_{LOF}. This will be done by a combination of the legs of the pilot and propeller thrust. In this section, the propeller assisted takeoff is discussed. Apart from the acceleration, the takeoff distances are discussed and the climb phase to a safe height is treated. The foot-launched takeoff will be discussed in section 10.3.

Resisting this acceleration are two sources of drag. These are the ground drag on the support wheels and the aerodynamic drag. The ground drag depends on how much the pilot and wing lift, hence on how much normal force the support wheels have to carry. Furthermore, it depends on the type of surface. The rolling resistance coefficient of tarmac for example is 0.002, whereas for grass this can reach values up to 0.010 [Steyn & Warnich (2015)]. In the worst case, this would mean a roll drag ($D_{gr} = \mu \cdot g \cdot m$) of 18.6 N. This value, however, is quite small compared to the aerodynamic drag, which is shown in Figure 6.6. Two cases are given, the level position $\alpha = 0°$, and the takeoff angle $\alpha = 7.8°$. During the acceleration phase, the pilot will try to keep the aircraft level, up until the rotating velocity (V_R) is reached. This velocity is usually above V_{stall}, to make sure the pilot does not accidentally stall the aircraft after lift-off.
As can be seen in Figure 6.2, the available thrust at takeoff is around 385 N. At the same time the average drag with $\alpha = 0°$ plus the roll resistance is around 65 N. This means that on average during takeoff 320 N is available to accelerate the aircraft. Using $F = m \cdot a$, an average acceleration of 1.7 m/s^2 is obtained. Hence, to reach V_R at 9.6 m/s, one should accelerate for 5.7 s. As $s = 0.5 \cdot a \cdot t^2$, the distance needed is 27 m. This meets the requirement set at 50 m.

Usually, after lift-off, the pilot wants to gain altitude as quickly as possible, in order to reach a safe height where the pilot has time to correct an error or a gust for example. This means that the pilot wants to fly at the highest rate of climb, which was determined in section 6.1.2. In case the takeoff field is restricted by an obstacle like a tree at the end of the runway, the pilot may want to fly at the highest climb angle. This angle was determined to be 8.3°, which means that in order to surpass a tree of 15 m, a field length of at least 100 m is needed after lift-off.

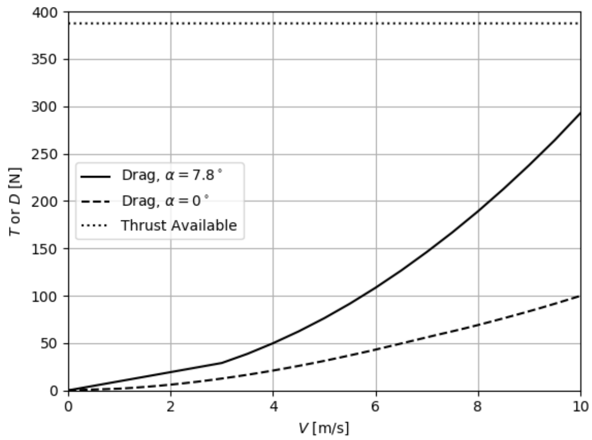

Figure 6.6: Aerodynamic drag during takeoff

6.1.5 Soaring

Soaring is the way of flying gliders use to maintain altitude. With the use of hot, upwards flowing air called thermals, the altitude of the glider can be increased. For the Velo-E-Raptor this is also a good option to extend flight endurance and save battery usage. The minimal turn radius of less than 15 m from Figure 6.5 is sufficiently low to stay within most thermals [FAA (2013)].

6.1.6 Drag sensitivity analysis

Due to uncertainties when estimating the body drag in section 5.4.2, a sensitivity analysis is performed here to evaluate what will happen to the performance in case the drag increases. In Table 6.1, the results are presented. First, the results as they were presented throughout this chapter are stated, after which in the next column the same performance characteristics are stated, but now with an increase in zero-lift drag of 20%. As can be seen, the major implication is the glide ratio. However, all requirements are still met.

Table 6.1: Drag sensitivity analysis

Parameter	Unit	Nominal	$C_{D0} \cdot 1.2$
L/D	-	19.4	17.4
$P_{r,cr,shaft}$	kW	2.57	2.84
γ	deg	8.3	8.0
RC	m/s	2.33	2.21

6.2 Noise Analysis

In this section, the noise emission of the Velo-E-Raptor is analyzed. First, a short research is performed regarding the emission of the Lockheed YO-3 “Quiet star”, after which the most important sources of noise are stated. It concludes with an estimation of the emission of the Velo-E-Raptor itself.

6.2.1 Lockheed YO-3 “Quiet star”

A low noise emission is an important requirement from the customer. The target is to be as silent as the Lockheed YO-3 “Quiet Star". This aircraft was specially designed to go unnoticed. NASA used it as a test aircraft to measure the noise emission of other aircraft. The background noise generated by the YO-3 for which the test had to be corrected is shown in Figure 6.7. The pressure level for this aircraft peaks between 85 and 92 dB at a frequency of 100 Hz on the tail. This spectrum can be translated to the A-weighted pressure level, as defined in ISO 226:2003 (2003). It corresponds to the loudness as perceived by the human ear, which is less sensitive to lower frequencies. At 100 Hz the loudness is for example attenuated by 15 dB.
If this translation to dBA is performed, the maximum perceived loudness as measured for the YO-3A flying at 60 kts (31 m/s) is around 70 dB. At a distance of 150 m, this value attenuates to 40 dB, comparable to the sound of moderate rainfall.

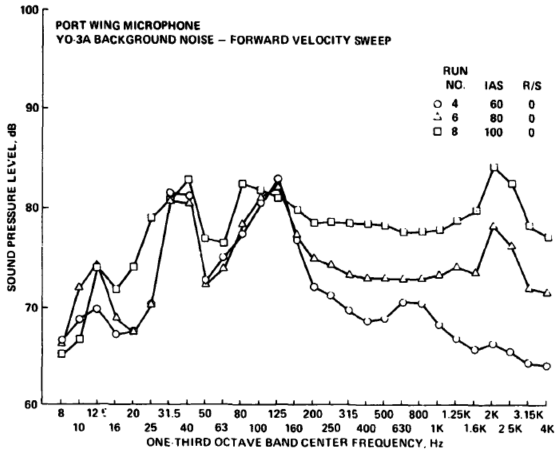

(a) Port microphone noise levels

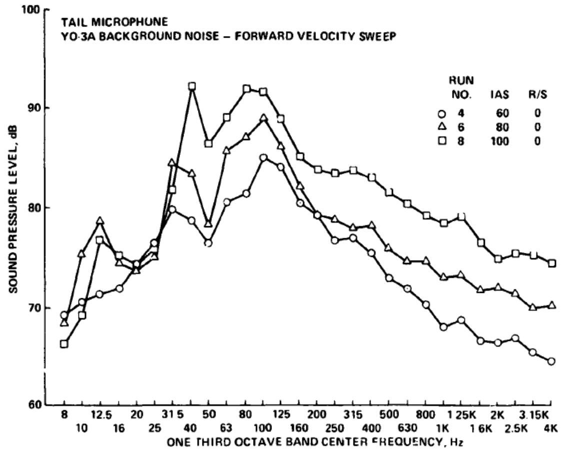

(b) Tail microphone noise levels

Figure 6.7: Noise levels of the Lockheed YO-3A [Cross (1984)]

The low noise emission was achieved by implementing a propeller with a diameter of 100 in (2.54 m), turning at a constant velocity of 800 rpm. This corresponds to a tip velocity of 106 m/s, or Mach 0.31. Three blades were used in combination with a variable pitch [Cross (1984)].

6.2.2 Noise Sources

For the noise of the Velo-E-Raptor, the main source of noise will be the propeller. The engine will not add much noise, as an electric engine is used. Another usually big source of noise is the airframe noise. However, according to a research by Lasagna *et al.* (1980), airframe noise increases by the fifth power of flow velocity. A quick calculation taking the Lockheed Jetstar for reference, which has an airframe noise of 90 dB for a velocity of 180 m/s, leaves 40 dB for a flight velocity of 15 m/s. Although this research was performed on jet aircraft flying much faster, other sources like Müller & Möser (2013) even state that the airframe noise scales to the sixth power of the flow speed. The 40 dB found makes a small difference compared to the propeller noise, hence only the propeller will be discussed. In the end, a safety factor will be used to take into account the extra noise from the airframe, engine and other possible sources.

According to both Müller & Möser (2013) and Marte & Kurtz (1970), the noise emission of a propeller has two main types of noise. Rotational noise describes all sounds identified as harmonics of the blade passage frequency. Vortex or broadband noise concerns the remaining sources. Both are then further split into more types. Müller & Möser (2013) state that broadband noise of the propeller is of minor importance with respect to the total aircraft noise signature for a horizontal flyover. The main contributing subtypes remaining are the loading noise and thickness noise. Loading noise is the dominating source up to tip Mach numbers of 0.6-0.7, whereas thickness noise typically dominates for the higher Mach numbers.

Hence, the first main question is what Mach number the propeller tip speed of the Velo-E-Raptor will reach. This impacts the manner with which the sound pressure level decreases per harmonic order, as shown in Figure 6.8. Furthermore, the presence of sonic booms occurring at the propeller airfoil should be avoided. A quick calculation for the tip speed Mach number with a propeller of 2 m diameter turning at 2000 rpm gives a Mach number at sea level of 0.61. As will be shown later, the chosen diameter is lower, hence the loading noise is the dominating type. Loading noise typically has its maximums in forward and rear arc direction.
It becomes clear that the blade tip Mach number should be decreased as much as possible. In addition, the radius, the blade area, and the number of blades should be maximized [Brown & Ollerhead (1971)]. However, these steps all result in lower thrust coefficients, which can only be reduced to a certain level before an increase in noise results due to wake impingement. The research suggests that a tentative lower limit for the blade thrust coefficient (C_{T_b}) is between $0.07\sqrt{B}$ and $0.1\sqrt{B}$, where B is the number of blades. Please note that the C_{T_b} here is defined in imperial units.
Furthermore, it is stated that detailed blade design is important due to the boundary layer instability effects that can occur with the quiet, low-speed propeller designs.

On top of the previous discussion, it should be noted that the location of the propeller greatly impacts the noise emission of the propeller. The difference between disturbed and undisturbed inflow can become 20 dB for higher frequencies, as shown in Figure 6.9. This research was performed on ultralight aircraft using a full-scale wind tunnel and is therefore very relevant for the design of the Velo-E-Raptor. The difference is due to the

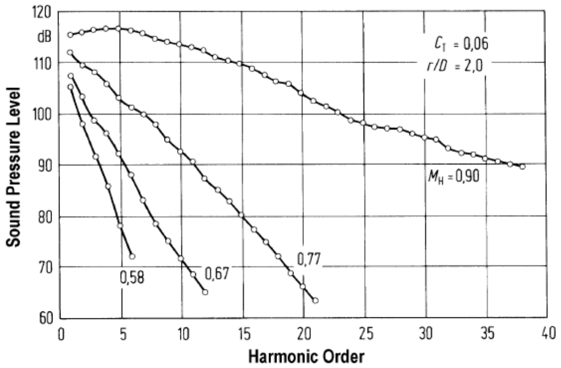

Figure 6.8: Increase in harmonic sound pressure levels for different tip Mach numbers [Müller & Möser (2013)]

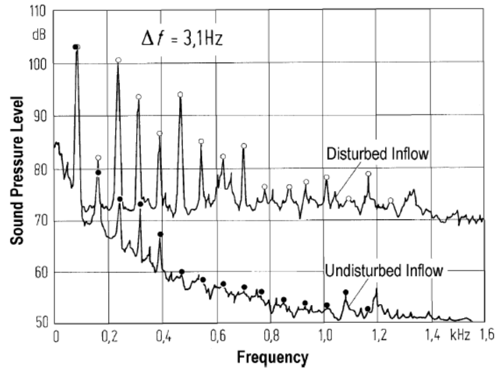

Figure 6.9: Difference in sound pressure levels for disturbed and undisturbed flow [Müller & Möser (2013)]

additional unsteady blade forces created by the turbulent inflow. Unfortunately, a pull prop configuration on the front is not possible as then the propeller would be right in front of the pilot. Using a combination of two pull props on the main wing leaves them in the wake of the canard and pilot and therefore in turbulent flow as well.

Lastly, it is investigated further whether proplets, thus small winglets for propeller blades, will be of any use regarding noise and efficiency for the propeller. A study by Xu *et al.* (2011) shows that the proplet leads to a change of the flow around the propeller tip, such as weaker blade tip vortex. This weaker vortex is helpful to improve the efficiency of the propeller and thereby reduces the noise. However, he also notes that improper parameters may have a negative effect. In addition, the added efficiency is in a range from 0 to 0.05. The effort needed to design a suitable proplet, therefore, does not outweigh the same effort put into the design of the propeller itself.

6.2.3 Propeller Noise Comparison

An estimation for the propeller noise is given by Brown & Ollerhead (1971). First, the blade thrust coefficient shall be calculated according to Equation (6.8). It should at all times be kept above $0.1\sqrt{B}$ to prevent wake interference. The estimation is validated in case this is satisfied. In this equation, T is the thrust, ρ the air density, V_t the tip speed and A_b the total blade area.

$$C_{T_b} = \frac{T}{0.5\rho V_t^2 A_b} \tag{6.8}$$

Four different propellers with more or less equal thrust values around 125 N at cruise velocity are investigated. Their properties are listed in Table 6.2. For all propellers, the unsteady and steady loading noise is calculated. The latter proved to be negligible compared to the unsteady noise. The results from the unsteady noise calculation are shown in Figure 6.10. All propellers meet the C_{T_b} requirement for this configuration. However, when the thrust is doubled, for example when a maximum thrust is needed, the four bladed and three bladed propellers already run into problems regarding the thrust coefficient.

Table 6.2: Propeller properties, as used in the noise comparison of Figure 6.10

Propeller	1	2	3	4
No. of blades	2	3	4	4
Diameter	1.40	1.22	1.11	1.40
RPM	1000	1000	1000	690
Mach tip	0.22	0.2	0.18	0.16

Figure 6.10 shows the results of the estimation of the four propellers. The estimation is taken at a distance of 10 m from the aircraft. According to the estimation, the most silent propeller is the four bladed one, running at a lower rpm but having a higher diameter. In addition, an A-weighted version of the noisiest propeller is included. An average human only hears the noise for the two-bladed propeller with a maximum of around 60 dBA.

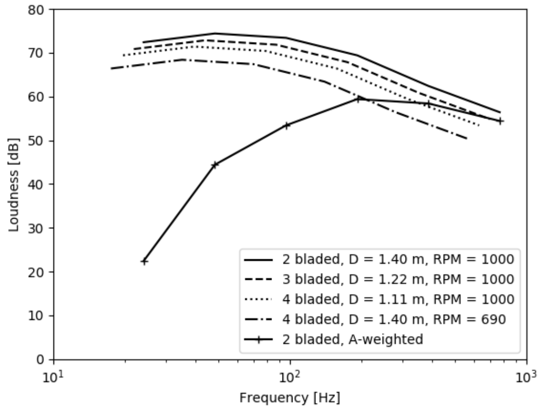

Figure 6.10: Noise comparison for different propellers with the same thrust output in a laminar flow field at a distance of 10 m

6.2.4 Final Estimation

All in all, for the choices made throughout the rest of the report, the maximum noise of the Velo-E-Raptor is estimated to be 60 dB(A) at a distance of 10 m. In Table 6.3, a summary is given of the different sources. Furthermore, an overview is given of the values attenuated for hearing distance. The propeller and gearbox noise is discussed in section 6.3. The safety factor of 45 dB at 10 m is composed of an estimation for airframe noise, engine noise, and other remaining sources, as discussed in section 6.2.2.

Table 6.3: Estimation of A-weighted noise emission [dB(A)] of the Velo-E-Raptor at different hearing distances

Hearing distance [m]	10	250	1500
Propeller Noise	60	30	15
Gearbox Noise	40	10	-5.0
Safety Factor Noise	45	15	0.0
Total Noise	60	30	15

The result shows that the noise emission of the aircraft meets the requirement of being quieter than the Lockheed YO-3A “Quiet Star". However, the noise estimate is still a bit rough. Only the propeller noise is taken into account, which has a suitable estimation for laminar inflow. Even though the 20 dB extra that is chosen to compensate for the turbulent inflow is an estimation that is normally used for ultralight aircraft, the Velo-E-Raptor might have a completely different value there. Therefore, the recommendation is to investigate this further in a full-scale wind tunnel test when deemed necessary.

6.3 Propeller, Motor, Gearbox and Battery Selection

With the noise and flight envelope limits determined in the previous sections, the propulsion system layout is selected in this section. The selection will start off with a propeller that meets the noise and thrust requirements and a motor that meets the noise and power requirements. A gearbox will be selected, based on the rotational speeds and torques. Based on the motor selection and desired flight time, the batteries will be chosen.

6.3.1 Propeller

For a good design of a propeller, one could say that the propeller with the highest efficiency on the design point is a good start. However, in case of the Velo-E-Raptor, the propeller should also perform very good in the off-design points. Especially during takeoff and climb the available thrust is an important factor for the performance, but also for maneuvering possibilities the available thrust is to be maximized. During cruise, on the other hand, the thrust is not so important, but more the necessary shaft power. All in all, the propeller of the Velo-E-Raptor needs to perform well in broader circumstances than a normal airliner propeller, as those are mostly optimized for cruise flight. The requirements and as set by other design choices are summarized in Table 6.4.

Table 6.4: Propeller requirements and limitations

Parameter	Unit	Value
Diameter	m	≤ 1.4
Thrust available TO	N	≥ 400
Power required cruise	kW	≤ 2.5
Noise at 10 m during cruise	dBA	≤ 60

To design a suitable propeller, JavaProp[1] is used. It is validated by Hepperle (2015), who compared it to a full-scale wind-tunnel test as performed by Theodorsen *et al.* (1937). The inputs needed for JavaProp are summarized in first two columns of Table 6.5. Based on the noise research from section 6.2 and a parameter study in JavaProp, the first design parameters were chosen. They are chosen in such a way that the requirements are not violated and that the efficiency will be maximized throughout the whole flight envelope.
As researched by Gur & Rosen (2005), a variable pitch mechanism would make it possible to obtain a high efficiency at a wider range than a fixed-pitch mechanism could. However, due to the weight-critical design, the lower price and the reliability, the decision is made to implement a fixed-pitch mechanism.

First, an analysis is performed comparing three different propeller airfoil designs for the same design point. The design properties are shown in the table as well. Four locations along the propeller radius R are defined, with r noting the distance from the center. The first airfoil (at 0% r/R) is always a Flat Plate with a Reynolds number of 100k, as the spinner is located there. For the airfoils at location 2 and 3 (33% r/R and 67% r/R), it is important to check whether the Reynolds number selected for the airfoil corresponds to the design in the end. As the Reynolds number depends on the chord length, which is in turn determined by JavaProp, it has to be done by hand for each design. A quick research showed that the Reynolds number varies between 100k for low lift, longer chord airfoils and 300k for high lift, shorter airfoils. For the tip (100% r/R) a Reynolds number of 100k is selected. Here, the velocity is quite high, but the chord length decreases down to zero, such that the 100k is a valid estimation.

Table 6.5: Inputs for JavaProp and airfoil trade-off

Parameter	Unit	Design 1	Design 2	Design 3
No. of Blades	-	2	2	2
Design RPM	-/min	1000	1000	1000
Diameter	m	1.4	1.4	1.4
Spinner Diameter	m	0.12	0.12	0.12
Design Velocity	m/s	12	12	12
Design Power	kW	1.2	1.2	1.2
Airfoil 1 [Re,α]	-	Flat Plate [100k,3°]	Flat Plate [100k,3°]	Flat Plate [100k,3°]
Airfoil 2 [Re,α]	-	Flat Plate [100k,3°]	ARA-D 6% [100k,3°]	E 193 [300k,3°]
Airfoil 3 [Re,α]	-	Clark Y [100k,3°]	ARA-D 6% [100k,3°]	E 193 [300k,3°]
Airfoil 4 [Re,α]	-	Clark Y [100k,3°]	ARA-D 6% [100k,3°]	ARA-D 6% [100k,3°]

The resulting efficiency curves and thrust curves at 10 kW are shown in Figures 6.11a and 6.11b, respectively. The thrust curve at 10 kW is taken to check whether the off-design performance at takeoff or maximum velocity passes the check. It can clearly be seen that the third design option is the best here. This is, therefore, the airfoil design chosen for the rest of the propeller selection.

Then, the other design factors have to be determined. For five cases, the available thrust for takeoff, the power required for cruise, the maximum possible velocity, the achievable rate of climb, and the maximum climb angle are investigated. They are compared to the nominal case, which is the third design from Table 6.5. For the available takeoff thrust and all maximums, the off-design analysis is set at maximally $P = 9.4$ kW or 1940 RPM. Both numbers follow from the engine and gearbox selection of the upcoming subsection. For the cruise power, the analysis is performed at a thrust of 100 N, which is the required thrust as shown in the performance analysis. The result is shown in Table 6.6. Apparently, an increase in design power leads to a better design, hence this was investigated further. It turned out that the increase in design power mainly leads to an increase in chord length. Although this leads to a better performance, it is not a desirable feature in this case. The disk loading becomes too high, reducing the efficiency. The addition of a third blade only leads to a slight increase in performance, which does not counter the added mass. In the end, the nominal configuration was chosen as a suitable design option. The maximum efficiency of the design is 79%, as can be seen in Figure 6.11a.

[1]URL `http://www.mh-aerotools.de/airfoils/javaprop.htm` [cited 20 June 2017]

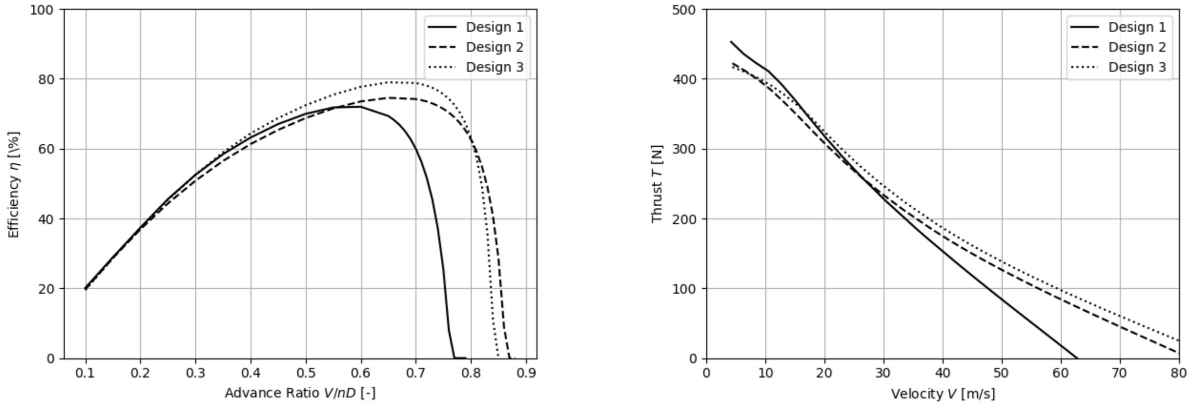

(a) Efficiency versus advance ratio

(b) Thrust versus velocity

Figure 6.11: Trade-off between the different airfoil designs from Table 6.5

Table 6.6: Propeller design parameter trade-off

Parameter Unit	New value -	$T_{a,TO}$ N	$P_{s,req,cr}$ kW	V_{max} m/s	RC_{max} -	γ_{max} deg
Nominal	-	388	2.42	28.5	2.33	8.28
No. of blades	3	391	2.40	28.5	2.36	8.40
Design RPM	1500	154	2.49	17.8	0.24	1.02
Diameter	1.0	323	2.54	28.4	1.87	6.46
Design velocity	16.5	325	2.32	31.8	2.13	6.85
Design power	4.0	399	2.58	31.9	2.33	8.72

Lastly, it was investigated whether it would be beneficial to make the propeller foldable. Regarding both glide performance and safety, it is deemed indeed beneficial if it does not impact the mass budget too much. Unfortunately, no good estimation could be made up to how much added mass it would outperform a non-folding propeller. The decision is made, nevertheless, to implement a folding propeller. Further research should prove whether this is the right decision.

With the decision made of going with the nominal propeller, a market analysis is performed to find a suitable propeller. This resulted in the H25K 140m R-E-13-2, folding propeller, of Geiger Engineering [Geiger (2009)]. The power curve and thrust curve of both the designed propeller and the given data from Geiger are compared in Figures 6.12a and 6.12b, respectively. The shaft power required curve of JavaProp matches the propeller from Geiger within 10%. The thrust curve is off by 100 N on average, which can be due to two things. Either the efficiency of the Geiger propeller is higher for this speed, or the Geiger propeller is tested at a lower speed. A combination of both is also possible. Therefore, the suggestion is made to test the H25K 140m R-E-13-2 propeller to see whether it indeed as the design propeller. As already stated in section 6.2, proplets will not be used in the design. In Table 6.7, some geometric properties of the final propeller are given.

Table 6.7: Final JavaProp propeller geometric properties with $v_\infty = 12$ m/s and RPM = 1000

Spanwise location r/R [-]	0.1	0.35	0.65	0.9
Chord length [cm]	12.7	14.4	9.1	4.2
Reynolds number [-]	$1.22 \cdot 10^5$	$2.79 \cdot 10^5$	$3.06 \cdot 10^5$	$1.92 \cdot 10^5$

In the performance analysis of section 6.1, to be able to perform an analysis at different velocities, the results from the JavaProp propeller are used. The research is however performed until 2200 RPM, as that is the maximum velocity of the Geiger propeller.

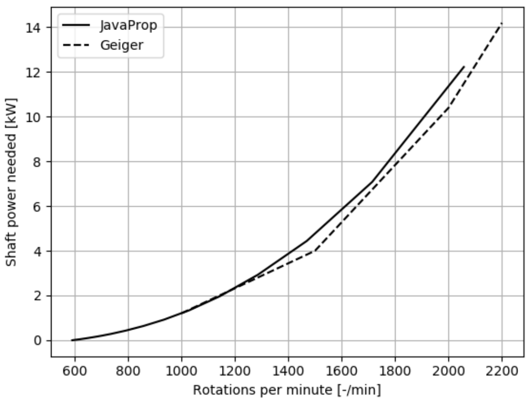

(a) Shaft power required versus RPM

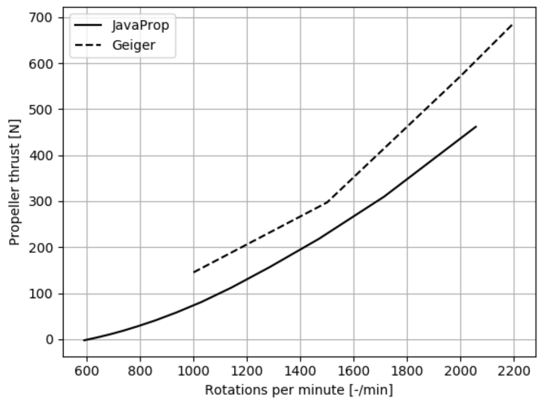

(b) Thrust versus RPM

Figure 6.12: Comparison between the H25K 140m R-E-13-2 [Geiger (2009)] and the designed propeller at a velocity of 12 m/s

6.3.2 Motor

Now the propeller is selected in section 6.3.1, a proper motor can be selected which meets the requirements. In the ideal case, a gearbox will be unnecessary. This means that the torque, rotation speed and power of the motor match those of the propeller for each flight condition. However, this is quite difficult and increases the complexity of the motor selection process. Motor weight, noise level, and power are considered to be leading factors. Weight should be minimized and the desirable noise and power limits are stated in Table 6.8. As batteries are the power source, a direct current motor will be selected.

Table 6.8: Motor requirements

Parameter	Unit	Value
Noise at 0m	dBA	60
Power	kW	10

Based on these requirements, the Turnigy RotoMax 150cc Size Brushless Outrunner Motor[2] is selected. This is a motor for large scale model aircraft and closely matches out requirements. The specifications of this motor are given in Table 6.9 and the drafts are displayed in Figures 6.13 to 6.15.

Table 6.9: Motor specifications

Parameter	Unit	Value
Current	A	190
Power	kW	9.8
Rotational constant	kV	150
Voltage	V	51.8
Weight	kg	2.53

Figure 6.13: Turnigy RotoMax motor

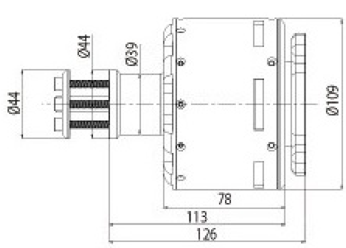

Figure 6.14: Motor draft side view

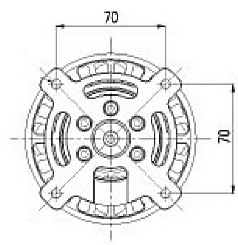

Figure 6.15: Motor draft front view

[2]URL `https://hobbyking.com/en_us/turnigy-rotomax-150cc-size-brushless-outrunner-motor.html` [cited 19 June 2017]

The efficiency of the motor is taken at 95%, based on high efficient brushless DC motors [Gossler & Murray (1996)]. The propeller performance calculations in Section 6.3.1 are performed taking a 9.4 kW propeller power input into account. This can not be achieved with the power of this motor considering the motor and gearbox efficiency. Hence, either less optimistic climbing performance should be considered or a different motor should be selected during further research. Nevertheless, this motor is used for further calculations.

The noise level of this motor is within the safety factor as mentioned in section 6.2. In order for the specifications to be usable for further selection processes, some values require additional calculations. The output rotation speed of the motor has to be changed to rounds per minute (ω_{RPM}) instead of kilovolts (ω_{KV}). This is done with the use of Equation (6.9), where U is the input voltage.

$$\omega_{RPM} = \omega_{kV} \cdot U \tag{6.9}$$

This results in a maximum rotation speed of 7770 rpm. The rotation depends on the voltage through the motor. As batteries have a minimum discharge voltage (section 6.3.3), the minimum rotation speed is limited by the battery specifications. The rotation speed (in radians per second) is used to calculate the maximum torque on the motor shaft (Equation (6.10)).

$$T_{max} = \frac{P}{\omega} \tag{6.10}$$

The maximum torque on the shaft is 12 Nm. Furthermore, these motor specifications will be important for the battery and gearbox selection process in sections 6.3.3 and 6.3.4, respectively.

Table 6.10: Motor performance

Parameter	Unit	Value
Rotation speed maximum	RPM	7770
Rotation speed minimum (LiPo)	RPM	5670
Rotation speed minimum (LiIon)	RPM	5250
Torque maximum	Nm	12

6.3.3 Battery

In order to obtain optimal performance, the battery selection process is of great importance. The battery current and voltage should match the required motor input to obtain maximum motor performance. In order to remain light weighted, the battery specific energy should be as high as possible. The subsystem analysis conducted in the midterm report [Aarts *et al.* (2017b)] shows that lithium-ion and lithium polymer batteries are considered to be the most feasible options. Lithium polymer has the highest specific energy, but a lower number of cycles and a higher safety risk than lithium-ion batteries. However, lithium polymer batteries have already been used on electric trikes as the Icaro 2000[3] and these specific batteries are considered to be safe enough for this purpose.
For the Velo-E-raptor, the selection process is mainly influenced by the battery quality and weight, both lithium polymer and lithium ion batteries are considered. The main requirements are stated in Table 6.11. This does not necessarily mean that a single battery should comply with these requirement to qualify for the selection process. Single high energy cells are also considered and they are connected in both series and parallel to obtain a satisfactory battery current and voltage.

Table 6.11: Battery requirements

Parameter	Unit	Value
Current	A	190
Power	kW	9.8
Voltage	V	51.8

Taking safety into account eliminates the high-performance lithium polymer model aircraft batteries as their quality standards are not comparable to those of manned flight. Based on this and the requirements in Table 6.11, the lithium polymer (LiPo) Akku (14s1p) from Geiger Engineering is selected [Geiger (2009)], which is a suitable option for high performance. The battery specifications are listed in Table 6.12.
This battery has a weight of 16 kg, which leaves 2 kg of the 18 kg battery weight budget unused. The power of the battery is calculated with Equation (6.11).

[3] URL `http://www.icaro2000.com/Products/Trike/Trike.htm` [cited 12 July 2017]

Table 6.12: Lithium polymer battery specifications

Parameter	Unit	Value
Capacity	Ah	39
Cell Number	-	14
Charge Rate	C	2.1
Discharge Rate	C	5.1
Energy Content	kWh	2.07
Height	mm	215
Length	mm	280
Voltage Charge Maximum	V	58.8
Voltage Discharge Maximum	V	51.8
Voltage Discharge Minimum	V	37.8
Volume	L	9.63
Weight	kg	16
Width	mm	160

$$P = U \cdot I \tag{6.11}$$

The power of the battery is 10.36 kW, this is sufficient to provide the motor with its maximum required power. During climbing flight, maximum power settings are used and the battery can provide for an assisted climb of 13 minutes (Equation (6.12). Less power is required during cruise flight and the batteries can provide for an assisted flight of 29 minutes (Equation (6.13)).

$$t_{climb} = \frac{E_{batt}}{P_{max}} \cdot 60 \tag{6.12}$$

$$t_{cruise} = \frac{E_{batt}}{P_{cruise}} \cdot 60 \tag{6.13}$$

Hence, the battery discharge voltage decreases to its minimum during the discharge period. This results in a maximum power of 7.52 kW at the end of each battery cycle. A climb gradient of 6.5° and rate of climb of 1.75 m/s can still be performed with this power. This is sufficient for a go-around.

These performances are already quite marginal and further research has to be conducted to determine if the risk of these lithium polymer batteries is within acceptable limits. However, as this specific battery has already been used on electric trikes, it is expected to be safe. Although this specific battery has already been used on comparable products, lithium-ion batteries are still considered to be safer in general. Therefore, a substitute for the lithium polymer battery is selected for the time being. This is the LiIon accupackage (14s20p) from Geiger Engineering [Geiger (2009)]. The specifications are presented in Table 6.13. Some of these characteristics differ from the lithium polymer battery and additional performance calculations will be done.

Table 6.13: Lithium-ion battery specifications

Parameter	Unit	Value
Capacity	Ah	23.4
Cell Number	-	14
Charge Rate	C	1.0
Discharge Rate	C	8.5
Energy Content	kWh	1.37
Height	mm	220
Length	mm	260
Voltage Charge Maximum	V	57.4
Voltage Discharge Maximum	V	51.8
Voltage Discharge Minimum	V	35
Volume	L	8.01
Weight	kg	13
Width	mm	140

The weight of this battery is 13 kg. This is below the 18 kg battery weight budget and leaves 5 kg unused weight, thus less effective than the lithium polymer battery. Nonetheless, the product has an assisted climb and cruise time of 8 and 18 minutes, respectively. The end of cycle power is 6.96 kW. With this power, a climb gradient of 5.95° and rate of climb of 1.6 m/s can be performed. With these performances, a safe go-around can be performed.

In order to give more insight into the different performances, some additional calculations on the charging time and battery performance have been made (Equations (6.14) to (6.17)).Furthermore, the batteries are scaled to the 18 kg limit, to give an overview of the maximum achievable performance.

One thing to take into consideration is battery degradation. This reduces the power severely with an increasing number of cycles. The battery degradation of lithium ion batteries is superior as it takes more cycles. For lithium polymer batteries, only 80% of the capacity remains after 300 to 500 cycles. Compared to 500 to 1000 cycles for lithium ion batteries [4]. The 80 % limit is considered to be the degradation limit as the battery should be replaced beyond this point [5]. For flight time calculations at this point, a constant battery discharge rate is assumed. At this point, the battery can only provide for a maximum climbing time of 12 and 7 minutes and cruise time of 23 and 14 minutes for lithium polymer and lithium ion batteries, respectively. Degradation also affects the end of cycle power. This is reduced to 6.17 kW and 6.28 kW for lithium polymer and lithium ion, respectively. This leads to reduced achievable climbing gradients and rate of climbs.

$$t_{ch} = \frac{E_{batt}}{I_{ch}U_{ch}} \quad (6.14) \qquad u = \frac{E_{batt}}{V} \quad (6.15) \qquad E_{spec} = \frac{E_{batt}}{m} \quad (6.16) \qquad P_{spec} = \frac{P_{batt}}{m} \quad (6.17)$$

Table 6.14: Battery performance

	Unit	LiPo	LiIon
Charging Time	min	26	60
Charging Time (degraded)	min	21	48
Charging Time (scaled)	min	29	83
Charging Time (degraded & scaled)	min	24	66
Climbing Flight	min	13	8
Climbing Flight (degraded)	min	12	7
Climbing Flight (scaled)	min	15	11
Climbing Flight (degraded & scaled)	min	14	10
Cruise Flight	min	29	18
Cruise Flight (degraded)	min	23	13
Cruise Flight (scaled)	min	33	25
Cruise Flight (degrade & scaled)	min	26	18
Energy Density	Wh/L	259	142
Specific Energy	Wh/kg	130	105
Specific Power	W/kg	648	797

The results are compared in Table 6.14. As can be noticed, the lithium polymer battery is performing better on both flight times and charging time. Therefore, this battery is preferred if proven to be sufficiently safe.

6.3.4 Gearbox

As mentioned in section 6.3.2, a gearbox is required if the motor outputs (Table 6.9) and the propeller inputs do not match. As this is the case for the rotational speeds and torques of the propeller and motor, a gearbox is required. The torque and rotational speed are related to each other via the power (Equation (6.10)). The gearbox can connect the propeller and motor either with use of a shaft or a direct connection. The specifications which the gearbox has to cope with are stated in Table 6.15.
The power output is determined by the power input of the motor and the gearbox efficiency. The rotation output limits are both minimums and determined by the propeller performance. Furthermore, the rotation input is the maximum rotation speed of the motor and the torques are both maximum limits.
These limits result in a required gearbox ratio of 3.9, based on the rotation ratio of the motor output and required propeller input (Equation (6.18)).

$$R_{gear} = \frac{\omega_{maxin}}{\omega_{maxout}} \tag{6.18}$$

As mentioned in section 6.3.2, the rotation speed of the engine can not reach limits below the minimum

[4]URL `http://batteryuniversity.com/learn/archive/whats_the_best_battery` [cited 30 June 2017]
[5]URL `http://batteryuniversity.com/learn/article/capacity_loss` [cited 30 June 2017]

Table 6.15: Gearbox requirements

Input parameter	Unit	Value
Power input	kW	9.8
Rotation speed input	min^{-1}	7770
Rotation speed output maximum	min^{-1}	2000
Rotation speed output minimum	min^{-1}	1000
Torque input	Nm	12
Torque output	Nm	50

discharge voltage of the batteries due to their dependence (Equation (6.9)). This means that the minimum propeller rotation speed is above the 1000 RPM requirement. A power management system (PMS) is required to get the voltage below the minimum battery discharge voltage (Tables 6.12 and 6.13). The Motorcontroller PI300 [Geiger (2009)] has been selected as this controller is applicable for the used voltages and currents. Its weight is estimated at 0.15 kg, taking a comparable controller into account[6].

With these requirements know, a type of gearbox can be selected. This is done based on general gearbox characteristics to provide for a preliminary estimation. Due to the weight criticality, a low-weight and high-efficiency gearbox is preferred. Planetary gearboxes have these characteristics [Concli (2016)][7], but they are also known for a higher than average noise level [Gawande *et al.* (2014)].

Table 6.16: Gearbox performance

Parameter	Unit	Value
Axial force	N	3900
Efficiency at full load	%	96
Gearbox Weight	kg	1.4
Mechanical input speed	min^{-1}	13000
Operating temperature	°C	-25/90
Radial force	N	3200
Ratio	-	4
Running noise	dB(A)	58
Torque output	Nm	64

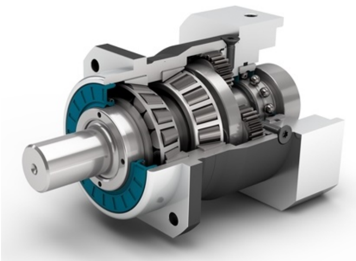

Figure 6.16: Gearbox open section view

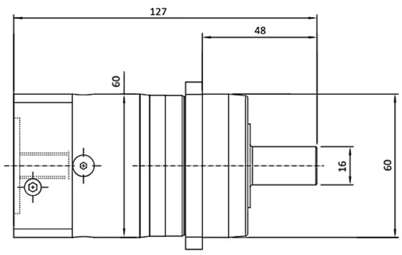

Figure 6.17: Gearbox side view

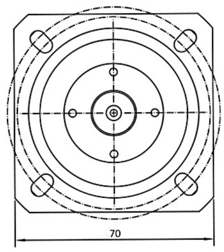

Figure 6.18: Gearbox frontal view

Based on the requirements, the PLHE060 Economy Planetary Gearbox from Neugart GmbH[8] has been selected. This gearbox has a ratio of 4, so a maximum output rotation speed of 1940 RPM is achieved. This is insufficient for obtaining the desired flight velocity and a custom made gearbox is required to obtain the 2200 RPM rotation velocity.

However, further improvement can be achieved by choosing a motor with a higher maximum rotation speed as energy loss of the controller can be prevented. The gearbox ratio can then be determined by Equation (6.19).

$$R_{gear} = \frac{150 \cdot U_{md}\eta_{gear}}{\omega_{minout}} \tag{6.19}$$

This results in a gearbox ratio of 5 for the selected lithium polymer and lithium ion batteries. The maximum rotation speed of the motor is then determined by Equation (6.20).

[6]URL `http://www.ecolight.ch/Images/Flytec.pdf` [cited 15 June 2017]
[7]URL `https://gearmotorblog.wordpress.com/2013/05/07/planetary-gearmotors/` [cited 14 June 2017]
[8]URL `https://www.neugart.com/en/products/planetary-gearboxes-with-output-shaft/plhe/#PLHE60` [cited 14 June 2017]

$$\omega_{maxin} = \frac{R_{gear}\omega_{maxout}}{\eta_{gear}} \quad (6.20)$$

This results in a maximum motor rotation speed of 11500 RPM. The power requirement remains unchanged.

6.4 Hardware Positioning

Now the parts for the power and propulsion system have been selected, they are positioned in the product. A brief overview of the position constraints and the final positions of each part will be given in this section.

Propeller
The main position restrictions for the propeller are set by the stability & control and the safety department. According to the propeller manufacturer, sufficient ground clearance shall be taken into account to prevent the blades from damaging. An angle of attack (α) of 10° is used to calculate the required position of the propeller to prevent ground impact. This comes from the stall angle of 9° including a safety factor of 1.1. Furthermore, an additional obstacle clearance (h) of 0.1 m is used for safety reasons. Using Figure 6.19, propeller dimensions from section 6.3.1 and landing gear position and dimensions from section 10.3.1, this results in a vertical propeller position of 0.53 m above the frame. The horizontal position has already been fixed at 7.83 m from the canard leading edge for a clear rotation. Figure 6.20 visualizes the propeller between the V-tail, mounted to the rear structure.

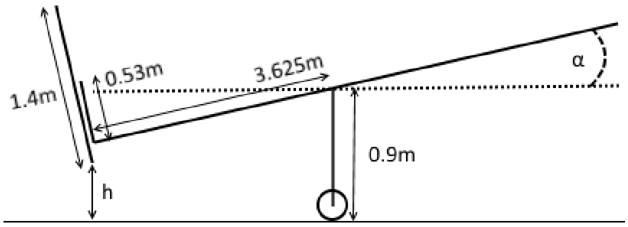

Figure 6.19: Propeller height determination

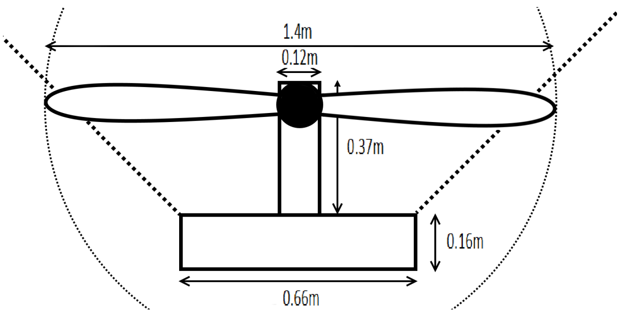

Figure 6.20: Front view of propeller positioning on the rear structure

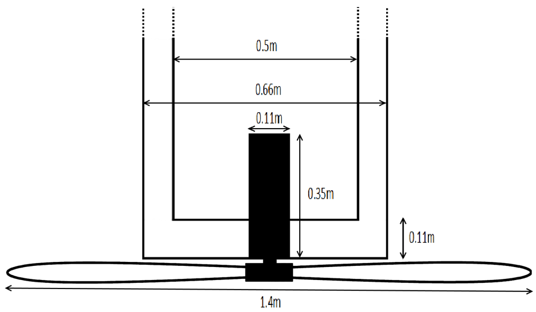

Figure 6.21: Top view of the propeller, motor and gearbox positioning

Gearbox & Motor
In order to reduce the weight of the product, the gearbox and motor are positioned right behind the propeller to avoid the use of a shaft. Figure 6.21 gives an overview of the dimensions of the gearbox and motor casing behind the propeller. The minimum casing dimensions are 35x11x11 cm. This results in a vertical position for both the motor and gearbox similar to that of the propeller. The horizontal positions taken from the leading edge of the canard are 7.76 m and 7.59 m for the gearbox and motor, respectively.

Control Unit
The controller is positioned between the motor and the batteries. No position limitations are set by the stability & control engineers, as the weight of the controller is quite marginal. The main position requirement is that the cables connecting the controller and motor are not longer than 0.5 m. According to the power unit manufacturer, a cable thickness of 16 mm^2 is required to conduct currents up to 200 A [Geiger (2009)].

Cables
The motor and batteries have to be connected via cables. As mentioned above, these cables have a thickness of 16 mm^2 to support the required current. To estimate the weight of the cables, the used material and the required length have to be determined. The cables run from the batteries to the engine. This is a total length of 4.4 m. The cable from the pedal system to the PMS has a total length of 3.6 m. Assuming copper for the material with a density of 8960 kg/m^3, the weight of the cables is calculated with Equation (6.21).

$$W_{cable} = \rho A l \tag{6.21}$$

This results in a total mass of 1.15 kg.

Battery
In order to have sufficient power, quite some batteries are required. The stability & control engineers set the x-position of the batteries between 2.5 m to 4.1 m from the canard leading edge. As the batteries are responsible for a considerable part of the weight, they will be positioned in such a way that a part of them can be taken as luggage into the product. Hence, not the entire battery weight contributes to the empty weight of the product. For the positioning, the lithium polymer is considered, because it has larger dimensions. The selected battery in section 6.3.3 consist of 14 cells. These cells are split up into three parts. The first part, two cells, is fixed to the structure to assure for an assisted takeoff with the empty weight structure. This part is positioned in the front square beam right in front of the pilot. The remaining cells are divided into two packages of six cells each and can be placed in the same front beam. Figures 6.22 and 6.23 give an overview of how the batteries (indicated by the red lines) are positioned in the structure. The grey areas on the side of the structure can be opened to insert the batteries. Placing the batteries in the structure is desirable for the stability and control, safety, and performance of the product. In order to prevent overheating air is lead around the batteries. The air enters the structure at less heavily loaded areas in the cylindrical beam and exits the structure at the sidebars.

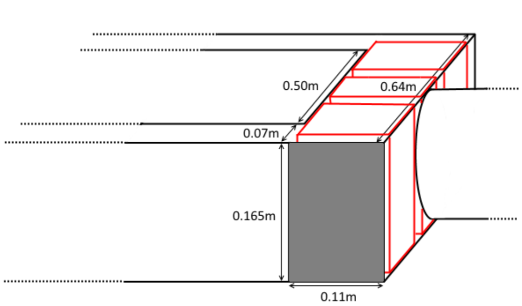

Figure 6.22: Side view battery position

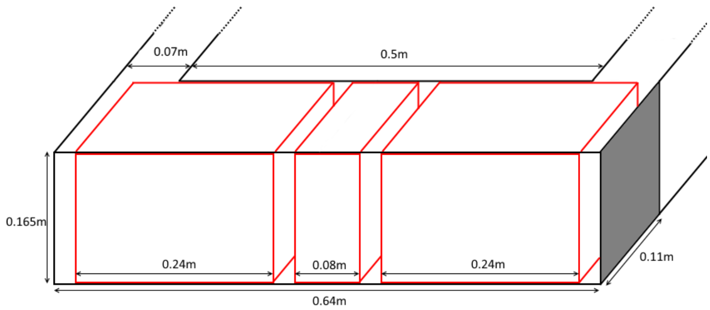

Figure 6.23: Front view battery position

With all the hardware elements of the Performance, Power, and Propulsion section known, a final overview of the weights is presented in Table 6.17. Of these masses for the lithium polymer and lithium ion battery, 13.7 kg or 12 kg respectively is taken as luggage weight, thus does not account for the operational empty weight. This results in a significant weight margin and leaves budget for the other subsystems and departments. In addition, an electrical block diagram is presented in Figure 6.24. This block diagram shows the flow of data in the propulsion system.

Table 6.17: Masses of the selected parts

Part	Mass [kg]
Battery (LiPo)	16
Battery (LiIon)	13
Cables	1.15
Control Unit	0.15
Gearbox	1.4
Motor	2.53
Propeller	1.3
Total Mass (LiPo)	22.5
Total Mass (LiIon)	19.5
Total Mass (scaled)	24.5

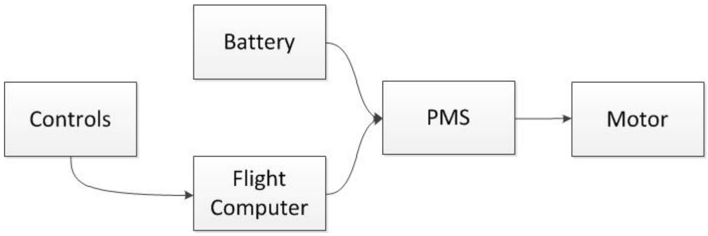

Figure 6.24: Electrical block diagram

7 Stability and Control

This chapter will analyze the stability and controllability of the Velo-E-Raptor. The used tools are described, and during the assessment, several decisions are made regarding the layout of the aircraft and control surfaces. In the end, there is a center of gravity range for which the aircraft is stable and the maneuver performance is discussed. When the center of gravity position is discussed without further information, this means the position of the center of gravity along the body axis, starting from the leading edge of the canard.

7.1 Tools

7.1.1 Python

To help determining the location of the canard, a tool was developed in Python. The purpose of the tool was to find the angle of attack α at which longitudinal stability is maintained. One of the driving factors of this is the tail volume, which allows one to size for a particular canard distance. The basis of the tool is the method presented in Gudmundsson (2013), reproduced below for legibility in Figure 7.1 and equation (7.1). The figure indicates the distances h, h_{AC} and l_c used in Equations (7.1b) and (7.1c). M_{AC}, L_c and L_w denote the forces and moments on the system.

$$C_m = C_{m_0} + C_{m_\alpha}\alpha + C_{m_{\delta_e}}\delta_e \tag{7.1a}$$

$$C_{m_0} = C_{m_{0_{AC}}} - \frac{h + h_{AC}}{\bar{c}} C_{L_{0_w}} + \frac{S_c l_c}{S\bar{c}} C_{L_{0_c}} \tag{7.1b}$$

$$C_{m_\alpha} = C_{m_{\alpha_{AC}}} - \frac{h + h_{AC}}{\bar{c}} C_{L_{\alpha_w}} + \frac{S_c l_c}{S\bar{c}} C_{L_{\alpha_c}} \tag{7.1c}$$

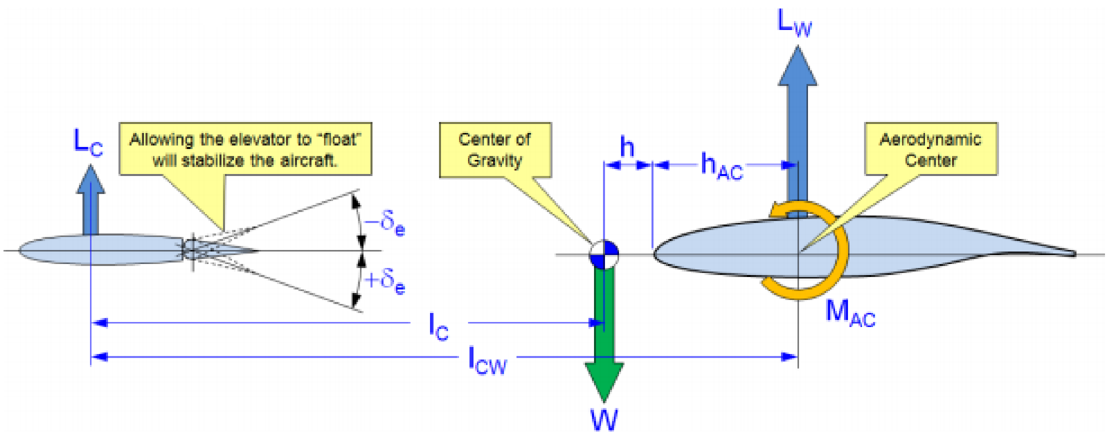

Figure 7.1: The distances, forces and moments acting on the canard configuration (Figure C2-4 from Gudmundsson (2013))

Equation (7.1) allows for a linearized $C_m - \alpha$ curve around a flight point to be created, based on non-dimensional parameters. As the model used is all in one plane, is does not take into account the drag of the wing and canard, nor the force of the propeller. This meant that the configuration described in Chapter 2, these equations were not applicable, and an expanded set based was derived.

The full diagram used for the Python tool is shown in Figure 7.2. The addition of drag, thrust and vertical distances change Equation (7.1) into Equation (7.2). For the purpose of the tool, the influence of the elevator, $C_{m_{\delta_e}}\delta_e$, from Equation (7.1a) was neglected, as during cruise the elevator deflection (δ_e) should be zero. Fur-

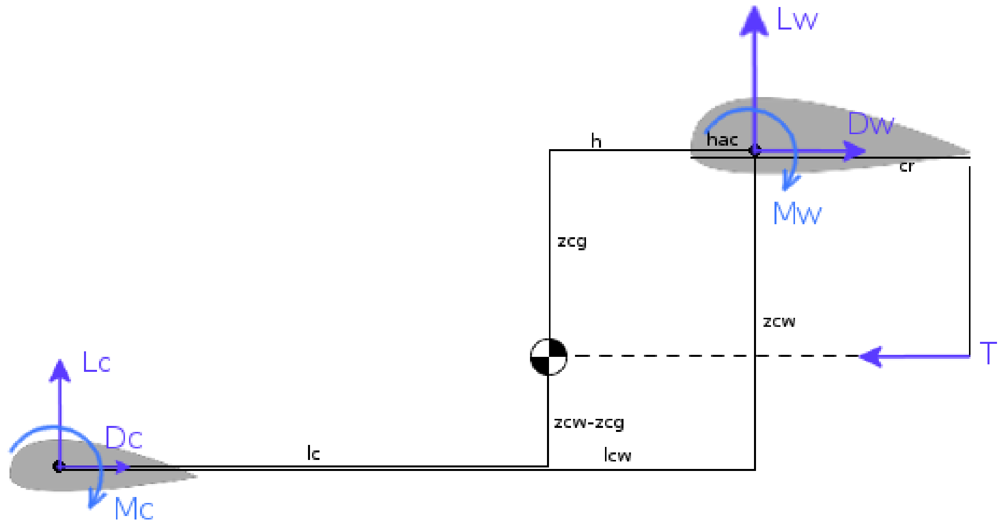

Figure 7.2: Side view (aircraft facing left) of the model used in the Python tool, indicating the distances, forces and moments on the aircraft

thermore, elevator deflection could be better modeled in AVL, as described in Section 7.1.2. The full derivation of the $C_m - \alpha$ curve can be found in Appendix A.

$$C_m = C_{m_0} + C_{m_\alpha}\alpha \tag{7.2a}$$
$$C_{m_0} = C_{m_{0_{AC}}} + U_c C_{m_{0_c}} + C_{m_{0_w}} - V_w C_{L_{0_w}} + V_c C_{L_{0_c}} + W_w C_{D_{0_w}} + W_c C_{D_{0_c}} - W_p T_c \tag{7.2b}$$
$$C_{m_\alpha} = C_{m_{\alpha_{AC}}} + U_c C_{m_{\alpha_c}} + C_{m_{\alpha_w}} - V_w C_{L_{\alpha_w}} + V_c C_{L_{\alpha_c}} + W_w C_{D_{\alpha_w}} + W_c C_{D_{\alpha_c}} \tag{7.2c}$$
$$U_c = \frac{S_c c_c}{S\bar{c}} \quad V_c = \frac{S_c l_c}{S\bar{c}} \quad W_c = \frac{S_c}{S}\frac{z_{c.g.} - z_{cw}}{\bar{c}} \quad V_w = \frac{h + h_{AC}}{\bar{c}} \quad W_w = \frac{z_{c.g.}}{\bar{c}} \quad W_p = \frac{2D^2}{S}\frac{z_{c.g.}}{\bar{c}}$$

To precisely define the location of the tail, the program allows for four parameters to be changed. These are the area ratio (S_c/S), the horizontal distance between aerodynamic centers (l_{cw}), the vertical distance between aerodynamic centres (z_{cw}), and the angle of incidence of the canard (AoI). These are controlled by sliders, with the graph updating to user inputs.

Aside from the $C_m - \alpha$ curve, it also relevant to know the stability margin of the aircraft. Gudmundsson (2013) also provides a formula to determine the neutral point, reproduced below in Equation (7.3). As with Equation (7.1), this expands from Equation (7.3a) to Equation (7.3b) with inclusion of drag and vertical distances. The derivation of Equation (7.3b) can be found in Appendix A.

$$\frac{h_n}{\bar{c}} = \frac{\frac{l_{cw} - h_{AC}}{\bar{c}} S_c \cdot C_{L_{\alpha_c}} + S \cdot \left(C_{m_{\alpha_{AC}}} - \frac{h_{AC}}{\bar{c}} C_{L_{\alpha_w}} \right)}{S \cdot C_{L_{\alpha_w}} + S_c \cdot C_{L_{\alpha_c}}} \tag{7.3a}$$
$$\frac{h_n}{\bar{c}} = \frac{1}{C_{L_{\alpha_w}}} \left(C_{m_{\alpha_{AC}}} + V_c C_{L_{\alpha_c}} - \frac{S_c z_{cw}}{S\bar{c}} C_{D_{\alpha_c}} \right) - \frac{h_{AC}}{\bar{c}} + \frac{z_n}{\bar{c}} \frac{1}{C_{L_{\alpha_w}}} \left(C_{D_{\alpha_w}} + \frac{S_c}{S} C_{D_{\alpha_c}} \right) \tag{7.3b}$$

Both Equation (7.2) and Equation (7.3b) are used in the tool, to generate two plots. The left plot, visible in Figure 7.3, shows the $C_m - \alpha$ plot, while the right plot shows the location of the center of gravity in relation to the neutral line. For the aircraft to be stable, the center of gravity should stay on the left of the blue line. Additionally, the red line in the $C_m - \alpha$ plot visualizes the amount that C_{m_0} would have to increase for the line to cross the x-axis at the desired angle of attack (α).

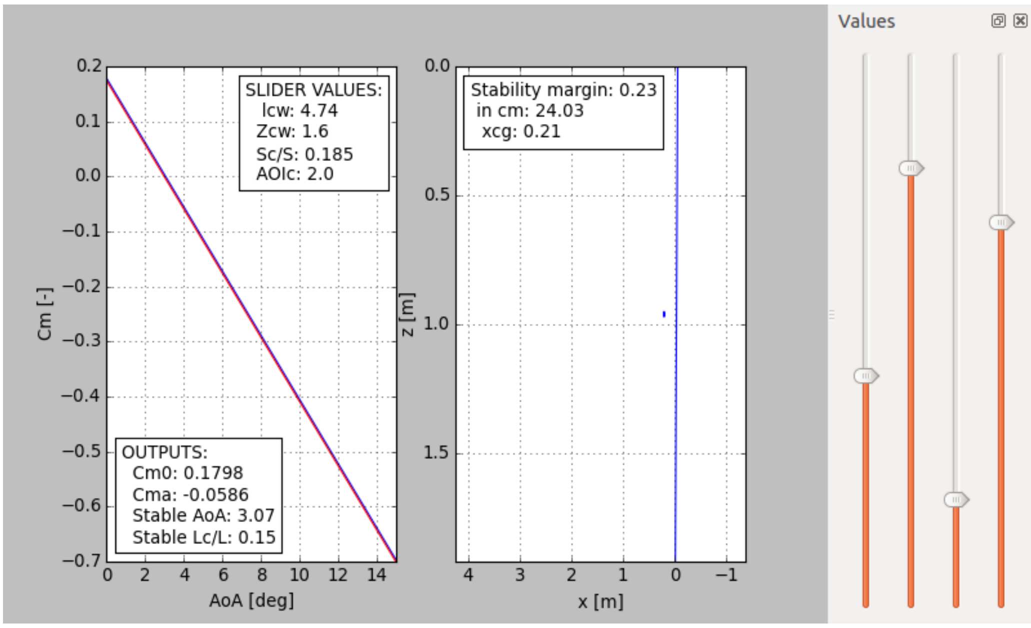

Figure 7.3: GUI of Python tool, displaying the final output with the front of the aircraft to the left. The slider values box in the plot correspend to the sliders on the right. From left to right, the sliders are l_h, z_{cw}, S_c/S and AoI

Validation

To validate the tool, data was used of reference aircraft, as well as comparing the output with the outputs of both AVL and XFLR5. The tool directly outputs the same values as the reference aircraft taken from Gudmundsson (2013), and was deemed accurate enough for the level of calculations required.

7.1.2 Athena Vortex Lattice

Athena Vortex Lattice, AVL in short, is a tool used to analyze the stability and controllability of the aircraft[1]. The tool is developed by Prof. M. Drela from MIT, also the creator of XFOIL. It employs an extended vortex lattice model for lifting surfaces and makes use of a slender-body model for fuselages. For the dynamic performance, a linearization of the aerodynamic model is used, together with the specified mass properties.

When using the tool, the limitations of the method have to be kept in mind. The method is best suited for lifting surfaces at small angles of attack and sideslip. These surfaces and wakes are modeled as single-layer vortex sheets, with trailing legs parallel to the x-axis.

One main factor is that the model does not include viscosity. This means that the tool cannot be used for accurate drag calculations. A more accurate drag estimation is performed by the aerodynamics department, and this tool will only be used for stability and controllability analysis. This missing viscous drag would normally create a moment around the center of gravity. As the point of action of this drag is unknown, its moment can not be included properly in the model. It is expected to have a relatively small arm, and as both the arm and force of the viscous drag are significantly smaller than that of the lift, the moment of viscous drag can be excluded without inducing large errors.

For the fuselage modelling, a slender-body model is used. The author mentions that this model is rather limited and advises to leave the fuselage out if it is expected to have little influence on the aerodynamic loads. For our case, the pilot and windshield are included in the model, as they do have a significant influence on the aerodynamic properties. However, the rest of the structure is left out, as it cannot be modeled properly and thus can induce errors. This again influences the drag calculations, which were already deemed inaccurate due to the missing viscosity.

Furthermore, the tool assumes quasi-steady flow, neglecting unsteady vorticity shedding. In order for the method to be accurate, any periodic motion must have a period longer than the time it takes for the flow to pass an airfoil chord.

Compressibility is accounted for in the program using a Prandtl-Glauert transformation. This is expected to be accurate up to Mach numbers of 0.6, significantly higher than the maximum velocity of the aircraft.

[1] URL `http://web.mit.edu/drela/Public/web/avl/` [cited 13 June 2017]

Validation

As part of a project, the aerodynamic properties of existing aircraft calculated by software are compared to wind tunnel tests. This project was executed at the Linköpings University in 2009-2010[2]. The aircraft most similar to ours considering the size is the Aero Commander 680 Super, the full-scale test conditions are at a Mach number of 0.2 and a Reynolds number of $6.3 \cdot 10^5$. It is shown to have a root mean squared error of 5% for the lift and 14% for the drag, over an angle of attack ranging between -4° and 8°. As expected, the drag estimation is not very accurate, and thus the program is not used for drag estimations. However, the lift lies close to that of the real-life case, and thus the lift forces can assumed to be relatively accurate, also making the stability analysis usable.

Model

The model used in AVL can be seen in Figure 7.4.

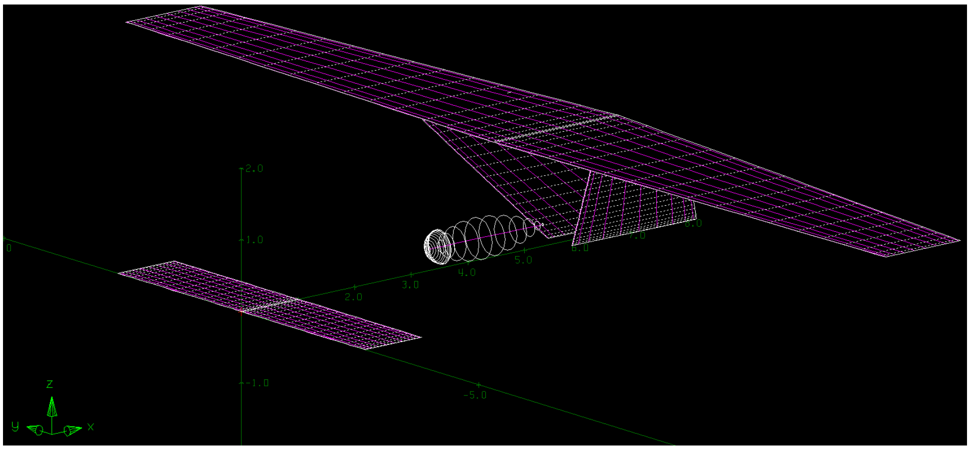

Figure 7.4: AVL model geometry

The geometry of the aircraft is according to the parameters given in Figures 2.1 and 2.2. Next to the planform, several other factors had to be defined. These are the airfoil and incidence angle over the wing and the size and location of the control surfaces, the airfoils were given by the aerodynamics department, and the incidence angle was discussed together. The length, width, and position of the control surfaces are then adjusted to meet the necessary performance, without increasing the weight unnecessarily.

Next, the center of gravity and mass moments of inertia are needed. Using the position of each component and their weights, the center or gravity is calculated of the aircraft. The center of gravity is varied over a range around this point to find a stable and controllable range which can actually be achieved with the current design.

The mass moment of inertia is calculated by adding the Steiner terms of each component and including the additional inertia due to the shape of large components, such as the wing. A table with the center of gravity and moment of inertia contributions can be found in Appendix C.

The pilot is modeled as thick symmetrical NACA rotated around its center to create a solid body. In front of the pilot is a circular windshield.

One last factor that was included is the moment generated by the propeller. If the propeller would be positioned above the center of gravity, it would generate a pitch down moment when producing thrust. This was accounted for by defining the generated moment for each case, and the program trims the aircraft to fly at an angle according to this moment. The original concept had a propeller mounted at the main wing. However, due to the large moments generated during takeoff, it was later decided to put the propeller within centimeters of the center of gravity height. Together with the clearance angle needed for takeoff, this resulted in a limit for the propeller size, which was then used by the power and propulsion department. For the final configuration of the aircraft, the thrust moment is too small to be relevant.

Assessment

The performance of the model that is defined can now be investigated for varying cases, after which the model is improved.

First, the several run cases are defined. In the run case the velocity, air density and lift coefficient (C_L) are varied. Per case, the velocity and air density are defined to be the ones according to takeoff, cruise, and

[2]URL `www.diva-portal.org/smash/get/diva2:329418/fulltext01.pdf` [cited 20 June 2017]

maximum velocity, at their respective altitudes. The C_L can then be calculated using the lift equation.

$$C_L = \frac{L}{0.5\rho V^2 S} \tag{7.4}$$

The program then iterates the control surface angles and angle of attack to find a stable condition. The lift distribution can then be shown, and the stability derivatives and force distributions can be outputted. Next to this, the eigenvalues are given and the corresponding eigenmotions are shown in slideshow format. An example of the output can be seen in Figure 7.5.

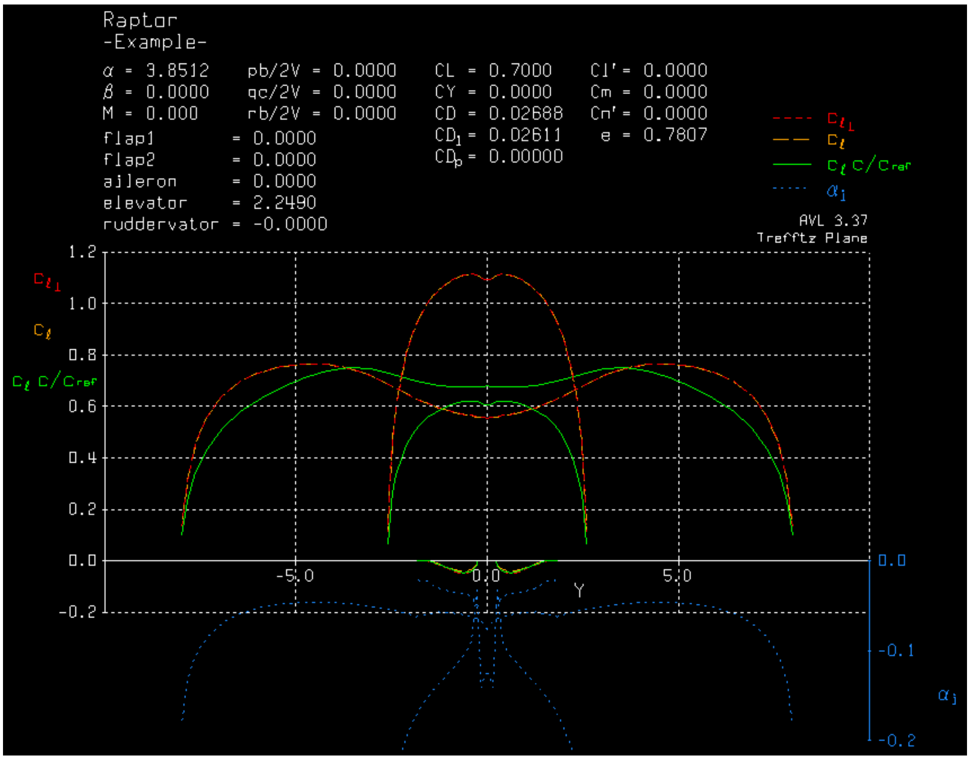

Figure 7.5: AVL trim output

The green lines represent the lift distribution, the x-axis in the plot is the wingspan of the aircraft. The center of the wing experiences disturbances from the canard, resulting in a lower amount of lift near the center. The very small dip at the center of the canard is due to the elevator. In this situation the elevator has a small deflection increasing the lift, but for structural reasons, there is no elevator for a small portion in the middle. The small bump at the bottom of the graph is due to the V-tail. This has a very small effect on the lift though, as a symmetrical airfoil is used, and even at higher angles of attack the surface is insignificant compared to the wing surface. For the stability and control, the deflections of the control surfaces are the most relevant.

The first goal of the analysis is to find a configuration that is stable during all flight conditions. This was achieved by adjusting the canard and rudder size and position and comparing the results, which was iterated multiple times with the other departments. During these iterations, multiple factors were considered such as the convenience of the center of gravity position, practical limits to the distances and drag performance with the sizes.

After the overall design started to converge to a certain layout, the controllability was also considered in the analysis. Practical limits are set to the deflection of each control surface and then the maximal achievable rotational rates are calculated using AVL, with the chosen size of the control surfaces. The design is then adjusted to achieve higher rates if necessary and the hinge moments calculated by AVL are used by the structures department to find the required weight.

The procedure to find these rotational rates were to define a certain rotational rate and make the program iterate the deflections until the moment around each axis is zero, meaning that this is the steady rotational rate that can be achieved. This rate is adjusted until the one at maximum deflection is found.

With this procedure, the stability and rotational performance of the aircraft are investigated for different situations and center of gravity positions. By limiting the stability margin and minimum turn rates, an acceptable c.g. range is found. Remarkable for our aircraft is that the center of gravity lies behind the horizontal control surface, but in front of the vertical one. This means that moving the center forward increases the effectiveness of the rudder, but moving it rearward makes the elevator more effective.

The center of gravity range that it found is highly relevant to the operations. The aircraft should behave properly regardless of the pilot's size and weight, within reasonable margins. Therefore the center of gravity of both the aircraft and pilot should lie close to the optimal found position. How this position further influences the pilot and possible landing gear position is further discussed in Chapter 10.

In order to achieve this center of gravity of the aircraft, parts that can be moved, such as the battery, were moved to convenient positions.

7.2 Canard Sizing

The first task regarding stability and control was to determine the size and position of the canard. Different aspects played a role in this, also considering the other departments. From a structural point of view, it would be beneficial to have a relatively large canard. This could then take up a portion of the lift generated by the wing with as result a smaller wing. Especially if the wingspan decreases, the weight needed for the structure gets significantly lower. However, a smaller canard reduces the disturbed flow around the main wing and reduces the drag. Different sizes also require a different position of the canard and center of gravity.

The aerodynamics department provided the airfoils to be used on the canard and main wing. Next to this they analyzed the stall performance and made adjustments to for example the aspect ratio of either wing when needed. After multiple iterations, the final canard area is slightly less than 20% of the main wing area. The distance between quarter chords is then 4.75 m, resulting in 4.45 m between leading edges, the planform can be seen in Figures 2.1 and 2.2.

The distance between the canard and wing was determined using the Python tool described in section 7.1.1, with its size and several coefficients as inputs.

7.3 Control Surfaces

7.3.1 Layout and Deflections

One conflict in the design is that the takeoff should happen at very low speeds, and the aircraft should be agile. The takeoff has to happen at low speeds, as the aircraft will be foot-launched. This requires a large wing surface in order to provide sufficient lift. However, a large wing surface damps the rotating motions, which is not beneficial for the aerobatic performance. The result is a rather large wing with large control surfaces, the layout can be seen in Figures 7.6 and 7.7

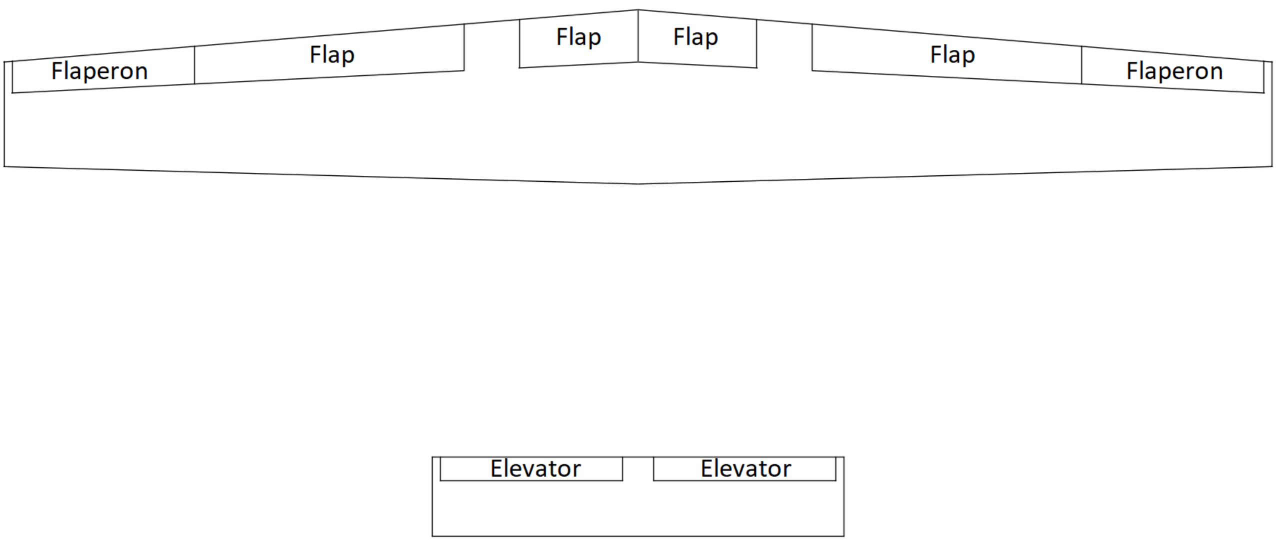

Figure 7.6: Control surfaces layout top view, flight direction is towards the bottom of the page

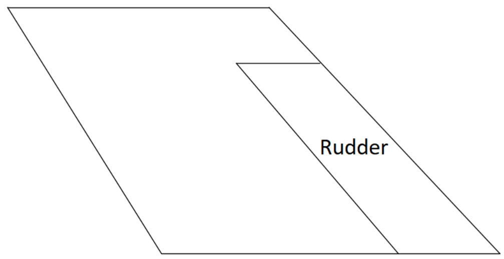

Figure 7.7: V-tail sideview, flight direction is towards the left

The sizes and maximum deflections of the control surfaces are shown in Table 7.1, the sizes are per surface, meaning that for example, the total elevator area is the one shown doubled. The size and deflection of the flaps were determined by the aerodynamics department, designed for the stall requirement. The flaps span nearly the whole wing, and thus flaperons are used near the tip. During takeoff, the flaps extend 12°, any aileron deflections mentioned further during takeoff are with respect to this downward deflection.

Table 7.1: Control Surface Parameters

Surface	Part of Chord	Length	Avg. Width	Area	$\delta_{max,up}$	$\delta_{max,down}$
-	%	m	m	m^2	deg	deg
Elevator	30	2.3	0.3	0.69	30	30
Aileron	30	2.3	0.5	1.1	30	15
Rudder	30	1.2	0.6	0.74	45	45

The chord percentage of each surface is 30%, the same was used for the flaps. This was decided by looking at existing aircraft and taking a size that is on the high side. However, having too large chord percentages result in less optimal performance due to large drag and negatively influences the structure.

One thing to note is that the ailerons have a larger upward deflection than downward. The differential is set so that the upward aileron has double the deflection of the downward one. The reason for this is to reduce the required rudder deflection during roll in order to counter adverse yaw, and keeping a margin from the maximum deflection to keep yaw control. In Table 7.2 this setup is compared to a configuration with the same deflection in both directions, during cruise condition with a roll rate of 15 deg/s.

Table 7.2: Aileron differential comparison

Case	$\delta_{aileron,up}$	$\delta_{aileron,down}$	δ_{rudder}
Without Differential	18	18	16
With Differential	24	12	9

Clearly, the situation with differential lowers the load on the rudder. During takeoff, this effect is of large importance, as the maximum rudder deflection actually limits the roll rate during takeoff. Next to this, the ailerons double as flaps during takeoff, meaning that part of the downward deflection is already taken up to increase the lift. All in all the differential improves the controllability of the aircraft. Additionally, the flight computer can automate the rudder-aileron mixing to completely dismiss the adverse yaw experienced by the pilot if necessary.

Another issue encountered when sizing the control surfaces was the risk of hitting parts of the structure and limits for the construction. At the edge of each control surface, a margin of at least 10 cm was implemented in order to be able to attach them. The rudder required a larger margin at the top side. When the flaps are extended, a full rudder deflection should not make it hit the flaps. Because the rudders are in a diagonal position, the rudder could not be at the top of the V-tail. The result is a margin of almost 40 cm at the top before the rudder begins.

The elevator length is almost the complete canard's width. This was necessary in order to provide a sufficient c.g. range where a decent pitch rate can be achieved. As the rudder lies rather close to the c.g. its arm is not too large. In order to have a sufficient yaw control, a sweep angle at the front is implemented, increasing the arm at the bottom. Here also the chord is increased, resulting in a properly effective rudder. The ailerons take up just over a quarter of the wingspan. This was needed to achieve proper roll rates during takeoff and cruise.

7.3.2 Mechanism

To control the deflection of the surfaces, the current design makes use of linear actuators combined with a simple mechanism to convert the motion, as shown in Figure 7.8. The actuator receives its input from the flight computers, as described in section 10.2.1.

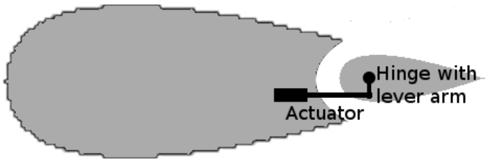

Figure 7.8: A side view of the control surface, indicating how the actuator controls the flap deflection by use of a hinge with lever arm

7.4 Results

7.4.1 Center of Gravity Range

Stability

The stability of the aircraft is investigated by analyzing the eigenvalues given by AVL. As long as these eigenvalues are negative, each eigenmotion converges after a small deviation in the flight path. If the eigenvalue is equal to zero, the motion is neutrally stable. Deviations will then not result in a correcting motion, but it will not intensify either. This situation is seen as the acceptable limit for stability. Strongly positive eigenvalues will result in an unstable aircraft, which cannot be flown without a highly accurate flight computer.

The aircraft has to be stable during all operations. The center of gravity limits for takeoff (with flaps), cruise, and maneuvering speed are analyzed. The rearward limit that was found is 4.3 m from the leading edge of the canard, 15 cm in front of the main wing. This was limited by takeoff, with both yaw and pitch stability around neutral.

One thing to note is that the yaw stability lies very close to neutral for every case. At the most critical case, the eigenvalue is slightly positive. However, the doubling time is over 8 seconds, and thus this was still deemed acceptable. This neutral behaviour can be desirable, as this makes that small moments on the aircraft are needed to make it yaw. However, it should stay within limits. This is further discussed in section 7.4.2.

Controllability

The stability analysis has shown that the center of gravity can be at 4.3 m from the canard leading edge at maximum. Having it too much in front of this will result in problems regarding controllability. As the center of gravity comes closer to the canard, the effectiveness of the elevator decreases. At the same time, the moment generated by the lift of the wing increases and that of the canard decreases, due to changing arms. The result of this is that larger elevator deflections are needed in leveled flight and the pitch rate that can be achieved with maximum deflection decreases. This makes that regarding pitch control the center of gravity is preferred to be as far near the rear as possible.

The required elevator deflections for leveled flight found by AVL can be seen in Table 7.3. The rearward c.g. position clearly shows smaller deflections, and therefore has less drag due to the elevator. The 9 m/s velocity includes the deflection of the flaps, requiring larger elevator deflection to counter the additional moment due to the extra lift on the wing.

One thing that has been included in the design to achieve these deflections is an incidence angle of the canard of $2°$ with respect to the wing. For the current planform, this results in lower required elevator deflections, giving more room for control.
As the rudder is located at the V-tail behind the center of gravity, the yaw control increases when the center of gravity is moved forward. During the iterative phase, adjustments have been made to make both a good pitch and yaw control possible for the convenient c.g. position. The result is a backward swept V-tail, with a larger chord at the bottom, where the distance to the c.g. is also largest. This makes that there is sufficient yaw control present without influencing the other parameters negatively.

The size and position of the control surfaces can be found in Section 7.3.1. The resulting steady rotational rates that can be achieved for different c.g. positions and speeds are shown in Table 7.4. The reason that a velocity

Table 7.3: Elevator deflections for leveled flight

c.g. m	V m/s	δ_e deg
4.1	9	18
	16.5	3.5
	35	1.6
4.2	9	14
	16.5	2.2
	35	1.3
4.3	9	9.1
	16.5	0.9
	35	1.0

below the stall speed is shown is that before takeoff, while still on the ground, the pilot should already be able to change the different angles in order to take off properly, these rates would not be possible when stalling in air. At this speed, the flaps are deflected in the analysis.

Table 7.4: Rotational performance

c.g. m	V m/s	Roll p deg/s	Pitch q deg/s	Yaw r deg/s
4.1	7	6	9	10
	16.5	19	47	>200
	35	43	100	>200
4.2	7	5	12	10
	16.5	19	53	>200
	35	43	107	>200
4.3	7	5	16	9
	16.5	19	57	>200
	35	43	110	>200

It is clear that the rates at low velocity are rather limited. FAA part 23.157 states aircraft below 2700 kg should be able to restore a 30° bank angle turn in order to reverse a turn within 5 seconds at 1.2 V_{s1}[3]. Although these regulations are not aimed at our aircraft, the roll rate achieved before takeoff is around the value required for airliners at 1.2 V_{s1}, which would be 6 deg/s. At cruise speed higher rates are achieved, making it possible to make sharper turns. In order to perform aerobatics, higher speeds are needed.

As expected, the center of gravity position does not influence the roll rate much as the arm does not change. There is a difference at the low speed however, this has to do with adverse yaw. As mentioned in Section 7.1.2, as the ailerons deflect, one side of the aircraft has more drag than the other generating a yaw moment. This is reduced by having the upward deflecting aileron move more, but this effect is not completely dismissed. At low speeds this effect is the largest, requiring large rudder deflections to roll without yawing. For our aircraft, the rudder deflection is limiting for roll during takeoff, where a 5° deflection buffer is kept in order to also have enough control of yaw.

The pitch rate is highly dependant on the c.g. position. Especially at low speeds, the pitch rate nearly doubles when moving 20 cm backwards. This shows the importance of the aircraft c.g. and pilot placement, as small deviations can lead to a difference in performance.

The yaw rate does not change much with a different c.g., something that is not as expected. However, the explanation is that the rudders are positioned diagonally, creating a roll moment when deflected. This roll moment has to be countered by the ailerons, also keeping a margin for roll control during yaw. At takeoff this aileron deflection is limiting the yaw rate, making it similar for the investigated c.g. range.

As mentioned, the mixed input of rudder and aileron plays a large role in sizing the control surfaces. In the investigated cases the rudder size limits the roll possible during takeoff. These large rudders cannot be fully deployed during cruise for yaw control. As this induced a roll moment that is too large for the ailerons.

[3]URL `https://www.ecfr.gov/cgi-bin/text-idx?SID=3c238b6691c8e0e97b67c17594420480&node=14:1.0.1.3.10.2.62.32&rgn=div8` [cited 22 June 2017]

The yaw rate at cruise and maximum velocity are shown as >200, as extremely large values are found. These are not considered to be accurately calculated in AVL. The author of the program mentions that extreme rotational rates, such as this yaw rate, should be avoided and can result in large errors. Next to this, the amount of detail of the structure and pilot is fairly limited, something that plays a large role in yaw damping as no fuselage is present.

Next to the steady roll rates, it is relevant how fast these rates can be achieved. The angular acceleration is dependant on the moment of inertia of the aircraft and the moment generated by control surfaces. Next to this, the air damps the motion, lowering the acceleration. In our case, the effect of the moment of inertia is very small, due to the relatively low mass and thus low moment of inertia. The calculated values are shown in Appendix C. The highest value is around 650 kg/m^2. This implies that a moment of 650 Nm would already result in an acceleration of 1 rad/s^2, which is nearly 60 deg/s^2. This is even rather conservative regarding the actual moments generated by the control surfaces. This means that the magnitude of angular acceleration is dominated by the air damping, as without this damping the steady rates would be achieved nearly instantly. At this point however it is difficult to estimate this damping, and estimations would be inaccurate if no sufficient amount of time would be put in. Therefore this effect remains to be investigated when the designing continues after this period.

All in all the forward center of gravity limit is set at 4.1 m from the canard leading edge. Although having it in front of this does not make the aircraft unflyable, it will not be fit for aerobatics anymore. This 20 cm c.g. range is deemed large enough, as by moving the battery to the preferred position the c.g. of both aircraft and pilot can be placed around 4.2 m from the front. This gives plenty of room for the pilot to move without exceeding these limits.

7.4.2 Eigenmotions

The eigenmotions have shortly been mentioned in Section 7.4.1 considering the stability. It was found that the center of gravity can be at a distance of 4.3 m from the canard at maximum. It is also relevant how these values change over the c.g. range. The behaviour during phugoid, dutch roll and yawing in cruise can be found Table 7.5.

Table 7.5: Eigenmotions

	Phugoid		Dutch Roll		Yaw	
c.g. m	λ -	T s	λ -	T s	λ -	T_2 s
4.1	$-0.012 \pm 0.30i$	21	$-0.46 \pm 1.3i$	4.9	0.077	9.0
4.2	$-0.021 \pm 0.24i$	27	$-0.45 \pm 1.2i$	5.1	0.076	9.1
4.3	$-0.032 \pm 0.12i$	53	$-0.44 \pm 1.2i$	5.4	0.073	9.5

It is clear that the period of the phugoid and dutch roll increases with a more aft c.g.. The damping is lower, and thus it takes longer to restore from a disturbance. As mentioned, the yaw motion is on the unstable side of the neutral axis. the eigenvalue is slightly positive, and the time needed to double the sideslip angle is around 9 seconds. Although this behaviour was expected to be acceptable at first, flying the model in X-Plane[4] at the ending stage of the project has shown that at low speeds the yaw control might be an issue. Therefore this stability will have to be investigated further in the following stages of the design. Possible improvements would be to include a sweep and/or dihedral angle.

7.4.3 Overall Performance

In conclusion, the aircraft has a center of gravity range that allows for any pilot size or small adjustments in weight and positions. During cruise, minimal deflections are needed in order to stay leveled. Next to this, it is controllable before takeoff speed is reached, allowing for safe operations. Lastly, decent rotational rates can be achieved at higher speeds, making aerobatics possible.

[4]URL http://www.x-plane.com/ [cited 22 June 2017]

8 Structures and Materials

In this section, the structural analysis of the Velo-E-Raptor is explained. This is done by showing to which loads the aircraft is subjected to. The assumptions are stated and the load carrying structure is defined. After this the methods used are stated, the materials used in the construction are elaborated. The results that were found in the analysis are shown after that and are discussed. An assembly section can be read after this. And at last, the verification and validation, and the recommendations on further design are shown.

8.1 Load Cases

In order to calculate all of the loads, the load cases present on the aircraft need to be considered. Possible load cases are takeoff, cruise, maneuvering, gusts, landing, and stationary on the ground. A useful tool in order to determine the maximum load case is the V-n diagram, where load factors are calculated for the entire velocity range. The limit load factor is set at 6, from the key requirements [Aarts *et al.* (2017a)]. This is a standard value, together with a maximum negative load factor of -3, for aerobatic aircraft. Looking at the V-n diagram for the Velo-E-Raptor parameters, Figure 8.1, it is clear that the maximum load factor is achieved at moderate speed maneuvering and gusts near the maximum velocity.

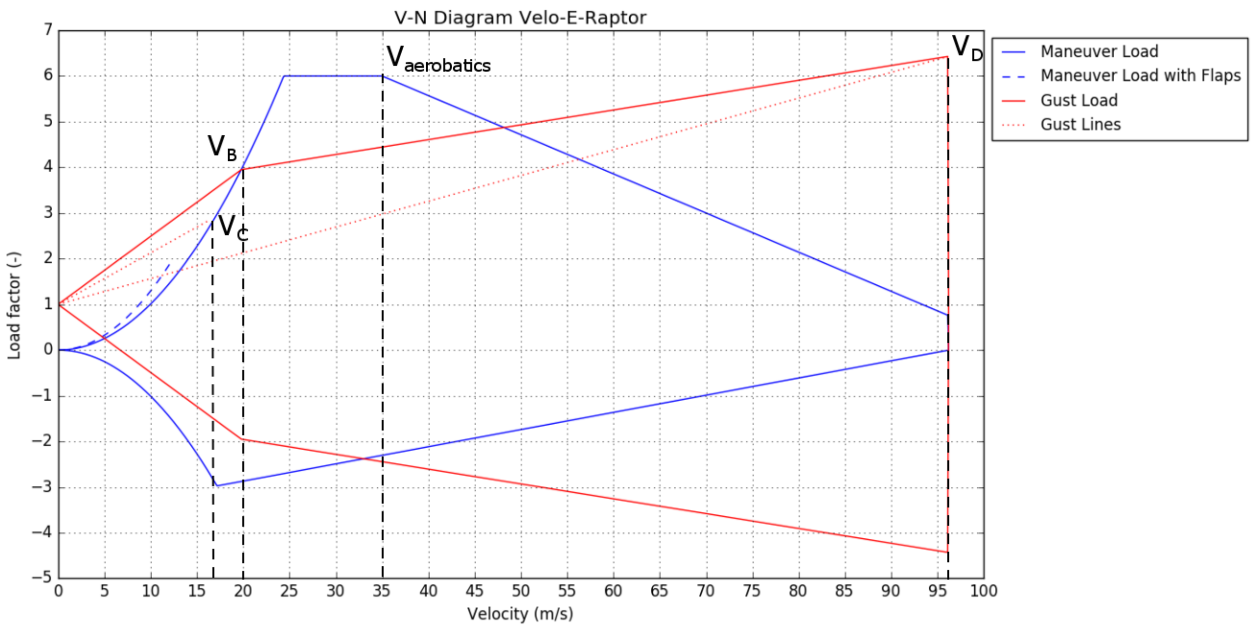

Figure 8.1: V-n diagram, with an estimated Cl of 1.4

The blue line indicates the loads achieved at a certain velocity due to maneuvering and the red line the loads due to gusts. The dotted blue line indicates the load factor when flaps are deployed. This only occurs at low speeds, when taking off or landing. The gust is evaluated at three velocities: V_B, V_C, and V_D. V_B is the speed at which highest lift and maximum angle of attack occur, V_C is the cruise speed, and V_D is the dive speed. Due to the unconventional nature of the Velo-E-Raptor, V_C occurs before V_B. This is also the reason why there is no horizontal line at the -3 load factor limit: the cruise speed is reached before this point, and from the cruise speed onwards the line will have a positive slope towards 0G. This highlights one of the drawbacks of the use of the V-n diagram: it is intended for CS-23: certification specifications for commercial aircraft[1]. One conclusion

[1]URL `https://www.easa.europa.eu/system/files/dfu/CS-23%20Amdt%203.pdf` [cited 19 June 2017]

that can be drawn is that the dive speed, at 96.25 m/s is below the never exceed speed; at 100 m/s and a load factor of zero. The never exceed speed is indicated by the blue line with a decreasing slope at the top of the V-n diagram.

Aircraft with high aspect ratios and relatively low wing loading experience higher gust load accelerations [Saarlas (2007)]. Thus, gusts are quite critical for the Velo-E-Raptor, especially at higher velocities. However, again the gust lines are based on CS-23 statistics. The Velo-E-Raptor will fly at much lower speeds and better weather conditions. Consequently, the structure is not designed for a load factor of 6 at 90 m/s; rather at the maximum load factor and aerobatic speed $V_{aerobatics}$ of 35 m/s. This is the load case used in all structures calculations.

8.2 Assumptions

Now that the maximum load case is defined, certain assumptions are made in order to simplify the structural analysis.

- The load case with a maximum load factor of 9 is used, 6 multiplied by a safety factor of 1.5, for all structure calculations.
- All structural analysis is done for an aircraft at sea level. At this level the loads are highest due to highest air density.
- Both symmetrical and asymmetrical flight conditions (roll, yaw, sideslip) fall within this maximum load factor.
- The total lift on the airfoil acts through the aerodynamic center.
- The aerodynamic center is located at 25% of the chord, measured from the leading edge.
- Where circular beams are used, the cross section is assumed to be thin-walled.
- The reference frame used in this analysis is the body-fixed reference frame, as shown in Figure 8.2.
- For the idealized structure in the wing, the skin between the booms only carries shear stresses.
- The Velo-E-Raptor will always fly in reasonable weather conditions, where extreme gusts, as defined from statistics in CS-23, do not occur.
- All connections between structural elements are seen as clamped connection points.
- The composite used, with 4 layers in a 0/90/45/-45 degree orientation, has quasi-isotropic properties.
- The sandwich core in the composite sandwich panel does not contribute to the properties of the carbon fiber laminate.

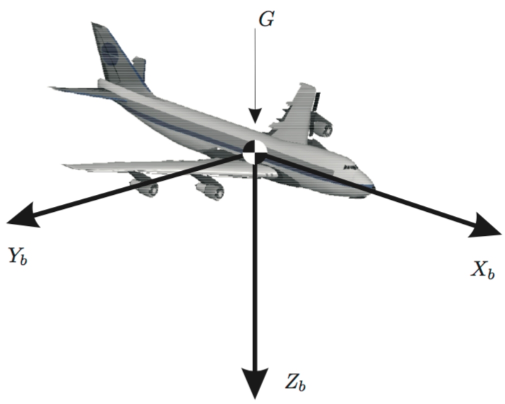

Figure 8.2: Body-fixed reference frame [Mulder & et al. (2013)]

8.3 Structure

The overall layout of the aircraft was shown in Chapter 2. The aircraft consists of four main structural parts; the main wing, the canard, the fuselage, and the V-tail.

For structure of the main wing, two options were considered. The first option is a complete load carrying wing, where the wing skin in combination with an I-beam carries the loads. The second option is a D-cell in the leading edge of the wing that carries all loads. Ribs are attached to this D-cell that maintain the airfoil shape and provide structural connection points for the control surfaces. A Dacron sailcloth is wrapped around the ribs to provide the remaining airfoil shape. The main wing is connected to the V-tail and is therefore made out of three parts, two outer sections and a middle section. Since the wing is tapered, all structural elements will be tapered too.

The canard consists of the same structural elements as the main wing. There is also the option between the D-cell and rigid skin with I-beam. It is connected in one piece to the fuselage. It is fully cantilevered, unlike the main wing.

The V-tail has two rectangular spars connecting the fuselage to the main wing. The rudders are connected to the spars with two ribs. An aerodynamically beneficial fairing is added to this spar using foam ribs and sailcloth.

The fuselage consists of two main parts. The first section consists of a circular tube. The first part has a constant radius, whereas the last section is tapered towards the main frame. This tube connects the canard with the main frame. The main frame is a box section, made from four rectangular beams. At the front of the box section, the beam is wider to accommodate space for the batteries. The section furthest back will provide an attachment point for the propeller and engine. A rough structural schematic is illustrated by Figure 8.3.

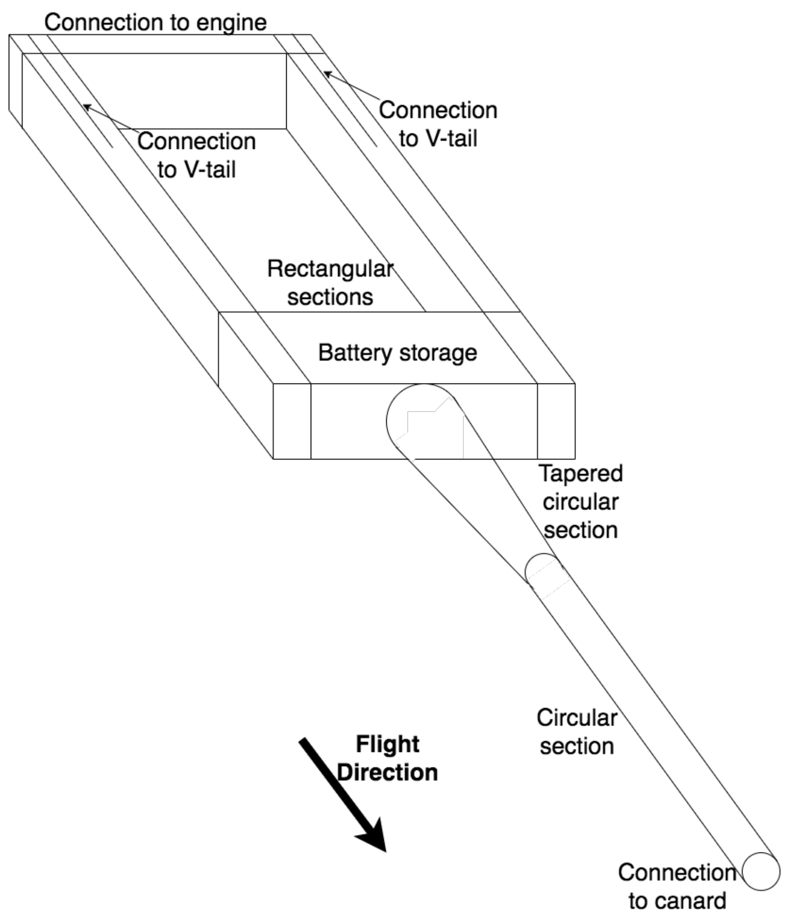

Figure 8.3: A schematic of the idealized fuselage, illustration not to scale. Only the relevant structural elements of the Velo-E-Raptor are shown.

8.4 Method

After the critical load case is known, the forces and stresses in the structure can be calculated. Each section was analyzed for bending, shear and torsion using Python. A simple guideline for the Python tool was followed, which is shown in Figure 8.4.

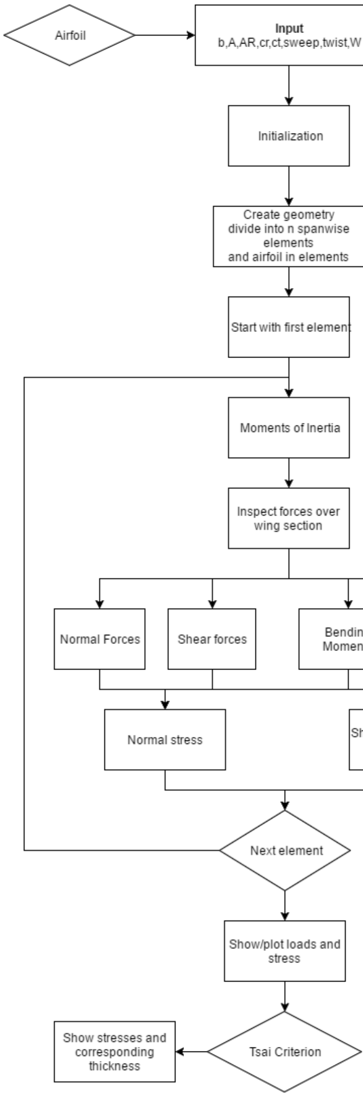

Figure 8.4: Flow diagram for structural analysis

The methods and equations used in the python tool and also in the verification model are described below.

8.4.1 Lift Distribution

The lift distribution determines the shear and bending forces on the wing and canard. For the first iterations, an elliptical lift distribution was assumed. However, especially for the tapered wing, this is not an accurate assumption. As the final planform was decided, the program used for the aerodynamics of the aircraft, XFLR5 provided the normalized lift coefficient per section. This allowed for an accurate representation of the lift distribution.The distribution is illustrated in Figure 8.5, for half of the wing/canard from root to tip. The canard does approach an elliptical lift distribution, as it does not have any sweep, twist or taper. This lift distribution (C_l) is for values at 17.67 m/s, or steady, level cruise speed. This is also the speed where the lift distribution is most punishing on the wing structure. The lift distribution is also multiplied by 9, the maximum load factor including a safety factor.
The dip in lift distribution of the main wing is explained by the connection with the V-tail at that point. The lift distribution will also change when there is a flap, flaperon or elevator deflection. This is assumed to be included in the load factor, and thus not calculated separately. The torque on the wing caused by a control surface deflection is taken into account, also in order to estimate the size of the ribs.

The drag distribution is based on a minimum lift over drag ratio of 8, whereby all lift forces are divided by eight

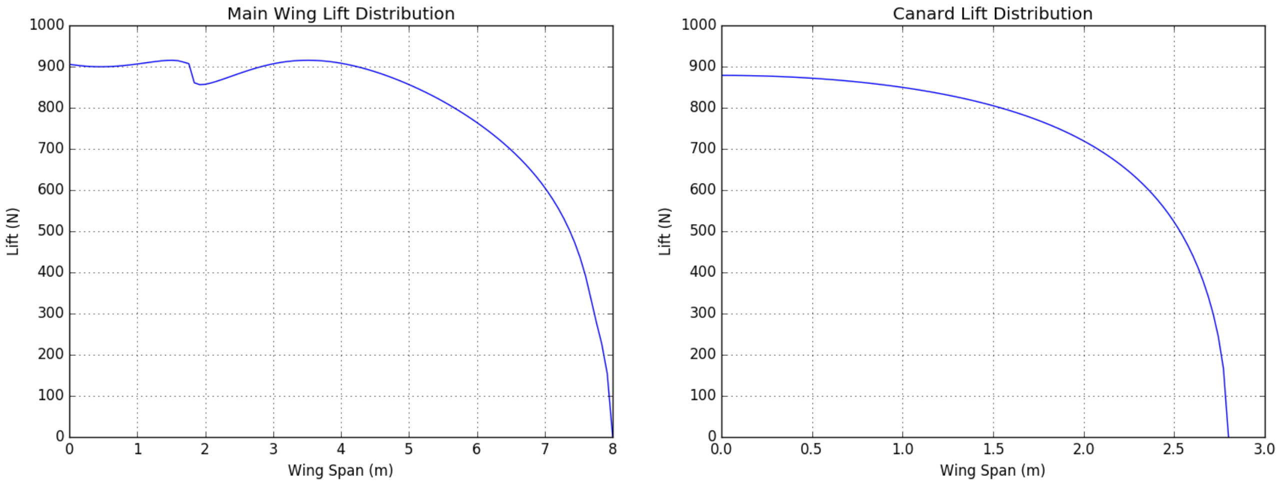

Figure 8.5: Lift distribution for the main wing and the canard

to form the drag distribution curve. The drag is also multiplied by the maximum load factor.

8.4.2 Structural Idealization

To calculate the stresses on a structure in a numerical way, it is chosen to use boom theoryMegson (2012). This way of structural idealization divides the skin into booms and assumes that the skin between the booms only takes shear loads. The wings are modelled with boom theory. The booms of both canard and wing are placed at the coordinate locations of the airfoil along the wingspan as can be seen in Figure 8.6a. The D-cell has the same boom locations as the first cell of the rigid skin construction (Figure 8.6b).

The stresses are calculated for half a wing which is divided into sections. Where each section is a wing cross-section as discussed above.

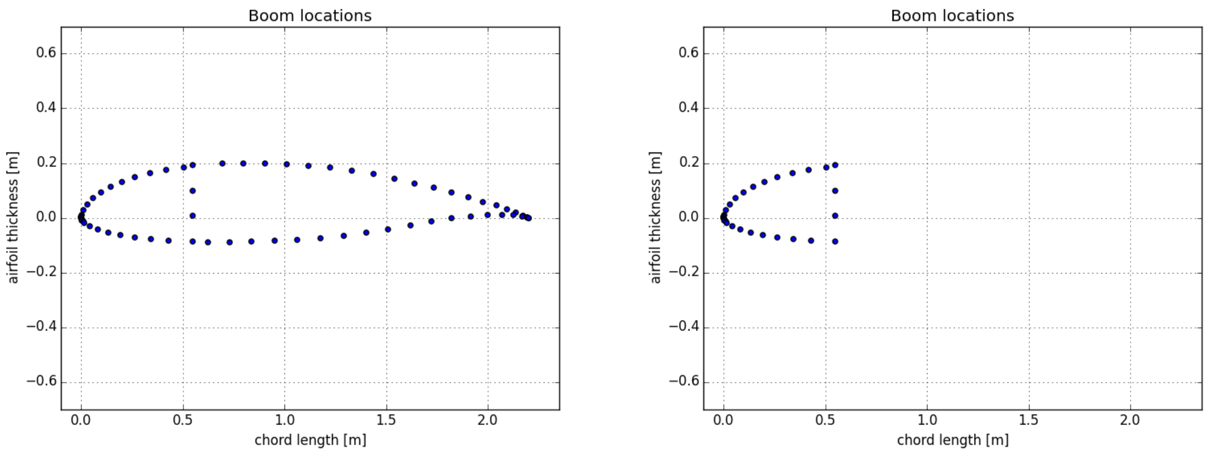

(a) Rigid wing (b) D-cell

Figure 8.6: Boom locations at the root of the wing

8.4.3 Stress Analysis

The structure is subjected to several loads. In this section is shown how the loads are used to calculate the stresses and whether the structure fails.

First, an analysis is conducted to see what loads the Velo-E-Raptor is subjected to. The main loads acting on the aircraft are the lift, weight and drag. The lift and a large part of the drag are acting on the wings. The weight consists of the structural weight, and the payload weight. The payload weight is positioned at the fuselage. This translates in that the wings experience normal, shear and bending forces. Also, because of aerodynamic properties of the airfoil, pitching moments act on the wing. The moments and total lift are carried through the tail, in combination with ruddervator loads. The fuselage connects the wing, canard, payload and engine. A special case is investigated for the fuselage: where a roll motion is initiated and the inertia of the canard prevents this, creating internal torque.

Loading Diagrams

In order to know how the stresses are acting on the structure, free body diagrams are constructed. This is done by analyzing every force acting in the y-direction and z-direction, which will give normal and shear diagrams respectively. Shear forces cause a moment that is calculated on each point along the span of the analyzed section. This moment can then be plotted into a bending moment diagram.

Moment of Inertia

The moment of inertia calculation was done in two different ways. For the wings, the calculation was done using the assumption that the structure is idealized and only booms carry bending stress. With this assumption, the skin thickness can be set to zero and only the Steiner term has to be used in the moment of inertia calculation. This leads to Equation (8.1),Equation (8.2), and Equation (8.3).

$$I_{xx} = \sum_{i=1}^{n} y_i^2 A_i \qquad (8.1) \qquad\qquad I_{yy} = \sum_{i=1}^{n} x_i^2 A_i \qquad (8.2) \qquad\qquad I_{xy} = \sum_{i=1}^{n} x_i y_i A_i \qquad (8.3)$$

However, for the body and the V-tail the structure is not idealized and the Equation (8.4),Equation (8.5), and Equation (8.6) were used.

$$I_{xx} = \iint y^2 dA \qquad (8.4) \qquad\qquad I_{yy} = \iint x^2 dA \qquad (8.5) \qquad\qquad I_{xy} = \iint xy dA \qquad (8.6)$$

Normal Stress

The normal stresses are calculated by dividing the normal stress by the area using Equation (8.7).

$$\sigma = \frac{F}{A} \tag{8.7}$$

If an element is subjected to compression forces there has to be checked for buckling. This is done with the use of Equation (8.8).

$$P_{crit} = \frac{n^2 \pi^2 EI}{L^2} \tag{8.8}$$

Bending

Inertial unloading of the wing/tail is included in the calculated moment, as the weight of the wing or tail/canard counteracts the lift force. Equation (8.9) shows how the stresses resulting from bending are calculated.

$$\sigma_z = \frac{I_{xx}M_y - I_{xy}M_x}{I_{xx}I_{yy} - I_{xy}^2}x + \frac{I_{yy}M_x - I_{xy}M_y}{I_{xx}I_{yy} - I_{xy}^2}y \tag{8.9}$$

Shear

The shear flow is calculated by first determining the shear flow for an open cross-section. Subsequently, the cross section is closed and a constant shear flow is added. This was done with Equation (8.10).

$$q_s = -\frac{I_{xx}S_x - I_{xy}S_y}{I_{xx}I_{yy} - I_{xy}^2} \sum_{r=1}^{n} B_r x_r - \frac{I_{yy}S_y - I_{xy}S_x}{I_{xx}I_{yy} - I_{xy}^2} \sum_{r=1}^{n} B_r y_r + q_{s_0} \tag{8.10}$$

For the load carrying skin, the wing is divided into two enclosed areas. Therefore the rate of twist of each area has to be set equal to the other, such that the constant shear flow can be calculated. Equation (8.11) is used to calculate the rate of twist, where t is the skin thickness and G is the shear modulus.

$$\frac{d\theta}{dz} = \frac{1}{2A_e} \oint \frac{q_s}{tG} ds \tag{8.11}$$

After the shear flow is calculated in each skin section, the shear stress can be calculated by using Equation (8.12).

$$\tau = \frac{q}{t} \tag{8.12}$$

Torsion

The aerodynamic moment of an airfoil and flap/aileron deflection induce a torque on the wing beam. The aerodynamic moment ($C_{m_{ac}}$) is given per wing section by the aerodynamics of the airfoil. A flaperon or flap deflection also causes a force and a hinge moment, which is converted to a torque. The spar, located at a quarter chord, splits the wing box into two sections. Thus, the total torsion is divided into the two sections as follows:

$$T_{total} = 2A_{e_L}q_L + 2A_{e_R}q_R \tag{8.13}$$

Where A_e is the enclosed area and q is the shear flow. L and R indicate the left and right sections, respectively. The torque in each closed section causes a resultant shear flow in the skin, as is shown in Figure 8.7. In order to find this shear flow, the assumption is made that the rate of twist in both sections is equal. The rate of twist of a section is given by Equation (8.11).

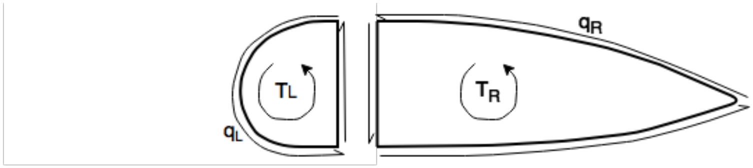

Figure 8.7: The torsional and resultant shear flow around the two closed sections

Equation (8.13) and Equation (8.11) together allow the calculation of the torque in each closed section and the resultant shear flow in the skin due to this torsion. This can then be represented as a stress by using Equation (8.12), by dividing by the skin thickness.

8.4.4 Tsai-Hill Failure Criterion

Now that the bending, shear, and torsion stresses are known, a criterion is needed that accounts for interaction between different failure modes. As most of the structure will be made from composites, the Von Mises yield criterion cannot be applied. A conservative criterion that does work for composites is the Tsai-Hill criterion[2][3]. This criterion, shown in Equation (8.14), compares the actual stresses, in the numerator, to the ultimate properties of the specific composite, in the denominator. If the value is higher or equal to one, the material will fail at that point on the airframe.

$$\left(\frac{\sigma_y}{\sigma_{y_u}}\right)^2 + \left(\frac{\sigma_x}{\sigma_{x_u}}\right)^2 - \frac{\sigma_y\sigma_x}{\sigma_{y_u}^2} + \left(\frac{\tau_{yx}}{\tau_{yx_u}}\right)^2 \leq 1 \tag{8.14}$$

8.4.5 Deflection

Wing deflection is a parameter that needs to be kept under close scrutiny. A structure may be designed that does not fail under limit loads but will have a significant wing deflection that is unsuitable for aerobatics. An initial estimate of the wing deflection is made by modelling the wing as a cantilever. Subsequently, for a more accurate method is used in the form of the second moment-area theorem. This is given in Equation (8.15) below[4].

$$\delta_{max} = \int_{root}^{tip} \frac{M}{EI} x dx \tag{8.15}$$

Where δ_{max} is the maximum deflection at the tip with respect to the root, M is the moment, E is the elastic modulus of the material, I is the moment of inertia, and x is the distance along the wing measured from the root. This method still models the wing as a cantilever beam, but the more accurate representation of the moments and moments of inertia give better results. For the main wing, the wing is assumed to be clamped at the V-tail. This reduces the maximum deflection at the tip.

8.5 Materials

In the trade off performed in the baseline report (Aarts *et al.* (2017b)), it became clear that metals are not adequate for the design of the Velo-E-Raptor. Even the properties of the aerospace grade aluminum alloy

[2]URL `https://www.doitpoms.ac.uk/tlplib/fiber_composites/laminate_failure.php` [cited 16 June 2017]
[3]URL `http://scmero.ulb.ac.be/Teaching/Courses/MECA-H-406/H-406-4-Failure.pdf` [cited 16 June 2017]
[4]URL `http://www.engr.mun.ca/~katna/5931/Deflections_Area-moment2p.pdf` [cited 12 June 2017]

Al7075-T6 did not allow the structure to meet the weight requirements. Thus, as a starting point, composites were used in this design phase. Furthermore, materials like sandwich panels, foam and sailcloth were used.

8.5.1 Laminated Composite Structures

An obvious choice for composites is carbon fiber. This material was selected above others such as glass fiber and Kevlar. Although the density is slightly higher and ultimate strength lower, the abundance of available information on this composite is a great advantage in this structural analysis. Its mechanical properties are known in different orientations of fiber lay-ups, and the manufacturing is a well-documented process. The mechanical properties of carbon fiber are shown in the Table 8.1 below.

Table 8.1: Mechanical properties of carbon fiber, with a volume fraction of 50%[5]

Carbon fiber properties	Unit	0/90° orientation	45/45° orientation	0/90/45/-45°
Ultimate compressive strength	MPa	570	110	340
Ultimate tensile strength	MPa	600	110	355
Ultimate in-plane shear strength	MPa	90	260	175
Young's modulus	GPa	70	17	43.5
In-plane shear modulus	GPa	5	33	19
Density	kg/m^3	1600	1600	1600

The different properties in different orientations of carbon fiber give great flexibility on its use. Uni-directional carbon fiber would give the lightest structure, but this is not possible due to the different loading directions present on the Velo-E-Raptor. For the main wing and canard, a 4-layer composite lay-up is used, with fibers in a 0, 90, 45, and 45 degree orientation. This will give it quasi-isotropic properties, used to counter the stresses from bending, shear and torsion in the wing and canard. However, its properties will also decrease for the same density, as is shown in the last column of Table 8.1. For the fuselage, V-tail and ribs, it is possible to use either the 0/90° or 45/45° oriented composite. It is assumed that the carbon fiber composite used has a volume fraction of 50% fiber, 50% epoxy resin with a 120°C cure. Also, the minimum thickness of one layer of carbon fiber composite is assumed to be 0.1 mm.

8.5.2 Composite Sandwich Panels

Especially in the wing and canard, in order to keep the weight to a minimum, extremely small thicknesses are required. A significant problem is the buckling of such very thin skin panels. The composite structure is calculated so that it can withstand the compression, tension and shear stresses, but buckling is a difficult phenomenon to calculate. One solution is to make the skin from a composite sandwich panel. Inserting a lightweight honeycomb or foam structural element between two layers of carbon fiber greatly increases its buckling resistance. Thus, this was incorporated into the design for the wing and canard skin. For this preliminary design, it was not possible to calculate the exact properties of a carbon fiber sandwich panel. Thus, in the following sections, the properties of carbon fiber as explained above in Section 8.5.1 will be used and an additional density will simply be added to the final weight. The additional density of the sandwich material is assumed to be 140 kg/m^3.[6] This is a Divinycell H100 sandwich core, together with a CFRP pyramidal lattice as described in George *et al.* (2013). It is a new and upcoming method, showing promising results when compared to conventional honeycomb structures, and is thus ideal for the next-gen Velo-E-Raptor. The Divinycell foam has a density of 100 kg/m^3, whereas the carbon fiber lattice adds 40 kg/m^3. The sandwich panel is described in Figure 8.8.

8.5.3 Foam

Next to structural integrity, it is also necessary for the wing, canard, and V-tail to keep its airfoil shape. This is done using ribs. These ribs need to be manufactured from a lightweight rigid material, that does not need to carry loads. Polyurethane foam is often used in micro-light to light aircraft, as it possesses the right properties for this purpose. It has around the same density of polystyrene foam but is more rigid. The density of polyurethane foam that is suitable for application on the Velo-E-Raptor is assumed 50 kg/m^3. [7][8]

[5] URL http://www.performance-composites.com/carbonfiber/fiberangles.asp [cited 21 June 2017]
[6] URL http://www.diabgroup.com/en-GB/Products-and-services/Core-Material/Divinycell-H [cited 23 June 2017]
[7] URL https://www.generalplastics.com/rigid-foams [cited 22 June 2017]
[8] URL http://www.pg.gda.pl/mech/kim/AMS/022006/AMS02200605.pdf [cited 23 June 2017]

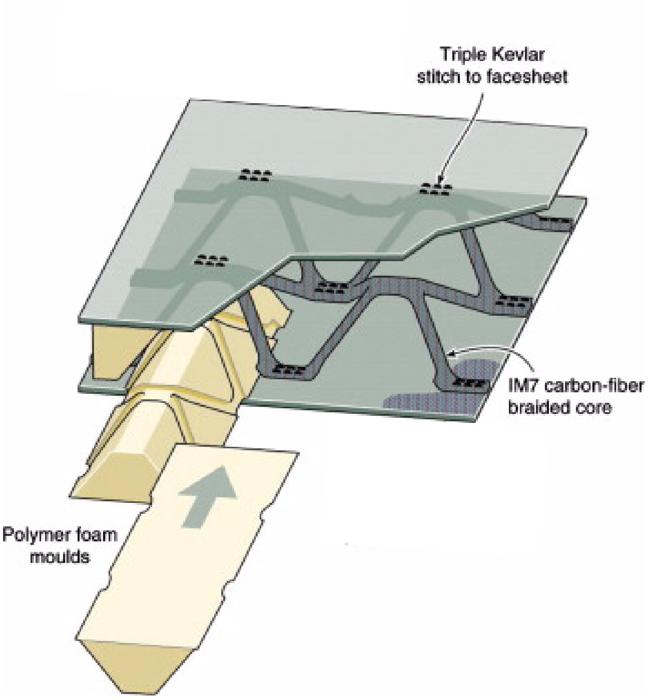

Figure 8.8: CFRP composite pyramidal lattice structure from George *et al.* (2013)

8.5.4 Sailcloth

For the D-cell, additional skin material is needed in order to shape the rear 75% of the airfoil. Looking for inspiration at hang gliders, an obvious solution is a sailcloth. The AIR Atos V shows that it is possible to combine a D-cell with sailcloth. The most frequently used materials are Dacron and Mylar. Dacron is a woven polyester fiber, whereas Mylar is a composite laminated fabric. For the Velo-E-Raptor, a sailcloth is used that has a combination of Mylar and Dacron, with woven fibers covered by Mylar film on each side. There is also a coating that provides high UV resistance. The exact name of the sailcloth is UVODL06[9]. The X-ply fiber is Technora, an aramid that is three times stronger than polyester[10]. It has a mass of 180 g/m^2. Carbon reinforcing tape can also be added at critical sections like connection points with the D-cell and ribs.

8.6 Results

This section will display the results from the structural analysis tool, as outlined in the previous sections. A comparison is made between a wing with a rigid skin and a wing with a D-cell as load carrying wing box.

8.6.1 Wings

The results in this section are shown by first displaying all stresses and then stating the corresponding thicknesses and weights. To get to these thicknesses and weights is an iterative process. If the skin thickness changes other stresses will occur in the structure. Thicknesses are chosen so that the structure would not fail, but also the layer thickness of standard carbon fiber laminate (as shown in section 8.5.1) is taken into account.

Main wing

First, all the forces were evaluated in the entire structure for the main wing. An overview of the normal forces, shear forces, and bending moments on the structure can be found in Figure 8.9. As expected, there is a significant change in the shear and normal force at the location of the V-tail due to the clamped position.
From the forces, stresses in the entire structure could be evaluated using Equations (8.7) to (8.14). The structure is evaluated for bending stress and shear stress, in which the torsion is included, such that the critical stress can be determined. Whether the stresses are critical is determined by the Tsai-Hill failure criterion which is given in Equation (8.14). If the criterion has a value larger than one, the structure fails. For each situation

[9]URL `https://www.willswing.com/hang-gliders/hang-glider-sailcloth-information/` [cited 21 June 2017]
[10]URL `http://www.jkasailmakers.co.uk/Sail%20Fabrics%20Explained.pdf` [cited 21 June 2017]

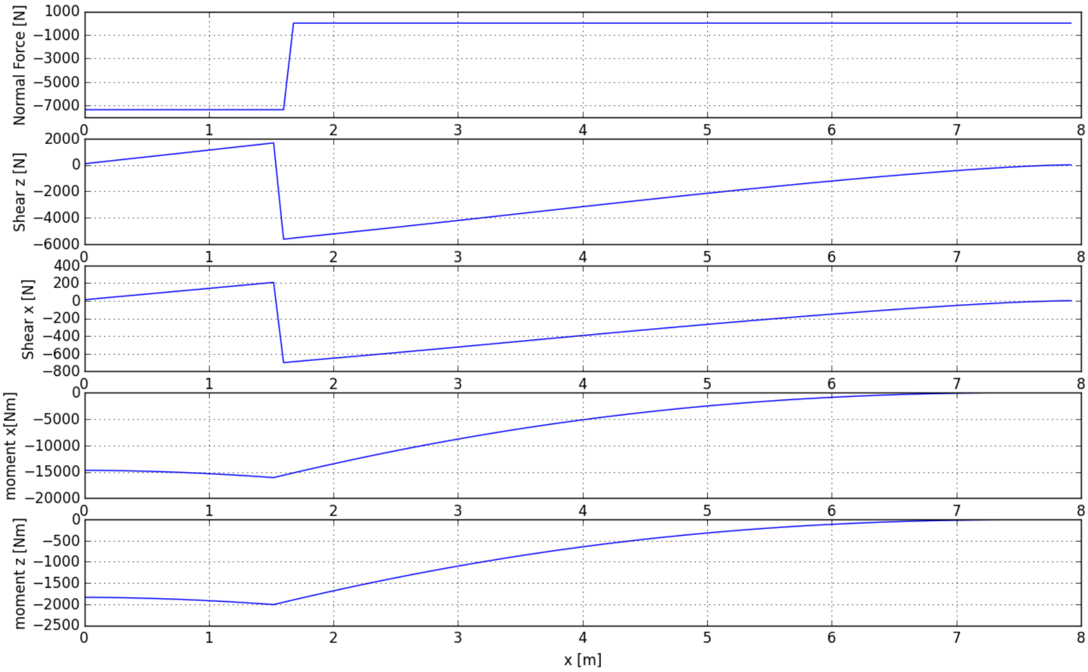

Figure 8.9: Loading diagrams for the main wing right half

the stresses are shown in Figures 8.10a, 8.10b, 8.11a, 8.11b, 8.12a and 8.12b for both a load carrying skin as a D-cell structure. In Appendix B the stresses on the bottom of both wing options are shown. Note that the figures do not depict the wing exactly to scale.

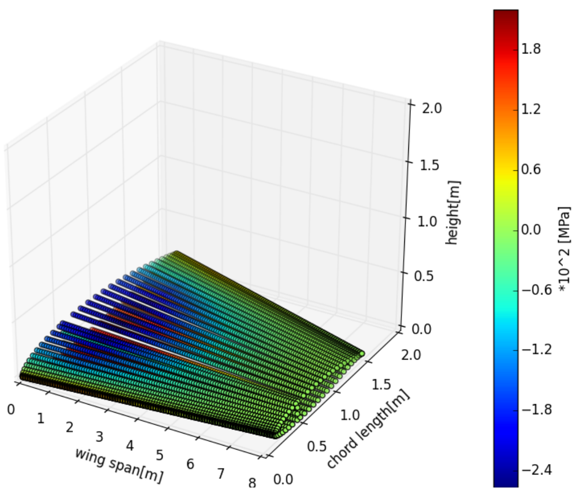

(a) Rigid wing

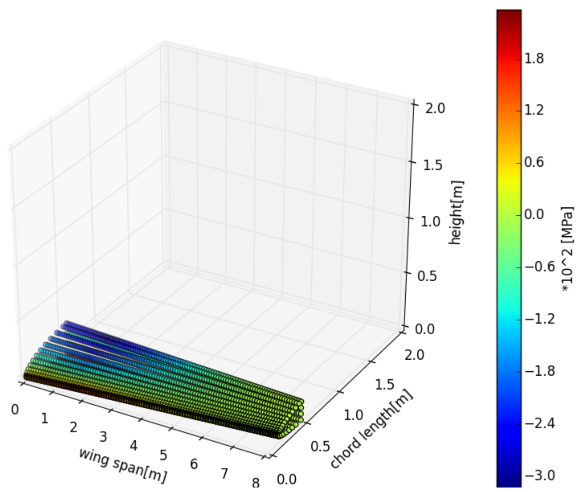

(b) D-cell

Figure 8.10: Bending Stresses in the main wing

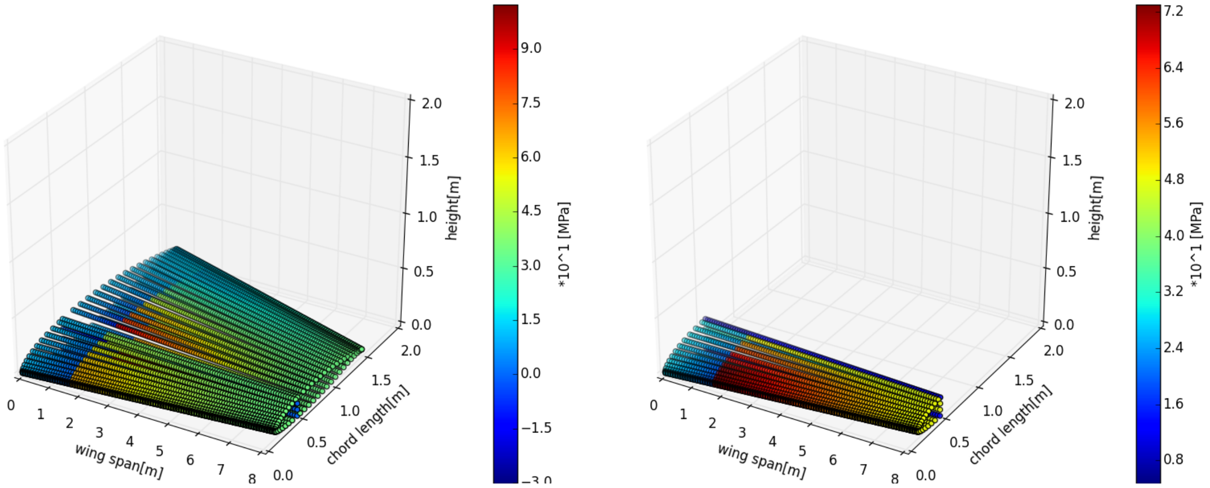

(a) Rigid wing (b) D-cell

Figure 8.11: Shear Stresses in the main wing

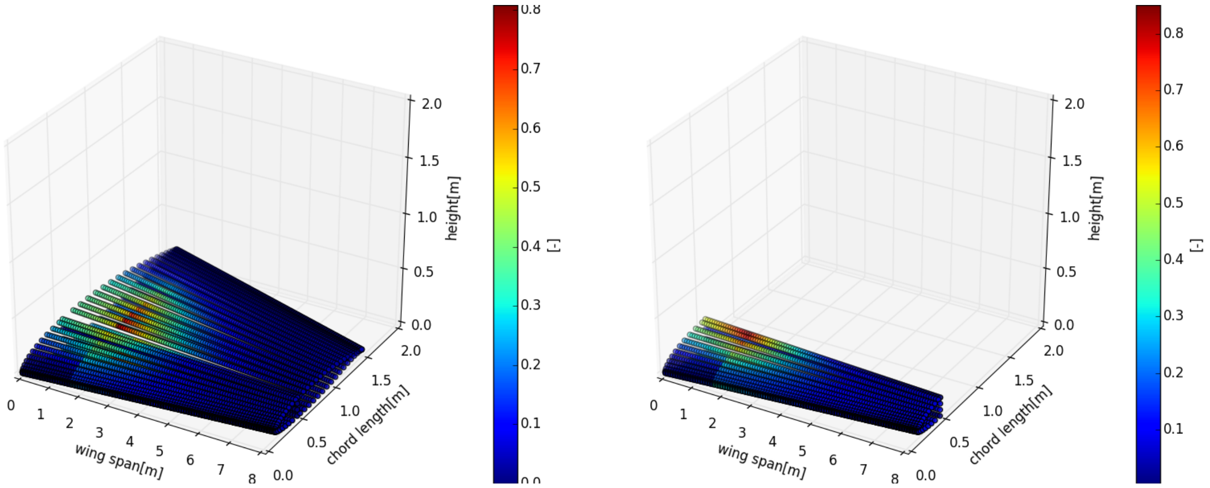

(a) Rigid wing (b) D-cell

Figure 8.12: Tsai-Hill failure criterion for the main wing

The thicknesses used in these stress plots are shown in Table 8.2, with these thicknesses, masses can be calculated.

Table 8.2: Wing option properties

Parameter	Unit	Wing Rigid skin	Wing D-cell
Mass	kg	28.99	15.05
Skin thickness	mm	0.2	0.4
Spar cap thickness	mm	0.2	1.5
Spar cap width	mm	35	35
Spar web thickness	mm	0.2	0.4
Sail cloth mass	kg	-	3.84
Sandwich core thickness	mm	2	2
Sandwich core mass	kg	17.15	5.21
Total wing mass	kg	46.14	24.10

Canard

For the canard, the normal and shear forces are given in Figure 8.13. As can be seen in the figure, the normal forces are equal to zero due to the fact that the canard is clamped at the root in contrary to the main wing. The shear forces are caused by the lift and drag, which results in a bending moment on the canard.
Just as the main wing, the canard is evaluated in shear and bending stress for both the load carrying skin as the D-cell structure. The results can be found in Figures 8.14a, 8.14b, 8.15a, 8.15b, 8.16a and 8.16b. The

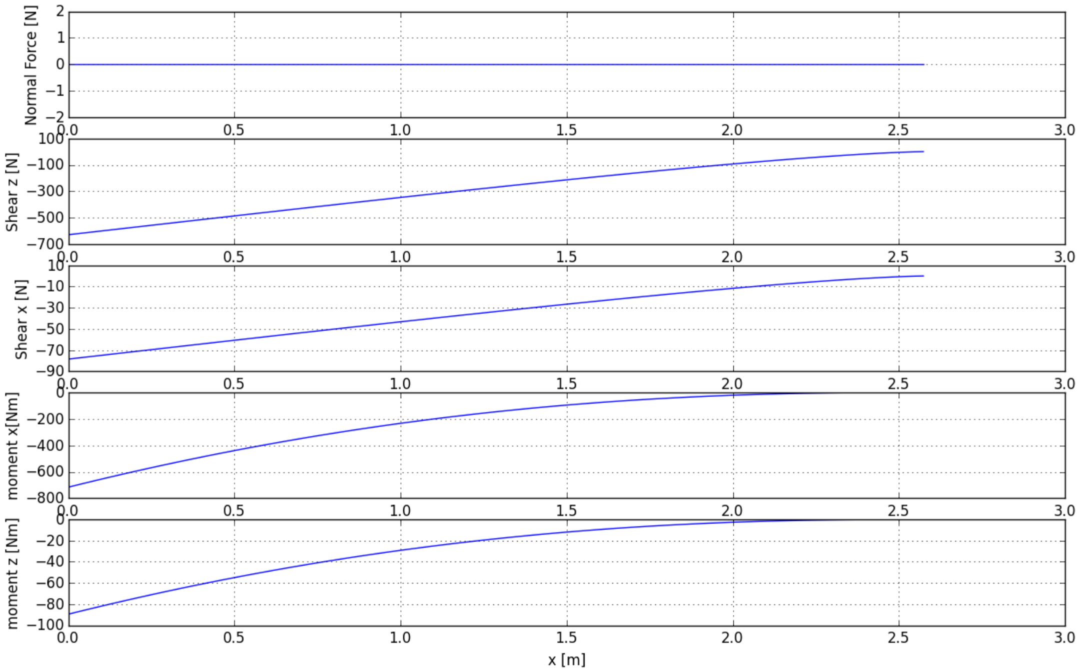

Figure 8.13: Loading diagrams for the canard

thicknesses and masses are listed in Table 8.3.

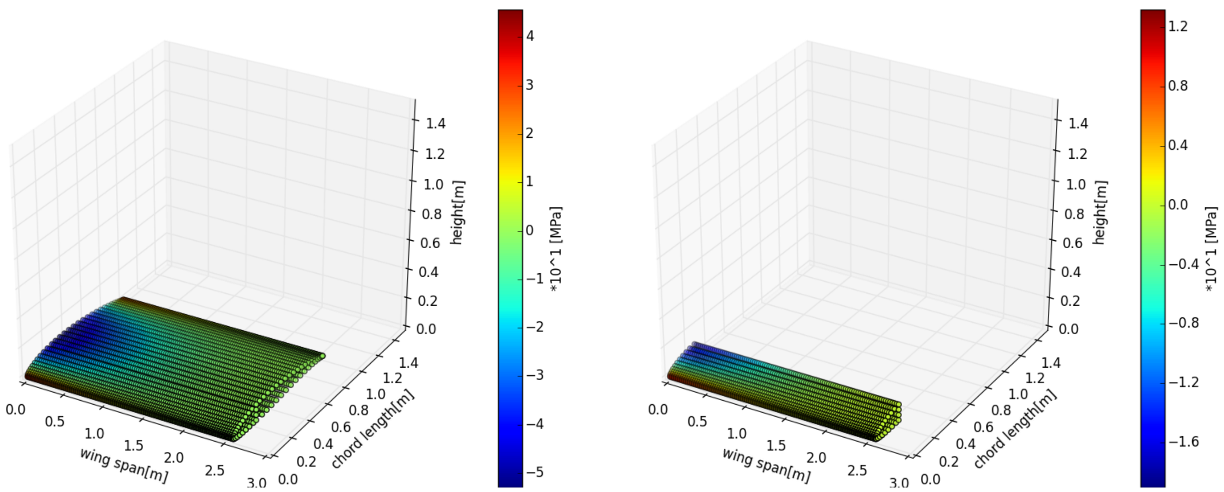

(a) Rigid wing

(b) D-cell

Figure 8.14: Bending Stresses in the canard

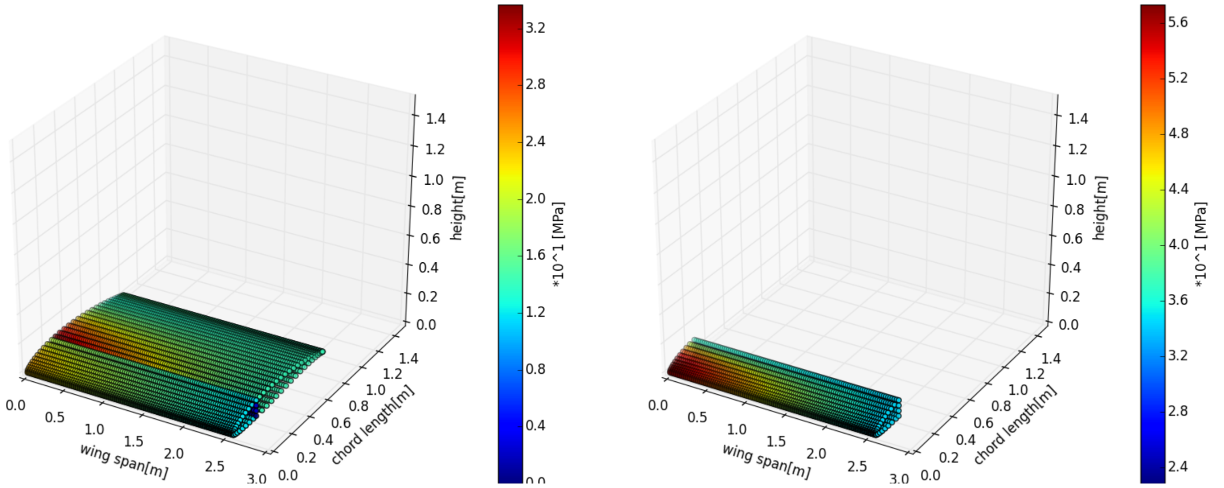

(a) Rigid wing (b) D-cell

Figure 8.15: Shear Stresses in the canard

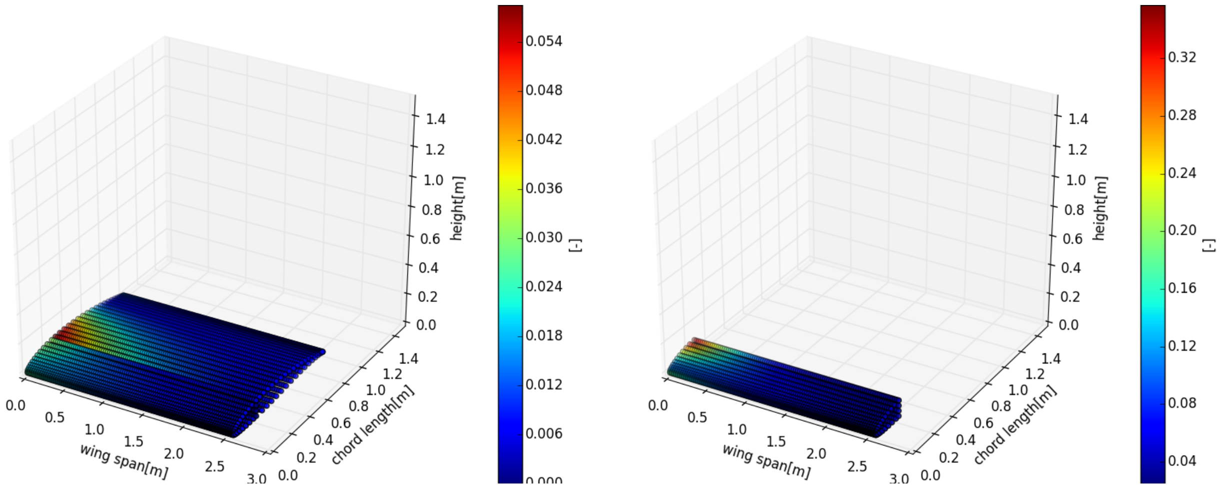

(a) Rigid wing (b) D-cell

Figure 8.16: Tsai-Hill failure criterion in the canard

Table 8.3: Canard option properties

Parameter	Unit	Canard Rigid skin	Canard D-cell
Mass	kg	6.79	1.22
Skin thickness	mm	0.2	0.2
Spar cap thickness	mm	0.2	0.2
Spar cap width	mm	20	20
Spar web thickness	mm	0.2	0.2
Sail cloth mass	kg	-	1.25
Sandwich core thickness	mm	2	2
Sandwich core mass	kg	3.13	0.93
Total wing mass	kg	9.92	3.4

8.6.2 V-Tail

The V-tail is subjected to the lift, drag, and pitching moment acting on the wing. With these loads, the largest needed skin thickness is chosen. The mass and dimensions of the load carrying beam are shown in Table 8.4.

Table 8.4: V-tail properties

Parameter	Unit	V-tail
Mass	kg	6.8
Skin thickness	mm	1.3
Height	mm	200
Width	mm	50
Sailcloth mass	kg	1.3

8.6.3 Fuselage

The fuselage is subjected to several loads. Lift, drag and pitching moments from both of the wings; the thrust of the propeller and a constant torsion by aileron deflection in a rolling motion (not shown in loading diagram). The loads on the fuselage, and corresponding tube radius and beam width, are shown in Figure 8.17. The dimensions and weights are stated in Table 8.5.

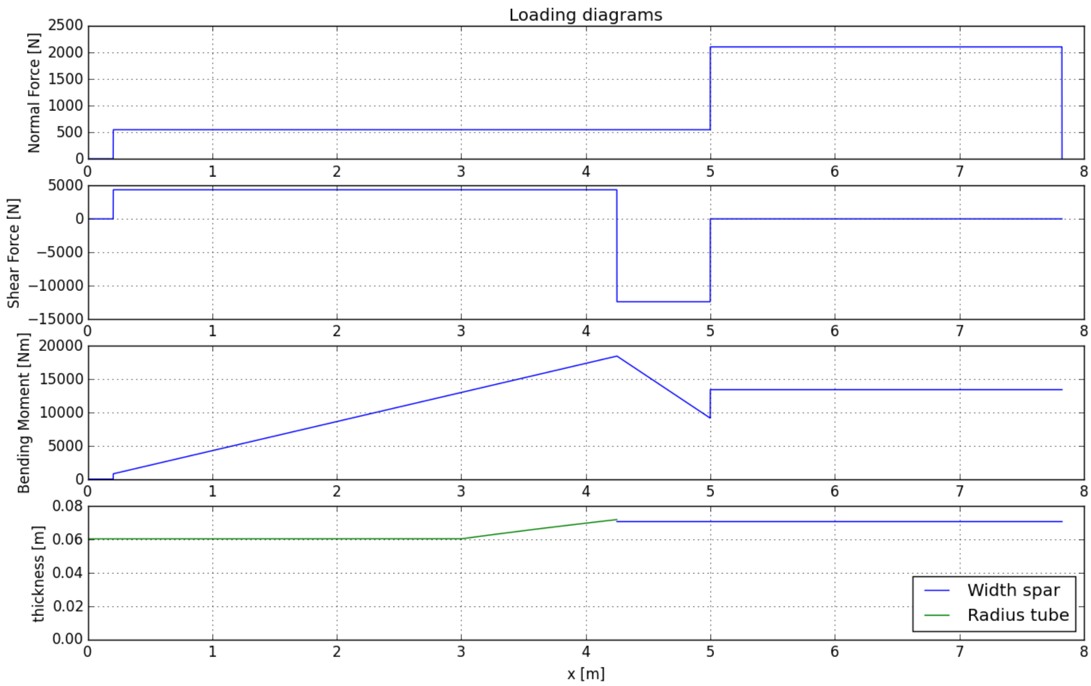

Figure 8.17: Loading diagrams for the fuselage

Table 8.5: Fuselage properties

Parameter	Unit	Circular beam	side beams	front beam	rear beam
Mass	kg	5.3	2.2	0.6	0.4
Skin thickness	mm	2	1	1	1
Diameter/height	mm	120-144	165	165	165
Width	mm	-	70	110	56

8.6.4 Tip Deflection

Beside the bending and shear stress and the Tsai-Hill failure criterion, tip deflection was also calculated for the wing and canard, in both the rigid skin and D-cell configuration. A low tip deflection is desirable, especially for performing aerobatics. The tip deflection is measured as the vertical distance between the root chord and the tip chord. The results are shown in Table 8.6 below. Values are shown for maximum maneuvering (load factor of 9 including safety factor) and steady cruise velocity (load factor of 1).

Since the skin thickness of the canard is equal to that of the wing while the span is considerably smaller, the canard experiences very little tip deflection. The wing has a tip deflection of around 0.5 m at high velocity

Table 8.6: Tip deflections of the wing and canard

	Load factor	Unit	Wing	Canard
D-Cell	1	m	0.05	0.03
	9	m	0.48	0.26
Rigid	1	m	0.04	0.01
	9	m	0.36	0.08

maximum maneuvering, which is decided to be within the limits of safe flight. The tip deflection is quite low due to a constant spar cap thickness throughout the wing.

8.6.5 Ribs

The ribs play and essential role in the wing, V-tail, and canard, providing structural integrity, keeping the airfoil shape, and granting the implementation of control surfaces. For this structural analysis, ribs are split up into two types: structural ribs and shape-maintaining ribs. The first type is made from carbon fiber, and provide the connections points for the flaps, flaperons, rudders and elevators. The second type of ribs are made from polyurethane foam, described in Section 8.5.3, and their purpose is to keep the airfoil shape when using sailcloth and prevent buckling in case of a rigid skin. The different types of ribs are shown in Section 8.6.5.

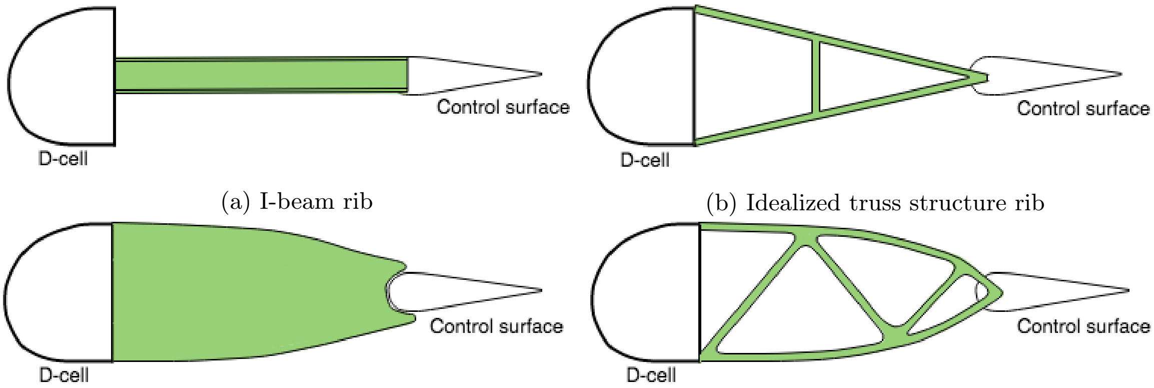

(a) I-beam rib

(b) Idealized truss structure rib

(c) Polyurethane foam rib

(d) Actual truss structure rib

Figure 8.18: Different rib configurations

For the structural analysis, the actual structural rib (Figure 8.18d), was simplified to either an I-beam (Figure 8.18a) or a simple idealized truss rib (Figure 8.18b). In the V-tail, the I-beam rib is used. This proved a more lightweight design than a truss structure mainly due to the very thin airfoil (NACA 0005) on the V-tail and the high moments due to the rudder. For the wing and canard, an idealized truss structure rib is used. The two trusses are connected to the flanges of the D-cell, and the hinge point of the control surface. The middle vertical truss is added because buckling was the main failure mode of the upper and lower truss. The trusses are made from a hollow circular tube. The truss rib needs to be enclosed or close to a foam rib, for the shape of the sailcloth. In case of a rigid skin, this is not necessary.

The location of the ribs is decided by the position of the control surfaces. The main wing has nine structural ribs, a configuration shown in Figure 8.19. The canard has four structural ribs, shown in the same diagram. Each V-tail also has two structural ribs, indicated in red in Figure 8.20.
The parameters of all of these ribs were calculated using the forces and moments caused by maximum control surface deflection, times a safety factor of 1.5. The results are shown in Table 8.8 and Table 8.7. In these tables, diameters and flange widths have been rounded up to the whole millimeter for ease of manufacturing. The V-tail structural ribs are remarkably heavy due to the thin airfoil and large rudder moments. The total mass is a summation of all the ribs in that particular element. The density used for the mass calculations is 1600 kg/m^3 for structural ribs, and 50 kg/m^3 for foam ribs.
The main wing has 35 foam ribs, two end caps, one center rib, and 16 ribs throughout the span with a spacing of 0.5 m. The canard has the same layout, but with a slightly smaller spacing of 0.47 m. Each V-tail also has three foam ribs for rigidity. These ribs encase the rectangular spar, and thus also continue to the leading edge of the airfoil, unlike in the wing and canard, where they end at the D-cell. The final mass for all of these foam ribs is documented in Table 8.9.
Combining all results to get a total mass is shown in Table 8.10.

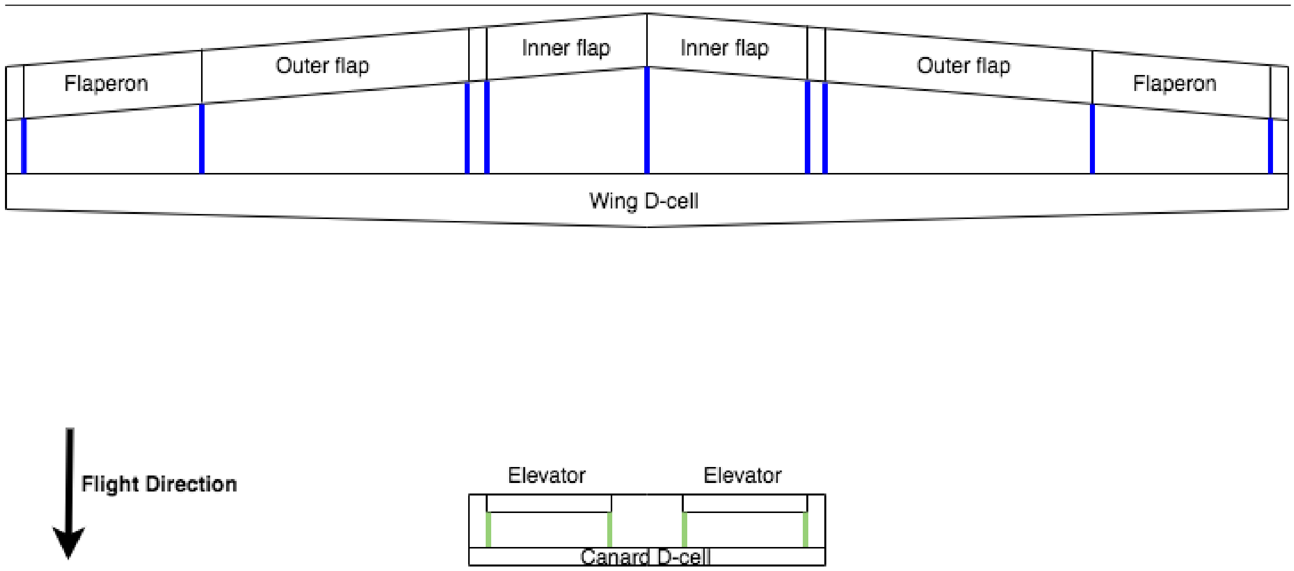

Figure 8.19: Top view of the placement of the structural ribs in the wing (blue) and canard (green), the illustration is not to scale

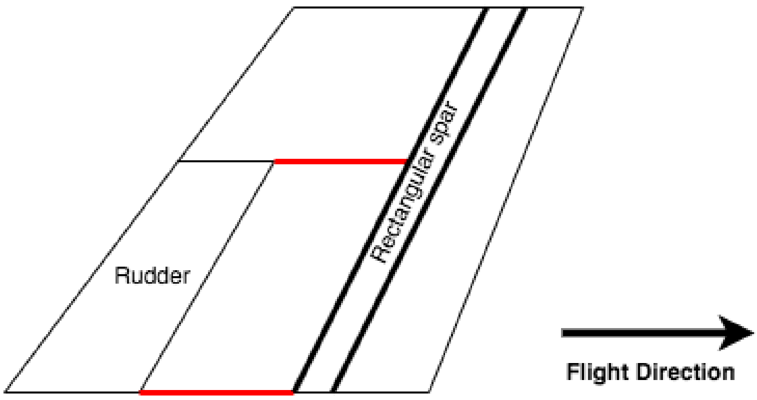

Figure 8.20: Side view of the V-tail, with the structural ribs indicated in red, the illustration is not to scale

Table 8.7: Wing and canard rib parameters

Parameter	Unit	Wing ribs	Canard ribs
Number of ribs	-	9	4
Truss tube diameter	mm	12	10
Truss thickness	mm	1	1
Total mass structural ribs	kg	0.948	0.178

Table 8.8: V-tail rib parameters

Parameter	Unit	V-tail
Number of ribs	-	4
I-beam height	mm	60
I-beam flange width	mm	50
I-beam thickness	mm	1
Total mass	kg	1.099

8.7 Discussion

As can be seen in Table 8.10 the D-cell wingbox design has a significantly lower mass than the rigid skin design. This is entirely caused by the large surface area of the wing. Also, the skin thicknesses needed to carry all stresses are very small for both design options. A sandwich core is added for structural integrity, and to help

Table 8.9: Foam rib parameters for the wing, canard and V-tail

Parameter	Unit	Wing	Canard	V-tail
Number of ribs	-	35	12	6
Rib thickness	m	0.015	0.015	0.05
Rib spacing	m	0.5	0.47	0.53
Total mass	kg	5.16	0.46	0.31

Table 8.10: Total mass

Parameter	Unit	Rigid wing	D-cell
Wing	kg	46.14	24.10
Canard	kg	9.92	3.4
Fuselage	kg	8.5	8.5
Tail	kg	8.1	8.1
Structural ribs	kg	2.22	2.22
Foam ribs	kg	5.87	5.93
Total mass	kg	80.81	52.25

with local buckling. The thicknesses found are sufficient in theory, but will most likely cause problems when manufacturing. For this matter, the D-cell option is also favorable since its carbon fiber skin thickness is double that of the rigid skin. Thus, for the final design, a D-cell in combination with ribs and sailcloth is selected.

8.7.1 Sensitivity

Now that the D-cell structure is determined, the Velo-E-Raptor is subjected to a sensitivity analysis. The outcome is that the structure is relatively insensitive to a mass or load factor change. Increasing the maximum load factor by 15 percent will cause the main wing to fail, but this is because the design is highly optimized to minimize total mass. Increasing the thickness of the D-cell spar flanges slightly negates the failure, and adds 0.71 kg of mass. This is an increase of 5% with respect to the initial wing mass.

8.8 Assembly

A key requirement of the Velo-E-Raptor is that it must be easy to transport. This necessitates the need for a structure that can be disassembled and stored in an efficient manner. One of the reference aircraft used in designing the Velo-E-Raptor is the Archeopteryx, a Swiss made glider. For transport, the Archeopteryx has a detachable 2-part wing, horizontal and vertical tail surfaces[11]. The Velo-E-Raptor will have a similar system, where the main wing is split into three parts, with the joints located at the V-tail. The two V-tails and the canard as a whole can also be detached from the fuselage. The fuselage is also split up into two sections, the rectangular airframe and the nose tube. Finally, the propeller can also be unfastened. This gives a compact package comprised of the nine parts listed below in Table 8.11.

Table 8.11: Disassembled Velo-E-Raptor parts and their lengths

Parameter	Length (m)
Wing section 1	6.4
Wing section 2	3.2
Wing section 3	6.4
Left V-tail	2.3
Right V-tail	2.3
Canard	5.2
Airframe	3.575
Nose tube	4.25
Propeller	1.4

[11] URL `https://www.ruppert-composite.ch/en/` [cited 6 June 2017]

The Archeopteryx is transported in a 6.5 m long trailer, which is exactly what the Velo-E-Raptor will also fit into. The exact layout of how all the different parts fit into the trailer is expanded upon in Section 10.1.2. In order to reduce costs, it might also be considered in a later design phase to reduce the largest wing section to 6.1 m, so that it will fit into a standard small truck cargo hold.

Once the Velo-E-raptor has been transported to its location, it needs to be assembled. The joints necessary for this need to be simple yet robust. These joints will give extra stresses and thus a weight penalty on the structure. When looking at the Archeopteryx and other gliders, the wings and tailplanes are fitted to the fuselage using ball locking pins. This approach is also utilized on the Velo-E-Raptor when connecting the wings to each other and to the V-tail. A piece of the D-cell will be extruded from the wing section and slid into the other wing section. It is subsequently secured using two locking pins. These to extruding D-cell pieces also have a hole in the bottom, which fits into the V-tail spar. Another locking pin secures the wing to the V-tail. The snug fit of the rectangular V-tail spar in the D-cell cutout guarantees a clamped construction, which is beneficial to the buckling of the V-tail. A rigid carbon fiber rectangular extrusion on top of the airframe is the connection point with the V-tail. The rectangular spar is slid over this extrusion and two locking pins anchor the V-tail. Joining the airframe to the nose tube is done in the same fashion. The propeller is screwed on a threaded bolt and fastened with a nut and a cotter or locking pin. Lastly, the canard is connected to the nose tube by means of a double lap joint. The notch is located on the nose tube, and the canard slides into the joint and is secured by double locking pins. This process is illustrated in Figure 8.21, and is also roughly how the rest of the locking pins work.

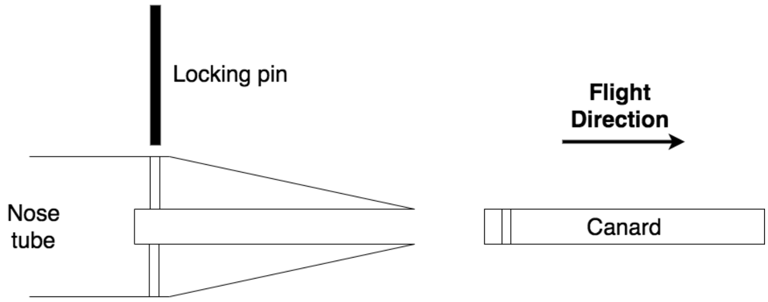

Figure 8.21: The double lap joint connecting the nose tube to the canard

8.9 Verification and Validation

In order to check whether the calculations done for the structure are correct, it is important to verify the code. First of all, the force and bending diagrams were verified using an external simplified calculator, in which the signs and the value of the maximum bending moment and shear force were checked[12]. The code for bending, shear and torsion was checked using a simplified geometry, such that calculations could be done easily by hand and Excel. The simplified geometry used can be seen in Figure 8.22.

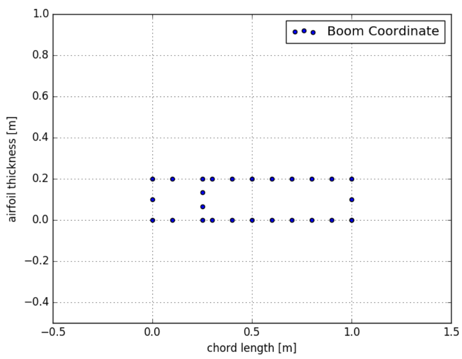

Figure 8.22: Simplified geometry

Every stress was verified with this simplified geometry by comparing the Python code with an Excel file, in which calculations were done by hand. After correcting small errors in the code, the same results were obtained for both the Excel file as the Python code. To show an example the bending stress, shear stress and the Tsai-Hill criterion for the simplified geometry using an average chord of 1.75 m can be found in Figures 8.23a,

[12]URL https://bendingmomentdiagram.com/ [cited 16 June 2017]

8.24a and 8.25a together with the bending stress, shear stress and the Tsai-Hill criterion for the rigid wing as comparison in Figures 8.23b, 8.24b and 8.25b.

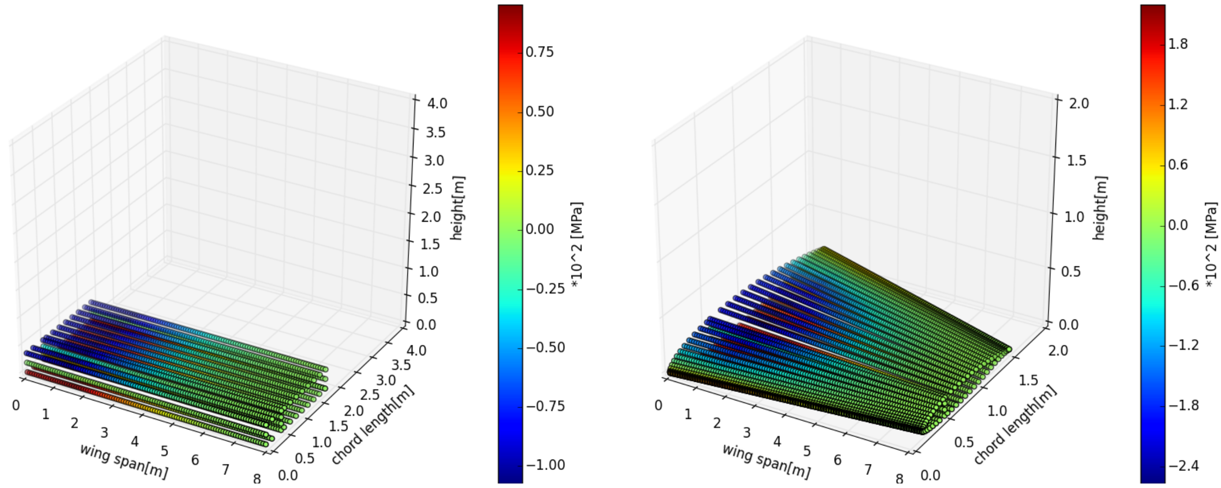

(a) Simplified geometry (b) Rigid wing

Figure 8.23: Bending Stresses

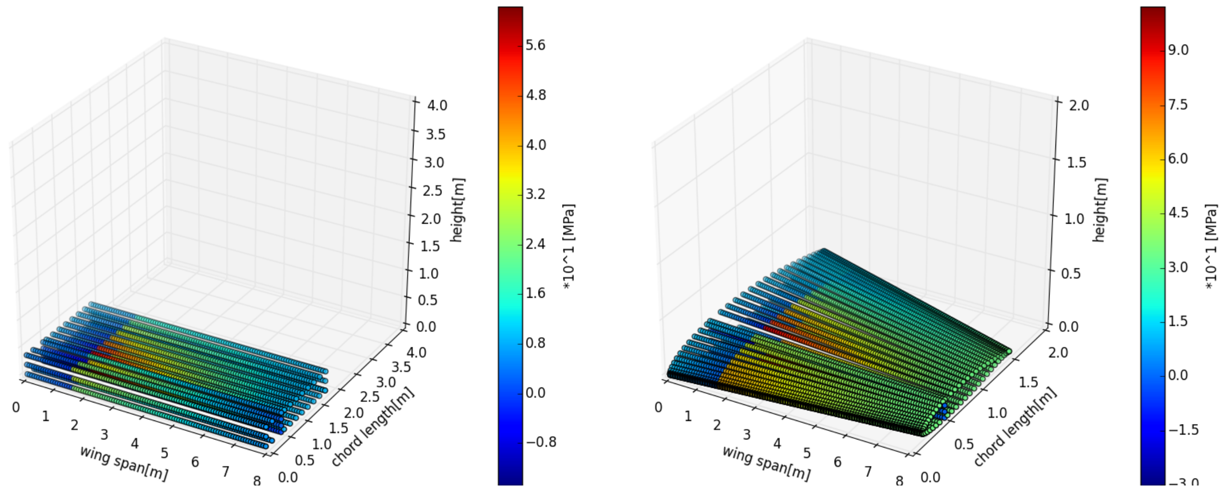

(a) Simplified geometry (b) Rigid wing

Figure 8.24: Shear Stresses

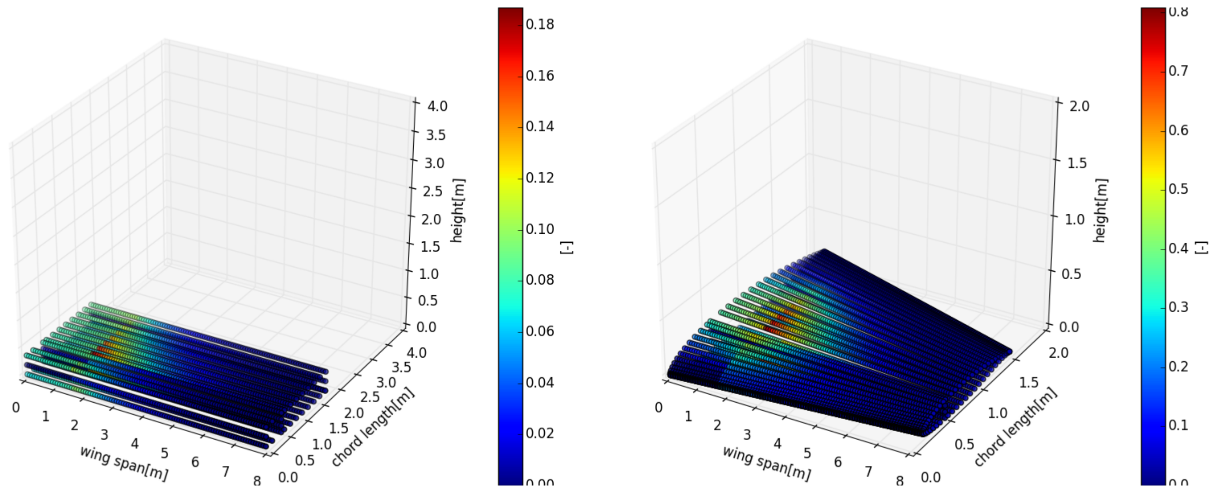

(a) Simplified geometry (b) Rigid wing

Figure 8.25: Tsai-Hill failure criterion

After the verification was done, it is necessary to validate the model. However, since no real tests were done for this design, nothing can be said about the results. For the next design phase, it is of utmost importance that validation is done using FEM analysis with CATIA V5 or by the use of stress testing, such as wing loading tests[13].

8.10 Recommendations

In this structural analysis, several assumptions and simplification were made in order to keep the amount of work to an acceptable level. The current design of the Velo-E-Raptor is very broad but, as seen through verification, accurate, but lacks detail in some areas.

First of all, there is a great deal of material analysis to be done. The current structure, with the composite sandwich panels, is greatly simplified. Also, the asymmetric carbon fiber layering might give problems in reality, and although a sandwich core in between will reduce this issue, it is still in need of investigation. To improve the load carrying wing structure, there could be looked at reducing the size of the D-cell, for example, only use the front 15% of the chord. An extra torsion will be created by not having a load carrying structure on the aerodynamic center. This results in a larger skin thickness which is easier to manufacture. The mass of the wing may be influenced by this.

[13] URL `https://ntrs.nasa.gov/archive/nasa/casi.ntrs.nasa.gov/20050160482.pdf` [cited 22 June 2017]

9 Sustainability

During the projects design phase a sustainability plan has been made. In this section the sustainability of the Velo-E-Raptor is described. All the design aspects and also material choice will be explained from a sustainability point of view.

The Velo-E-Raptor will be a good example of a circular economy. In a circular economy model the system is as closed as possible meaning that every component can be reused, resulting in a minimal amount of material losses.

Just like sailplanes the Velo-E-Raptor will not be primarily owned by individuals but by clubs or associations. Members can than take the aircraft for a flight when available. As a result the Velo-E-Raptor will be used by multiple pilots during the week. This not only splits the costs of the aircraft but also the maintenance.

Maintenance to the Velo-E-Raptor will be easy and structured. As the aircraft will be owned by clubs it will be used a lot. After every flight standardized checks will be held. Some parts of the aircraft will have to be replaced after a certain amount of flight hours. Maintenance standards will be drafted, which the clubs will perform.

During the design process the modularity has been kept in mind. For a product to be sustainable it should be designed to keep future perspectives in mind. The design should be valid for a long period of time. An important element that shapes this long term viability is the adaptability or modularity of the product. It is possible that in the future regulations are changed, and thus the aircraft must then be easily adapted in order to retain operation. Another possible circumstance is that there is a change or expansion of the market. If in the future it is evident that there is a different profitable market that can be tapped into, the design must be able to accommodate this. The new or improved parts will be easy to implement in the current design which also improves the maintainability. An example is the battery, in the future there will be better techniques available and updates are required. For the sport aspect it is expected for example that the battery capacity will be increased or a more powerful engine is chosen.

For the sustainability the social aspect does also play a large role. The goal is to make the Velo-E-Raptor as accessible as kite surfing or similar sports. This means that the aircraft can be flown almost everywhere. Therefore it is important no one will think its presence will be annoying. A final product that does not cause noise pollution is sustainable in this aspect.

This is done by setting a limit to the noise levels. Paragliders nowadays use combustion engines which make a lot of noise. When flying over a neighbourhood everybody can hear the engine and this is considered annoying. The Velo-E-Raptor will almost not be noticeable by people on the ground. Due to the almost silent electrical engine and quiet propeller this problem will not be present.

Another aspect of using electric propulsion is that in-flight emissions will be eliminated and there will no dependence on fossil fuels. This makes the design very sustainable during flight. Also in the mission the sport is to be in the air as long as possible not using the electrical support engine.

The aircraft will be one of the safest to fly with. Due to the flight computer which is capable controlling the aircraft all sorts of safety systems are implemented. It will even be possible to control the aircraft from the ground just like radio controlled model aircraft in order to train beginner pilots. The use of the flight computer will make flying the Velo-E-Raptor even more easy and accessible than kite surfing.

At last the sustainability of the materials and fabrication will be discussed. As a material for the structure carbon-fiber is used. The production of carbon fiber is a energy intensive process[1]. It costs about 14 times more energy to produce compared to steel production. In the process of production a lot of greenhouse gases are expelled. On the other hand the life time of carbon fiber is expected to be much longer than materials like steel. The reason is that carbon fiber does not degrade (almost no degradation), corrode, rust or fatigue. The

[1] URL `https://recyclenation.com/2015/10/is-carbon-fiber-better-for-environment-than-steel/` [cited 26 June 2017]

full lifetime impact thus looks a lot better and as carbon fiber is a lot lighter than other materials the battery can be smaller which reduces the footprint again.

However, metals can easily be reused. When the aircraft is disposed the metal can be remelted into all sorts of things. For carbon-fiber this is not the case. Carbon-fibers can not be reworked to manufacture it for an other use. The material has to be broken down in order to get the fibers out. The carbon-fiber is heated sealed from oxygen so that all other material but the fibers are melted away. This recycle method cost more energy than is needed for steel.

As the Velo-E-Raptor is going to be used by clubs the maintenance is expected to be well performed. Also the usage and flying will be controlled as a lot of experience is present. Combined with the long life time expectancy the carbon fiber is the best choice regarding the sustainability.

10 | Operations

In this chapter the operational aspects of the Velo-E-Raptor are designed and discussed. First the production and transport is discussed, next the human/machine interface. After that the summarizing operational and logistic concept description is given.

10.1 Production and Transport

As the assembly of the Velo-E-Raptor is discussed in the structures chapter, this chapter describes the production process of the Velo-E-Raptor and the transport possibilities.

10.1.1 Production

As the Velo-E-Raptor is made primarily out of carbon fiber, the amount of production processes are limited. Carbon fiber is used in ribs, spars, and the main body structure, while foam and sailcloth are also used in the lifting surfaces. Some of the subsystems are purchased off the shelf, and thus only need to be integrated in the Velo-E-Raptor. These are marked in gray in Figure 10.1. The lowest level of Figure 10.1 are the parts which the pilot assembles at the location. The connections between the different parts still need to be designed, as indicated in Section 16.1.

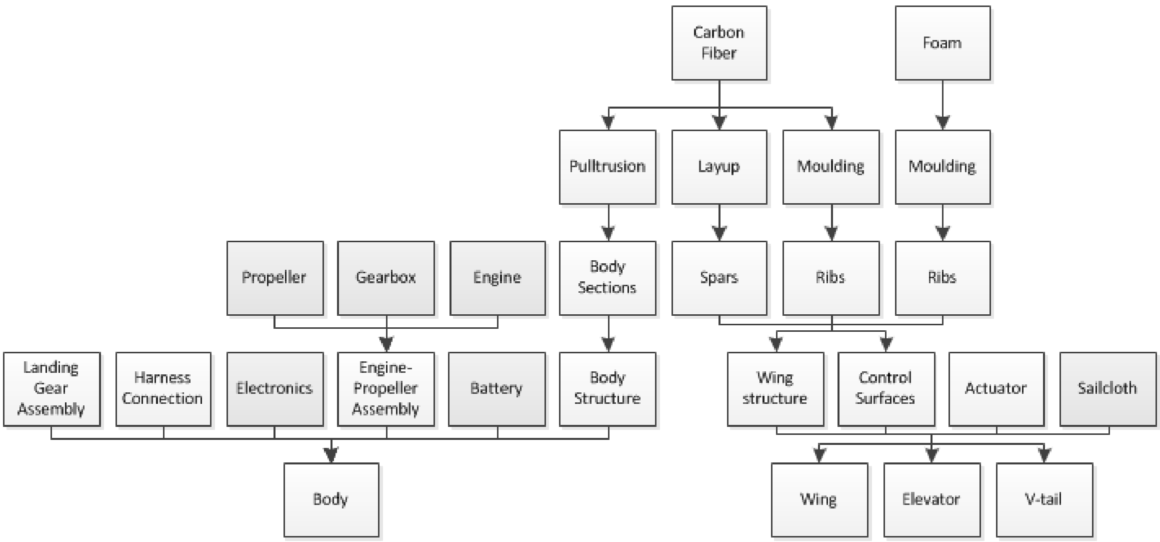

Figure 10.1: Diagram showing the method by which the different subsystems are produced

10.1.2 Transport

The Velo-E-Raptor is designed so that it is transportable by car on the road. This makes it possible to go to interesting locations to fly and go to other clubs or maintenance companies. According to dutch regulations trailers for normal cars may not be larger than 12 m in length, 4 m in height and 2.55 m wide[1]. This makes it possible to design a trailer which is capable of transporting the Velo-E-Raptor. Since the wing is separated into three parts of which the longest is 6.6 m, thus the trailer length will be 7.1 m. The trailer configuration is shown in Figure 10.2. Explanation of the parts shown in this figure are presented in Table 10.1. Wing section 1 is the left wing of the aircraft, section 2 the right section, and section 3 the middle section. As can be seen

[1]URL https://www.anwb.nl/juridisch-advies/in-het-verkeer/verkeersregels/afmetingen-van-autos-en-aanhangers [cited 21 June 2017]

the trailer is 6.6 m in length and 2.55 m in width. It has to be at least 2.2 m in height due to the root chord of wing section 2. Because of this it is possible for people to walk through the trailer and load and unload the Velo-E-Raptor parts.

Table 10.1: Aircraft Parts

1	Wing section 2	7	Left V-tail
2	Wing section 1	8	Right V-tail
3	Wing section 3	9	Storage box for batteries etc.
4	Airframe	10	Nose tube
5	Propeller	11	Windshield
6	Nose tube		

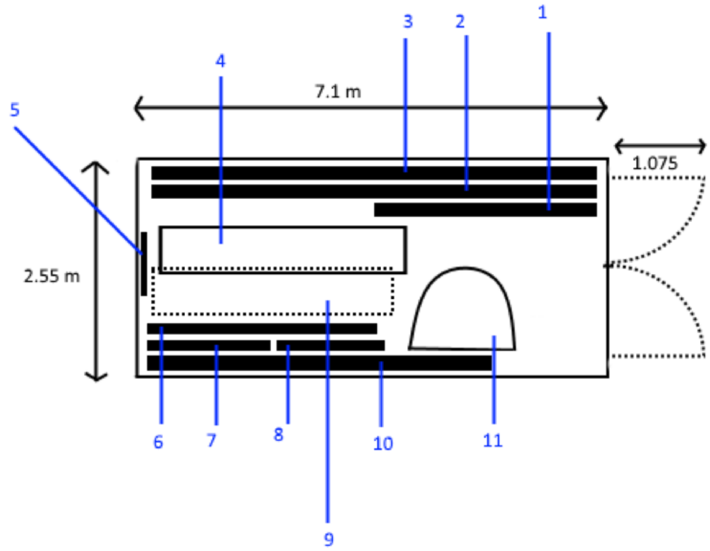

Figure 10.2: Possible trailer configuration for Velo-E-Raptor

10.2 Human/Machine Interface

The Velo-E-Raptor is an aircraft with an interesting and important human/machine interface. First the takeoff and landing methods will be discussed. Next, after the takeoff, the pilot position while flying is explained. During flight the pilot will have to use the pedal system, which will be addressed. Finally, the controls and instrumentation and communication for the Velo-E-Raptor is described.

10.2.1 Controls

Fly-by-wire

The controls of the aircraft will be fully fly-by-wire. This offers significant advantages concerning safety, entry level, weight, and flight comfort. Special attention to aspects like redundancy has to be given. Loss of control in traditional mechanical aircraft often is gradual and not on all the control surfaces. With a fly-by-wire system however, all the control is lost instantaneous on all the surfaces when power is lost, according to Yeh (2002). For this redundancy the fly-by-wire is performed by triplex redundant computers, these computers monitor each others faults and even when one computer fails completely the other two can keep the aircraft controllable, according to Yeh. These three computers are placed at different locations to make sure that events like impact or small fires do not destroy the three computers at the same time. Furthermore, the wires going from the computer to the control surfaces go by different routes to the actuators for the same reason. Two of these computers are placed at the tapered circular section below the chestplate of the pilot when in prone position, one is placed at the left side in the rectangular section, see Figure 8.3.

Not all the flight computers are placed in the same location due to redundancy. The two computers placed in front are computers 1 and 2, the one in the back is indicated as computer 3. If during an accident the tapered circular section is damaged and the flight computers are damaged the pilot is still able to make an emergency landing on the third flight computer in the side of the aircraft. In this emergency the aircraft is controlled asymmetrically, as can be seen in Table 10.2 but the pilot is still able to make a relative safe crash landing. The control surfaces and flight computers are connected as indicated in Table 10.2.

Furthermore, the cables going from the flight computer to the control surfaces go by different routes. Some go through the leading edge of the wing, some through the trailing edge. In the fuselage of the wing this is the same, some go by the left side, some by the right side. This is for redundancy. When a bird strike or another impact occurs in flight and because of this a part of the wing or fuselage is damaged where all the wires would run through, the aircraft would become uncontrollable. The exact locations of the wires would have to be investigated when knowing more about the impact zones in flight and the weak spots.

Table 10.2: Flight computer connection to control surfaces

Control surface	Flight computers
Left elevator	1, 3
Right elevator	2, 3
Left flaperon	2, 3
Left inner flap	2, 3
Left outer flap	1, 3
Right flaperon	1, 3
Right inner flap	1, 3
Right outer flap	2, 3
Left rudder	2, 3
Right rudder	1, 3

In order to further reduce weight, optic fibers are used. According to Garl *et al.* (2014) this offers advantages concerning weight, size and bandwidth. Furthermore, optic fibers do not present a spark hazard since they are a dielectric, which is good for the safety of the Velo-E-Raptor. Also, using optic fibers is cheaper than copper cables since the raw material is cheaper and they last longer. Concerning safety, it is of the essence to encase the fibers in a plastic case since they can break when bent over a radius that is too small.
Finally, an antenna is integrated on the flight computer in order to allow people on the ground to check the behaviour of the aircraft and give advice or feedback through the headset. Also it is possible to control the Velo-E-Raptor from a distance through radio-control.

Harness and Chestplate

The controls of the Velo-E-Raptor are unprecedented. Unlike conventional aircraft where the controls are attached to the aircraft, the controls of the Velo-E-Raptor are connected to the pilot. This means that the pilot will have complete control of the aircraft in both upright and prone position. The custom harness is shown in Figure 10.3. Here, connection points to aircraft are indicated by the two black lines at the front and back of the waist. The harness combines three elements:

1. Harness with back-protector
2. Comfortable breastplate with frontal airbag
3. Rotatable controls

This rotatable control arm is implemented due to the change in position between takeoff and landing and prone flight. When in takeoff and landing position, this being both when lifting part of the aircraft with the harness or when hanging in the harness before landing, the pilot has to be able to control the aircraft. In t his upright position, the pilot has to keep control of the aircraft. As can be seen in Figure 10.3b, the pilot has to rotate his arm about 90° to grab the control stick. In upright position the pilot has his right arm on the control stick and his left arm is free. For left handed pilots a different harness has to be constructed. The harness is constructed of strong Dyneema, which is a new, very strong material in the full body harness industry[2]. Dyneema distinguishes itself by its excellent abrasion and cut-resistance with respect to Kevlar or Nomex. The chestplate consists of several parts:

1. An inner layer made of memory foam to accommodate for various chests of various people.
2. A middle layer to provide support while prone with a power and data cable running through and coming out at the left side.
3. An outer layer with three connection pins and rotating arm connection with unlock button as can be seen in Figure 10.3a.

[2]URL http://www.rigidlifelines.com/blog/entry/harness-materials-and-degradation [cited 8 June 2017]

4. Connection point for optional chin support

5. Frontal airbag

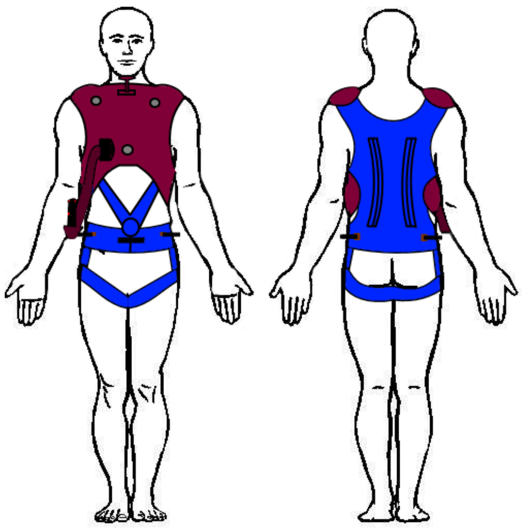

(a) Front- and back-view

(b) Side-view

Figure 10.3: Front-, back- and side-view of the custom Velo-E-Raptor harness with back-protector. Connection pins to aircraft indicated at the waist.

The data and power cables between the aircraft and this chestplate are connected to the left side of the chestplate and go through a reinforced cable to the flight computer in the rectangular section in front of the pilot. There is no risk of overheating since modern computers have far more computational power than required for flight computers and these can operate without problems. This goes by means of a resilient reel near the flight computer, keeping this cable tight both when in upright and prone position. Extra margin is taken for this cable and its reel is near the location of the flight computer. Because of this, both in upright position and in prone position, the power and data cable will never be dangling below the aircraft risking damages or unplugging. This data cable is connected to the chestplate by a strong, double locked system so that it can never come off during flight.

The harness is connected to the aircraft by means of a one degree of freedom rotating joint. This is because joints like carabiners offer too many degrees of freedom and do not offer a tight enough connection between the harness and the aircraft. The pilot connects the connection pin of the harness to the rotating joint and tightens the connection. The harness is designed in such a way that the connection pins are at the height of the human center of gravity. The human center of gravity is located anterior to the second sacral vertebra, according to Hirokazu & Takao (1987). In useful terms, this is 1.03 meter above the ground for the average human male, see Figure 10.7. With the connection pins located located at this location on the harness we can assure that when the pilot rotates, the pilot's center of gravity remains in the same location with respect to the aircraft.

One reason for the implementation of chin support is to prevent injuries to the pilot when cornering with positive G values. When corners like these occur the neck of the pilot is bend forward and thus putting a strain on the rear neck muscles. This might be uncomfortable for the pilot and even lead to neck injuries. Another reason for the chin support is comfort. Some pilots might find it comfortable to rest their heads during longer flights. This chin support is made of a material which is able to absorb some shocks. When a hard landing or a gust is experienced the pilot should not be afraid of biting off his tongue or getting sustained injuries to his jaw. The top of the chin support is rotating, so the pilot is able to look left and right while resting his head on the support. Furthermore, it is possible to slide down the chin support when the pilot wants to.

The frontal airbag is to save the pilot's neck in a crash landing. This airbag is integrated into the chestplate of the pilot. It is one similar to the Dianese D-air racing airbags[3]. This airbag is connected to a sensor in the front skid which senses the impact load. When a certain threshold is sensed by this sensor the airbag is inflated. This threshold can be adjusted in the flight computer and further research on this threshold is advised. This inflation is positioned above the connection point of the chin support and thus will blow down the chin support when when airbag opens. More on the airbag is explained in Chapter 11.

[3]URL `https://www.dainese.com/d-air/` [cited 9 June 2017]

Control Stick

The Velo-E-Raptor control stick offers many options. It is designed in such a way that it is the only control input the pilot needs. It is a 3-axis control stick; controlling pitch, roll, and yaw. Conventional control offers the pilot the possibility to control the rudder by making use of the feet. For the Velo-E-Raptor, however, the feet are used for cycling so the yaw control is integrated in the stick. Another function of the control stick is to facilitate the power control. Since during takeoff and landing the pilot can be in upright position, he will not have power control with his feet on the pedals. However, since power control is of the essence in both these flight phases, a power control lever is integrated on the control stick. An off the shelf control stick which facilitates these options is the Hotus Thrustmaster[4]. Using this, the pilot will have power control both when prone and when in upright position. Since control sticks like these have many buttons and levers other options can be integrated as well. The functions programmed into this control stick are:

1. Pitch, roll, and yaw control
2. Power control
3. Flaps control
4. Emergency power stop

The emergency power stop is to turn off the power going to the propeller. This emergency power stop is connected to the PMS. When during takeoff something goes wrong and the pilot loses control over the aircraft, this red button can be pressed which stops the power going to the propeller so that the pilot can abort the takeoff. This is an important safety function since uncontrolled takeoff can result in a crash. Especially with a push propeller behind the pilot this is something that should always be avoided. Even when a crash is unavoidable it is safer to have the push propeller behind you not generating much trust, this reduces the forward momentum of the blades when they might break.

The controls of the Velo-E-Raptor are so that the pilot is in full control of the aircraft. Meaning that, for instance, when the pilot fully pulls back on the stick, the elevators will go to their maximum deflection. Another fly-by-wire system was also considered by the team; one where the flight computer limits the behaviour of the aircraft within the flight envelope. The choice was made however not to implement this kind of fly-by-wire because it was deemed important to give the pilot full control over the aircraft, both for cases of emergency and giving the pilot the feeling of control. This can be experienced as comforting, especially for the pilots who will fly the Velo-E-Raptor as a sport. A safety interface however will be implemented in the HUD to keep the pilot up to date on his flight behaviour and the limits. This will be discussed in Section 10.2.4.

The control stick produces no force feedback to the pilot. There are two reasons for this decision; one is that feedback by force producing systems are too heavy for our aircraft, the other one is that the pilot is in the open. The pilot can feel the wind and the behaviour of the aircraft and thus is not dependent on force feedback to know how the aircraft is behaving. Furthermore, the HUD also offers information on the behaviour of the aircraft as will be described later.

10.2.2 Pilot Position

During takeoff the pilot has to rotate into flying position. For some takeoff methods, which will be discussed later, this is even before the takeoff is initiated. This rotation consists of the following steps:

1. **Unlock control arm**
   Unlocking the control arm is done pressing the unlock button on the left side of the chestplate. When the arm is unlocked it can rotate freely.
2. **Rotate into prone position**
   Now that the control arm is unlocked the pilot can rotate into the prone position. Since the harness is tuned in such a manner that the pilot rotates around his center of gravity this rotation is almost effortless. The pilot can control this rotation using the handgrip on his left. During the rotation the pilot can keep the control stick in his favorite position.
3. **Click body-set into aircraft**
   Now the pilot can click the chestplate into the receivers on the aircraft. This is done using three connection pins on the chestplate. The top of these receivers are shaped like funnels in order to make this step easier. When inserting the connection pins into the funnel a clicking sound is heard and the chestplate is now sturdy in position.

[4]URL http://www.thrustmaster.com/nl_NL/producten/hotas-warthog-flight-stick [cited 6 June 2017]

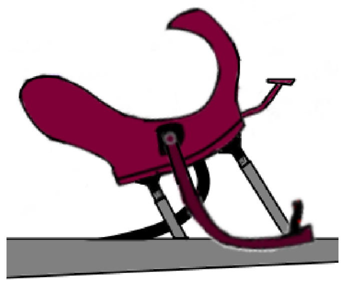

Figure 10.4: Sideview of the chestplate clicked into aircraft, the power and data cable going to the flight computer can be seen in black

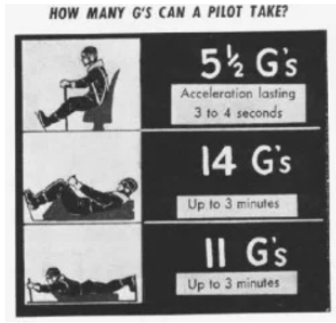

Figure 10.5: As indicated, the human body tolerates many more G's in the 'x' and 'y' axes than the z-axis[5]

4. **Lock control arm**
   When the pilot has the control stick in a comfortable position he or she can lock it into that position by pressing the lock button next to the unlock bottom on the left side of the chestplate.

5. **Extend hip seat**
   Now the pilot is in prone position with his chest resting in the chestplate and his hips supported by the harness. Since this is not comfortable a small hipseat can be extended. This hipseat is integrated in the beam below the pilot. The pilot can extend this seat as far as he or she deems comfortable or necessary.

6. **Retract landing gear if necessary**
   In the case of a takeoff with the use of the support wheels, these wheels have to be retracted as soon as possible after the takeoff since they are producing drag. This retraction is done by pulling the lever on the left of the pilot.

7. **Click feet into pedals**
   Now that the pilot is in prone flight position the sport element of flying the Velo-E-Raptor can be initiated. The pilot can click his shoes into the pedals and start pedalling to gain power.

During some of these procedures a slight center of gravity shift of the aircraft occurs. The rotation of the pilot, the retraction of the landing gear, and the extension of the hip seat all shift the center of gravity in some way.

- When the pilot rotates into the prone position he is rotating around the center of gravity of his or her body. The chestplate however, is not taken into account for the determination of this center of gravity of the body. The chestplate has an anticipated weight of 3 kg. During the rotation from upright position to prone position the center of gravity of this chestplate moves 0.46 m to the front as can be seen in Figure 10.7.

- As for the landing gear, the center of gravity movement is dependent on the initial height it was set on. The gears have a mass of 3 kg each. When set at an initial waist height of 1.3 m the center of gravity of the support wheels move 5 cm to the back and 50 cm up. When set at an initial waist height of 0.7 m the center of gravity of the support wheels move about 2 cm to the back. In both cases the center of gravity also moves 45 cm in upwards direction.

- The extension of the hip seat is negligible in terms of center of gravity movement. The hipseat has an anticipated mass of 0.5 kg and its center of gravity moves about 12 cm back when extended.

The prone position of the pilot is based on two researches. One research conducted by Hurley & Vandenburg (2002) in which there is a elaborate part on the human body and its deflections and a research conducted by Cammerson *et al.* (1988) on the prone flown Meteor. In section 4-5 of Hurley & Vandenburg (2002) the deflections of human body parts are discussed. Both the voluntary deflections and the deflections when extra force is exerted by a third party are presented. From these deflections multiple prone positions can be thought of. However, Cammerson *et al.* (1988) have already researched a comfortable prone flight position. This prone position was designed for the Meteor. When checking the angles in this position against the angles found by Hurley & Vandenburg (2002) it is found that this prone position from the meteor is feasible also when the legs would be cycling. This prone position, as presented in the report, is illustrated in Figure 10.6.

[5]URL `http://goflightmedicine.com/pulling-gs/` [cited 21 June 2017]
[6]URL `http://www.arch.mcgill.ca/prof/castro/arch304/winter2001/dander3/frame/ergo1.htm` [cited 19 June 2017]

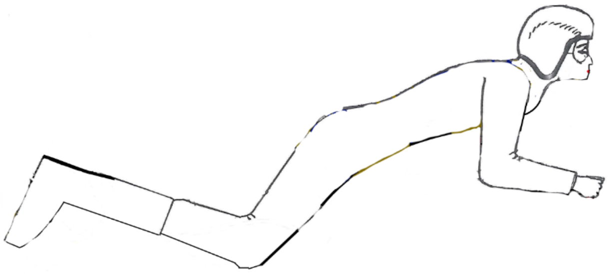

Figure 10.6: Prone position used in the prone meteor by Cammerson *et al.* (1988)

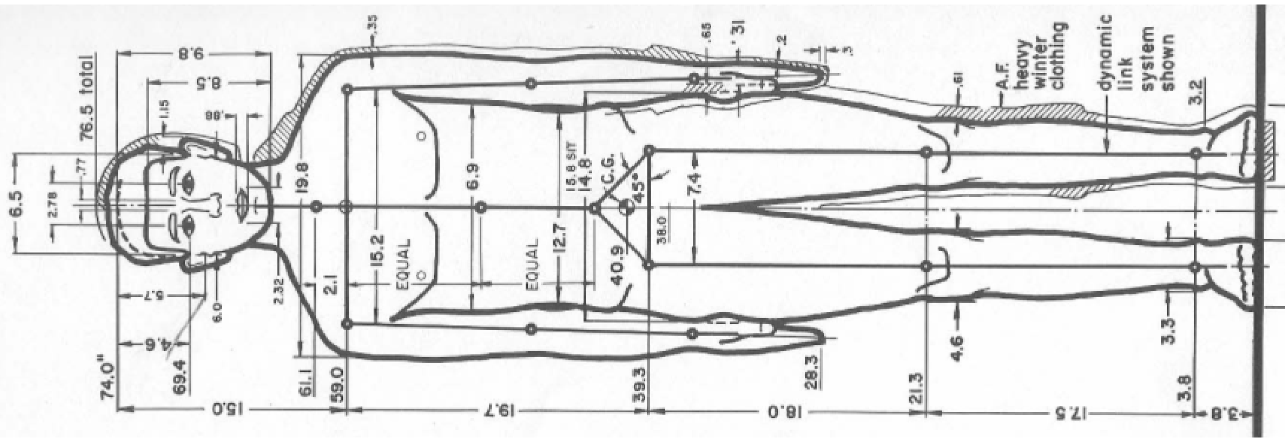

Figure 10.7: Anthroprometric data of standing human male accomodating 95% of U.S. adult male population[6]

It is of the essence that the pilot feels that he is in a sturdy position and that maneuvers like cornering offer no problems. As described before the chestplate has three connection pins in triangle configuration. This ensures that the pilot's chest is firmly in position and not rolling around the x, y, or z axis, when the harness is tightly attached to the pilot's body. As for the hips of the pilot, they are already firmly in place due to the one degree of freedom rotating joint. When the hip seat is extended an even more firm pilot position can be achieved. The hip joints then pull the pilots hips into the seat offering the more firm position on the hips and less deflections while still remaining able to cycle. In the pilot position just described the pilot can perform aerobatics and make turns while remaining in position.

Furthermore, a small investigation was conducted by the design team considering the control stick location when in prone flight. Some subjects found it more natural and comfortable to fly with the control stick perpendicular to the human body and some found it more natural and comfortable when the control stick was parallel to the human body. When small turbulence were simulated most subjects found it to be comfortable if the control stick was perpendicular to the human body. Because of this it was decided that the arm of the chestplate is rotatable. Some pilots will set it perpendicular during prone flight, others might not. Both options are available.

When more advanced aerobatics are performed and more g-forces are exerted on the pilot the use of the optional chin support is advised. When pulling corners of 2 G's or more a dangerous force on the neck can be experienced, especially when the maneuver is suddenly initiated. Pilots in prone position can sustain more G values than pilots in upright position. This is due to less difficulty in maintaining cerebral perfusion under large positive G values in z direction, see Figure 10.5. However, the muscles in the human neck are not so resistant to these G values. For negative G values there is no great injury danger to the pilot due to the neck position seen in Figure 10.6. This is due to the fact that the pilot's head will rotate 55° backwards under these G values in this prone position. An average human male can voluntarily make a rotation of 61° in this direction with his head, according to Hurley & Vandenburg (2002).

10.2.3 Pedal System

Pedals

The Velo-E-Raptor is not only an aircraft, but can also be flown as a sport. Since the power delivered by a human being while cycling is not sufficient for flight, this power is amplified. The human power output on the pedals serves as a throttle. Humans produce up to 298 W while cycling for longer times, according to Whitt & Wilson (1984). A baseline of 74 W is measured for average humans without training, they can endure this power for multiple hours. Because the Velo-E-Raptor has to provide a sport element for everybody, a multiple friction system is integrated. This means that less fit people can set the friction scale at a lower gain to still be able to get 100% out of the aircraft. Research conducted by Hansen *et al.* (2002) showed that a pedal rate of around 80 RPM is experienced as comfortable for human legs when outputting sub maximal power. Because the dynamo to which the pedals are attached does not produce much negative feedback in the sense of friction, two small friction pads are attached to each of the pedals. This is essential for the sport element since otherwise the pilot would just pedal frictionless at an uncomfortable high RPM. These friction pads are attached to the dynamo and increase the friction on the pedals as a function of the RPM. The amount of friction they exercise on the pedals is determined by the pilot through an interface.

The amount of power the propellers give is determined by the linear curves Equation (10.1) and Equation (10.2). When cycling at 110 RPM the pilot gets full power from the PMS. A function is built in to modify this relation to the pilots wishes. The choice has been made for a circular pedal system instead of an elliptical or more 'up and down' pedal system. This is because for newer pilots this movement is more familiar and some human legs are already trained at this movement if the pilot cycles in daily life. Furthermore, since the power delivered from the pilot is not directly used to power the aircraft a more power generating cycle method is not of the essence.

$$P_1 = 37.18 \cdot \text{RPM} \qquad \text{(Up to 80 rpm)} \tag{10.1}$$

$$P_2 = 2975 + 217.3 \cdot (\text{RPM - 80}) \qquad \text{(From 80 rpm to 110 rpm)} \tag{10.2}$$

Position

When cycling, the pilot wants to exert a force on the pedals. When in upright position, normal cyclists do this by means of their weight. In prone position, however, this works slightly different. For a Velo-E-Raptor pilot, the exerted force is carried by the harness and partly the hip seat. Because the harness is attached tightly around the hips and goes over the shoulders of the pilot, the pilot is able to exert force on the pedals. To accommodate for different sizes of pilots, the dynamo location is adjustable, one can put it further to the front or back of the aircraft as can be seen in Figure 10.8. The reasons for attaching the pedal system at three points to the body of the aircraft are bending due to g values when maneuvering and making the system more sound. In a maneuver, the pedal system does not only experience a force due to its own weight but also due to the human legs which are clicked in. The human body is bending around the hip seat as it were and exerting a force on the pedal system as a result of the g values in the maneuver.

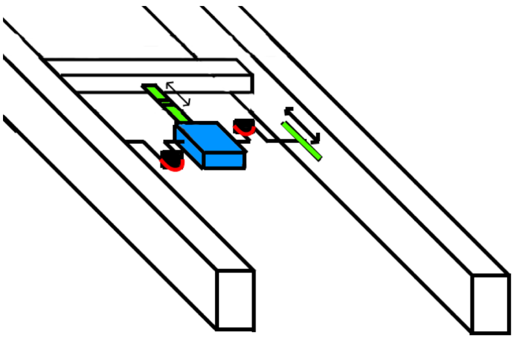

Figure 10.8: The Velo-E-Raptor pedal system, in blue the dynamo is indicated, while the adjustment interfaces are indicated by the arrows and the green colored parts

10.2.4 Instrumentation and Communication

In order to make the Velo-E-Raptor safe and flyable for everybody, advanced instruments are implemented next to good communication. First the Heads Up Display (HUD) will be discussed and then the communication system.

Instrumentation

The aircraft is equipped with a HUD integrated in the windshield, this is a see-through HUD. This HUD will be a fourth generation HUD, which uses a scanning laser to display images and even video imagery on a clear transparent medium. These images and video imagery are instruments and safety instruments, which will be discussed later in this chapter. The HUD will display airspeed, altitude, a horizon line, heading, turn/bank and slip/skid indicators. These instruments are the minimum required by 14 CFR Part 91[7]. Furthermore, to make it easier to fly for new pilots, a waterline, a flight path vector, and an angle of attack indicator is implemented. This angle of attack indicator is equipped with a stall warning system to prevent pilots from stalling unwanted. Another instrument implemented is a maneuver warning system, to prevent pilots from going into maneuvers that might break the aircraft due to their airspeed. Another piece of instrumentation installed is a tell-tale on the windshield. A tell-tale is a small piece of wire of which the end is glued to the top of the windshield. This tell-tale shows the pilot if the aircraft is at a certain yaw angle. It is an old-school piece of instrumentation. However, many pilots are accustomed to this instrument and it serves as redundancy might the HUD fail. For the in-flight navigation a system such as the Flytec Naviter[8] can be attached to the windshield or front tapered beam. Navigation systems like these offer the pilot the comfort of knowing where he or she is and being able to fly beautiful routes set out by others. Furthermore, a safe return to the takeoff and landing field is also assured when the pilot is flying with GPS navigation.

Communication

The Velo-E-Raptor is also equipped with a mode-S SSR Transponder which is mandatory in the Netherlands when flying in Transponder Mandatory Zones[9]. When the Velo-E-Raptors will be flying in other zones this is not mandatory. However, when a pilot wants to leave this area it is essential to have this transponder. The transponder is placed in front of the pilot's head and on top the beam going to the canard. Furthermore, a radio is installed so that the pilot can talk to other Velo-E-Raptor pilots or to the ground support. It is connected to a headset the pilot can wear. The pilot can lift his head from the chin support and talk into the microphone to communicate.

10.3 Takeoff

10.3.1 Takeoff and Landing with Support Wheels and Skid

Taking off with the Velo-E-Raptor is an exciting phase. The pilot is not only controlling the takeoff but is also an integral part of the aircraft. The takeoff method will be described in the following steps:

1. Lifting the Velo-E-Raptor
2. Taking-off with the Velo-E-Raptor
3. Rotating into flying position

Support Wheels and Front Skid

The Velo-E-Raptor comes with two attachable and detachable support wheels in addition to the front skid, the left support wheel can be seen in Figure 10.9 and the skid in Figure 10.10. These support wheels can be used for both takeoff and landing. They are retractable by unlocking the gears and sliding the lock in the adjustment box to the rear. This is why the gears are designed tilted backwards. Furthermore, because the gears are attachable a hinge is used on the fuselage to attach the gears. As can be seen in Figure 10.9 a suspension is used to soften a hard landing. This suspension decreases the shock load on the adjustment box as well, increasing its lifespan. The gears are designed to sustain a 2g landing, this is a heavy landing. Normal landings will never exceed 1g. When shorter pilots set the adjustment box so that their feet touch the ground, the gears are tilted backwards more. This makes the bending loads during a 2g landing, the critical loads in the rod, larger. The load on the legs are also larger in this case. However, since this difference is only small it presents no significant increase in danger to the pilot. In Table 10.3 the weight of one landing gear as a function of the waist height of the pilot is illustrated. Because the Velo-E-Raptor should also be flyable for smaller pilots the gears are designed strong enough for a waist height of 0.9 m. This way pilots of all sizes can make a hard g landing. It is designed to sustain a 2g landing with a safety factor of 3 on the yield stress.

Lifting the Velo-E-Raptor

The first step in taking off is getting yourself into the aircraft and going into takeoff position. In order to do this, the two gears have to be deployed. These two gears are located at 4.25 m from the front of the aircraft, the same location as the center of gravity as the aircraft. Deploying the gears goes in the following two steps:

[7]URL http://www.airweb.faa.gov/Regulatory_and_Guidance_Library/rgFAR.nsf/MainFrame?OpenFrameSet [cited 12 June 2017]
[8]URL http://www.flytec.com/index.html [cited 12 June 2017]
[9]URL http://www.euroglide.nl/eg2008/NL-AIC-V0408-20080522-NL.pdf [cited 20 June 2017]

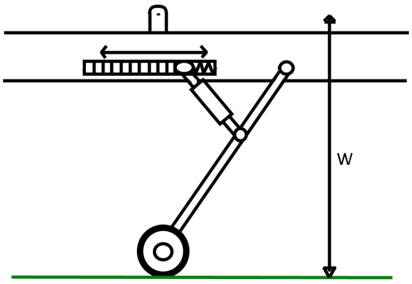

Figure 10.9: Support wheels of the Velo-E-Raptor, the W indicates the waist height

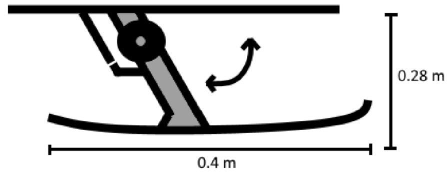

Figure 10.10: Front skid of the Velo-E-Raptor

Table 10.3: Waist heights and corresponding mass of one single gear without wheels, suspension or attachment.

Waist height [m]	Mass of one support strut [kg]
0.9	0.68
1.0	0.64
1.1	0.59

1. Attach the support wheels.
2. Set the adjustment block at the correct pilot waist height.
3. Lift the Velo-E-Raptor at the rear-end of the aircraft at the lifting handles until clicking sound is heard. This lifting can be done by hand or by using a crank.

Now the aircraft is laying nose down on the front skid with its gears deployed. The next step is for the pilot to connect the two connection points on the harness to the aircraft. This is done using the two one-degree of freedom rotating joints. This connection is at the same longitudinal position as the center of gravity of aircraft. Now the pilot can balance the Velo-E-Raptor using a handle on the left side of the pilot. The pilot can also walk with the Velo-E-Raptor in this position and go into takeoff position. A little bit of power can be used as well to make the walking more effortless.

Takeoff

Now that the Velo-E-Raptor is lifted and the pilot is in takeoff position the takeoff can be initiated. The pilot has his right hand on the control stick and his left hand on the handle. Now the pilot can slowly start increasing the power by using the power control on his control stick. As the aircraft starts accelerating the pilot will have to run along. During this initial running phase the aircraft is not yet controllable and the pilot will have to balance the aircraft using the harness and the handle on his left. At a speed of 7 m/s the aircraft becomes controllable and thus the pilot can use the control stick to control the pitch and roll. Since the pilot is connected to the aircraft at the center of gravity he or she can not retract his or her legs and keep accelerating while controlling the aircraft. When at 10.5 m/s the takeoff speed is achieved the pilot can pitch up and eventually go into prone position to start the climb.

10.3.2 Foot Launched Takeoff and Landing without Use of the Support Wheels

Taking off and landing with the Velo-E-Raptor is also possible without the use of the support wheels, although this does require quite some physique from the pilot. Research showed that human males between 70 and 90 kg are capable of squatting between 60 and 80 kg[10]. As can be read on the site the data standards are based on 1,780,000 lifts collected from users of the app Strength Level. Females however, with a weight between 60 and 80 kg, are able to squat respectively between 27 and 35 kg. Average females are thus not able to lift the Velo-E-Raptor in order to be fully foot launched. Research conducted in 1989 by TNO showed that male soldiers are capable of carrying 23 kg on a tightly attached hip belt before the belt started slipping off, as described by Holawijn (1989). This means that the pilot has to carry the remained of 67 kg on his shoulders since carrying weight on the hips is experienced as the most pleasurable, according to Heller *et al.* (2009). The Velo-E-Raptor custom harness is designed in such a way that it is able to transfer the 90 kg in the most optimal and well distributed way possible.

[10] URL `http://strengthlevel.com/strength-standards/squat` [cited 13 June 2017]

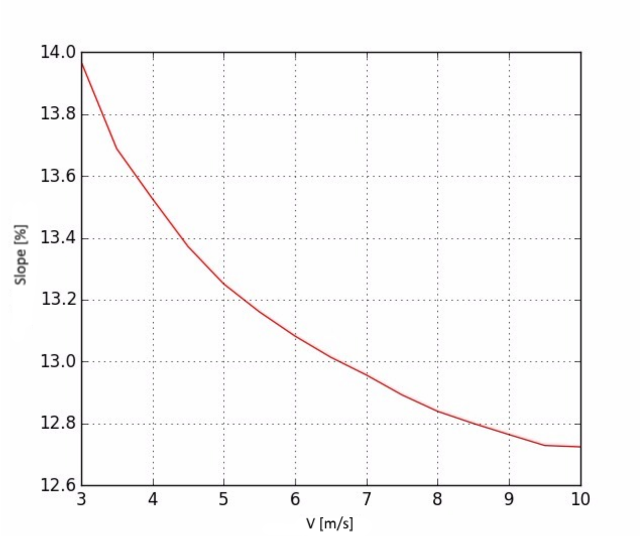

Figure 10.11: Sink rate versus velocity at cruise height

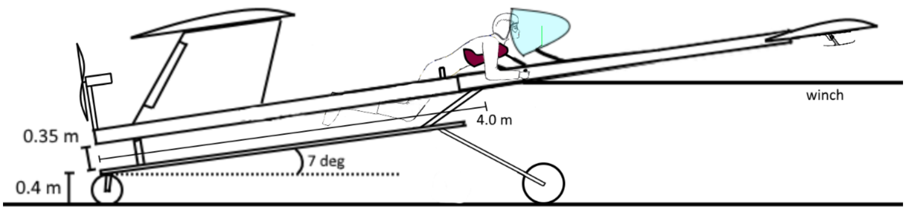

Figure 10.12: Take-off cart connected to the winch.

Since the Velo-E-Raptor has a takeoff speed 10.8 m/s it cannot be expected of the pilot to reach this speed at level ground while running. A down hill takeoff, however, is possible. At speeds below the stall speed, certain sink rates can be achieved. In Figure 10.11 these sink rates are presented. The data is generated at the takeoff A.O.A, which is $\alpha = 7.8°$. This means, for instance, that the pilot wants to retract his legs after reaching a running speed of 3 m/s, he or she will have to find a hill with a slope of at least 13.95%. This is at a height of 1500 m.

10.3.3 Takeoff and Landing with the Use of a Cart

The third takeoff option with the Velo-E-Raptor is making use of a cart. In this configuration the aircraft is accelerated upon a cart. This can be done on two ways: accelerating using the propeller and accelerating using the cart. This cart can be seen in Figure 10.12.

Accelerating using a cart and the propeller

In this takeoff option the Velo-E-Raptor is positioned upon a cart. This cart is not connected to a winch. This cart has two front wheels and one rear wheel, the same configuration as many hang-glider takeoff carts. The aircraft is positioned on this cart at the takeoff angle of attack. Now the pilot can enter the Velo-E-Raptor in prone position since the aircraft does not have to be lifted or balanced by the pilot. Now the pilot can initiate the takeoff and accelerate the aircraft and cart. When the takeoff speed of 10.5 m/s is reached the pilot can pitch up and fly away. The cart is left on the ground.

Accelerating using a cart and a winch

This same cart can also be used to initiate a takeoff without the use of the propeller. Just as on sailplanes, the winch is connected to the Velo-E-Raptor slightly before the center of gravity. This is essential for the stability during the winch launch[11]. The connection is a hook located at the bottom of the front bar of the body, very near to the longitudinal location of the center of gravity. This winch can be released using a pull mechanism

[11] URL `http://nature1st.net/soarns/winch_article1.html` [cited 19 June 2017]

connected with a rope to the left side of the pilot. The pilot can then use his free left hand to release the winch when desired.

10.3.4 Landing

Landing with the Velo-E-Raptor can be done in two ways, using the support wheels or not using the support wheels. First the method using the support and front skid is discussed, then the method of landing without the support wheels is discussed.

Landing with the support wheels and front skid

For safety reasons, a gliding landing is advised. This is due to the dangers of a push propeller hitting the ground and breaking off in the direction of the pilot when the pitch angle is too high during landing which causes the propeller to hit the ground. As the pilot approaches the landing zone he or she has to let down the support wheels. Unlike the takeoff, however, the pilot does not have to rotate into upright position. It is possible to land using only the support wheels and front skid while remaining in prone position. As the pilot glides over the grass field he or she can see the pitch angle of the aircraft on the HUD. This pitch angle may not be larger than 10° considering the propeller hitting the ground and the additional obstacle clearance of 0.1 m. However, the aircraft canard stalls at 9°. A stall of the canard is dangerous during the landing due to the high wing loading of the canard, when it stalls during landing the nose will drop and the the aircraft will fall due to the significant loss in lift. Therefore, giving special attention to the angle of attack indicator on the HUD and the stall alarm is essential during the landing.

When the support wheels hit the ground an initial negative moment is experienced due to the drag of the support wheels. Either the pilot is capable of sustaining this moment using the pitch control or the front skid touches the ground. The landing can be successfully performed in both of these situations. However, the case where the pilot keeps the canard in the air as the support wheels roll over the ground can be experienced as more comfortable since the pilot can gently let down the front skid. As the front skid hits the ground, the drag from that skid will slow the aircraft down. When the option of a headwind landing is present this should always be the preference. With headwind the pilot can reduce the speed at which the support wheels hit the ground. This has the advantage of the pitch down moment being smaller as the drag from the wheels is smaller and the landing distance is smaller since the aircraft comes down at a lower speed relative to the ground. Now the pilot has landed the Velo-E-Raptor in prone position using the support wheels and the skid. He or she can not go in upright position and release himself from the joints connecting the harness and aircraft.

Landing without the use of the support wheels

Landing the Velo-E-Raptor without the use of the support wheels is very similar to taking off without the use of support wheels or cart. As in takeoff a strong headwind is preferable. As the pilot glides over the grass field in upright position it is essential to glide as long as possible as low as possible. When the stall speed of 8.75 m/s is achieved, either the pilot can let his feet touch the ground and carry a small part of the aircraft while running or the pilot can flare a little bit to reduce the speed of the aircraft. This speed is very fast to run for a human so it is advised to do a flaring landing. When the legs of the pilot are on the ground he or she can choose to run a while before letting the front skid hit the ground and decelerate the aircraft or the pilot can let the front skid down as soon as his feet touch the ground to start the deceleration. This landing method, especially when flaring, is only advised for experienced Velo-E-Raptor pilots.

10.4 Operational and Logistic Concept Description

The operational and logistic concept description is a summary of the operational and logistic steps involved. Because the Velo-E-Raptor is a versatile aircraft which does not have one specific way to use it, some processes are summarized. The pre takeoff actions are different for each different takeoff method chosen. In some cases the pilot will want to attach the support wheels, and in some not. The operational and logistic concept description can be seen in Figure 10.13. More in-depth information and more options for each action was given in this chapter.

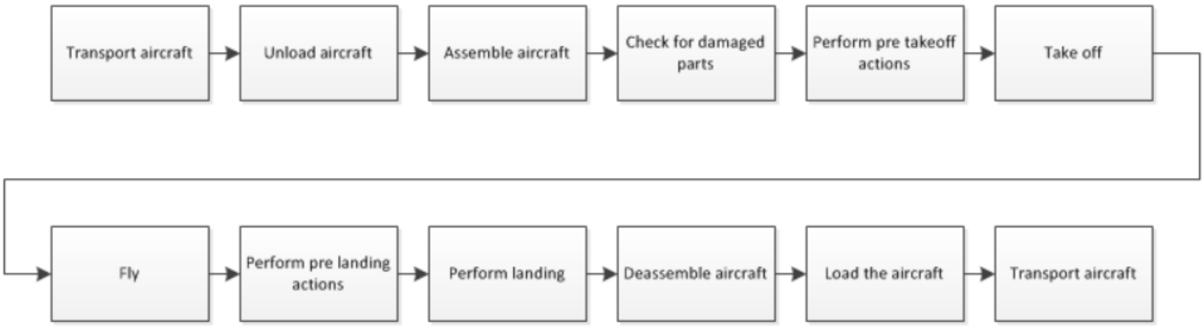

Figure 10.13: Operational and logistic concept description

11 | Safety

The Velo-E-Raptor is a safe and enjoyable aircraft for everybody. The focus is not on what happens when you crash, but how the aircraft helps you not to crash. This way, pilots of every skill level can have an enjoyable flight in the Velo-E-raptor. A beautiful and relaxing flight for new pilots, and a challenging and intensive flight for experienced pilots. First, the stall and controllability behavior of the aircraft is discussed. In this chapter, the prevention of stall systems and also the recovery when a stall occurs will be explained. Landing and takeoff are always dangerous phases, the various safety precautions in that phase will be discussed next. After that, the behavior in turbulence, gusts, and g-forces will be discussed along with the integrity of the aircraft in various phases. Of course everybody makes mistakes and the Velo-E-Raptor is fool proof, so even when an uncorrectable mistake occurs and a crash is evident there are safety precautions. These safety precautions for a crash are discussed next. Finally, the visibility for other pilots and people on the ground is explained, which is essential for safety when both flying high and low to the ground. Many safety precautions are discussed in the operations chapter, the ones that were not addressed in that chapter or when they deserve more attention are addressed in this chapter.

11.1 Stall and Controllability Behaviour

Stall and loss of controllability are scary and dangerous phenomenons for pilots. First the behaviour of stall is recapped, then the stall prevention and recovery is discussed.

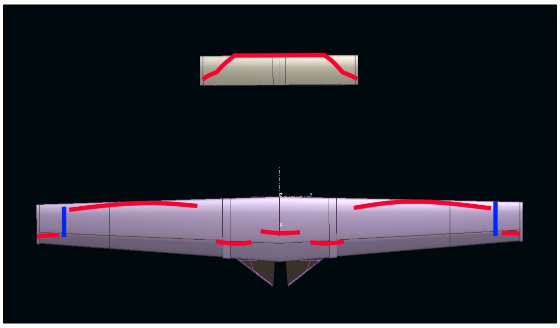

Figure 11.1: Top view of Velo-E-Raptor in full flaps configuration near stall, transition layers are indicated by the red lines

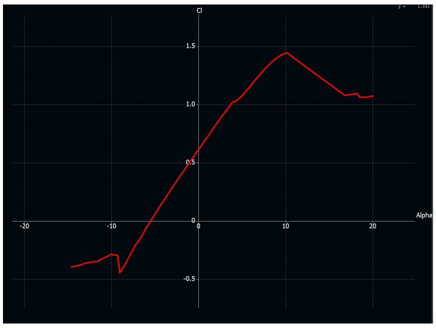

Figure 11.2: C_l versus α for the canard airfoil

11.1.1 Behaviour

The canard of the Velo-E-Raptor stalls before the main wing. This means that when the angle of attack becomes too large the canard will stall and the nose will drop, thus decreasing the angle of attack again. Since the Velo-E-Raptor has a high wing loading on the canard this nose drop is quite noticeable. This way the main wing will never stall which is safer than conventional configurations. As mentioned in the aerodynamics chapter, the canard stalls at 9.3° and the main wing at 14.2° in clean configuration. With the flaps deployed the canard stalls at 8.9° and the main wing at 10.1°. The stall behaviour of the airfoil of the canard is illustrated in Figure 11.2. In clean configuration the difference between the stall angles of attack is larger than in flaps configuration. The transition layers near canard stall are illustrated in Figure 11.1. As can be seen, the main wing is not fully stalling at the tip at the moment the canard is stalling. This is good for safety since the aircraft remains roll controllable near stall. Because of this, stall safety mechanisms such as stall shields are not necessary in the design. When cornering wing drop is a dangerous stall phenomenon. In a turn, climbing and descending too, the wings each have a different angle of attack. Thus, if the stall is approached during turning maneuvers one wing will stall before the other. In climbing turns the higher wing will stall first, in descending turns the lower wing stalls first. The latter is dangerous because a lower wing stall might result in a spin.

11.1.2 Prevention

Because the Velo-E-Raptor has to a flyable aircraft for everybody, various stall prevention measures are taken. These are discussed in this subsection.

HUD

An angle of attack indicator is connected to the HUD. This angle of attack indicator has to be placed in a free stream for accurate measurements. A good position would be between the canard and the windshield, on the circular beam. This indicator shows the angle of attack at which the Velo-E-Raptor is flying. In clean configuration an alarm should go off when the angle of attack nears the canard stall angle of attack to notify the pilot of the dangerous situation. Because in the flaps out configuration the difference between the stall angles of the canard and main wing is smaller this alarm should go off sooner. The alarm system works as shown in Table 11.1. As can be seen in this table, in clean configuration an alarm goes off 0.5° before canard stall and in flaps configuration 1.0° before canard stall. Furthermore, an angle of attack indicator with these limits in the indicator is a good addition. This way the pilot can keep the aircraft at a high angle of attack during takeoff and landing without risking a sudden stall.

Table 11.1: Alarm thresholds for both clean and flaps out configuration

Parameter	Clean configuration	Flaps out configuration
Alarm start	8.8°	7.9°
Stall Canard	9.3°	8.9°
Stall main wing	14.2°	10.1°

Considering slip and skid, the HUD has a slip/skid indicator. Flying in slip is not as dangerous as flying in skid when cornering. Therefore, a warning system is implemented into the HUD to warn the pilot when the aircraft is in skid while turning. This could prevent the aircraft going into spin when less experienced pilots fly the Velo-E-Raptor.
A stall prevention method that also can be implemented on the Velo-E-Raptor are stall shields. As indicated by the blue lines in Figure 11.1 there is a location on the wing where one part of the wing has its transition layer closer to the leading edge than the part next to it. Because of this, the turbulent flow from the part with its transition layer more front disturbs the flow from the part with its transition layer more aft and thus causing that part to stall sooner. A stall shield in between these two parts could prevent this. Especially when keeping in mind that the outer parts of the wing have the most influence on the roll behaviour of the aircraft. It is important to keep these control surfaces as long in clean non turbulent flow as possible. A stall shield taking care of this causes the controllability speed to lower even more, making the Velo-E-Raptor even safer.

Alarms and instructions

When pilots are in trouble and one of the dangerous phenomenon, such as nearing stall or skid while turning, is evident, just a blazing alarm could not be of as much support as one would like to. Therefore, a system is programmed into the HUD to not only tell the pilot that something is about to go wrong, but also to tell the pilot what to do about it. First of all, a voice tells the pilot what is about to go wrong and what he can do about it along with visual instructions on the HUD. When nearing stall for instance, this could be; "Nearing stall, pitch down" along with an arrow on the HUD indicating this maneuver. This way, when a pilot is panicking, he or she can just follow the instructions until the aircraft is in a safe attitude again and the pilot regains control.

11.1.3 Recovery

All pilots make mistakes, in the Velo-E-Raptor this will be no different, despite the prevention measures taken. So when the aircraft goes into stall or spin a recovery plan is essential to ensure the pilot's safety. In the case where the canard stalls, the nose will drop. Due to the high wing loading on the canard this drop is quite notable. It is essential that the pilot pitches up after speed has been regained in this nose drop. However, when flying at a lower altitudes there might not be enough height to make this recovery. Therefore, a pyrotechnic parachute is integrated into the Velo-E-Raptor, this parachute is the EVO Cross 235[1]. This parachute can be successfully deployed at heights of 50m and higher using a pyrotechnic rocket such as the one from the Archaeopteryx,[2]

[1]URL https://www.independence.aero/en/products/rescue-parachutes/evo-cross.html [cited 21 June 2017]
[2]URL https://www.ruppert-composite.ch/en/ [cited 5 June 2017]

due to the high opening time of this parachute, which is 3 seconds. This parachute is integrated in the nose of the aircraft, below the canard, so that when deep stall occurs the parachute can be deployed and the pilot and the aircraft go down at a sink rate of 5.5 m/s. These parachutes are produced by Ballistic Recovery Systems, Inc. and as of 15 August 2016, the CAPS has been activated 83 times, 69 of which saw successful parachute deployment. In those successful deployments, there were 142 survivors and 1 fatality. This parachute can be deployed at heights of 50 m and higher. Below that altitude there is not enough time to fully eject the parachute and guarantee the success of the parachute.

The reason for integrating the parachute in the nose of the aircraft is due to the deep stall behaviour of canard aircraft. When canard aircraft go into deep stall they fall belly down towards the earth. When the parachute ejects and deploys the aircraft is let down with the pilot's feet down which is safer than letting the aircraft and the pilot down with the pilots head first. Because the parachute is bright orange it is easy to see when deployed and when landed in forests or other rough terrain. The reason for attaching the parachute to the aircraft and not to the pilot only is due to safety reasons. At a height of between 50 and 100 meters the pilot will most likely not have enough time to leave the aircraft and get clear of it to open his parachute. Because the maximum weight of the Velo-E-Raptor with pilot is 190 kilograms, and the maximum weight of the parachute used is 235 kilograms, the parachute is strong enough to safely carry both the aircraft and pilot.

11.2 Turbulence, Gusts and g's

Turbulence and gusts present a danger to the pilot and aircraft, especially with a pilot in prone position with as little support in the Velo-E-Raptor. During flight, when a gust or turbulence occurs, it is essential that the pilot's body is in the clear and that he or she can not injure themselves to the aircraft. Looking at the deflections of the human body parts presented in section 4-5 of Hurley & Vandenburg (2002) it can be seen that this prone position is experienced as comfortable. As for the legs, the pilot can not see the area of the aircraft where the legs and pedal system is located. Therefore, it was made sure that all the cables were integrated into the skeleton and none were out in the open. Because of this, the pilot is unable to destroy and kick loose any essential cables in the aircraft. Especially with the rotation between upright position and prone position during takeoff and landing in mind as well as strong gusts and turbulence. In these gusts and turbulence the legs of the pilot cannot come loose of the pedal system due to the foot straps integrated on the pedal system as can be seen by the red lines in Figure 10.8.
When performing aerobatics or quick maneuvers it is important that the pilot feels safe and in a sturdy position. Because of this, it is important that the one-degree of freedom rotation joint, the hip seat, and the connections both between the pilot and the chestplate and between the chestplate and the aircraft are tight and sturdy. For the harness this can be achieved by correctly tuning the harness for the pilot's body. For the hip seat this can be achieved by using small design tolerances and ejecting the hip seat far enough that the harness connection pulls the pilot into the seat well enough. The connection between the chestplate and the aircraft should also be designed with small tolerances and be well maintained.

11.3 Integrity

It is important that the pilot feels safe in the Velo-E-Raptor and that there is not fear of the aircraft breaking. This process starts on the ground when assembling the aircraft. It is of the essence that the pilot assembles the aircraft correctly so that the risk of say, a wing, coming off mid flight is minimized. This can be achieved by having very clear pictures near locations on the aircraft where parts come together. These pictures show the process of assembly and make sure the pilot does it in the correct order. Furthermore, a system can be implemented where a green pin is shown if the assembly of that part was performed correctly. This reduces the chance of the pilot thinking he or she has performed the assembly correctly while in reality it has not greatly.
When in flight the chance of the pilot breaking the aircraft has to be minimized as well. The structures department has determined the never exceed speed to be 100 m/s. The Velo-E-Raptor has a maximum dive speed 96.2 m/s. Looking at Figure 8.1 it can be seen that at this maximum dive speed a load factor of 0.8 can be sustained with a safety factor of 1.5. The pilot can not pull a 2g corner at this speed for instance because that would break the aircraft. However, when the pilot starts the maneuver at this speed the drag starts increasing and the velocity will drop, thus allowing for higher load factors. This is why a maneuver diagram is integrated into the HUD. This maneuver diagram can be designed as in Figure 11.3. Here, the current speed is 83 m/s and load factor is 1. As can be seen in Figure 8.1 the critical load factor at this speed is 1.6. When the pilot nears the red line, the critical load factor, an alarm goes off and the pilot is told to stop the maneuver. This too, could be supported by an arrow in the HUD indicating this stop of the maneuver. Because of this, it becomes quite hard for the pilot to break the aircraft. So even then the pilot is in a full dive, which the aircraft can sustain, the pilot can get out of the dive safely using this instrument.

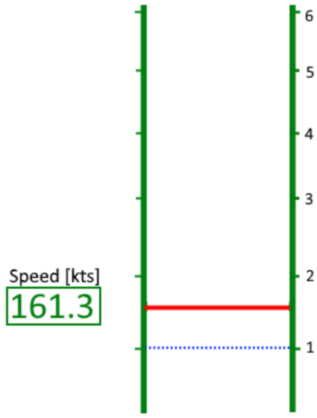

Figure 11.3: Load factor safety indicator integrated in HUD

Considering the Lithium Polymer batteries, they are placed inside the structure so that when accidents with them occur the pilot is not immediately hurt by the inflamed fluid. The two most dangerous failure modes are overheating and tearing which might have the fluids leak out. To prevent these two from occurring a temperature regulator is implemented in the batteries which turns them off when overheating and shock absorbing material is placed below the batteries to reduce the wear due to hard landings.

11.4 Crash

Airbag

In the case of an imminent crash there are various safety precautions to make sure the pilot remains as unharmed as possible. The first of these precautions is the airbag integrated in the chestplate. In the case where the pilot comes in too hard both in upright and prone position this offers safety. In the case where the pilot is in upright position and lands too hard the support wheels will sustain the hard landing and the front of the aircraft will smack into the ground. During this event either the pilot's legs will hit the ground first and cause the pilot to rotate to the front at a dangerously fast rotational speed, or the front skid hits the ground and this impact might cause the pilot to make the same dangerous rotation. In both cases the frontal airbag offers protection. The two main dangers during this rotation are impact on the pilot's chest as the chestplate hits the connection pins and the neck of the pilot hitting the front beam either injuring the head or the pilot experiencing whiplash. Since the frontal airbag of the chestplate blows both in the direction of the connection pins and the to front of the chestplate causing the head of the pilot to stop making the rotation, both dangers are minimized. This airbag can be seen in Figure 11.4. The Insurance Institute for Highway Safety (IIHS) tests the airbag of modern cars for 'full frontal, rigid-barrier' crashes at 35 mph[3] or 15.6 m/s. This speed roughly corresponds with $1.2V_{stall}$, which is usually taken as the takeoff and landing speed. In addition, it corresponds to the inviscid free fall speed from a height of 12 m.

Suit

Since the pilot of the Velo-E-Raptor is flying in the open and not in a complete fairing, a danger of certain body parts sliding over the ground is present. During all of the suggested takeoff and landing methods there is a risk of knees, elbows, feet or other body pars scraping over the ground. This can cause both light and heavy injuries depending on the and duration. Because of this the use of skin protection is advised when flying the Velo-E-Raptor. The use of a certified motor suit offers the best protection due to it being designed for such high speeds, but other options are also possible. When looking at Figure 11.5 the impact zones for motorcycle riders are illustrated. For the pilot of the Velo-E-Raptor these impact zones are similar. As indicated by the red zones in this figure, the knees, hips, elbows and shoulders are the critical parts. When a pilot does not want to wear a full motor suit at least these areas need to be well protected by certified material such as the material used in the harness.

Wheels

Crash landings can present a big danger to the human legs when the pilot is in upright position during the crash. In a landing with a g value of 2 or more the pilot's legs endure a force of about 4000 N. This is enough to

[3]URL `http://www.iihs.org/iihs/sr/statusreport/article/35/6/1` [cited 16 June 2017]

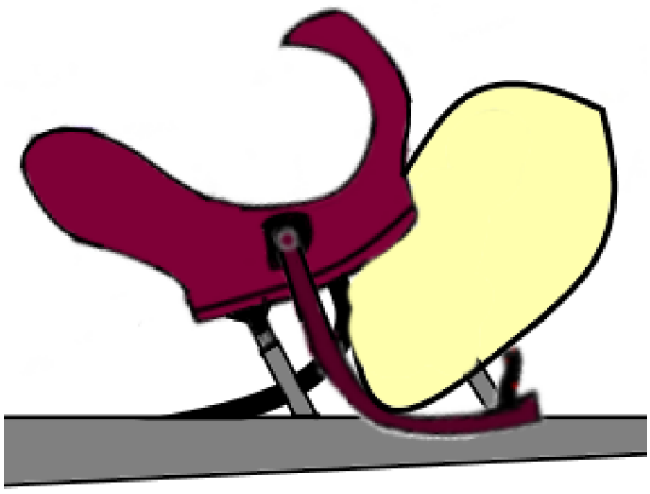

Figure 11.4: Velo-E-Raptor chestplate with inflated airbag

fracture the leg or foot in the Calcaneus, which is the heel bone, according to Funk *et al.* (2002). Therefore it is advised to always bring the support wheels when flying the Velo-E-Raptor. The support wheels are designed to sustain a landing of 2g's with a safety factor of 3. In a crash, these support wheels will sustain the crash landing and the pilot's legs will not have to carry this load.

Propeller

Since the aircraft is equipped with a push propeller there is a risk during a crash landing. Since the propeller is generating thrust, the blades will break off in frontal and outward direction when breaking off. This is a risk that has to be mitigated since the pilot is located at the front of the propeller. Therefore, when landing, both normal or under crash circumstances, it is advised to turn the propeller off and let the propeller fold itself. This way, the risk of letting the propeller it the ground when landing at a too high pitch angle and having a blade shoot off is minimized. This glider landing is possible since the Velo-E-Raptor has a L/D ratio between 7.5 and 12.5 in 'flaps out' configuration during landing.

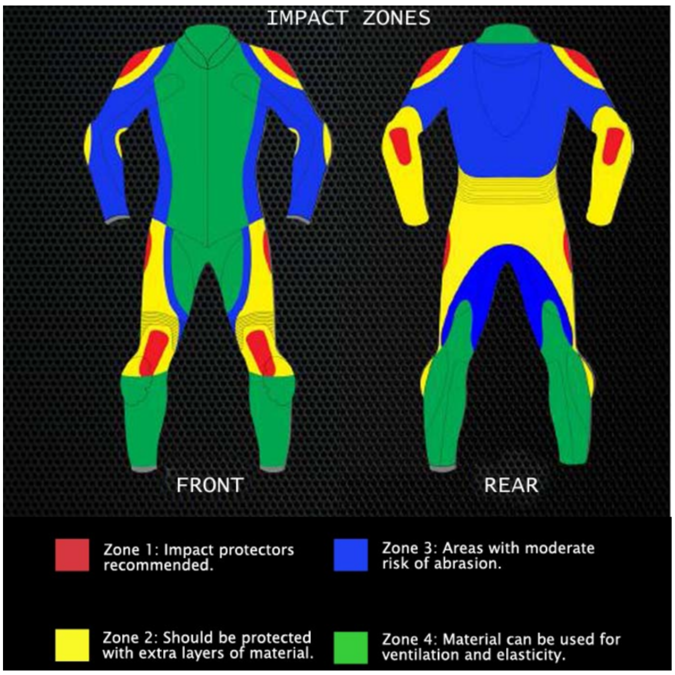

Figure 11.5: Critical parts on the human body in impact and during slide [4]

[4]URL `http://www.webbikeworld.com/Motorcycle-clothing/ce-certified-vs-approved.htm` [cited 23 June 2016]

11.5 VFR

The aircraft will be flying under VFR, Visual Flight Rules. Visual flight rules are a set of regulations under which a pilot operates an aircraft in weather conditions generally clear enough to allow the pilot to see where the aircraft is going. Specifically, the weather must be better than basic VFR weather minima, i.e. in visual meteorological conditions (VMC), as specified in the rules of the relevant aviation authority. The pilot must be able to operate the aircraft with visual reference to the ground, and by visually avoiding obstructions and other aircraft [FAA (2014)]. The Velo-E-Raptor is a sport and a hobby and thus will not be required to fly during the night. In order to fly under these visual flight rules it has to be daytime. In the Netherlands this daytime is defined as the period starting 15 minutes before sunrise to 15 minutes after sunset[5]. When flying outside of these regulations the Instrumental Flight Rules apply. This requires more instruments and more certification from both the pilot and the aircraft.

11.6 Reliability, Availability, Maintainability

It is essential to keep the Velo-E-Raptor in a proper and well-functioning state. Inspection after each flight and before takeoff is important to guarantee the safety of the pilot. In this section some important aspects of these procedures are discussed. A full investigation into the reliability of each part has to be conducted in a later design phase.

11.6.1 Dacron foil with Mylar coating

Part of the wing is made of the Dacron and Mylar film, more specifically, the trailing 75% of the chord is made of this film. Dacron is known for its sensitivity to UV radiation[6]. When exposed to UV radiation the cloth becomes brittle and might start tearing. The Dacron fibers have been painted black to protect them against this UV radiation. Furthermore, the Mylar film also protects these fibers against UV radiation and increases the operational life of the film[7]. To increase the operational life of this part of the Velo-E-Raptor it is advised to keep the wings out of the sunlight when the aircraft is stored. Dacron has an operational lifespan of 2000 hours after which it is advised to replace the material[8]. The material is commercially available and thus can be replaced by the pilot or flightclub to which the Velo-E-Raptor belongs. It is highly important to keep this foil up to date since a failure of this foil will most likely result in a crash.

11.6.2 Carbon Fiber Degradation

Carbon fiber is subjected to degradation. According to Kumar *et al.* (2002) matrix dominated properties are affected the most, with the transverse tensile strength decreasing by 29% after only 1000 h of cyclic exposure to UV radiation and condensation. While, the longitudinal fiber-dominated properties are not affected for the exposure durations investigated, it has been noted that extensive matrix erosion would ultimately limit effective load transfer to the reinforcing fibers and lead to the deterioration of mechanical properties even along the fiber dominated material direction. Furthermore, after 1000 hours the material becomes 1.25% lighter due to this degradation. It is recommended to investigate a coating which protects the carbon fiber against these UV radiations and condensation. As long as a coating like this is not implemented the Velo-E-Raptor has to be checked after 500 flight hours to establish the strength of the carbon fiber. The delamination temperature of 120° will not be reached during normal flight operations. It is highly important to keep this structure up to date and inspected since failure of the structure mid flight will most likely result in a fatal accident.

11.6.3 Propeller Motor

The propeller motor is brushless. Brushless BLDC engines have an expected life of 10000 hours[9]. The motor is commercially available by Hobbyking as indicated in the Power and Performance chapter. Keeping the propeller up to date is important but not critical. When the motor fails mid flight the pilot can still soar home and land the aircraft so that no fatal accident occurs.

[5]URL http://wetten.overheid.nl/BWBR0005775/2012-01-01#HoofdstukI_Artikel1 [cited 22 June 2017]
[6]URL https://www.willswing.com/hang-gliders/hang-glider-sailcloth-information/ [cited 23 June 2017]
[7]URL http://www.jkasailmakers.co.uk/Sail20Fabrics20Explained.pdf [cited 23 June 2017]
[8]URL https://northsails.com/sailing/resources/cruising-sail-durability [cited 22 June 2017]
[9]URL http://www.nmbtc.com/brushless-dc-motors/why-brushless-motors/ [cited 20 June 2017]

11.6.4 Batteries

The batteries are supplied by Geiger (2009), a German company. These batteries have a lifetime of 300 to 500 cycles. It is advised to replace the batteries after 300 cycles. These batteries are commercially available by Geiger engineering and can easily be replaced by the pilot before or after flight. Geiger provides a warranty of 12 months for their batteries. Keeping the batteries up to date also is important but not critical. When the batteries are worn down the flight mission is shorter and the power might change but no critical accident will occur. There is no reason to assume dangerous accidents with the batteries when they are worn down.

11.6.5 Wings

As for the wings, it is important to keep them clean and smooth. As filth and other things collect on the wing the aerodynamic properties decline and vibrations occur due to the turbulent flow around these areas. This wears down the wings of the Velo-E-Raptor. When the wings are well-maintained, they are not a limiting the operational life of the Velo-E-Raptor. Keeping the wings in good shape is important and might be critical. A takeoff or landing might have to be performed other than expected by the pilot due to the higher stall speed which might result in an accident during these phases.

11.6.6 Actuators

Linear actuators are used for the control surfaces. These linear actuators are commercially available and can be replaced when broken. If one actuator fails during flight the pilot can still land the aircraft and replace this actuator. Keeping the actuators in good shape is important but not critical. A failure of an actuator does not make the aircraft unflyable and the pilot is thus able to land the aircraft and replace the actuator without a fatal accident occurring.

11.6.7 Propeller

The propeller is manufactured by Geiger (2009). For propellers it is hard to determine what the lifespan will be. In the manual from the Geiger propeller it is stated that the propeller has to be inspected before and after flight. If the pilot sees no anomalies during inspection, the propeller can be used for another flight. If the pilot is aware of a pebble hitting the propeller or high grass, but there is no visual damage, the propeller should still be sent back for inspection. In the case of visual damages, the propeller should also be sent back to Geiger for inspection. Keeping the propeller in good shape is important and critical. A propeller failure mid flight might result in pilot injury as discussed earlier in this chapter.

12 | Market Analysis

In order for the Velo-E-Raptor to succeed, its market position has to be understood and reinforced. Therefore the market in which the Velo-E-Raptor will compete is analyzed. Below, the inherent strengths of this concept are explained in Section 12.1. The costs related to the development, production and use of the Velo-E-Raptor are also outlined. Competing aircraft types are also evaluated in Section 12.2. This uncovers the strengths and weaknesses of the Velo-E-Raptor when compared to these other aircraft. Lastly, the basis for the business plan is laid out. The return on investment, operational profits and a brief marketing plan are summarized in Section 12.3.

12.1 The Velo-E-Raptor

12.1.1 Design Goals

The Velo-E-Raptor is designed to provide a flying experience which is accessible and gives a feeling of freedom. Several key goals are achieved by the Velo-E-Raptor. Firstly, the aircraft had to be accessible and available for any novice pilot. Therefore, no previous flying experience or any pilot training is required to fly the Velo-E-Raptor except for basic training with the Velo-E-Raptor itself. This is made possible by the low weight of the aircraft, preventing it from being restricted by a multitude of regulations, and the fly-by-wire system, which allows the flight computer to correct or limit any errors made by the pilot. It also allows new pilots to safely train flying the aircraft, for example by having instructor guidance via remote control.

A second goal was for the flying experience to be as free as possible. Again, this is enabled by the low weight and the foot-launch capabilities of the aircraft. A pilot can take off from virtually any location and fly in whichever direction he or she desires, without the need of an airfield. The only restriction are given by Dutch law.

Thirdly, the Velo-E-Raptor requires muscle power from the pilot. By coupling the power delivered by the propeller to the pedalling power put in by the pilot, flying the Velo-E-Raptor becomes an intensive activity, which could easily be transformed in an air sport. Such possibilities include, but are not limited to, endurance competitions, races and aerobatic events. The latter option is further motivated by the fact that the Velo-E-Raptor is designed to be able to perform high-speed, high-g maneuvers, being certified of loads up to 6g.

The combination of these aspects in one package make the Velo-E-Raptor a very attractive product for any potential pilot and allow it to create its own, new market segment of human-powered air sports whilst simultaneously competing in other, related markets. It must be noted that there are some weaknesses which should be focused on in further design phases as well, mainly related to the foot-launch and landing capabilities without support of the aircraft. Reducing these weaknesses will increase the competitiveness of the Velo-E-Raptor in the current mrket.

12.1.2 Cost Breakdown

As there was uncertainty on how to do a cost estimation, it was chosen to include the salaries of the employees as described in Chapter 16 and the material cost of the carbon fiber multiplied by a factor of 10. For testing purposes, it is assumed that the value of four Velo-E-Raptors are used. Due to knowledge gained throughout the development, it is also assumed that after testing the factor applied to the cost of a Velo-E-Raptor decreases to 7.5. The specific cost of carbon fiber, including its production process, is taken from an article by Bader (2002), while the salary costs come from section 16.1. The total cost can be found in Table 12.1

12.2 Competing Market

Currently, there are two major types of aircraft whose role, at least partially or for some pilots, could be taken over by the Velo-E-Raptor. These aircraft types are sailplanes and hang gliders. Below, the current state of these

Table 12.1: Costs and their origins

Parameter	Unit	Value
Weight of carbon fiber	kg	48.08
Specific cost of carbon fiber	€/kg	157
Total production cost	€	7 549
Production costs with safety factor	€	75 486
Total salary costs	€	666 600
Total cost	€	742 086

aircraft markets will be discussed. These types of aircraft as well as two aircraft, the Ruppert Archaeopterix and the Aériane Swift, similar in role to the Velo-E-Raptor will also be compared with the Velo-E-Raptor.

12.2.1 Sailplanes

A sailplane is a fixed-wing, typically unpowered aircraft. Sailplanes in the Netherlands are usually launched with a winch, selfstarter or with the use of another airplane. By the use of thermals, it can extend its flight duration from several minutes to hours, dependent on the skill level of the pilot. Sailplanes are often in possession of clubs where members can use the planes available. Pilots need several dozens of training flights before they can fly solo and need to stay within range of the home airfield. In the Netherlands, there are about 40 of these clubs and 4000 pilots[1]. There are three leading manufacturers in Europe, producing about 240 gliders a year collectively. These gliders usually cost about €80 000,- for the simple, unpowered one-seater models.

Most users fly sailplanes as a relaxing activity. Pilots fly these aircraft for the feeling of challenging gravity by staying airborne as long as possible using thermals. Furthermore, the activity feels safer than flying with a hang-glider. The Velo-E-Raptor could challenge the sailplane in this role. If the cost of the Velo-E-Raptor remains below or at least comparable to the cost of regular sailplanes, it could serve as a more mobile alternative, both on the ground as in the air which is more easily accessible too.

12.2.2 Hang Gliders

A hang glider is a non-motorized foot-launched aircraft that consists of frame covered with sailcloth to form a wing. The pilot hangs in prone position under the wing inside a harness. The hang glider is controlled by shifting the body with respect to the control frame. If thermals are being used properly, thousands of feet of altitude can be gained and pilots can soar for hours. Learning the basics on flying hang gliders takes several days. In the Netherlands, hang-gliding is not a very popular activity, at it is usually practiced in mountainous regions. Only about 20 new hang gliders are sold in the Netherlands yearly, as the market saturation is currently quite high. The cost of new hang gliders typically range between €4 000,- to €8 000,-.

The hang gliding market has been in a decline in the Netherlands since the 1990's. The average user age has also increased significantly. Most pilots enjoy hang gliding because of the experience of freedom it gives them, more so than other aircraft. Additionally, the transportability of the aircraft is a bonus over, for example, flying sailplanes, but is still not as good as in the case of paragliding. A prime concern for hang gliders is safety. The pilot is minimally protected from its environment, so a predictable and reliable glider is desired. Improvements to the glide ratio also allow to increase the performance and flight time of hang gliders. In this case, the Velo-E-Raptor could fill the same desire of being free as a bird and having a transportable system, although less so than with a hang glider. It also provides a significant increase in both pilot safety and performance. Because of the significantly higher costs of the Velo-E-Raptor, it mainly focuses on hang gliding pilots which are prepared to spend more in exchange for a strongly enhanced gliding experience.

12.2.3 Archaeopterix and Swift

Next to the more familiar aircraft described above, two more unique aircraft similar in role to the Velo-E-Raptor exist. These are the Ruppert Archaeopteryx and the Aériane Swift. Both designs bridge the gap between sailplanes and hang gliders. They are discussed separately below.

[1] URL `http://www.knvvl.nl/afdelingen/zweefvliegen/` [cited 2 May 2017]

Ruppert Archaeopteryx

The Archaeopteryx is a foot-launched hang glider with a configuration close to conventional airplanes. The aircraft is essentially a small, minimalistic sailplane which can be carried on one's shoulders and launched by foot[2]. There are three versions available. The standard version includes the minimum for the functioning of the product, which is the wing, tailplane, pilot seat, controls and safety system. The race version adds a cockpit fairing and windshield, protecting the pilot from the environment to some extent and improving aerodynamic performance. The electric version further adds electric propulsion, but can only be used for wheeled take-off[3].

Despite good performance and a mature design, the Archaeopteryx never saw large success. Only 18 models have been built so far since the product was made available in 2010. The Archaeopteryx is expensive, costing between €77 000,- to 100 000,- depending on the version. This more than conventional hang gliders. The performance is between that of regular hang gliders and sailplanes, while controlling the aircraft is very similar to piloting a sailplane. Because of this, most potential customers choose to fly sailplanes instead, because they are generally more available at local clubs and have better performance, despite the foot launch capability of the Archaeopteryx. The likely reason for the lack of success of the Archaeopteryx is limited accessibility. In order to fly the powered version of this aircraft, basic pilot licensing is required. Furthermore, the Archaeopteryx is relatively easy to transport, when compared to conventional sailplanes.

Aériane Swift

The Swift is a direct competitor of the Archaeopteryx. It is a single-seater swept wing aircraft, conceptually very close to the Archaeopteryx[4]. It is also foot-launched and controlled like normal aircraft, and thus falls between hang gliders and sailplanes. Multiple versions of this aircraft are produced: a standard version, a version with a fairing and windshield, a version which further adds a combustion engine and one which uses an electric engine instead[5]. Again, the powered version is not able to perform foot-launched take-off. Despite having lower gliding performance, the Swift is a lot more successful than the Archaeopteryx, with at least 138 models sold[6]. This is due to significantly lower costs, ranging from €25 750,- to 42 000,- depending on the version, where the version with combustion engine is the most expensive. In order to fly the powered aircraft, a pilot license is required. It is because of the significantly lower costs that the Swift manages to fill most of the market for foot-launched sailplanes. Still, this does not lead to large production volumes as the demand is limited.

The Velo-E-Raptor could compete with both the Archaeopteryx and the Swift by providing the pilot with a more free, thrilling and sportive experience, instead of the sailplane-like experience offered by the alternatives. It also offers increased accessibility and mobility. The Velo-E-Raptor allows for foot-launching and landing when using the powered vehicle.

12.3 Return on Investment

In order for the Velo-E-Raptor to be a economically viable product to develop and produce, there must be a return on investment on the development and production of the aircraft. As mentioned in Section 12.1.2, first the costs for the development of the aircraft have to be accounted for. The production costs for a single aircraft in this stage are estimated to be €75 486. Assuming that for development, the equivalent of four Velo-E-Raptors are built, in combination with the aforementioned salaries of €666 600 over this 5 year period, the initial investment costs can be estimated. The costs of acquiring the necessary tooling is assumed to be €250 000. This assumption motivated as it deemed likely that a manufacturer of the Velo-E-Raptor would already have a significant amount of the necessary experience, equipment and factory space for the production of the Velo-E-Raptor. Thus, the investments to be made before production of the aircraft can commence is estimated to be €1 218 542.

During production, a lower production cost of €56 614 can be assumed, as explained in Section 12.1.2 due to a more streamlined process. The production time of a single Velo-E-Raptor is likely to be relatively long, mainly limited by the curing time of composite parts. However, production can commence on the next product as the previous one is curing. Because of this, a production volume of two Velo-E-Raptors per month is achieved. For the production of the Velo-E-Raptor, a different set of employees is required than for the development phase as mentioned in Chapter 16. Instead, one manager and two technicians will be hired. Also, one engineer will be hired part-time, in order to solve potential issues. This leads to a yearly salary cost of €225 000. Using these

[2] URL `https://www.ruppert-composite.ch/#wk-304e` [cited 1 May 2017]
[3] URL `https://en.wikipedia.org/wiki/Ruppert_Archaeopteryx` [cited 1 May 2017]
[4] URL `http://www.aeriane.com/products/aircrafts/swift/swiftlight/` [cited 1 May 2017]
[5] URL `http://www.icaro2000.com/Products/Products.htm` [cited 1 May 2017]
[6] URL `http://www.ultralight-glider.fr/fr/` [cited 1 May 2017]

values, the return of investment, calculated as the ratio between the net profit and the investment costs can be calculated. This is done assuming that the number of Velo-E-Raptors sold is equal to the number produced at all times. This is a big assumption, based on the current state of the relevant market, hence the price of the Velo-E-Raptor should be kept low in order to maximize sales. The return of investment versus the number of aircraft produced is shown in Figure 12.1 for the sales prices of €90 000, 100 000 and 110 000. It can be seen that the Return on Investment is higher for higher sales prices of the Velo-E-Raptor. Therefore, a price of €100 000 is recommended. It should be noted that interest on the costs in not accounted for in this calculation.

Figure 12.1: The relationship of return on investment and number of aircraft produced

Using the values above, a monthly operational profit can be estimated as well. This value is simply the difference between the monthly income and monthly expenses. Using a sales price of €100 000, it is found that the profit margin per aircraft sold is €34 011. Since in the method above two aircraft are produced and sold each month, the monthly operational profit is simply twice this amount, €68 022. Logically, this scales linearly with the sales price for each aircraft. Thus, if the aircraft are sold for €90 000, the operational profit is €48 022 and in the case of a product price of €110 000, the operational profit is €88 022. Again it should be noted that, despite the higher operational profit, it is likely that supply will exceed demand if the asking price is increased too much. The most ideal product price of the Velo-E-Raptor has to be investigated further in future cost estimations and market analyses.

13 System Lay-Out

In this system lay-out chapter, the relation between subsystems is explained with use of diagrams. Figure 13.1 gives an overview of the physical connection between the parts. As the physical connection is in both ways, the connecting lines have two arrows. It can be noticed that the airframe is connected to most parts.

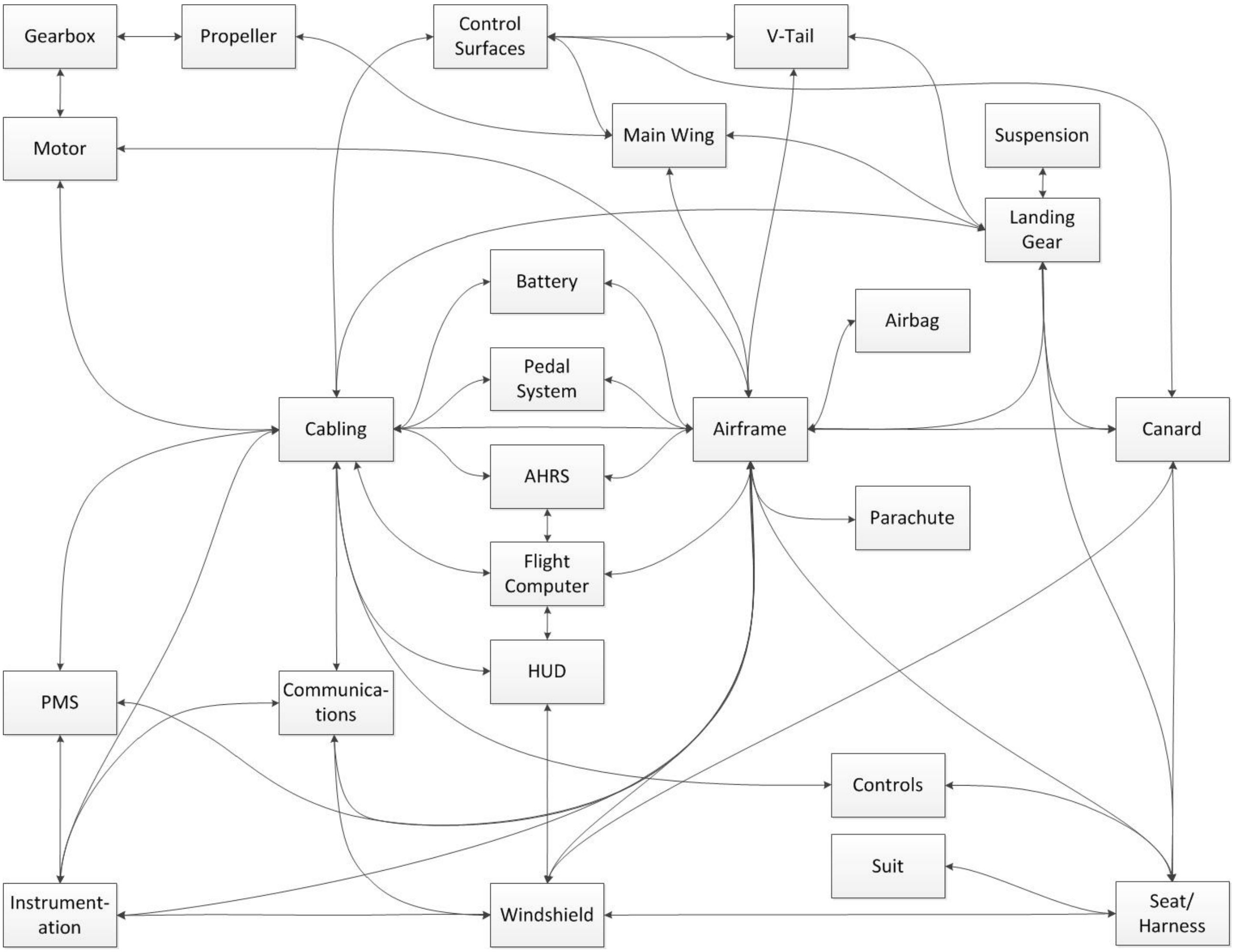

Figure 13.1: Hardware diagram

The second diagram is the software diagram (Figure 13.1). This gives a representation of the processing relationship between the different subsystems. The AHRS and Controls are the input of the flight computer. The flight computer processes these inputs and sends the information and signals to the power management system, instrumentation, and head-up display.

Finally, a data handling and communication flow diagram is presented in Figure 13.3. This gives a detailed overview of the interaction between pilot and the products subsystems. The flight computer is important for the processing of the input data and presenting useful outputs to the pilot.

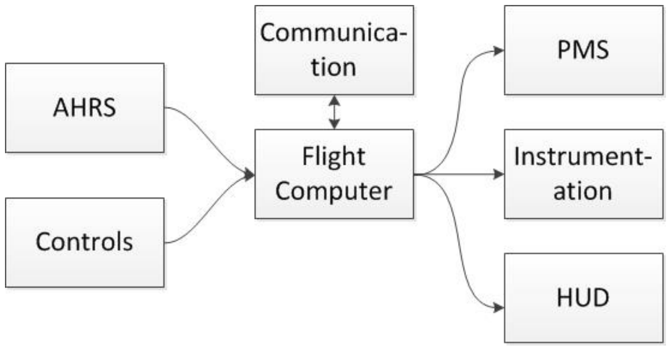

Figure 13.2: Software diagram

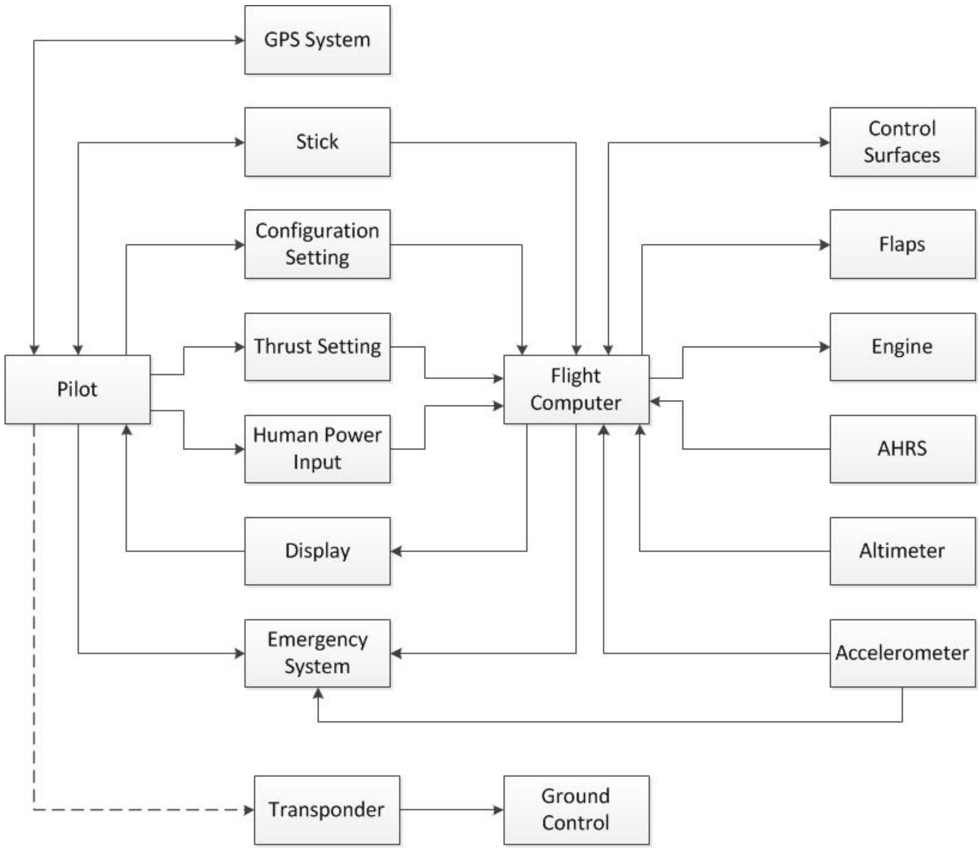

Figure 13.3: Datahandling and communication flow diagram

14 Results

In this chapter the final design will be discussed and checked against the predefined requirements. Subsequently, it will be reviewed whether it is actually possible to create such an aircraft in the feasibility analysis.

14.1 Layout and Mass

The final design is a 100.5 kg aircraft that can be launched in multiple ways. The mission consists of 30 minutes sustained flight, or a shorter period at higher speeds, when possibly performing aerobatics. 52 kg of the weight is made up by the structure, ensuring its integrity up to a maximum load factor of 6. Safety measures are taken and there is a flight computer present. The exact layout and dimensions were the result of multiple iterations. Consequently, a model is made in CATIA. This model is then used as blueprints for the next design phase. These technical drawings illustrate the final dimensions of the Velo-E-Raptor very accurately and are shown in Appendix D. The general layout is shown in Figure 14.1. The complete mass distribution can be seen in Table 14.1.

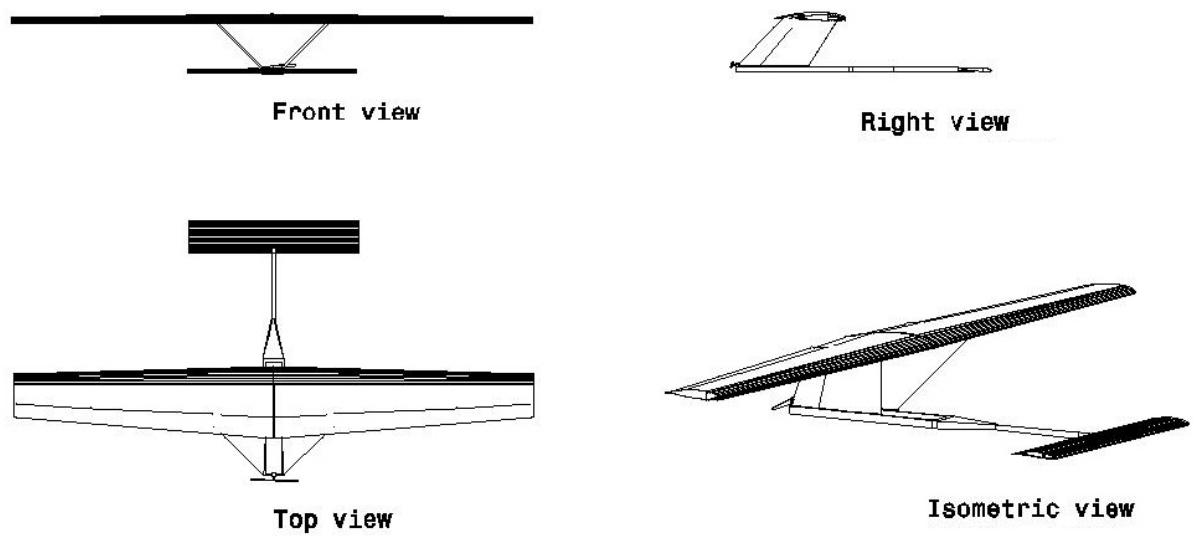

Figure 14.1: Front, right, top and isometric view of the Velo-E-Raptor

In order to meet the requirement stating a maximum weight of 70 kg several parts will be excluded from the general aircraft when going through certification. These parts are not essential and can then be added on again before actual flight. These parts are: the battery, windshield and components for safety and comfort such as the parachute. The maximum takeoff weight is 190.5 kg.

14.2 Compliance

The most important requirements for the Velo-E-Raptor are shown in Table 14.2, as is their compliance. As can be seen, none of the primary requirements have not been met. Some however, cannot be determined definitely, and some others require additional explanation. These will now be discussed shortly.

Table 14.1: Mass Budget

Item	**m**
-	kg
Structures	
Wing	24
Canard	3.5
Vtail	8
Fuselage	8.5
Rest	8
Power	
Propeller	1
Motor	2.5
Battery	16*
Gearbox	1.5
Rest	1.5
MOS	
Minimum	3
Additional	14*
Control	
Servos	6
Rest	1
Aerodynamics	
Windshield	2*
Pilot	90
Total	190.5

*Can be excluded to meet the 70 kg requirement

VER-REG-01, VER-REG-02 In order to comply with the regulations, the Velo-E-Raptor must be foot-launched and have a maximum weight of 70 kg. As mentioned, the regulations contain some gray areas, making it difficult to predict whether the aircraft will cause problems after it is manufactured. The current design requires parts to be attached to the aircraft increasing its weight. Next to this an engine is used for takeoff and wheels are included, both discussed in chapter 10.

VER-SUS-01 The requirement regarding the generated noise has been altered since the original list of requirements. The original requirement stated that a noise level of 60 dB(A) at maximum should be present at 1 m distance. This requirement was given a value based on the original need for an undetectable aircraft at 200 ft (61 m), which was defined using the Lockheed YO-3. Later research has shown however that this value is not according to the amount of noise generated by this aircraft, and thus the requirement has been altered to the actual value, 64 dB(A) at 10 m. The Velo-E-Raptor is expected to generate 60 dB(A) at this distance, thus the requirement is met.

VER-SUS-02 Because the center of gravity of the pilot will be near that of the aircraft, any pilot size and weight is acceptable regarding stability and control. The length is limited by the size of the harness and distance of the pedals, but there is room for deviations in length, making that the requirement is met.

VER-SAF-07 The amount of critical failures within a certain amount of flight hours is difficult to estimate. The current design implements multiple safety measures to ensure the pilot's safety. Whether the given number will be met is not only dependant on the design however, but also the manner of construction and the people flying the aircraft.

Table 14.2: Compliance matrix

Requirement	Description	Compliant
VER-REG-01	The Velo-E-Raptor shall comply with European Regulations	Maybe
VER-REG-02	The Velo-E-Raptor shall comply with Dutch Regulations	Maybe
VER-SUS-01	The Velo-E-Raptor shall have a noise emission no higher than 64 dB(A) at 10 m distance	Yes
VER-SUS-02	The Velo-E-Raptor design shall be adjustable/suitable for different pilot characteristics	Yes
VER-SUS-05	The materials used for the Velo-E-Raptor shall not be hazardous to the environment	Yes
VER-SAF-01	The Velo-E-Raptor shall have a fail-safe system for emergency landing	Yes
VER-SAF-02	The pilot shall be able to fly and land safely when the motor fails	Yes
VER-SAF-03	The Velo-E-Raptor shall be a stable aircraft during all operations	Yes
VER-SAF-05	The Velo-E-Raptor shall be a controllable aircraft during all operations	Yes
VER-SAF-07	The Velo-E-Raptor shall have at most 20 critical failures per 100,000 flight hours	Maybe
VER-SAF-08	The Velo-E-Raptor shall not harm the pilot during normal operations	Yes
VER-SAF-11	During normal operations the legs of the pilots shall experience excessive force	Yes
VER-PER-01	The Velo-E-Raptor shall be able to reach a maximum airspeed of at least 75 kts (39 m/s)	Yes
VER-PER-02	The Velo-E-Raptor shall have a stall speed of at most 25 kts (13 m/s)	Yes
VER-PER-03	The Velo-E-Raptor shall have a takeoff length of at most 50 m	Yes
VER-PER-05	The Velo-E-Raptor shall have sufficient electrical energy to sustain flight for 30 minutes without the use of human power	Yes
VER-OPS-01	The Velo-E-Raptor shall be easily transportable	Yes
VER-OPS-02	The Velo-E-Raptor shall be easily maintainable	Yes
VER-OPS-07	It shall be possible to assemble the Velo-E-Raptor by an average person within at least 45 minutes	Yes
VER-OPS-08	It shall be possible to disassemble the Velo-E-Raptor by an average person within at least 45 minutes	Yes
VER-OPS-09	The main structure of the Velo-E-Raptor shall have a lifetime of at least 15 calendar years under normal operational circumstances	Yes
VER-OPS-11	The Velo-E-Raptor power output shall be controllable during flight	Yes

14.3 Feasibility Analysis

All in all, it seems feasible to meet all the requirements and actually manufacture a working Velo-E-Raptor. There are some factors that have to be investigated further, these are discussed in Chapter 16. Furthermore, the expected behaviour in some situations is precarious. Takeoff and landing could show to be more difficult then expected. If so, this would have a large impact on the feasibility of the design. Finally, the material used for the skin has to be extremely thin, which could cause problems during manufacturing and during impact.

15 Conclusion

The final design of the Velo-E-Raptor shows that it is feasible to develop an electrically assisted, human powered, next generation hang glider. It has become a very safe aircraft, by measures like airbags, a parachute, support wheels, and much guidance for the pilot. This is all achieved without losing the objective of flying free as a bird. The final Velo-E-Raptor design is, namely, capable of aerobatic maneuvers up to +6g, which, in combination with the prone flying position, delivers an unprecedented flight experience. Also, the sports aspect is possible, with the pedal system that is used as direct power control.

Regarding the driving requirements, none of them is definitely not met. Requirements, where more attention have to be paid to in further research, are the foot-launched and the empty mass of 70 kg requirement. The question is whether the versatile option of adding a battery pack is allowed, as well as if support wheels are allowed in the foot-launched case.
Important requirements that are met are the noise requirement, the stall speed, the takeoff length, the power control by pedaling, the 30 minutes unassisted flight, and the fail-safe landing mechanism. The noise signature is determined to be as silent as 30 dBA at 250 m, as silent as a library. The stall speed of 17 kts (8.75 m/s) also well satisfies the 25 kts (12.9 m/s) requirement. The Velo-E-Raptor can take off within 30 m, well below the 50 m requirement.

The current design is determined to be a canard configuration with a V-tail leading to a higher placed main wing. The pilot lies in a prone position and has a push propeller behind him attached to the structure. On the canard, a skid is implemented, which, in combination with the support wheels, makes it possible to land without the pilot's legs in case of emergency.

16 Recommendations for Further Development

16.1 Post DSE Activities

Although the design presented in the preceding chapters is viable, it does not contain the level of detail needed for production. In this chapter, an outline of the activities needed for production to start is given, based on the business plan in Chapter 12. This outline is split between a Design & Development flowchart in section 16.1.1, and a Gantt chart in section 16.1.2.

16.1.1 Project Design & Development Logic

As it is unlikely that the design will be developed by the team, the first part of the PD&D diagram is an analysis of the technical feasibility of this report. While it is the opinion of the team that this is not necessary, and the design as presented is feasible, it is included in the PD&D for sake of completeness. After this analysis, the development of the design can continue. This includes designing the connections between the wing sections, V-tail, canard, and body, as well as physical tests being performed on the systems and subsystems, as shown in Figure 16.1

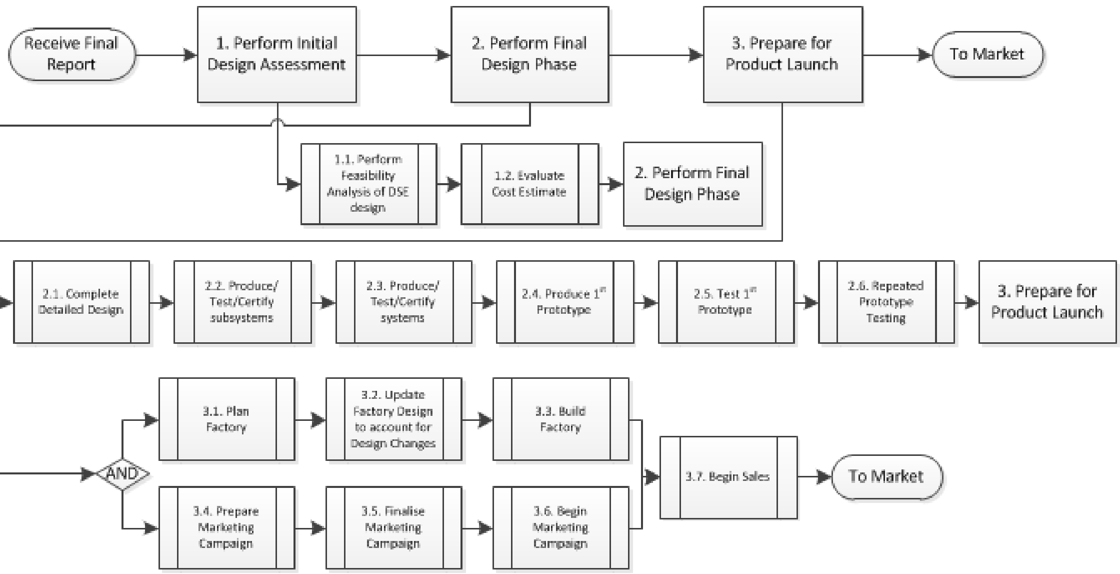

Figure 16.1: The project design & developement logic, showing the major blocks involved in preparing the design for sale

16.1.2 Project Gantt Chart

The Gantt chart uses the same numbering as Figure 16.1, but also shows the time relations between them. It was developed with Pon in mind, as the company has displayed an interest in the project. As such, the starting date is the 8th of August 2017, when the design is presented to Pon and covers a period of 5 years, as this was the estimated time to market. It includes an estimate of the costs, excluding the cost of building the factory and material costs. The two blocks, 3.2 and 3.5, are included in the case in which during the repeated prototyping (2.6) significant changes in the design happen. Additionally, although the repeated prototyping is planned for 16 months, this step is critical for the safety record of the product and can take longer if needed. Additionally, there is an estimated cost based on the working hours of the employees involved, based on a workforce of three engineers ($70 000 annual salary), two technicians ($50 000 annual salaries) and one manager ($90 000 annual salaries).

ID	Task Name	Duration	Cost
0	**Post DSE Activities**	**60 mons**	**$746.410,26**
1	**1 Perform Initial Design Assement**	**0,5 mons**	**$5.769,23**
2	1.1 Peform Feasibility Analysis of DSE Design	1 wk	$2.692,31
3	1.2 Evaluate Cost Estimate	1 wk	$3.076,92
4	1.3 Perform Initial Design Assement Complete	0 days	$0,00
5	**2 Perform Final Design Phase**	**32 mons**	**$477.948,72**
6	2.1 Complete Detailed Design	4 mons	$64.615,38
7	2.2 Produce/Test/Certify subsystems	2 mons	$15.384,62
8	2.3 Produce/Test/Certify systems	2 mons	$15.384,62
9	2.4 Produce 1st Prototype	4 mons	$30.769,23
10	2.5 Test 1st Protoype	4 mons	$34.871,79
11	2.6 Repeated Prototype Testing	16 mons	$316.923,08
12	2.7 Perform Final Design Phase Complete	0 days	$0,00
13	**3 Prepare for Product Launch**	**43,5 mons**	**$262.692,31**
14	3.1 Plan Factory	3 mons	$32.307,69
15	3.2 Update Factory Design to account for Design Changes	1 mon	$5.384,62
16	3.3 Build Factory	14 mons	$0,00
17	3.4 Prepare Marketing Campaign	4 mons	$27.692,31
18	3.5 Finalise Marketing Campaign	1 mon	$6.923,08
19	3.6 Begin Marketing Campaign	27,5 mons	$190.384,62
20	3.7 Begin Sales	0 mons	$0,00

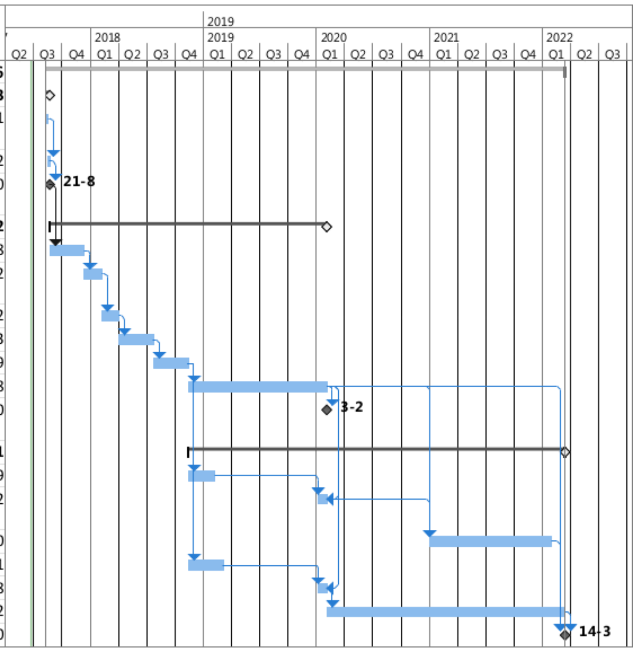

Figure 16.2: Gantt chart detailing activities that occur after the end of the DSE

16.2 Other Design Options

Below are a number of design options which have not yet been implemented in the design, but still remain a feasible option. Due to a lack of resources, knowledge or detailed knowledge of the design, these could not be investigated in further detail yet. Therefore it is recommended to revisit these topics in further design efforts.

1. The addition of winglets, which could:
    - improve the span efficiency factor
    - increase performance by reduction of induced drag
    - reduce the wingspan of the design
2. A variable taper Scheumann Planform, as discussed in Section 5.3.
3. Windtunnel tests and CFD analysis to improve estimations of aerodynamic characteristics.
4. The yaw stability is on the edge of neutral. This can be made more stable by implementing a dihedral or sweep angle, taking into account the effect on other aspects of the aircraft.
5. The rotational damping due to air can be investigated to find the accelerations that can be achieved. This will give more insight in the controllability performance.
6. Perform a detailed material analysis on composite sandwich panels, and local stresses induced by the orientation of carbon fiber layers.
7. Investigate composite manufacturing techniques to gain a comprehensive understanding of the fabrication possibilities.
8. Analyze the stresses present in each assembly joint and estimate the extra material needed in order to prevent failure at these points.

Bibliography

Aarts, M.J.M., Boon, K.M., Bourier, S.J.L.B, Geuens, C.S.E, van der Hulst, R.J.A, van der Maten, J.T., Mink, R.A.A, Nyessen, N.C., Rootliep, T.O., & Schaberg, W. 2017a (May). *DSE- Velo-E-Raptor Group 18 Baseline Report.*

Aarts, M.J.M., Boon, K.M., Bourier, S.J.L.B, Geuens, C.S.E, van der Hulst, R.J.A, van der Maten, J.T., Mink, R.A.A, Nyessen, N.C., Rootliep, T.O., & Schaberg, W. 2017b (May). *DSE- Velo-E-Raptor Group 18 Midterm Report.*

Anderson, J. 2010. *Fundamentals of Aerodynamics.* McGraw-Hill Education.

Bader, M. G. 2002. Selection of composite materials and manufacturing routes for cost-effective performance. *Composites Part A: Applied Science and Manufacturing*, **33**(7), 913–934.

Brown, D., & Ollerhead, J.B. 1971. *Propeller Noise at Low Tip Speeds.* Tech. rept. Air Force Aero Propulsion Laboratory, Hampton, United States of America.

Cammerson, J., Wilson, R., & Wadley, P. 1988. Flight trails of the prone meteor. *NASA.*

Concli, F. 2016. Thermal and efficiency characterization of a low-backlash planetary gearbox: An integrated numerical-analytical prediction model and its experimental validation. *Proceedings of the Institution of Mechanical Engineers, Part J: Journal of Engineering Tribology*, **230**(8), 996–1005. cited By 0.

Cross, J.L. 1984 (July). *YO-3A Acoustics Research Aircraft Systems Manual.* NASA, Ames Research Center.

Deperrois, André. 2013. XFLR5 Analysis of foils and wings operating at low reynolds numbers, 2013. *Guidelines for XFLR5.*

FAA. 2013. *Glider Flying Handbook.* Federal Aviation Administration, U.S. Department of Transportation.

FAA. 2014 (March). *General Operating and Flight Rules.*

Funk, JR., Crandall, JR., Tourret, LJ., MacMahon, CB., Bass, CR., Patrie, JT., Khaewpong, N., & Eppinger, RH. 2002. The axial injury tolerance of the human foot/ankle complex and the effect of Achilles tension. *NCBI.*

Garl, A., Islam Linda, R., & Chowhurdy, T. 2014. Application of fiber optics in aircraft control system & its development. *IEEE.*

Gawande, S.H., Shaikh, S.N., Yerrawar, R. N., & Mahajan, K.A. 2014. Noise Level Reduction in Planetary Gear Set. *Journal of Mechanical Design and Vibration*, **2**(3), 60–62.

Geiger, J. 2009. *Angewandte Sicherheitsprinzipien und Dokumentation zum ultraleichten, elektrischen Antriebssystem für Luftsportgeräte.* Tech. rept. Geiger Engineering, Bamberg, 96052.

George, T, V.S., Deshpande, Sharp, K, & Wadley, H.N.G. 2013. Hybrid core carbon fiber composite sandwich panels: Fabrication and mechanical response. *Elsevier.*

Gill, E. 2013. *Systems Engineering Methods.*

Gossler, S.E., & Murray, E.R. 1996 (May 7). *High efficiency DC motor with generator and flywheel characteristics.* US Patent 5,514,923.

Gudmundsson, S. 2013. *General Aviation Aircraft Design.* Elsevier, Inc. Chap. Appendix C2.

Gur, O., & Rosen, A. 2005. Propeller Performance at Low Advance Ratio. *Journal of Aircraft*, **42**(2), 913–934.

Hansen, E. A., Andersen, J. L., Nielsen, J. S., & Sjøgaard, G. 2002. Muscle fibre type, efficiency, and mechanical optima affect freely chosen pedal rate during cycling. *Acta Physologica*.

Heller, M. F., Challis, J. H., & Sharkley, N. A. 2009. Changes in postural sway as a consequence of wearing a military backpack. *Elzevier*.

Hepperle, M. 2015 (January). *JavaProp - Users Guide*.

Hirokazu, I., & Takao, Y. 1987. Kinetic analysis of the center of gravity of the human body in normal and pathological gaits. *Elsevier*.

Hoerner, Sighard F. 1965. *Fluid-dynamic drag: practical information on aerodynamic drag and hydrodynamic resistance*. Hoerner Fluid Dynamics Midland Park, NJ.

Holawijn, M. 1989. De Militaire bepakking, adviezen over het gewicht qua verdeling. *IZF*.

Hurley, T. J., & Vandenburg, J. M. 2002. *Small airplane crashworthiness design guide*. Tech. rept. Simula Technologies, 10016 South 51st Street. Phoenix, AZ 85044.

ISO 226:2003. 2003. *Acoustics – Normal equal-loudness-level contours*. Standard. International Organization for Standardization, Geneva, CH.

ISO 2533:1975. 1975. *Standard Atmosphere*. Standard. International Organization for Standardization, Geneva, CH.

Kumar, G., Raman, T. Singh, P., , & Nakamura, T. 2002. Degradation of Carbon Fiber-reinforced Epoxy Composites by Ultraviolet Radiation and Condensation. *IEEE*.

Lasagna, P.L., Mackall, K.G., Burcham Jr., F.W., & Putnam, T.W. 1980. *Landing Approach Noise Airframe Measurements and Analysis*. Tech. rept. NASA, Edwards, United States of America.

Marte, J.E., & Kurtz, D.W. 1970. *A Review of Aerodynamic Noise from Propellers, Rotors, and Lift Fans*. Tech. rept. NASA, Pasadena, United States of America.

Megson, T.H.G. 2012. *Aircraft Structures for Engineering Students*. Oxford, United Kingdom: Butterworth-Heinemann.

Mulder, J.A., & et al. 2013. *Flight Dynamics, Lecture Notes*. TU Delft.

Müller, G., & Möser, M. 2013. *Handbook of Engineering Acoustics*. Berlin, Germany: Springer-Verlag.

Saarlas, M. 2007. *Aircraft Performance*. Hoboken, United States of America: John Wiley & Sons.

Steenhuizen, D. 2015 (September). *Aerospace Design & System Engineering Elements II - AE2111-II Aircraft part*.

Steyn, W., & Warnich, J. 2015. The impact of tyre diameter and surface conditions on the rolling resistance of mountain bikes. *Innovate*, **10**.

Theodorsen, T., Stickle, G.W., & Brevoort, M.J. 1937. *Characteristics of Six Propellers Including the High-Speed Range*. Tech. rept. NACA, United States of America.

Whitt, F., & Wilson, D. 1984. Bicycling Science. *Second International Human Powered Vehicle Scientific Symposium*.

Xu, J.H., Song, W.P., & Yang, X.D. 2011. *Effects of Proplet on Propeller Efficiency*. Proceedings of the Sixth International Conference on Fluid Mechanics. Northwestern Polytechnical University, Xi'an, China.

Yeh, Y.C. 2002. *Design Considerations in Boeing 777 Fly-By-Wire Computers*. Tech. rept. Boeing, Seattle, WA 98124-2207.

A Derivation of the Math Used in the Python Tool from Chapter 7

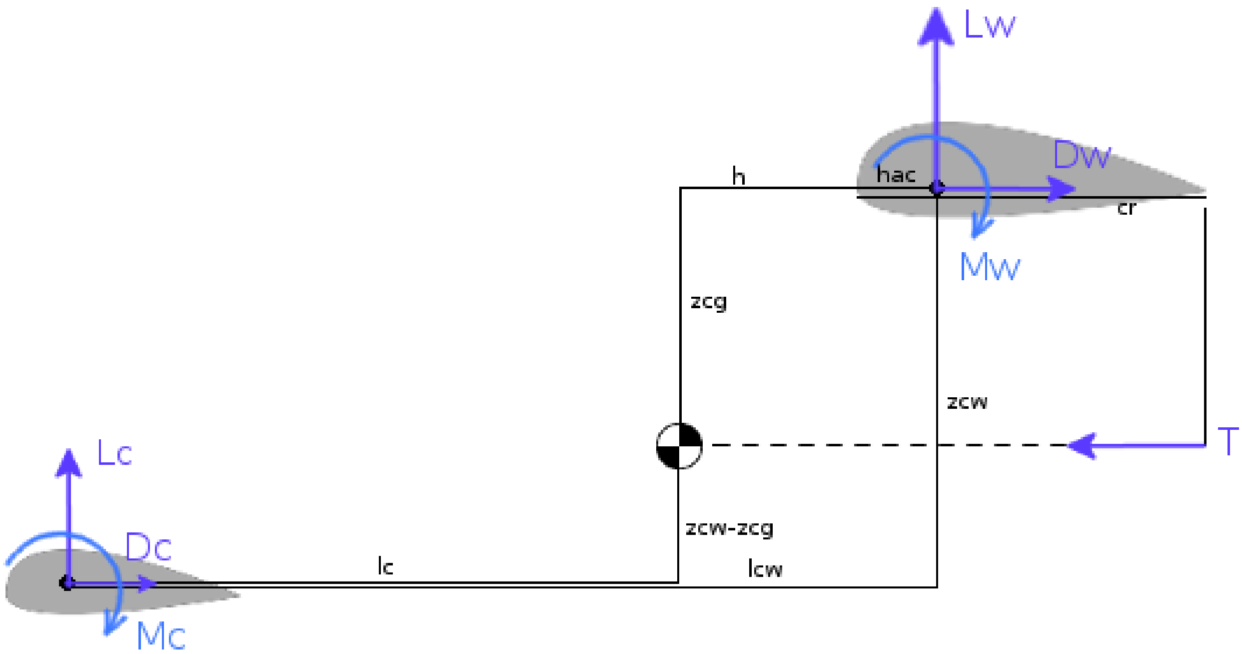

Figure A.1: Figure 7.2 reproduced here for coherence

First, the moments are the center of gravity are summed together:

$$\sum^{\circlearrowright} = M_c + L_c \cdot l_c + D_c \cdot (z_{cg} - z_{cw}) + M_w - L_w \cdot (h + h_{AC}) + D_w \cdot z_{cg} + M_{ac} = M$$

Where:

$$\begin{aligned} M_c &= qS\bar{c}C_{m_c} & L_c &= q\left(\frac{V_c}{V}\right)^2 S_c C_{L_c} & D_c &= q\left(\frac{V_c}{V}\right)^2 S_c C_{D_c} \\ M_w &= qS\bar{c}C_{m_w} & L_w &= qSC_{L_w} & D_w &= qS_w C_{D_w} \\ M_{ac} &= qS\bar{c}C_{m_{ac}} & l_c &= l_{cw} - h - h_{ac} \end{aligned}$$

Dividing by $qS\bar{c}$, one is left with:

$$C_m = C_{m_c} + \left(\frac{V_c}{V}\right)^2 \frac{S_c l_c}{S\bar{c}} C_{L_c} + \left(\frac{V_c}{V}\right)^2 \frac{S_c\,(z_{cg} - z_{cw})}{S\bar{c}} C_{D_c} + C_{m_w} - \frac{h + h_{AC}}{\bar{c}} C_{L_w} + \frac{z_{cg}}{\bar{c}} C_{D_w} + C_{m_{AC}}$$

As $\frac{V_c}{V} = 1$, it simplifies to:

$$C_m = C_{m_c} + \frac{S_c l_c}{S\bar{c}} C_{L_c} + \frac{S_c\,(z_{cg} - z_{cw})}{S\bar{c}} C_{D_c} + C_{m_w} - \frac{h + h_{AC}}{\bar{c}} C_{L_w} + \frac{z_{cg}}{\bar{c}} C_{D_w} + C_{m_{AC}} \tag{A.1}$$

Additionally, the coefficients of lift and drag are dependant on the angle of attack, as shown:

$$
\begin{aligned}
C_{L_c} &= C_{L_{0_c}} + C_{L_{\alpha_c}}\alpha \\
C_{L_w} &= C_{L_{0_w}} + C_{L_{\alpha_w}}\alpha
\end{aligned}
\qquad
\begin{aligned}
C_{D_c} &= C_{D_{0_c}} + C_{D_{\alpha_c}}\alpha \\
C_{D_w} &= C_{D_{0_w}} + C_{D_{\alpha_w}}\alpha
\end{aligned}
$$

Inserting them into Equation (A.1) results in Equation (A.2):

$$
\begin{aligned}
C_m =& C_{m_c} + C_{m_w} + C_{m_{AC}} + \frac{S_c l_c}{S\bar{c}}\left(C_{L_{0_c}} + C_{L_{\alpha_c}}\alpha\right) + \frac{S_c\left(z_{cg} - z_{cw}\right)}{S\bar{c}}\left(C_{D_{0_c}} + C_{D_{\alpha_c}}\alpha\right) \\
&- \frac{h + h_{AC}}{\bar{c}}\left(C_{L_{0_w}} + C_{L_{\alpha_w}}\alpha\right) + \frac{z_{cg}}{\bar{c}}\left(C_{D_{0_w}} + C_{D_{\alpha_w}}\alpha\right) \\
=& \left(C_{m_c} + C_{m_w} + C_{m_{AC}} + \frac{S_c l_c}{S\bar{c}}C_{L_{0_c}} + \frac{S_c\left(z_{cg} - z_{cw}\right)}{S\bar{c}}C_{D_{0_c}} - \frac{h + h_{AC}}{\bar{c}}C_{L_{0_w}} + \frac{z_{cg}}{\bar{c}}C_{D_{0_w}}\right) \\
&+ \left(\frac{S_c l_c}{S\bar{c}}C_{L_{\alpha_c}} + \frac{S_c\left(z_{cg} - z_{cw}\right)}{S\bar{c}}C_{D_{\alpha_c}} - \frac{h + h_{AC}}{\bar{c}}C_{L_{\alpha_w}} + \frac{z_{cg}}{\bar{c}}C_{D_{\alpha_w}}\right)\alpha
\end{aligned}
\tag{A.2}
$$

Commonly rewritten as:

$$
\begin{aligned}
C_m =& C_{m_0} + C_{m_\alpha}\alpha \\
C_{m_0} =& C_{m_c} + C_{m_w} + C_{m_{AC}} + \frac{S_c l_c}{S\bar{c}}C_{L_{0_c}} + \frac{S_c\left(z_{cg} - z_{cw}\right)}{S\bar{c}}C_{D_{0_c}} - \frac{h + h_{AC}}{\bar{c}}C_{L_{0_w}} + \frac{z_{cg}}{\bar{c}}C_{D_{0_w}} \\
C_{m_\alpha} =& \frac{S_c l_c}{S\bar{c}}C_{L_{\alpha_c}} + \frac{S_c\left(z_{cg} - z_{cw}\right)}{S\bar{c}}C_{D_{\alpha_c}} - \frac{h + h_{AC}}{\bar{c}}C_{L_{\alpha_w}} + \frac{z_{cg}}{\bar{c}}C_{D_{\alpha_w}}
\end{aligned}
$$

The other part of the Python tool was the calculation of the neutral point. This is when $C_{m_\alpha} = 0$. In the 1 dimensional model, this happens at a specific value of $\frac{h}{\bar{c}}$, but in this two dimensional model it will be a line in the form of $\frac{h}{\bar{c}} = a \cdot \frac{z_{cg}}{\bar{c}} + b$. For clarity, $h = h_n$ is the horizontal position of the neutral point, while $z_c g = z_n$ is the vertical position.

$$
\begin{aligned}
C_{m_\alpha} = 0 =& \frac{S_c l_c}{S\bar{c}}C_{L_{\alpha_c}} + \frac{S_c\left(z_n - z_{cw}\right)}{S\bar{c}}C_{D_{\alpha_c}} - \frac{h_n + h_{AC}}{\bar{c}}C_{L_{\alpha_w}} + \frac{z_n}{\bar{c}}C_{D_{\alpha_w}} \\
0 =& \frac{S_c l_c}{S\bar{c}}C_{L_{\alpha_c}} + \frac{S_c\left(z_n - z_{cw}\right)}{S\bar{c}}C_{D_{\alpha_c}} - \frac{h_n}{\bar{c}}C_{L_{\alpha_w}} - \frac{h_{AC}}{\bar{c}}C_{L_{\alpha_w}} + \frac{z_n}{\bar{c}}C_{D_{\alpha_w}} \\
0 =& \frac{1}{C_{L_{\alpha_w}}}\left(\frac{S_c l_c}{S\bar{c}}C_{L_{\alpha_c}} + \frac{S_c\left(z_n - z_{cw}\right)}{S\bar{c}}C_{D_{\alpha_c}} + \frac{z_n}{\bar{c}}C_{D_{\alpha_w}}\right) - \frac{h_n}{\bar{c}} - \frac{h_{AC}}{\bar{c}} \\
\frac{h_n}{\bar{c}} =& \left(\frac{1}{C_{L_{\alpha_w}}}\left(\frac{S_c l_c}{S\bar{c}}C_{L_{\alpha_c}} - \frac{S_c z_{cw}}{S\bar{c}}C_{D_{\alpha_c}}\right) - \frac{h_{AC}}{\bar{c}}\right) + \frac{1}{C_{L_{\alpha_w}}}\left(\frac{S_c}{S}C_{D_{\alpha_c}} + C_{D_{\alpha_w}}\right)\frac{z_n}{\bar{c}}
\end{aligned}
$$

B | Stress plots

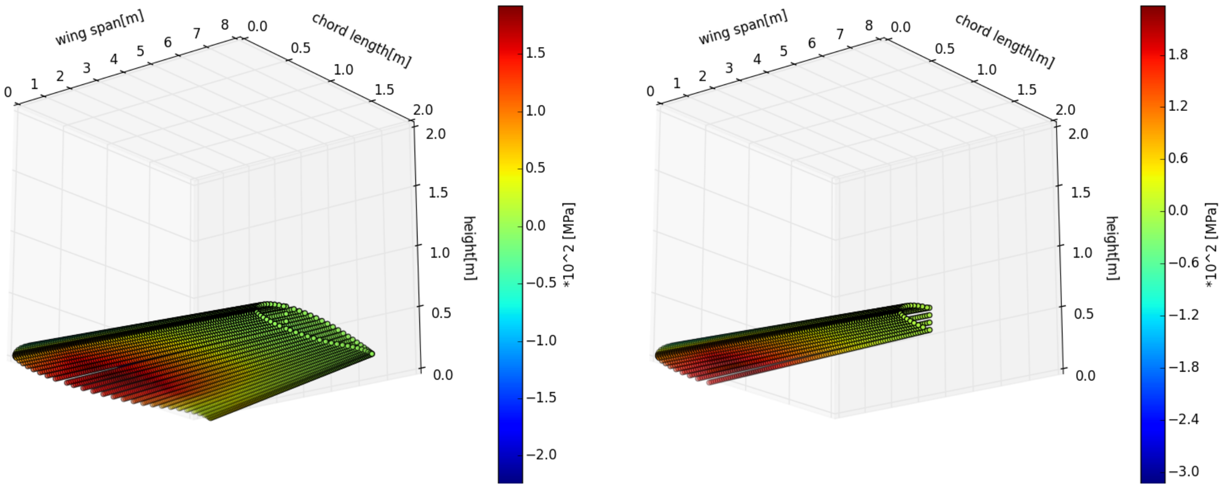

(a) Rigid wing (b) D-cell

Figure B.1: Bending Stresses in the main wing, bottom view

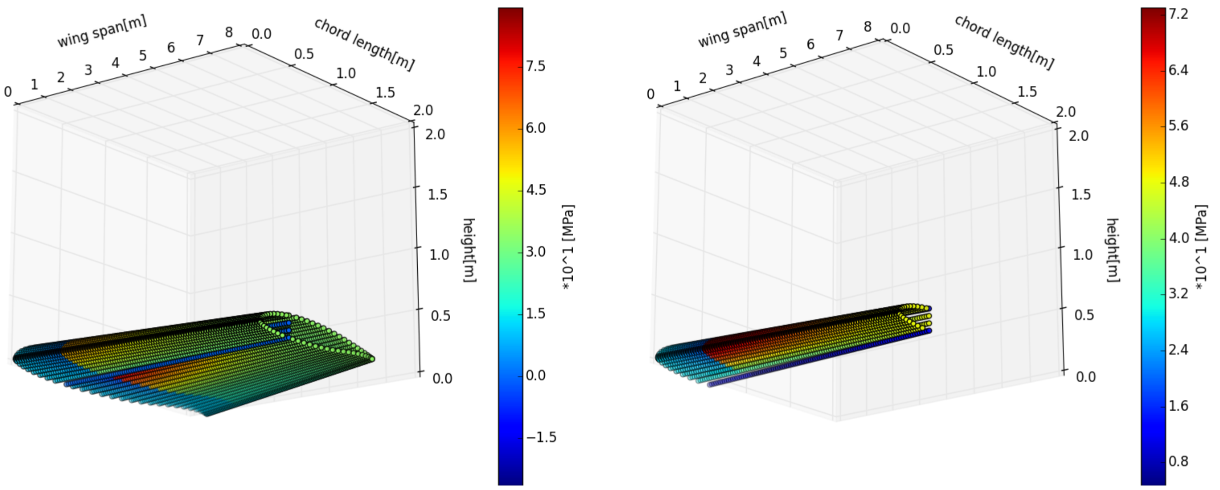

(a) Rigid wing (b) D-cell

Figure B.2: Shear Stresses in the main wing, bottom view

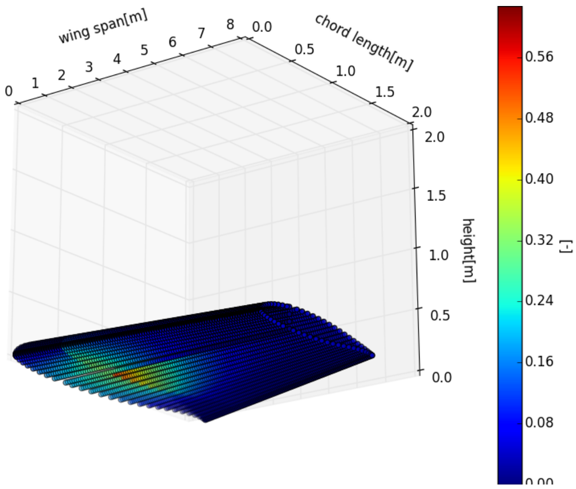

(a) Rigid wing

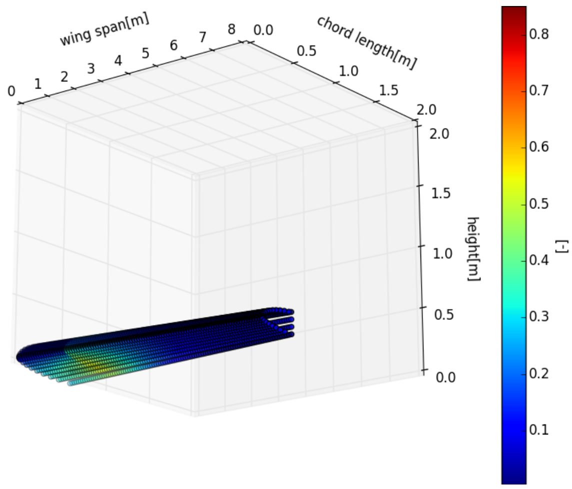

(b) D-cell

Figure B.3: Tsai-Hill failure criterion for the main wing, bottom view

C | Center of Gravity and Moment of Inertia

Table C.1: Center of Gravity and Moment of Inertia

Parameter Unit	m kg	x m	y m	z m	I_{xx} kgm^2	I_{yy} kgm^2	I_{zz} kgm^2
STRUCTURES							
Wing	24	5	0	1.6	539	40	538
Canard	3.4	0.25	0	0	14	20	31
Vtail	8	6	0	0.7	1.6	15	15
Fuselage	8.5	2.5	0	0.2	2.5	14	14
Rest	8	2.5	0	0.4	0.8	13	13
POWER							
Propeller	1	7.8	0	0.5	0	3.6	3.6
Engine	2.5	7.6	0	0.3	0.5	8.6	8.6
Battery min	16	4.1	0	0	8	8	1.1
Gearbox	1.5	7.7	0	0.3	0.3	5.3	5.35
Rest	1.5	4.1	0	0	0.7	0.8	0.1
MOS							
Minimal	3	3.5	0	0.3	0.6	2.1	2
Additional	14	4	0	0.2	4.2 0	4.8	2.3
CONTROL							
Servos	6	4	0	0.7	1.2	1.6	1
Rest	1	4	0	0.5	0	0.2	0.2
AERO							
Windshield	2	3.5	0	0.3	0.4	1.48	1.3
PILOT	90	4.2	0	0.4	8.8	35	29
TOTAL	192	4.2	0	0.5	582	173	666

D | CATIA Technical Drawings

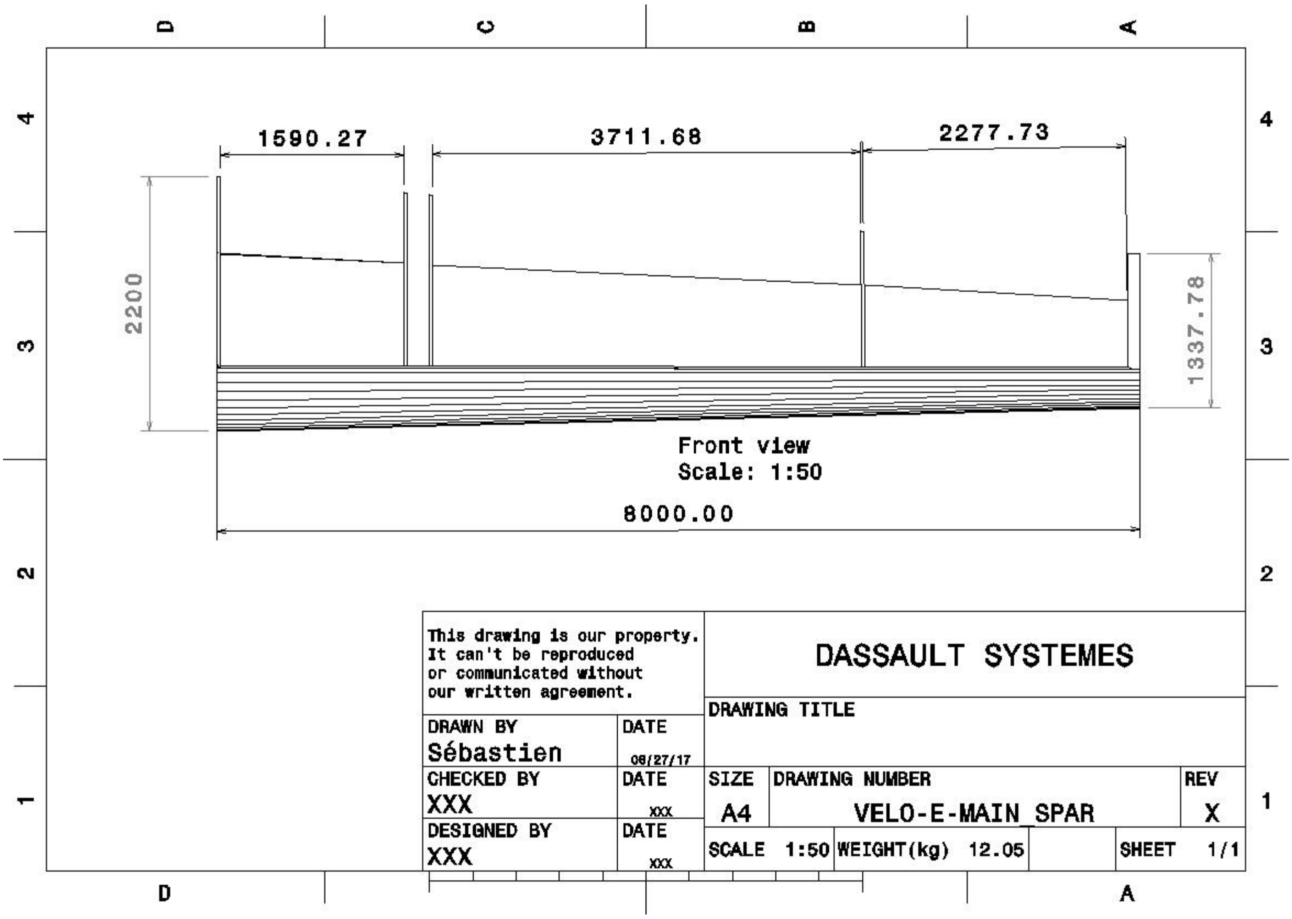

Figure D.1: Technical drawing of the right half of the main wing

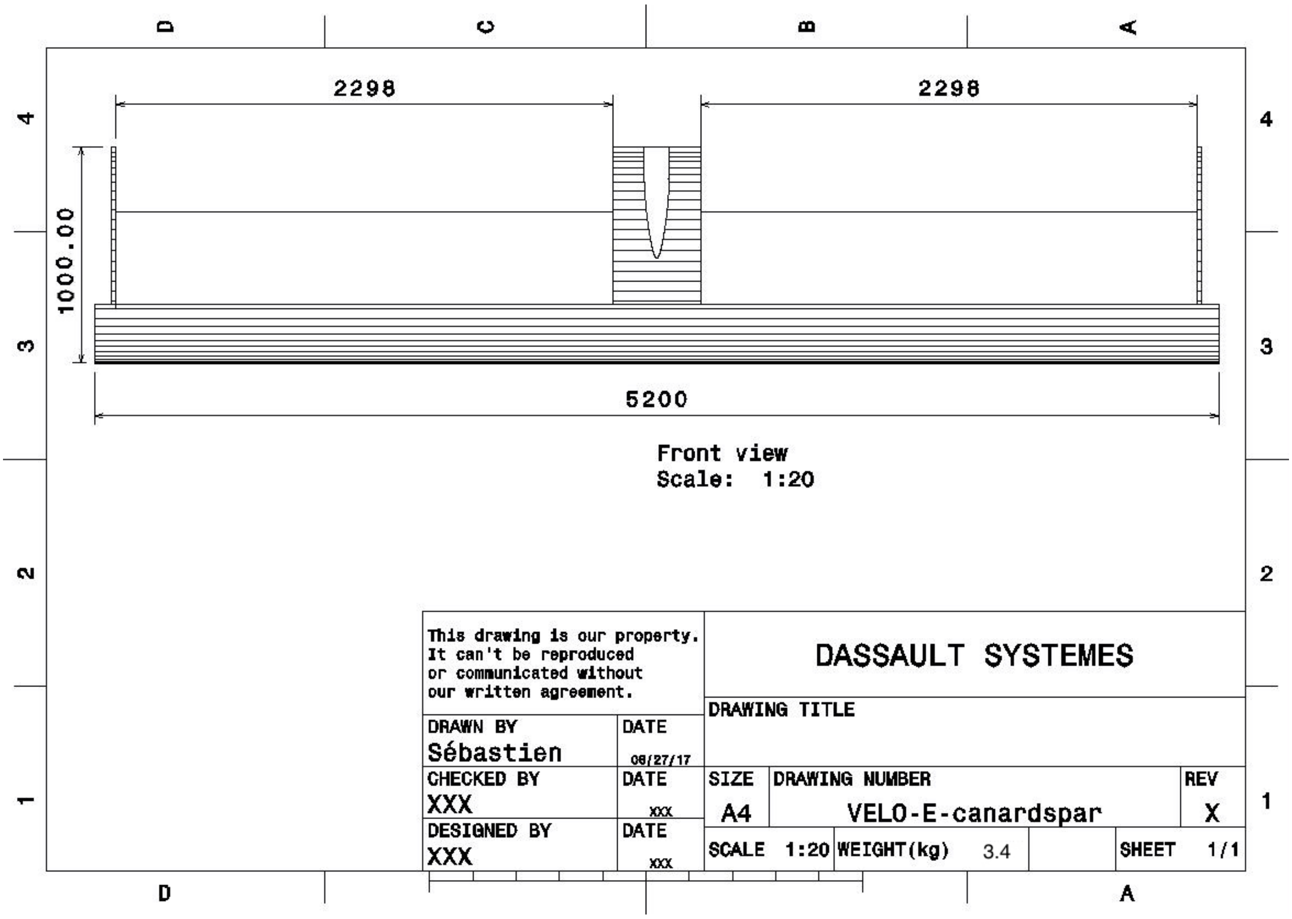

Figure D.2: Technical drawing of the canard

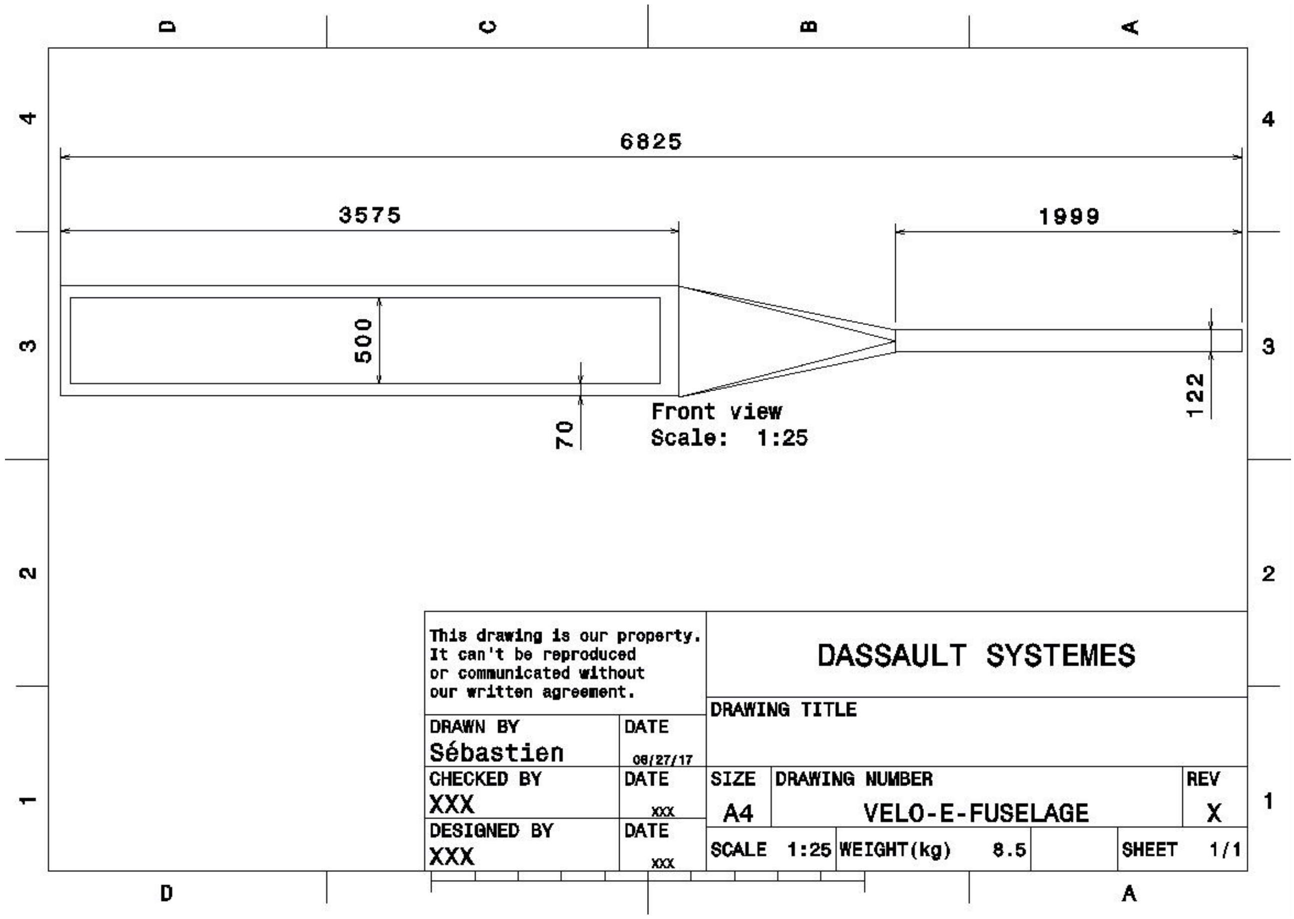

Figure D.3: Technical drawing of the fuselage

E Task Division

Section	Writer	Editor	Contributor
Executive Summary	Everyone	R.A.A. Mink, K.M. Boon, C.S.E. Geuens, W. Schaberg	Everyone
List of Figures		M.J.M. Aarts	N.C. Nyessen
List of Tables		M.J.M. Aarts	N.C. Nyessen
List of Abbreviations		N.C. Nyessen	C.S.E. Geuens, R.J.A. van der Hulst
List of Symbols	C.S.E. Geuens	N.C. Nyessen, C.S.E. Geuens	R.J.A. van der Hulst, N.C. Nyessen
1. Introduction	M.J.M. Aarts	S.J.L.B. Bourier	
2. Mission, Aircraft Configuration & Layout and System Characteristics		W. Schaberg	
2.1 Mission Analysis	R.A.A. Mink	W. Schaberg	
2.2 Aircraft Configuration & Layout	R.A.A. Mink	W. Schaberg	
2.3 Functional Analysis	C.S.E. Geuens	W. Schaberg	R.J.A. van der Hulst
3. Verification, Validation & Sensitivity	S.J.L.B. Bourier	T.O. Rootliep	C.S.E. Geuens
4. Technical Risk Management	W. Schaberg	N.C. Nyessen	
4.1 Approach	W. Schaberg	N.C. Nyessen	
4.2 Risk Events and Mitigation	W. Schaberg	N.C. Nyessen	
4.3 Risk Map Before Mitigation	W. Schaberg	N.C. Nyessen	
4.4 Risk Map After Mitigation	W. Schaberg	N.C. Nyessen	
5. Aerodynamics	C.S.E. Geuens, R.J.A. van der Hulst	W. Schaberg	
5.1 Fundamental Design	C.S.E. Geuens	W. Schaberg, R.J.A. van der Hulst	
5.2 Airfoil Selection	C.S.E. Geuens	W. Schaberg, R.J.A. van der Hulst	R.J.A. van der Hulst
5.3 Planform Design	C.S.E. Geuens	W. Schaberg	R.J.A. van der Hulst
5.4 Drag estimation	R.J.A. van der Hulst	W. Schaberg, C.S.E. Geuens	C.S.E. Geuens
5.4.1 Wing Drag	R.J.A. van der Hulst	W. Schaberg, C.S.E. Geuens	C.S.E. Geuens
5.4.2 Body Drag	R.J.A. van der Hulst	W. Schaberg, C.S.E. Geuens	C.S.E. Geuens
5.4.3 Interference	R.J.A. van der Hulst	W. Schaberg, C.S.E. Geuens	C.S.E. Geuens

Section	Writer	Editor	Contributor
5.4.4 Final Drag Estimate	R.J.A. van der Hulst	W. Schaberg, C.S.E. Geuens	
5.4.5 Other Drag Sources	R.J.A. van der Hulst	W. Schaberg, C.S.E. Geuens	
5.5 XFLR5 Model Description	R.J.A. van der Hulst	W. Schaberg, C.S.E. Geuens	
5.5.1 Airfoil Analysis	R.J.A. van der Hulst	W. Schaberg, C.S.E. Geuens	
5.5.2 3D Wing Analysis	R.J.A. van der Hulst	W. Schaberg, C.S.E. Geuens	
5.6 Design Performance	C.S.E. Geuens	W. Schaberg, R.J.A. van der Hulst	R.J.A. van der Hulst
6. Performance, Power & Propulsion	M.J.M. Aarts	K.M. Boon	N.C. Nyessen
6.1 Performance	M.J.M. Aarts	K.M. Boon	N.C. Nyessen
6.1.1 Cruise and Glide Performance	M.J.M. Aarts	K.M. Boon	N.C. Nyessen
6.1.2 Climb Performance	M.J.M. Aarts	K.M. Boon	N.C. Nyessen
6.1.3 Maneuver Performance	M.J.M. Aarts	K.M. Boon	N.C. Nyessen
6.1.4 Takeoff Performance	M.J.M. Aarts	K.M. Boon	N.C. Nyessen
6.1.5 Soaring	M.J.M. Aarts	K.M. Boon	N.C. Nyessen
6.2 Noise Analysis	M.J.M. Aarts	K.M. Boon	
6.2.1 Lockheed YO-3 "Quiet star"	M.J.M. Aarts	K.M. Boon	
6.2.2 Noise Sources	M.J.M. Aarts	K.M. Boon	
6.2.3 Propeller Noise Comparison	M.J.M. Aarts	K.M. Boon	
6.2.4 Final Estimation	M.J.M. Aarts	K.M. Boon	
6.3 Propeller, Motor, Gearbox and Battery Selection	N.C. Nyessen	K.M. Boon	M.J.M. Aarts
6.3.1 Propeller	M.J.M. Aarts	K.M. Boon	N.C. Nyessen
6.3.2 Motor	N.C. Nyessen	K.M. Boon	M.J.M. Aarts
6.3.3 Battery	N.C. Nyessen	K.M. Boon	M.J.M. Aarts
6.3.4 Gearbox	N.C. Nyessen	K.M. Boon	M.J.M. Aarts
6.4 Hardware Positioning	N.C. Nyessen	K.M. Boon	
7. Stability and Control		N.C. Nyessen	
7.1 Tools		N.C. Nyessen	
7.1.1 Python	R.A.A. Mink	N.C. Nyessen	
7.1.2 Athena Vortex Lattice	J.T. van der Maten	N.C. Nyessen	
7.2 Canard Sizing	J.T. van der Maten	R.J.A. van der Hulst	
7.3 Control Surfaces		R.J.A. van der Hulst	
7.3.1 Layout and Deflections	J.T. van der Maten	R.J.A. van der Hulst	
7.3.2 Mechanism	R.A.A. Mink	R.J.A. van der Hulst	
7.4 Results			
7.2.1 Center of Gravity Range	J.T. van der Maten	R.J.A. van der Hulst	
7.4.2 Eigenmotions	J.T. van der Maten	R.J.A. van der Hulst	
7.4.3 Overall Performance	J.T. van der Maten	R.J.A. van der Hulst	
8. Structures and Materials	K.M. Boon, T.O. Rootliep	N.C. Nyessen	
8.1 Load Cases	T.O. Rootliep	S.J.L.B. Bourier, N.C. Nyessen	R.J.A. van der Hulst
8.2 Assumptions	T.O. Rootliep	N.C. Nyessen	
8.3 Structure	T.O. Rootliep	S.J.L.B. Bourier, N.C. Nyessen	S.J.L.B. Bourier

Section	Writer	Editor	Contributor
8.4 Method			
8.4.1 Lift Distribution	T.O. Rootliep	N.C. Nyessen, S.J.L.B. Bourier	K.M. Boon
8.4.2 Structural Idealization	K.M. Boon	N.C. Nyessen	S.J.L.B. Bourier
8.4.3 Stress Analysis	K.M. Boon, T.O. Rootliep	N.C. Nyessen	S.J.L.B. Bourier
8.4.4 Tsai-Hill Failure Criterion	K.M. Boon, T.O. Rootliep	S.J.L.B. Bourier, N.C. Nyessen	
8.4.5 Deflection	T.O. Rootliep	S.J.L.B. Bourier, N.C. Nyessen	
8.5 Materials			
8.5.1 Laminated Composite Structures	T.O. Rootliep	S.J.L.B. Bourier, N.C. Nyessen	K.M. Boon
8.5.2 Composite Sandwich Panels	T.O. Rootliep	S.J.L.B. Bourier, N.C. Nyessen	
8.5.3 Foam	T.O. Rootliep	S.J.L.B. Bourier, N.C. Nyessen	
8.5.4 Sailcloth	T.O. Rootliep	S.J.L.B. Bourier, N.C. Nyessen	
8.6 Results			
8.6.1 Wings	K.M. Boon	N.C. Nyessen	S.J.L.B. Bourier, T.O. Rootliep
8.6.2 V-Tail	K.M. Boon	S.J.L.B. Bourier, N.C. Nyessen	T.O. Rootliep
8.6.3 Fuselage	K.M. Boon	S.J.L.B. Bourier, N.C. Nyessen	T.O. Rootliep
8.6.4 Tip Deflection	T.O. Rootliep	S.J.L.B. Bourier, N.C. Nyessen	
8.6.5 Ribs	T.O. Rootliep	S.J.L.B. Bourier, N.C. Nyessen	K.M. Boon
8.7 Discussion	K.M. Boon, T.O. Rootliep	N.C. Nyessen	
8.7.1 Sensitivity	T.O. Rootliep	N.C. Nyessen	
8.8 Assembly	T.O. Rootliep	N.C. Nyessen	
8.9 Verification and Validation	S.J.L.B. Bourier	N.C. Nyessen	K.M. Boon
8.10 Recommendations	K.M. Boon,T.O. Rootliep	S.J.L.B. Bourier, N.C. Nyessen	
9. Sustainability	R.J.A. van der Hulst	R.A.A. Mink	
10. Operations	W. Schaberg	J.T. van der Maten	
10.1 Production Transport and Assembly	W. Schaberg	J.T. van der Maten	
10.1.1 Production	R.A.A. Mink	J.T. van der Maten	
10.1.2 Transport	W. Schaberg	J.T. van der Maten	
10.1.3 Assembly	W. Schaberg	J.T. van der Maten	
10.2 Human/Machine interface	W. Schaberg	J.T. van der Maten	
10.2.1 Controls	W. Schaberg	J.T. van der Maten	
10.2.2 Pilot Position	W. Schaberg	J.T. van der Maten	
10.2.3 Pedal System	W. Schaberg	J.T. van der Maten	
10.2.4 Instrumentation and Communication	W. Schaberg	J.T. van der Maten	
10.3 Takeoff and Landing	W. Schaberg	J.T. van der Maten	
10.3.1 Takeoff and Landing with Support Wheels and Skid	W. Schaberg	J.T. van der Maten	
10.3.2 Foot Launched takeoff and Landing without Use of the Support Wheels	W. Schaberg	J.T. van der Maten	
10.3.3 Takeoff and Landing with the Use of a Cart	W. Schaberg	J.T. van der Maten	

Section	Writer	Editor	Contributor
10.4 Operational and Logistic Concept Description	W. Schaberg	J.T. van der Maten	
11. Safety	W. Schaberg		
11.1 Stall and Controllability Behaviour	W. Schaberg	J.T. van der Maten	
11.1.1 Behaviour	W. Schaberg	J.T. van der Maten	
11.1.2 Prevention	W. Schaberg	J.T. van der Maten	
11.1.3 Recovery	W. Schaberg	J.T. van der Maten	
11.2 Turbulence and Gusts and g's	W. Schaberg	J.T. van der Maten	
11.3 Integrity	W. Schaberg	J.T. van der Maten	
11.4 Crash	W. Schaberg	J.T. van der Maten	
11.5 VFR	W. Schaberg	J.T. van der Maten	
11.6 Reliability, Availability, Maintainability and Safety	W. Schaberg	J.T. van der Maten	
11.6.1 Availability	W. Schaberg	J.T. van der Maten	
11.6.2 Maintainability	W. Schaberg	J.T. van der Maten	
12 Market Analysis	C.S.E. Geuens	C.S.E. Geuens	
12.1 The Velo-E-Raptor	C.S.E. Geuens	T.O. Rootliep	
12.1.1 Design Goals	C.S.E. Geuens	T.O. Rootliep	
12.1.2 Cost Breakdown	R.A.A. Mink	T.O. Rootliep	
12.2 Competing Market	C.S.E. Geuens	T.O. Rootliep	
12.2.1 Sailplanes	C.S.E. Geuens	T.O. Rootliep	
12.2.2 Hang Gliders	C.S.E. Geuens	T.O. Rootliep	
12.2.3 Archaeopteryx and Swift	C.S.E. Geuens	T.O. Rootliep	
12.3 Return on Investment	C.S.E. Geuens	T.O. Rootliep	
13. System Lay-Out	C.S.E. Geuens		
14. Results			
14.1 Layout and Mass	T.O. Rootliep, J.T. van der Maten		
14.2 Compliance	J.T. van der Maten	T.O. Rootliep	
14.3 Feasibility Analysis	J.T. van der Maten	T.O. Rootliep	
15. Conclusion	M.J.M. Aarts	S.J.L.B. Bourier, R.J.A. van der Hulst	
16. Recommendations for Further Develepement	R.A.A. Mink	R.J.A. van der Hulst	
16.1 Post DSE Activities	R.A.A. Mink	R.J.A. van der Hulst	
16.1.1 Project Design & Development Logic	R.A.A. Mink	R.J.A. van der Hulst	
16.1.2 Project Gantt Chart	R.A.A. Mink	R.J.A. van der Hulst	
16.2 Other Design Options		C.S.E. Geuens, R.J.A. van der Hulst	
Bibliography		C.S.E. Geuens	
A Derivation of the Math Used in the Python Tool from Chapter 7	R.A.A. Mink		
B COG and MOI	J.T. van der Maten		
C CATIA Technical Drawings	S.J.L.B. Bourier		T.O. Rootliep
D Task Division	C.S.E. Geuens & R.A.A. Mink	C.S.E. Geuens	